Sizing-Design Method and Performance Improvement for Adiabatic Compressed Air Energy Storage Systems

by

Sepideh Sarmast

A thesis
presented to the University of Waterloo
in fulfillment of the
thesis requirement for the degree of
Doctor of Philosophy
in
Mechanical and Mechatronics Engineering

Waterloo, Ontario, Canada, 2024

Examining Committee Membership

The following served on the Examining Committee for this thesis. The decision of the Examining Committee is by majority vote.

External Examiner:	John McCartney Professor, Dept. of Structural Eng., University of California San Diego
Supervisor:	Roydon Fraser Professor, Dept. of Mechanical and Mechatronics Eng., University of Waterloo
Internal Member:	Michael Fowler Professor, Dept. of Chemical Eng., University of Waterloo
Internal Member:	XiaoYu Wu Assistant Professor, Dept. of Mechanical and Mechatronics Eng., University of Waterloo
Internal-External Member:	Maurice Dusseault Professor, Dept. of Earth and Environmental Sciences, University of Waterloo

Author's Declaration

I hereby declare that I am the sole author of this thesis. This is a true copy of the thesis, including any required final revisions, as accepted by my examiners.

I understand that my thesis may be made electronically available to the public.

Abstract

Electrification of the energy system through renewable sources is an effective solution to combat the adverse effects of climate change. Despite the potential, integrating renewables into the electrical grid faces a significant challenge due to their intermittent nature. This intermittency impedes a seamless transition to sustainable, low-carbon electricity systems. In response, grid-scale electrical energy storage (EES) systems facilitate the storage of surplus electricity generated during low-demand periods for subsequent use during peaks. Among various storage methods, compressed air energy storage (CAES) has gained attention for its mechanical nature spanning over four decades. The recent emergence of Adiabatic CAES (A-CAES) facilities, such as the Goderich deployment, emphasizes the need for advancements. A-CAES systems aim to overcome challenges linked to thermal energy storage (TES), which constrains the round-trip efficiency of these systems (TES in A-CAES systems stores compressed air heat for efficient energy recovery).

The present thesis delves into the pursuit of engineering utility-scale A-CAES systems, with a specific focus on system sizing and design considerations. The primary research objectives include introducing a novel CAES sizing method, designing a near-adiabatic CAES system with appropriate thermal energy storage size and design to improve the system performance, and evaluating the compatibility of small-scale CAES systems with wind-diesel systems for remote Canadian communities.

While prior research has explored configurations of A-CAES and TES to enhance round-trip efficiency, certain critical aspects have been overlooked. Previous studies lacked focus on 1) external factors like power grid fluctuations, 2) operational limits in CAES system sizing and design, and 3) challenges in A-CAES operation (as predicted efficiencies often failed during experiments). This thesis aims to address the gaps in the existing literature by investigating the reasons behind these limitations. Potential contributing factors include reliance on generic thermodynamic models, lack of power grid connectivity, neglect of heat losses, and flaws in system designs. The aim is to comprehensively tackle these issues by proposing the sizing and design of a Near-Adiabatic CAES (NA-CAES) system. This approach seeks to rectify the shortcomings identified in previous models and enhance the overall understanding and performance of A-CAES systems.

The first objective, fulfilled in Chapter 3, introduces a new CAES sizing method, the coverage-percentage method. This method builds upon the frequency-of-occurrence method, integrating time-dependent operational constraints, component limitations, and pressure considerations within a CAES reservoir. Applying this method to Ontario's electrical grid data optimally sizes compressors, expanders, and cavern capacities, significantly enhancing the accuracy of capturing excess energy.

The second objective, addressed in Chapter 4, explores the operational limits of A-CAES system components, particularly turbomachines and TES systems. The chapter addresses disparities between theoretical models and practical experiments, employing sensitivity analyses to optimize operational modes. This optimization aims to enhance overall system efficiency while minimizing the required volume of TES. Chapter 4 concludes by determining charging, idle, and discharging profiles for the reservoir and TES of the NA-CAES system, tailored for Ontario, bridging the gap between theory and practical implementation. The results highlight the practicality of the NA-CAES system with a round-trip efficiency exceeding 60%.

In Chapter 5, the study expands its scope by exploring the integration of a partially A-CAES (PA-CAES) system with wind-diesel systems in remote areas. Building on findings from Chapters 3 and 4, the research assesses the performance of a small-scale CAES system, emphasizing sizing, design, operation, and viability in isolated regions. Unlike previous studies focusing solely on diesel engine efficiency, this research analyzes power supply-demand patterns and assesses the full-year performance and feasibility of deploying PA-CAES within wind-diesel hybrid systems using an optimization-based sizing method.

To sum up the research findings, a three-year analysis of Ontario's electrical grid data and an assessment of 82,500 scenarios provide insights for determining the optimal size of a CAES system. The coverage-percentage method highlights the importance of economic considerations to avoid oversizing components. The study identifies that compressors and expanders between 30 MW and 70 MW, cavern energy capacity of 630 MWh to 770 MWh, can capture at least 42% of charging and 26% of discharging capacity in Ontario. Results show that increasing compressor and expander sizes enhance coverage percentages up to an optimal point.

For a NA-CAES system, it is recommended to use a multi-tank TES to efficiently capture compression heat. The ideal number of TES tanks corresponds to the number of expansion units. The choice of thermal fluid does not affect the optimal temperature for TES tanks but depends on the expander inlet temperature. Achieving this optimal temperature involves optimizing mass flow rates for charging and discharging TES fluid and sizing TES tanks appropriately. A constant-pressure reservoir in a CAES system offers greater utilization and flexibility compared to a constant-volume reservoir, allowing longer and more efficient operation periods.

Additionally, investigating the feasibility of an adaptive energy storage system for a remote Canadian community shows potential to reduce diesel fuel dependence. A specific CAES configuration for a remote community, e.g., a 300 kW compressor, 200 kW expander, and 18,000 kWh reservoir, achieves a 55% reduction in diesel fuel consumption, presenting

cost-effective solutions (an initial investment of $5,000,000). Another configuration with a 400 kW compressor, 290 kW expander, and 39,000 kWh reservoir achieves a higher reduction of 63.4%, albeit with a greater initial investment of $10,000,000. These findings contribute to optimizing CAES for both grid applications and sustainable energy solutions in remote areas.

Acknowledgements

I would like to express my genuine appreciation to Prof. Roydon Fraser for his valuable support, guidance, and encouragement throughout this study. I am also grateful to Prof. Maurice Dusseault for his advice and support.

Thanks to my friend, Kamyar Rouindej, for his kind support and friendship. Your advice and insightful discussions always put things in perspective.

I extend my heartfelt gratitude to my husband, my parents, and my sisters for everything you have done to support me in my life.

Dedication

To victims of flight PS752 ...

Table of Contents

List of Figures

List of Tables

List of Abbreviations

A-CAES	Adiabatic Compressed Air Energy Storage
BTM	Behind-the-meter
CAES	Compressed Air Energy Storage
CP	Compressor Power
D-CAES	Diabatic Compressed Air Energy Storage
EP	Excess Power
EXP	Expander Power
GSA	Global Sensitivity Analysis
HTES	High-temperature Thermal Energy Storage
HX	Heat Exchanger
I-CAES	Isothermal Compressed Air Energy Storage
LHV	Low Heating Value
LSA	Local Sensitivity Analysis
LTA-CAES	Low-temperature Adiabatic Compressed Air Energy Storage
LTES	Low-temperature Thermal Energy Storage

NA-CAES	Near Adiabatic Compressed Air Energy Storage
NTU	Number of Transfer Unit
PR	Pressure Ratio
PSH	Power Shortage
RTE	Round-trip Efficiency
SA	Sensitivity Analysis
TES	Thermal Energy Storage
TV	Throttling Valve
VPR-CAES	Variable-Pressure-Ratio CAES

List of Symbols

A	Area
A_1, A_2, A_3, A_4	Constants
α	Thermal Conductivity
B_1, B_2, B_3, B_4	Constants
C	Heat Capacity
C_1, C_2, C_3, C_4	Constants
C_p	Constant Pressure Heat Capacity
C_v	Constant Volume Heat Capacity
$\dot{Q}$	Heat Transfer Rate
δ	Slope of the Expander Efficiency Curve
$\dot{m}$	Mass Flow Rate
η	Efficiency
ϵ	Effectiveness
f	Function
γ	Heat Capacity Ratio
g	Gravity Acceleration

H	Head
k	Conductive Heat Transfer Rate
M	Mass
P	Power
p	Pressure
q	Heat Transfer
Q_c	Cold Temperature Source
Q_h	Hot Temperature Source
ρ	Density
R	Specific Gas Constant
t	Time
T	Temperature
u	Internal Energy
V	Volume
W	Work
ξ	Shape Factor

List of Subscripts

ch	Charging
com, c	Compressor
$disch$	Discharging
el	Electrical
exp, e	Expander
G	Generator
h	Enthalpy
H	High-temperature
$in, 1$	Inlet
ins	Insulation
L	Low-temperature
M	Mean-temperature, Motor
max	Maximum
min	Minimum
n	Time interval index

NG	Natural Gas
$out, 2$	Outlet
P	Pump
res	Reservoir
$surr$	Surrounding
tf	Thermal fluid

Chapter 1

Introduction[1]

Grid-connected energy storage systems (EES) have become increasingly important to address a significant challenge posed by renewable energy sources – their inherent unpredictability [97]. The need for EES arises from two primary factors: (1) unavoidable excess energy production and (2) inadequate generation from renewable sources. Compressed air energy storage (CAES) system is an established EES for MWh to GWh scale applications [183], which can add flexibility to the power grid [61, 52, 150]. However, the operation and performance of CAES systems are currently under investigation due to their low efficiency. This low efficiency stems from the challenge of effectively storing compression heat during the charging mode and subsequently utilizing it during the discharging mode [29].

As of the year 2023, the number of adiabatic compressed air energy storage (A-CAES) systems in operation worldwide is limited, primarily being situated within the experimental or pilot phase [29, 33]. Presently, the Canadian Goderich and Chinese Feicheng A-CAES systems are the only two operational A-CAES systems in the world [33], with respective

[1] This chapter is partially based on the introduction of the following journal article:
Sarmast, S., Fraser, R., and Dusseault, M., (2021), Performance and cyclic heat behavior of a partially adiabatic Cased-Wellbore Compressed Air Energy Storage system. *Journal of Energy Storage* [156].
Sarmast, S., Rouindej, K., Fraser, R., and Dusseault, M., (2023), Sizing-design method for compressed air energy storage (CAES) systems: a case study based on power grid in Ontario. *Energy Conversion and Management* [157].
Sarmast, S., Rouindej, K., Fraser, R., and Dusseault, M., (2023), Optimizing near-adiabatic compressed air energy storage (NA-CAES) systems: sizing and design considerations. *Applied Energy* [158].
Sarmast, S., Séjourné, S., Wigston, A. Fraser, R., and Dusseault, M., (2023), Adaptive hybrid energy system for remote Canadian communities: optimizing wind-diesel systems integrated with adiabatic compressed air energy storage. *Energy Conversion and Management* [159].

power outputs of 1.75 MW and 10 MW. Given this limited number of operational A-CAES systems and the associated challenges in enhancing their efficiency to establish competitiveness compared to other energy storage systems such as batteries, flywheels, gravity energy storage, and pumped-hydro (PH) storage systems, numerous studies have been conducted. These studies aim to assess the performance of A-CAES systems with the primary objective of improving their overall efficiency. The majority of these investigations center around various A-CAES and thermal energy storage (TES) system configurations [131, 119], the integration of CAES with other applications [34], or the economic assessment [16, 146] of these systems. However, comprehensively addressing and assessing the impact of external factors such as the electrical power grid on CAES sizing, design, and operation is crucial. This includes understanding the system's operational limitations, ensuring correct components sizing and design (components configuration), and optimizing CAES and TES operational modes to enhance system efficiency (the ratio of total output work to total input work, see Equation 4.46 in Chapter 4). Additionally, addressing challenges associated with CAES modeling and operation, such as reengineering diabatic CAES (D-CAES) systems for adiabatic operation, is a critical area that has not received thorough examination in previous studies.

This chapter presents the thesis in four parts, which include the motivation, the state-of-the-art in CAES modeling, the research objectives and methods, and an overview of the thesis structure.

1.1 Motivation

Global energy consumption per capita has increased in line with economic expansion, and improvements in living standards, reaching an average of 75.7 GJ per capita in 2022 [36]. North America has the greatest energy consumption per capita (235.6 GJ per capita, more than three times higher than the world average), with a total electricity generation of 5548 TWh (19% of the world's total electricity generation) in 2022. Accordingly, increasing generation capacity from renewable resources is becoming more vital in North America due to environmental legislation and the limitations of fossil fuel resources. However, integrating intermittent and uncertain renewable resources causes challenges such as grid instability, supply-demand mismatch, or elevated electricity costs [26].

The growth in electricity consumption, limitations associated with fossil fuels, and the rise in electricity prices represent only facets of a multifaceted scenario. Notably, the total curtailment of wind and solar energy resources within the state of California has exhibited a notable increase, growing from an average of 25,702 megawatt-hours (MWh) in 2016 to

204,104 MWh in 2022. This upward trend has experienced a dramatic spike, averaging 283,401 MWh during the period spanning from January to September 2023 [9]. This surge in curtailments indicates a greater probability of oversupply situations within California's electricity market, potentially leading to negative electricity prices.

In June 2020, the U.S. Energy Information Administration (EIA) projected that the summer of 2020 would experience the lowest levels of electricity demand in the United States since 2009. This decline in demand was primarily attributed to the COVID-19 lockdowns, where the increases in residential electricity consumption were disproportionately offset by reductions in commercial and industrial operations [6]. Consequently, the need for grid-scale energy storage technologies has surged significantly due to their capacity to address these challenges [97, 149]. Such storage systems facilitate the storage of excess electricity generated by renewables or any sources of energy in unexpected situations, thereby offering a flexible electrical power grid to mitigate the aforementioned challenges.

Although local and relatively small distributed energy storage systems have undergone significant developments, only pumped hydro (PH) and compressed air energy storage systems can combine high storage capacity (in the order of gigawatt-hours, GWh) and high power output (typically some 100 megawatts, MW) to accommodate large fluctuations in wind or solar power generation [15, 148]. Among these two types of energy storage systems, CAES has garnered favor among many researchers, and substantial efforts have been dedicated to developing new technologies aimed at enhancing CAES round-trip efficiency [34].

There is much literature on CAES configurations, that aims to enhance the performance of either existing or proposed CAES systems by proposing innovative TES types and system configurations that can yield notably higher efficiency levels, typically within the range of 50 to 70% [130, 34, 119, 28] (conventional D-CAES systems typically exhibit efficiency levels ranging from 40 to 55% [59]). However, it is noteworthy that a significant number of experimental CAES projects have encountered challenges in achieving efficiency levels within this aforementioned range. This research hypothesizes that possible reasons behind these failures could be generic thermodynamic modeling, non-grid-connected modeling, neglected heat losses, and incorrect design approaches. Furthermore, when examining reported efficiencies, such as the 60% efficiency mentioned for the Canadian Goderich A-CAES system, it remains unclear whether this figure represents an average, median, or maximum value. Additionally, it is unclear whether this efficiency data relates to short-term or long-term CAES operations. Moreover, it is imperative to acknowledge that many apparently A-CAES prototypes or research studies actually fall into the category of near-A-CAES systems. These systems incorporate some degree of external heating to compensate for inherent heat exchanger and TES heat losses. This compensation is typically achieved

through the use of a supplementary electric heater or a combustion chamber [56, 55, 142, 137, 113]. Another point to consider is that only a few research studies have focused on sizing the CAES system using transient power grid data [149, 150]. However, the method used in these studies (referred to as the frequency-of-occurrence method in this thesis) does not provide information on the coverage percentage of a CAES system and may also overestimate the actual coverage percentage, as it does not consider any operating limitations.

Motivated by these challenges in sizing and designing an A-CAES system with a high round-trip efficiency, this Ph.D. research is dedicated to proposing a new CAES sizing method that can accurately size the system components by considering the power grid's supply-demand patterns and incorporating time-dependent operational considerations. Additionally, it aims to address the deficiencies in previous research on CAES sizing and design, which have resulted in discrepancies between the efficiency of experimental and numerical studies (as discussed earlier). The ultimate goal is to identify a feasible operational framework for a near-adiabatic CAES system. Furthermore, the research applies these methods to two real case studies, including designing and optimizing a NA-CAES for Ontario and a hybrid A-CAES for a Northern Canadian community, where "Hybrid A-CAES" denotes a CAES system that does not maximize the use of compression heat and frequently relies on external heat sources for its operation, while a near A-CAES frequently relies on TES for its operation.

1.2 State-of-the-art and Objectives

This section reviews the latest relevant literature on CAES systems and modeling; additionally, Chapter 2 presents a comprehensive background and review of different CAES configurations and other kinds of EES.

1.2.1 State-of-the-art in CAES Modeling

In literature, CAES systems are studied and categorized based on different characteristics as illustrated in Figure 1.1. One main characteristic to classify CAES systems is based on the provided services. Much research has been done to improve the CAES performance for Front-of-the-Meter applications, including frequency regulation, voltage regulation, black start, and peak-shaving [53, 40, 62, 100]. Behind-the-meter (BTM) applications combined with CAES, such as time of use or self-production/consumption, have also been studied [20, 170], as have off-grid applications of CAES [32, 87].

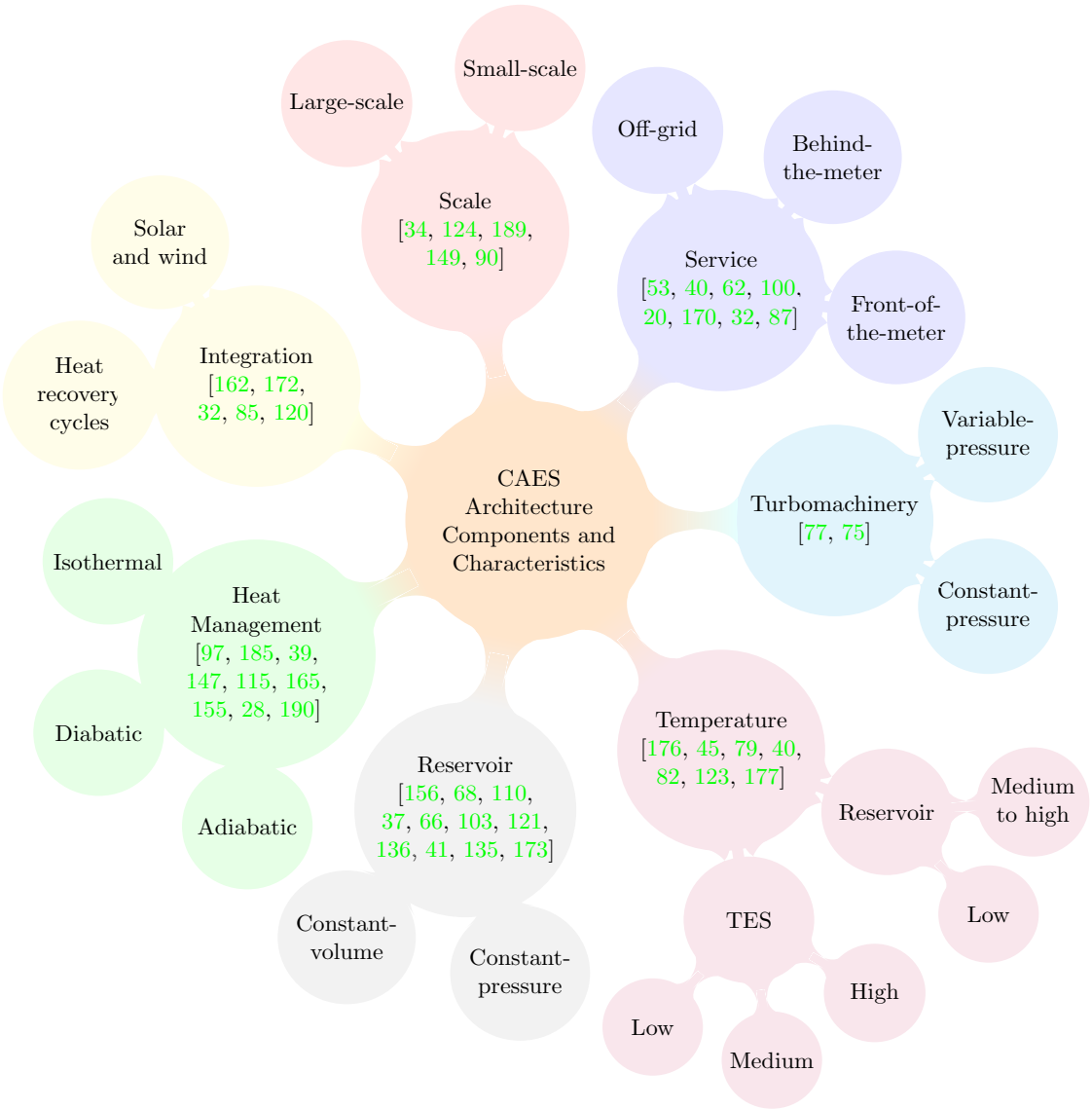

Figure 1.1: CAES architecture components and characteristics.

A second main characteristic to classify CAES systems is their capacity: small-scale (<10 MW) and large-scale (>50 MW) [34]. A few studies have proposed methods to size CAES systems when integrated into other power plants, including both renewable (wind or solar) and non-renewable power plants [124, 189]. A more general sizing method based on CAES operation energy input and output demands, referred to in this paper as the frequency-of-occurrence method, was previously introduced by Rouindej et al. [149], and which includes one of this paper's authors. The frequency-of-occurrence method sizes CAES components utilizing the distribution of surplus power and power shortage, as well as excess energy and energy shortage in terms of frequency. In other words, the frequency-of-occurrence method considers the frequency of CAES charging and discharging events to design an economically feasible CAES system, but it does not consider the specific timing of these charging and discharging events. One study by Jannelli et al. [90] has considered the timing of energy demand for a small-scale CAES system using a numerical iterative approach to fully satisfy the energy demand at a radio station. It should be noted that designing a CAES system to fully meet all energy demands is generally considered uneconomical in the frequency-of-occurrence sizing method.

While many CAES configurations are proposed in the literature, they can be divided into three main categories: diabatic CAES (D-CAES, also known as conventional CAES), adiabatic CAES (A-CAES), and isothermal CAES (I-CAES, which to date has not been implemented) [97]. The main difference between these three systems is their heat management processes. In a D-CAES system, the compression heat, generated during the charging process, is dumped into the environment. Due to the heat of compression losses to the environment during the charging process natural gas heating is utilized by D-CAES during discharging to avoid ice forming as the air cools through the expander [185, 39]. A-CAES systems involve the same water freezing concern, however, they store the heat of compression thermal energy for reuse during expansion to avoid the need for natural gas [147, 115]. The concept of I-CAES is to control heat removal and addition such that the air temperature during compression and expansion remains constant; no practical I-CAES system has been demonstrated to date. Many thermodynamic analyses (energy and exergy analyses) of A-CAES systems have been done to assess system efficiency and performance utilizing different thermal energy storage systems [165, 155, 28, 190].

A-CAES systems can be further classified into three types based on their thermal energy storage temperature: high-temperature (> 400°C), medium-temperature (200 to 400°C), and low-temperature (< 200°C) [176]. A study of high-temperature TES in CAES systems conducted by Biasi et al. [45] assessed the performance of A-CAES with compressor discharge temperature ranging from 380 to 760°C. The results show a 5 % round-trip efficiency improvement for the TES at 760°C compared to the TES at the lower 380°C tem-

perature. A high-temperature hybrid compressed air energy storage (HTH-CAES) system is also presented by Houssainy et al., as a viable solution to eliminate the need for combustion and its associated emissions in a conventional CAES plant [79]. The HTH-CAES incorporates two thermal energy storage units: low-temperature and high-temperature. The low-temperature thermal energy storage (LTES) unit stores the compression heat, while the high-temperature thermal energy storage (HTES) unit acts as a scalable energy reservoir that stores the heat produced by the direct conversion of electricity into heat. In medium-temperature TES, the thermal fluid temperature is between 200 to 400°C. Multi-stage compressors and expanders, along with TES heat exchange between compressors and expanders, are usually used in medium-temperature TES systems [40]. The main advantage of low-temperature A-CAES is the applicability of a liquid TES media which enables the use of common heat exchangers. Moreover, common compressors and expanders can be used when the discharge temperature is around 200°C. To achieve high-pressure low-temperature air, the number of compressors and expanders needs to be increased [82]. Many low-temperature A-CAES designs have been proposed. Examples include the TICC-500 and the LTA-CAES with efficiencies of 41.03%, and 52-60%, respectively [123, 177]. CAES can also be classified based on the air reservoir temperature. Most studies on CAES systems have considered low-temperature (usually equal to the ambient temperature) air reservoirs, while some have investigated the performance of CAES systems with medium to high-temperature stored air [156, 117].

CAES system viability for different pressure repositories, such as above-ground (high-pressure vessels), under-ground (salt cavern, abandoned mines, aquifers, cased-wellbores, and depleted gas wells), and under-water storage reservoirs have been investigated. However, for large-scale CAES systems, the feasibility of CAES remains demonstrated in practice only for salt caverns, which are impermeable and cost-effective [156]. Some mathematical and numerical studies have been conducted on aquifers to study their suitability as a large-scale reservoir for CAES plants [68, 110, 37], but no grid-scale prototype or plant yet exists due to challenges (geological complexity, permeability distribution, and anticline closure radius) [66]. CAES repositories can also be categorized by whether they are constant-pressure or constant-volume. There are also partial CAES systems such as those proposed by Kim et al. and Mazloum et al. in which a constant-pressure CAES system is combined with a pumped hydro storage to minimize air reservoir volume and to leverage the advantage of the higher efficiency of pumped hydro storage systems [103, 121]. The use of under-water constant-pressure energy bags as a repository has also been recently studied [136, 41, 135, 173].

As an improvement, a variable-pressure-ratio CAES (VPR-CAES) system, in which the compressor and expander pressure ratios are not constant, was proposed by He et al. [77],

to decrease the compression input work, while the expander's output work and the round-trip efficiency increase. A similar study conducted by Han et al. on a VPR-CAES system, demonstrated that the compressor's operating condition directly affects the compressor outlet temperature, the compressor power consumption, and the air temperature of the storage, all affect the round-trip efficiency of the system [75].

To enhance the efficiency of A-CAES, recent research has explored its hybridization with various waste heat recovery cycles. Soltani et al. [162] introduced a combination of A-CAES with organic Rankine cycles and Kalina cycles. The performance of this hybrid system was analyzed through the first and second laws of thermodynamics. According to the findings, ORC cycles exhibit the capability to recover a substantial portion of heat and exergy, with the ORC-R290 supercritical cycle demonstrating the highest efficiency at 96.41%. In another study, Wang et al. [172] proposed an integrated combined cooling, heating, and power (CCHP) system that integrates solar-compressed air energy storage and the organic Rankine cycle (S-CAES-ORC) to enhance the part-load performance of small gas turbine-based CCHP systems. The results indicate that the energy efficiency and exergy efficiency of the Solar-CAES with ORC system attain levels of 98.30% and 68.94%, respectively. Furthermore, several investigations have examined the integration of CAES with wind turbines in remote areas, aiming to enhance the efficiency of diesel generators and reduce fuel consumption within the community [32, 85, 120].

1.2.2 Research Objectives and Methods

The primary objective of this research is to provide a new sizing-design method for diabatic and adiabatic CAES systems to better consider the system's external factors such as system operational limitations, and electrical power grid, along with design challenges. The focus is on customizing CAES systems to align with specific, user-defined targets, particularly in terms of energy capturing, system utilization, and efficiency levels. To accomplish this central goal, this Ph.D. thesis is structured around three main objectives. In this section, these research objectives and methods employed to accomplish them are presented[2].

Objective 1: Develop a new CAES sizing method to size a CAES system based on its percentage ability to capture excess energy and deliver energy during a shortage

The first objective of this research entails the development of a novel CAES sizing method, designed to determine the appropriate size of CAES system components based

[2]The contributions and sub-objectives of each objective are presented at the beginning of each chapter in the introduction section.

on its capacity to capture surplus energy and deliver energy during periods of shortage. This new sizing approach, denoted as the Coverage-percentage method, represents an enhancement and refinement of the frequency-of-occurrence method initially introduced by Rouindej et al. [149, 150]. The Coverage-percentage method relies solely on electrical power grid supply-demand data as input (three years of 2018 to 2020) and conducts a comprehensive assessment by evaluating and comparing CAES utilization and coverage percentages across a multitude of scenarios. These scenarios take into account constraints inherent to CAES components, as well as the minimum and maximum pressure limits in the pressure vessel (reservoir) using thermodynamic modeling. This method aims to optimize CAES system sizing, ensuring the achievement of the desired coverage percentage while minimizing component size requirements. Subsequently, this method is applied to Ontario as a case study and undergoes theoretical validation.

This objective is fulfilled and expounded upon in Chapter 3, and it has also been documented in the following scholarly journal publication:
Sarmast, S., Rouindej, K., Fraser, R., and Dusseault, M., (2023), Sizing-design method for compressed air energy storage (CAES) systems: a case study based on power grid in Ontario. *Energy Conversion and Management* [157].

Objective 2: Address the shortcomings in previous research on CAES sizing and design, identify the fundamental causes for the observed discrepancies between round-trip efficiencies in current literature models and experimental results, and determine a system configuration for a nearly adiabatic CAES system

This objective is driven by the need to comprehend the underlying factors contributing to the observed disparity in efficiency between prototypes or experimental studies and numerical simulations. It aims to investigate the reasons behind the discrepancies in these efficiencies, specifically, why experimental studies often fall short. In the context of this research, it is observed that several factors are responsible for these shortcomings. These factors include the oversimplified modeling of heat management, including heat exchangers and TES, the neglect of heat losses within the thermal energy reservoir, the reliance on single-cycle modeling as opposed to grid-connected analyses, the substitution of a diabatic compressed air energy storage combustor with a TES without design modifications, the utilization of a mirrored compression-expansion configuration, and/or limitations in defining efficiency metrics. Therefore, the second objective of this thesis is to develop a novel configuration for adiabatic compressed air energy storage (A-CAES) systems. The primary aim is to maximize the utilization of compression heat during the charging phase and minimize the necessity for a supplementary combustor or heater during the discharging phases. This proposed configuration is denoted as the near adiabatic CAES (NA-CAES) system, which

incorporates a sensible multi-tank TES system. Additionally, the system's operational limits, such as turbomachinery start-up time and minimum load requirements, are considered in thermodynamic modeling, as these factors can constrain system operations and coverage percentages. Furthermore, a comprehensive sensitivity analysis, including both local and global analysis, is conducted to rank the influential parameters for optimization purposes. Subsequently, the newly proposed configuration is applied to the context of the Ontario power grid, serving as a case study to assess system performance, optimize operational modes, and determine the system cycling profiles and inefficiencies.

This goal is accomplished and further elaborated upon in Chapter 4, and it has been published in the subsequent journal publication:
Sarmast, S., Rouindej, K., Fraser, R., and Dusseault, M., (2023), Optimizing near-adiabatic compressed air energy storage (NA-CAES) systems: sizing and design considerations. *Applied Energy* [158].

Objective 3: Assess the viability of a small-scale NA-CAES system in a Northern Canadian community and evaluate the long-term operating performance of hybrid wind-diesel CAES systems in terms of diesel fuel reduction, and cost functions.

The third objective of this research involves integrating a partially A-CAES (PA-CAES) into a wind-diesel power system with the aim of further reducing diesel consumption beyond what can be achieved by the stand-alone wind-diesel power plant. This research specifically targets a small remote community located in Northern Canada. The feasibility assessment of the hybrid wind-diesel CAES system is conducted through the utilization of thermodynamic modeling and optimization processes. The main goal is to attain the highest level of community diesel fuel independence while minimizing the number of wind turbines and the size of the CAES components. This particular objective is expected to yield valuable insights into the feasibility and effectiveness of implementing CAES technology within this remote region, particularly in comparison to other forms of small-scale energy storage solutions, such as batteries. To accomplish this objective, an analysis is carried out on the diesel fuel consumption (demand) and wind power generation from the wind turbines, with a focus on identifying patterns of excess power and power shortages within the community for the year 2021. Furthermore, this research aims to propose an optimization-based sizing strategy for adaptive hybrid energy systems in remote areas. This strategy is intended to be particularly well-suited for regions with a high reliance on diesel fuels, where it is imperative to ensure that any designed system is robust and reliable in providing continuous power to the community.

This objective is achieved and further detailed in Chapter 5, and it has been published in the subsequent journal publication:
Sarmast, S., Séjourné, S., Wigston, A. Fraser, R., and Dusseault, M., (2023), Adaptive hybrid energy system for remote Canadian communities: optimizing wind-diesel systems integrated with adiabatic compressed air energy storage. *Energy Conversion and Management* [159].

1.2.3 Thesis Layout

In accordance with the aforementioned research objectives, this thesis is organized into six chapters. The subsequent section outlines the main chapters of this thesis:

Chapter 1 provides a summary of the research gap, challenges, and the driving factors behind the research presented in this thesis. It is then followed by the research objectives, methods employed, and an explanation of the thesis's overall structure.

Chapter 2 presents a comprehensive review of Large-Scale Electricity Energy Storage (LS-EES), with a particular emphasis on CAES system configurations. Various categories of EES are introduced, followed by a presentation of the CAES concept and its classification. The discussion subsequently delves into the classification of adiabatic compressed air energy storage based on its thermal energy storage system. Ultimately, the chapter summarizes the previous modeling and optimization of A-CAES systems.

Chapter 3 achieves the first objective by introducing a novel CAES sizing method referred to as the coverage-percentage method. This approach integrates time-dependent operational constraints, component limitations, and pressure considerations within a CAES reservoir to improve upon the previous CAES sizing methods in the literature

Chapter 4 delves into the second research objective by exploring the constraints associated with A-CAES system components, specifically turbomachinery and TES systems. It seeks to hypothesize the reasons behind the disparities between theoretical models and practical experiments, conducting sensitivity analyses to optimize operations and achieve heightened efficiency. The chapter concludes with cycling profiles for Ontario's NA-CAES system, demonstrating a round-trip efficiency exceeding 60%.

Chapter 5 extends the research to investigate the integration of a partially A-CAES (PA-CAES) system with wind-diesel systems in remote areas. This chapter focuses on CAES sizing, design, operation, and the feasibility of such integration in remote regions. The assessment of long-term performance and the viability of deploying PA-CAES within wind-diesel hybrid systems are conducted through power supply-demand analysis and optimization-based sizing.

Chapter 6 provides the concluding remarks, peer-reviewed journal papers that have originated from the research conducted during this Ph.D. program, and highlights potential areas for future research.

Chapter 2

Background and Literature Review[1]

This chapter presents an in-depth review of large-scale electricity energy storage (LS-EES), with a specific focus on the configurations of compressed air energy storage (CAES) systems. In Section 2.1, various forms of energy storage systems (EES) are introduced. Following this introduction, the CAES concept and its classifications are presented. Section 2.2 provides a detailed examination of the classifications of adiabatic compressed air energy storage. Finally, Section 2.3 offers a concise summary of the modeling and optimization of adiabatic compressed air energy storage (A-CAES) systems.

2.1 Large-Scale Energy Storage Systems

The worldwide market for renewable energy has the capacity to attain a value of USD 1,600 billion, according to historical compound annual growth rate (CAGR) data, in the forecast period from 2020 to 2027 [13]. The increasing demand for renewable energy is driven by

[1]This chapter is partially based on the introduction of the following journal article:
Sarmast, S., Fraser, R., and Dusseault, M., (2021), Performance and cyclic heat behavior of a partially adiabatic Cased-Wellbore Compressed Air Energy Storage system. *Journal of Energy Storage* [156].
Sarmast, S., Rouindej, K., Fraser, R., and Dusseault, M., (2023), Sizing-design method for compressed air energy storage (CAES) systems: a case study based on power grid in Ontario. *Energy Conversion and Management* [157].
Sarmast, S., Rouindej, K., Fraser, R., and Dusseault, M., (2023), Optimizing near-adiabatic compressed air energy storage (NA-CAES) systems: sizing and design considerations. *Applied Energy* [158].
Sarmast, S., Séjourné, S., Wigston, A. Fraser, R., and Dusseault, M., (2023), Adaptive hybrid energy system for remote Canadian communities: optimizing wind-diesel systems integrated with adiabatic compressed air energy storage. *Energy Conversion and Management* [159].

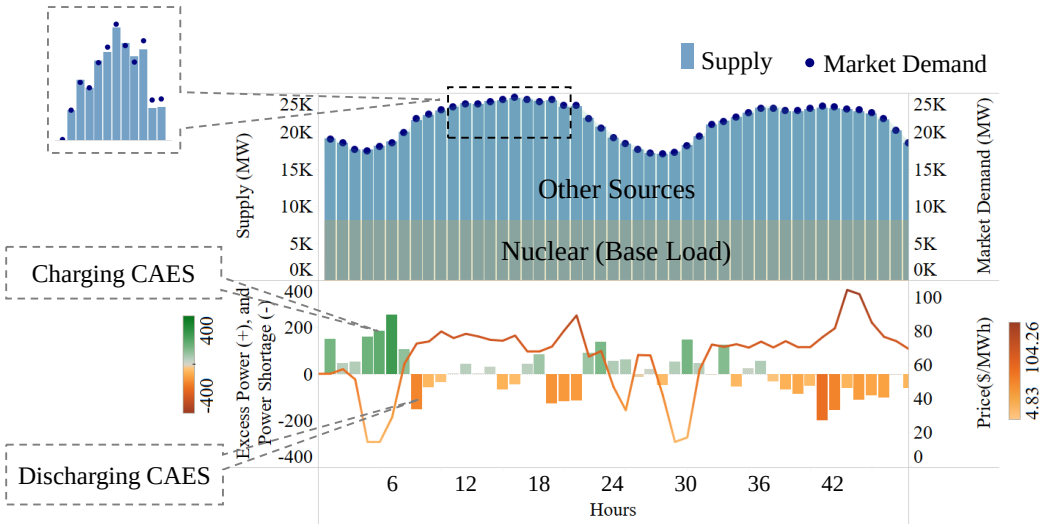

Figure 2.1: Ontario's demand, supply, and hourly price on June 27^{th} and 28^{th}, 2022 [8].

rising greenhouse gas emissions, the limited availability of fossil fuels, and escalating oil prices. Aggressive policy decisions, such as the increase in peak-demand electricity prices in some Canadian cities [19], could further boost this growth. Effective peak demand management can play a crucial role in reducing electricity costs, which can be achieved through EES strategies. EES systems not only manage electricity prices but also address one of the most significant challenges of renewable energy, namely, intermittency (which can vary at time scales from seconds to days).

Moreover, there is always a discrepancy between electricity generation and demand. For instance, Figure 2.1 depicts Ontario's demand, supply, and hourly electricity prices on June 27^{th} and 28^{th}, 2022. As shown in Figure 2.1, although supply follows demand, there is always a surplus or shortage of a few hundred megawatts. The electricity price tends to rise during shortages and decrease during excess power events (and sometimes could be negative). Therefore, grid-scale EES systems have become an essential component of the smart electrical grid, improving reliability and managing electricity prices during peak periods. Table 2.1 summarizes various energy storage systems and their forms, with a focus on large-scale mechanical energy storage methods [97]. Among the different energy storage technologies, pumped hydro (PH) energy storage and CAES, both subgroups of mechanical energy storage, are particularly suitable for grid energy storage.

Table 2.1: Different kinds of ESS system (grid-scale EES are highlighted).

EES type	Different forms
Mechanical Energy Storage	Flywheel energy storage
	Pumped Hydro (PH) energy storage
	CAES energy storage
Electro-chemical Energy Storage	Batteries (Sodium-sulfur, Lithium-ion, Lead acid)
Chemical Energy Storage	Hydrogen and Ammonia
	Methane
Electrical Energy Storage	Superconducting magnetic energy storage
	Supercapacitors

2.1.1 Pumped Hydro Energy Storage (PHES)

Pumped hydro energy storage, developed in the 1890s, is a commercially proven and long-term energy storage technology with an installed capacity of 159.5 GW and an energy storage capacity of 9000 GWh as of 2020 [129]. Half of this capacity is in China, the United States, and Japan [3]. Pumped hydro systems are suitable for grid energy storage due to their adequate energy capacity and long life cycle [126]. A pumped-storage plant operates much like a conventional hydroelectric station. Pumped hydro plants consist of two water reservoirs located at different elevations. During times of low electricity demand, excess electricity is used to pump water to the upper reservoir, with the turbine acting as a pump, moving water back uphill. During periods of high electricity demand, the stored water is released through turbines. The pumped hydro energy storage concept is depicted in Figure 2.2(a). Figure 2.2(b) illustrates a world map with all operational, under construction, and planned pumped-hydro storage plants, providing evidence that pumped hydro is a relatively mature and desirable technology due to its flexible operating range and low operation and maintenance costs [11]. Among its advantages, pumped hydro storage requires a long construction time, has a high investment cost ranging from 500 to 4600 USD/kW, and demands an appropriate geographical location [97]. Moreover, pumped hydro storage has relatively low energy density and is thus used in stationary large-scale energy storage systems [168].

The most consistently growing market for pumped hydro storage lies in the refurbishment of existing plants, accomplished by the installation of newer turbines and generators designed to produce more electricity with less water. Notably, China, Japan, and the United States with capacities exceeding 45,000, 21,000, and 19,000 MW of operating pumped-storage facilities, comprise the top three countries accounting for more than

half of the global fleet of pumped hydro plants [3]. In addition to rejuvenating existing pumped hydro facilities, new projects are also emerging in regions that currently possess limited or no pumped storage infrastructure, including Israel, Australia, Canada, Chile, Argentina, and parts of the Middle East. For instance, in the province of Alberta, Canada, the construction of the Canyon Creek pumped hydro energy storage project received approval in 2019, and it is poised to offer a storage capacity of 75 MW, enabling 37 hours of full-capacity operation [2]. Meanwhile, the Marmora pumped storage facility in Ontario, generating an average of 400 MW of power over 5 hours, is currently under development [4].

2.1.2 Compressed Air Energy Storage (CAES)

Compressed air energy storage represents a type of mechanical energy storage characterized by a power output comparable to Pumped Hydro systems [97]. Its operational history spans several decades, with its inception in Europe during the 1970s, followed by implementation in North America. The CAES system includes four integral components: a compressor, driven by surplus electricity from the grid to compress ambient air; a reservoir, dedicated to the storage of compressed air over a specified duration; a turbine, actuated by the pressurized air; and a generator, intricately linked to the turbine to harness electricity generation during peak-demand periods. The extant literature on CAES has proposed various configurations, but they generally fall into three primary categories: Diabatic CAES (D-CAES), commonly referred to as Conventional CAES; Adiabatic CAES (A-CAES); and Isothermal CAES (I-CAES), which, to date, lacks practical application or demonstration [97, 149, 40]. A main distinguishing feature among these three systems resides in their respective approaches to heat management.

2.1.2.1 Diabatic CAES (D-CAES) System

In a diabatic compressed air energy storage (D-CAES) system, the heat generated during the compression of air is dissipated into the surrounding environment. To mitigate heat loss during the charging process and prevent freezing of the turbine, natural gas is injected into the combustion chamber of the turbine during the discharging phase [76]. Notably, the two currently operational CAES systems, located in Germany and the United States, both employ the D-CAES configuration [97]. However, D-CAES exhibits a drawback in terms of its relatively low round-trip efficiency, with documented input-to-output electricity efficiencies of approximately 46% for the Huntorf plant (in Germany) and 54% for the McIntosh plant (in the US)[76]. The increased efficiency of the McIntosh plant can be

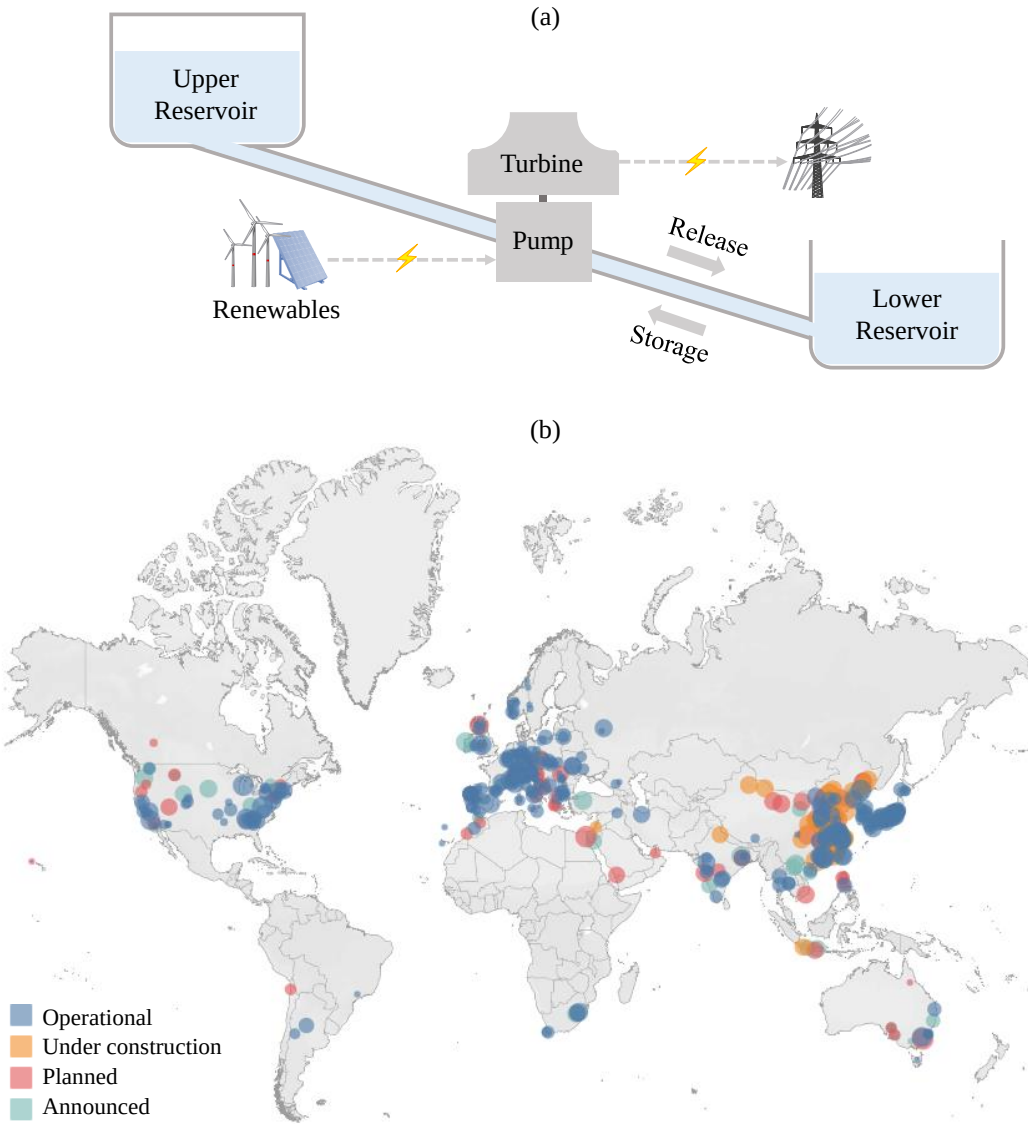

Figure 2.2: (a) Pumped hydro energy storage, (b) World map with all operational, under construction, and planned pumped-hydro storage plants [11].

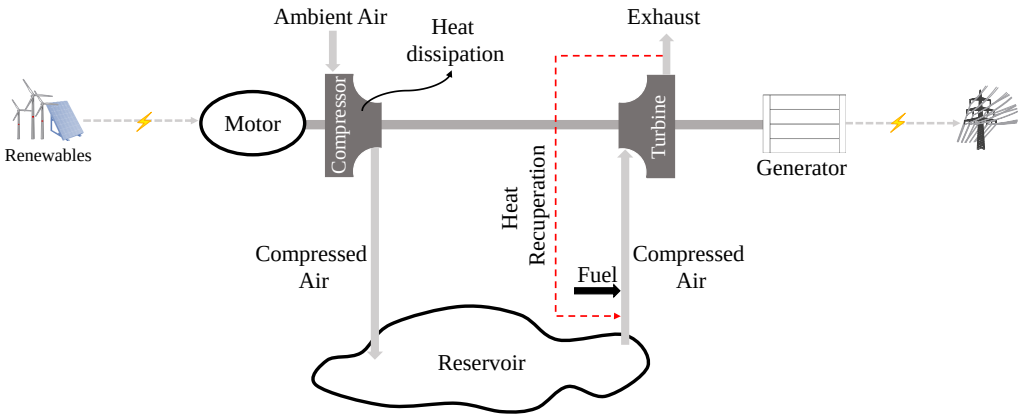

Figure 2.3: D-CAES plant.

attributed to the incorporation of a recuperation process. Figure 2.3 provides an illustrative depiction of the D-CAES system configuration.

2.1.2.2 Adiabatic CAES (A-CAES) System

The operation of Diabatic CAES (D-CAES) and Adiabatic CAES (A-CAES) systems shares similarities, but in the case of A-CAES, thermal energy storage is employed to capture and retain the thermal energy generated during compression, rather than dissipating it into the environment. During the discharging phase, this stored heat is utilized to reheat the air as it exits the cavern, just before it enters the turbine (as illustrated in Figure 2.4). Currently, some A-CAES plants are either in the early stages of planning and experimentation or are under construction worldwide, as outlined in Table 2.2.

It is worth noting that the outlet temperature of the compressor in A-CAES systems can reach as high as 700°C [95]. Consequently, this poses certain technological challenges, particularly concerning the management of elevated temperatures at the turbine inlet. In response to this challenge, alternative concepts such as low-temperature A-CAES have been proposed. In this case, the thermal energy storage temperature ranges from 90 to 200 °C, a considerably lower range compared to the conventional A-CAES design approaches [176].

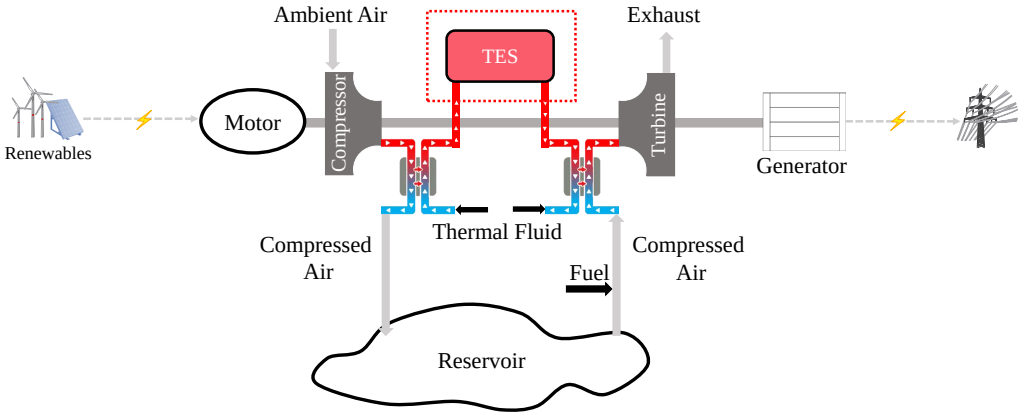

Figure 2.4: A-CAES plant.

Table 2.2: A-CAES facilities in operation (pilot-scale) or under construction in the world [33, 167].

Project	Current State	Power Capacity (MW)	Energy Capacity (MWh)	RTE (%)
TICC-500	Pilot-scale	0.5	0.5	33.3–41.03
ALACAES	Pilot-scale	0.6–0.7	1	-
Toronto, Ontario	Operation	0.7	-	60
Goderich, Ontario	Operation	1.75	10	-
Feicheng, Shandong	Operation	50	300	60
Zhangjiakou, Hebei	Under-construction	100	400	70.2
Zhongyan CAES	Commissioned	50	200	58.2

2.1.2.3 Isothermal CAES (I-CAES) System

In an ideal isothermal CAES (I-CAES) system, the heat removal and expansion processes are controlled to maintain a constant air temperature, as noted by [148]. Essentially, this entails precise adjustments in the temperature of pressurized air during the compression and expansion phases, ensuring that these adjustments occur in infinitesimal increments. This approach is designed to minimize thermodynamic losses of heat energy.

All known I-CAES concepts to date rely on piston machinery capable of executing slow compression and expansion processes. Practical isothermal heat removal systems require extensive heat exchange areas to facilitate efficient and real-time heat extraction. While certain proposals, such as the introduction of controlled water sprays into the plug room of a conventional piston machine, have been suggested [40], it is important to note that this type of CAES remains a conceptual idea without any real-world demonstration or implementation.

2.2 A-CAES Systems Classification

The A-CAES systems have gained significant attention in the literature, leading to a thorough investigation organized into some categories. These categories cover various aspects of A-CAES research and analysis, facilitating a comprehensive understanding of this energy storage technology. These categorizations include modeling approaches, varieties of TES, thermodynamic analysis, sizing considerations, and the integration of A-CAES with other energy systems.

2.2.1 Approaches in A-CAES Modeling

In the literature, the performance and behavior of A-CAES systems are evaluated using three methods: numerical modeling, experimental analysis, and analytical modeling. As of the present, utility-scale A-CAES plants involved in experimental studies appear to be in their early stages, and only limited operational data is available. Some pilot plants have been explored, such as one employing steel tanks with a pressure ranging from 3.05 to 8.65 MPa for air storage and pressurized water tanks for thermal energy storage, achieving an average round-trip energy efficiency of 22.6%. Another pilot plant, located in an underground hard-rock cavern in Switzerland, utilized a combined sensible and latent TES system at high temperatures and reported more promising cycle efficiencies ranging from

63% to 74%. However, it's important to note that this efficiency was estimated using measured mass flow rates and TES inflow/outflow temperatures, as the pilot-scale power plant does not include an expander for power generation. Due to the limitations in experimentally analyzing A-CAES systems, numerical and analytical models are frequently employed in research concerning A-CAES plants.

The most recent research on A-CAES systems predominantly employs numerical modeling, chosen for its inherent simplicity and flexibility to incorporate complexities into modeling. Furthermore, numerical modeling is both time- and cost-efficient when compared to experimental analysis. Examples of numerical modeling can be identified in the works of researchers like Hartmann et al. [76], Barbour et al. [28], Luo et al. [119], Sciacovelli et al. [160], Guo et al. [70], and Tola et al. [166]. Analytical modeling, an alternative to numerical modeling, is another method employed in the literature, and it offers the advantage of enhancing the physical understanding of the system behavior compared to the numerical approach; however, it is more challenging to find mathematical expressions for indicators in complex systems. Examples of analytical modeling can be found in [44, 179, 147]

2.2.2 Varieties of Thermal Energy Storage (TES) for A-CAES Systems

To date, various configurations of A-CAES systems have been proposed, each based on distinct thermal storage media for thermal energy storage [28, 145, 19, 6]. Two primary categories of TES systems exist:

1) Thermochemical energy storage (TCE): In TCE, a medium incorporates chemical components that store and release heat energy through endothermic and exothermic reactions [28, 187, 98].

2) Sensible/latent thermal energy storage (S/L TES): In S/L TES, compressed air comes into contact with a medium via a heat exchanger, which stores the heat either as sensible heat or through a phase change. For instance, sensible heat storage involves heating water, rock, or substances like thermally stable oils and refractory bricks. Latent heat storage, on the other hand, involves phase change, such as the melting of special salts within an insulated vessel [148, 50].

2.2.3 Thermodynamic Analysis of A-CAES Systems

A thermodynamic analysis, including both energy and exergy assessments, is a common practice in the literature when evaluating the performance of adiabatic CAES systems.

Energy analysis primarily focuses on quantifying the total energy input and output within the system, providing a broad assessment of its efficiency by considering the amount of energy lost during compression and expansion processes. In contrast, exergy analysis delves deeper, assessing not just the quantity of energy but also its quality and potential to perform useful work. It identifies sources of irreversibilities and losses within the system, offering a more detailed and insightful perspective on inefficiencies. Exergy analysis is particularly valuable in pinpointing the components or processes with the highest exergy destruction, thus guiding engineers and researchers to improve system performance.

Typically, modeling the A-CAES system involves breaking down the entire system into individual components, as discussed in [82]. The compressors and turbines are often characterized under steady-state conditions, assuming a constant compressor and expander power, which is a reasonable approximation for large-scale systems. This modeling involves considering polytropic or isentropic processes, and the power required for compression and expansion is determined based on parameters such as mass flow rate, pressure ratio, polytropic or isentropic efficiency [148]. Some research also explores transient modeling, as highlighted in the research done by [123]. In the context of heat exchange processes, the outlet air temperature of the compressor is commonly considered as the inlet air temperature for the heat exchanger, typically overlooking pipeline losses and heat losses [190], and heat exchanger effectiveness is often assumed to be constant.

2.2.4 Sizing Considerations for A-CAES Systems

Determining the appropriate sizing strategy for adiabatic CAES systems, including turbomachinery, reservoir, and TES, represents a pivotal decision in the seamless integration of renewable energy sources into electrical power grids. The complexity of A-CAES systems, with various components relying on each other, requires a careful and well-thought-out approach when deciding how to design and size them.

Historically, conventional sizing methodologies have relied on pessimistic scenarios, a practice that has often led to an overestimation of system dimensions, resulting in increased costs [188]. In contrast, an optimal sizing approach takes into account the specific prerequisites of the intended application, the accessible energy resources, and external factors [150, 157]. This perspective is essential to avoid both under-sizing and over-sizing, which, in turn, affects the system's profitability and reliability.

In the context of A-CAES systems, it is notable that no comprehensive study has been undertaken to assess the optimal sizing parameters of TES systems.

2.2.5 Integrating A-CAES Systems with Other Energy Systems

The integration of CAES systems with diverse energy cycles and renewable systems has garnered increasing interest, propelled by technological, economic, and environmental considerations. Research in this field can be classified into two main areas [34]:

1) The integration of CAES with auxiliary or energy conversion systems, with the aim of enhancing CAES performance by addressing concerns such as heat management, fossil fuel usage, and greenhouse gas emissions.

2) The integration of CAES with conventional grids and renewable energy sources (such as wind and solar) to tackle transient behavior and amplify the penetration of renewable energy.

In the first category, studies have investigated the integration of CAES with various technologies, including organic Rankine cycles (ORC) for waste heat recovery [162, 144], desalination technologies for power and freshwater production [143, 91], and biomass systems to harness compression-generated heat [180, 111]. These integrations have been assessed from energy, exergy, economic, and environmental perspectives, emphasizing the potential for optimizing system performance.

The second category of research is concentrated on integrating CAES with intermittent RESs, such as wind and solar power. This integration holds the potential to substantially increase the penetration of renewable energy, offering economic and environmental advantages. However, many studies have been conducted under steady-state [63, 124], whereas the integration of renewables necessitates the adaptation of CAES to intermittent power sources and load fluctuations. To tackle this challenge, there is a growing need for time-dependent models that examine the dynamic behavior of CAES under real-world operating conditions, optimizing CAES design and operation for various energy scales, including microgrids, distribution power systems, and energy markets.

2.3 State-of-the-art in Thermodynamic Analysis and Optimization of A-CAES Systems

this section explores the current state-of-the-art in the thermodynamic analysis and optimization of A-CAES systems, providing a comprehensive list of the latest developments in this rapidly evolving field. The insights and key data are summarized and presented in Table 2.3.

Table 2.3: Characteristics of studies on A-CAES systems.

Literature	Analysis method	Analysis time	System mode	RTE (%)
A-CAES [164]	Energy and exergy analyses	One cycle	Stand-alone	50 (1^{st} law)
A-CAES with low-temperature double-tank TES [55]	Exergy analysis	One cycle	Stand-alone	52.9 (2^{st} law)
A-CAES with low-temperature double-tank TES [71]	Energy analysis and optimization	One cycle	Stand-alone	-
A-CAES-GT [102]	Energy analysis and optimization	One cycle	Stand-alone	60 (2^{st} law): 3.4% increase
Cogeneration-Coupled CAES-ORC [23]	Energy, exergy, exergoeconomic analyses, and optimization	Full year	Stand-alone	$\approx$ 70 (1^{st} law) $\approx$ 50 (2^{nd} law)
Biomass-fired waste-to-energy-A-CAES [73]	Energy analysis and optimization	One cycle	Stand-alone	41.2 (2^{nd} law)
A-CAES [150]	Energy analysis	Full year	Grid-connected	-
PV-A-CAES [49]	Energy analysis	Full year	Grid-connected	33.7 (1^{st} law)
A-CAES [116]	Energy and exergy analyses	One cycle	Stand-alone	$\approx$ 54 (1^{st} law) $\approx$ 71 (2^{nd} law)
A-CAES with packed-bed TES [160]	Energy analysis	30 cycles	Stand-alone	70 (1^{st} law)

Literature	Analysis method	Analysis time	System mode	RTE (%)
A-CAES with packed-bed TES and heat recuperator [132]	Energy and exergy analyses	40 cycles	Stand-alone	57 (1^{st} law)
A-CAES with double-tank TES and recuperators [119]	Energy analysis	One cycle	Stand-alone	potentially reach to around 68 (1^{st} law)
Low-temperature A-CAES [127]	Energy analysis	One cycle	Stand-alone	31 (1^{st} law)
Small-scale A-CAES [128]	Energy analysis	Daily and weekly	Grid-connected	36 (1^{st} law)
A-CAES with double-tank TES[74]	Energy and exergy analyses, and optimization	One cycle	Stand-alone	57 (2^{nd} law)
CCHP integrated with A-CAES [75]	Energy analysis, and optimization	One cycle	Stand-alone	51 (1^{nd} law)
A-CAES [182]	Economy, and reliability analyses, and optimization	Daily	Grid-connected	-
Isobaric A-CAES [121]	Exergy analysis, and exergoeconomic optimization	One cycle	Stand-slone	55 (1^{st} law)
Polygeneration system based on A-CAES [93]	Exergy analysis, and optimization	One cycle	Stand-alone	90-106 (1^{st} law) 55-68 (2^{nd} law)

It is important to highlight that various efficiency definitions are utilized for CAES systems performance in the existing literature. It's crucial to note that not all the values presented in Table 2.3 correspond to round-trip efficiency, as per the definition outlined in Equation 4.46 in Chapter 4, which is the framework adopted in this research.

Chapter 3

Coverage-percentage Sizing method for CAES systems[1]

3.1 Introduction

Correctly sizing a compressed energy storage (CAES) system by considering external power grid requirements, component limitations, and operation restrictions is essential to successfully enhancing a CAES system's usability and effectiveness. Most recent studies on CAES systems have focused on thermodynamic modeling [140, 89, 67, 96], improving the efficiency [89, 60, 67], and cost analysis [16, 146] of the two existing CAES plants, Huntorf, and McIntosh. However, a deeper understanding of the power grid in any specific location and how the CAES system is operating (charging, idling, and discharging) is required when a CAES system is designed. Moreover, the use of CAES systems for energy arbitrage has been mostly studied [152, 48], while arbitrage service revenues cannot usually cover CAES capital costs in most locations [54].

UCD, the user-centered design approach introduced by Rouindej et al. [149] to size CAES systems, can successfully enhance the CAES system's usability and effectiveness by considering the power grid requirements. However, this study only focused on designing a CAES system integrated with gas and wind plants based on Ontario's one-week real-time power trend. Additionally, the sizing method in [149] only considers the supply-demand

[1]This chapter is based on the following journal article:
Sarmast, S., Rouindej, K., Fraser, R., and Dusseault, M., (2023), Sizing-design method for compressed air energy storage (CAES) systems: a case study based on power grid in Ontario. *Energy Conversion and Management* [157].

trend (defining excess power or power shortage, and employing the method of frequency of occurrence) to size the system, while the CAES component's limitations, such as the compressor size or expander size and the minimum or maximum pressure limits in salt caverns (or any kind of reservoir) can have a great influence on the CAES system operation and its correct sizing. Therefore, the main purpose of this chapter which addresses the first objective of this thesis, is to enhance the proposed CAES sizing method in [149], in which an economically feasible CAES system can be integrated with all kinds of power plants in Ontario (as a case study) to increase the share of renewables.

This chapter presents a new sizing method, referred to as the coverage-percentage method, developed and applied to Ontario as a case study, to size a CAES system based on its percentage ability to capture excess energy and deliver energy during a shortage. The coverage-percentage method builds upon and improves upon the frequency-of-occurrence method proposed by Rouindej et al. (2019) [150] by adding time-dependent operation considerations (cavern pressure and temperature), and component limitations (compressor, expander, and cavern sizes). These additional considerations improve both sizing accuracy and usability understanding.

The contributions and novelties of the present chapter can be outlined as follows:

- A comprehensive electrical grid analysis to calculate excess electricity and electricity shortage in Ontario, Canada for three full years: 2018 to 2020.
- Proposing coverage-percentage method to improve the method of frequency of occurrence (proposed by Rouindej et al. [150]) to correctly size CAES systems.
- Comparing the CAES utilization and coverage percentages for 65,550 scenarios, considering the CAES component's limitations, and the minimum and maximum pressure limits in the reservoir.
- Evaluating the effect of CAES component's sizing on charging and discharging power coverage, charging and discharging utilization percentages, compressor and expander loads of operation, and the system performance.
- Verifying the proposed sizing method (coverage-percentage method).

3.2 Method

The focus of this chapter is to size a CAES system based on actual observed electrical grid data. CAES systems can be sized and designed according to three different considerations:

the system cycling profile, the storage capacity, and the system reaction time [150]. These considerations can be either inputs to the design or outputs. For example, if the cycling profile, storage capacity, and system reaction time are fixed then they are inputs to the design outputs of the compressor, expander, and thermal energy storage sizes. In this chapter, the response time is not taken into account in sizing the compressor, expander, and reservoir, but is important for sizing the thermal energy storage (TES) system (presented in Chapter 4). Furthermore, in this chapter, storage capacity (reservoir and components sizes) and cycling metrics (charging, idling, and discharging profiles) are design outputs determined using the coverage-percentage method described in Section 3.2.2 with Ontario grid excess and shortage data as input.

In order to bring coverage percentage and utilization considerations into the sizing of a CAES system not only must the electrical grid excess and shortages be considered as per the frequency-of-occurrence method, but how the system operates needs to be considered as the operation puts constraints on CAES system capabilities. In particular, the new coverage-percentage method developed in this chapter necessarily incorporates CAES system operational limitations. The main focus of the coverage-percentage method is to reach the desired (or maximum) coverage percentage for a CAES system using the smallest, most economical, components. Figure 3.1 presents the coverage-percentage method in relation to the maximum-capacity and the frequency-of-occurrence methods (the two conventional methods used in literature for CAES sizing [34]). It is informative to note that the coverage-percentage method has inputs flowing from the maximum-capacity and the frequency-of-occurrence methods as they reduce the scope of the scenarios considered in the coverage-percentage method leading to fewer, more economical, scenario computations. Given the coverage-percentage method builds upon the maximum-capacity and the frequency-of-occurrence methods, it is clearly a refinement that provides sizing improvements associated with the additional inclusion of operational limit considerations.

The coverage-percentage sizing approach starts with collecting (data collection stage), summarizing visually (data visualization stage), and analyzing statistically (statistical analysis stage) the three-year Ontario hourly electrical grid data by the method of probability of distribution (PD), as described in details in section 3.2.1, in order to size components. This sizing step is based on the frequency-of-occurrence method, proposed by Rouindej et al. [150], in which a CAES can cover the majority of contingencies with the selected components size. In other words, according to the frequency of excess power or power shortage occurrences, the components' size (compressor, expander, and air reservoir) are determined. However, the frequency-of-occurrence method cannot correctly size a CAES system(the results of this chapter show that the frequency-of-occurrence method may overestimate the charging and discharging percentages of a CAES power plant). Therefore, the coverage-

percentage method is later employed to correctly size a CAES system's components. In this method, a thermodynamic model of a CAES system that considers operational limits is used to size the CAES system based on the desired percentage of coverage of charging and discharging events (these terms are defined in section 3.2.2). To size a CAES system by this method several thousands of scenarios (65,550 in this study) need to be run in order to determine coverage percentages. As different components sizes may result in the same coverage percentage, the components size of the scenario with the smallest component sizes (considered most economically viable) is identified as providing the preferred component sizes. It is worth mentioning that the outputs of the frequency-of-occurrence method are considered as upper limits of components size as shown in Figure 3.1 ($(W_{com})_{PD}$, $(W_{exp})_{PD}$, and $(W_{res})_{PD}$ are inputs for the coverage percentage method).

3.2.1 Electrical Grid data Analysis

This study is to size a CAES system for Ontario that can be integrated with any kind of power plant (to store excess power), increase the share of renewables to phase out gas-fired generation and provide reliable electricity services. To achieve this goal, transitioning from designated CAES systems to store bulk energy into more flexible and scalable CAES systems is required. To analyze the Ontario electrical grid, three-year data of hourly power generation and demand (35064 data points which is equal to the summation of hours in three years) was collected from the independent electricity system operator (IESO) [8] and visualized as described in this section. From the data, a probability of frequencies distribution is determined for the observed power excess or shortage occurrences which is then converted to a corresponding energy distribution. From these distributions a minimum size for the CAES system is found that can cover most foreseeable contingencies. This minimum size to cover most contingencies is also the maximum size when economic viability is also considered. Next, the coverage-percentage method is applied by developing a thermodynamic model for the CAES system to be used to identify system coverage and utilization, and to size the components as detailed in sections 3.2.2, and 3.2.3. The terms "coverage" and "utilization" in this study are defined as follows:

- Charging coverage: it refers to the ratio of total storable energy in CAES system to the total excess energy during a given period.
- Discharging coverage: it refers to the ratio of total released energy by CAES system to the total energy shortage during a given period.

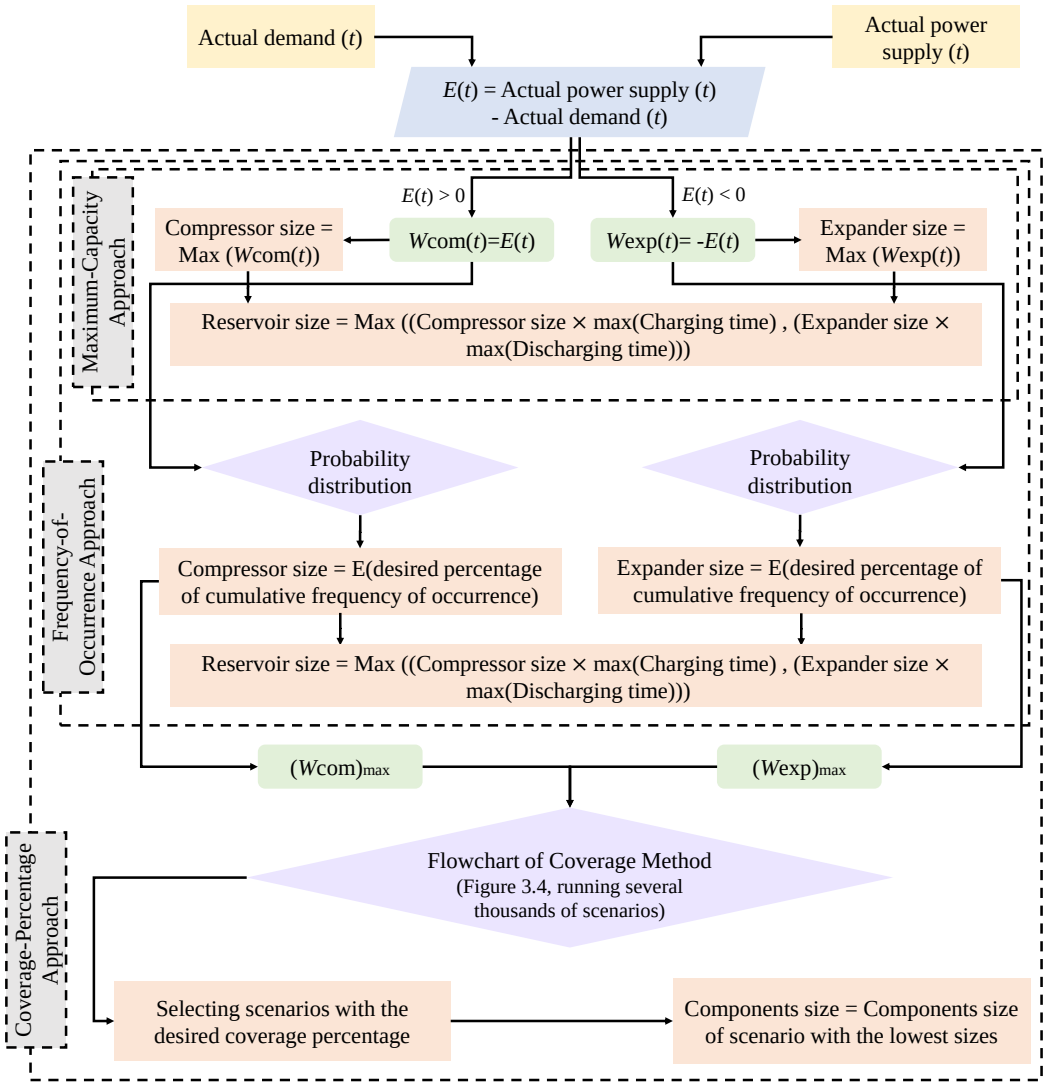

Figure 3.1: Relationship between CAES sizing methods.

- Charging utilization: it refers to the ratio of total hours that the CAES system operates as charging mode to the total hours of a given period.
- Discharging utilization: it refers to the ratio of total hours that the CAES system operates as discharging mode to the total hours of a given period.

where in this study the period is 3 years; where storable energy is equal to the multiplication of the compressor power and charging duration over a given period (compressor power is always less than or equal to the excess power as CAES cannot necessarily cover all excess power situations due to sizing and operational limits), where charging duration is the time the compressor can run while avoiding high pressure and high temperature limits, where released energy refers to the multiplication of expander power and discharging duration during a given period; and where discharging duration is the time the expander can run while avoiding the low pressure and low temperature limit.

3.2.1.1 Data Collection

Hourly Ontario grid operational data (imports, exports, market demand, and supply), as defined in the following, was collected from the IESO public reports website [7] over the period of three years (January 2018 to December 2020) [8].

- Hourly actual imports: hourly actual energy from another jurisdiction (Manitoba, Minnesota, Michigan, New York, and Quebec) into Ontario
- Hourly actual exports: hourly actual energy from Ontario to another jurisdiction (Manitoba, Minnesota, Michigan, New York, and Quebec)
- Hourly market demand: the total requirement, equal to hourly actual Ontario's demand plus hourly actual exports.
- Hourly power supply: the total amount of available resources, equal to the hourly actual internal generation (nuclear, gas or oil, hydro, wind, bio-fuel, and solar) plus hourly actual imports.

The electrical grid data was compiled into a matrix with 35064 records (rows) and twelve fields (columns) consisting of fields for date, time, and different sources of power generation (6 sources in Ontario: nuclear, hydro, wind, solar, natural gas, biofuel), import, export, market demand, and power supply. Raw data was cleaned by removing outliers

which are defined as spurious, one-of, data values more than six standard deviations from their respective mean. After generating the electrical grid matrix, the hourly excess power or power shortage can be calculated by subtracting the hourly market demand from the hourly power supply, where a positive difference implies that excess power is available (a charging or ramp-down event) and a negative difference represents electric supply shortages (a discharging or ramp-up event). Additionally, the duration of each event (charging or discharging) can be defined by finding the summation of consecutive ramp events [150]. Moreover, the total available energy (for charging events)or required energy (if there is an opportunity for a discharging event) can be calculated by multiplication of power by the duration of each event.

3.2.1.2 Data Visualization and Statistical Analysis

To find the pattern and regularities in grid excess or shortage capacity, data visualization is employed. The graphs presented in this section illustrate the magnitude and frequency, and duration, of excess power or power shortage to recognize the required actions that should be taken to ensure the stability of the grid.

- *Excess Power and Power Shortage*

  Figure 3.2 depicts the annual distribution of power grid capacity (excess power or power shortage) for the three years of 2018, 2019, and 2020. It is worth mentioning that the legend is restricted to values of -100 to 100 MW as the majority of charge and discharge capacities are in this interval. Additionally, these charts can rapidly illustrate the pattern of electricity excess or shortage capacity during a year at different hours. The daily pattern of excess or shortage capacity represents how much power is generated in excess or how much power is required at each hour of the day.

  In Figure 3.2, darker colors show hours with excess capacity (opportunity to charge the CAES system), while lighter colors portray hours with a capacity shortage (discharging the CAES system). Based on Figure 3.2, the heat map pattern of excess or shortage capacity is evidently the same for the studied years, but the amount of excess power increased from 2019 to 2020 due to the COVID-19 and lockdown impacts on energy demand [92]. The main advantage of the excess power shortage pattern graphs shown in Figure 3.2 is that they provide a quick way to see how similar or different the operation of CAES will be from year to year, along with revealing a sense of how much excess is available for CAES each year.

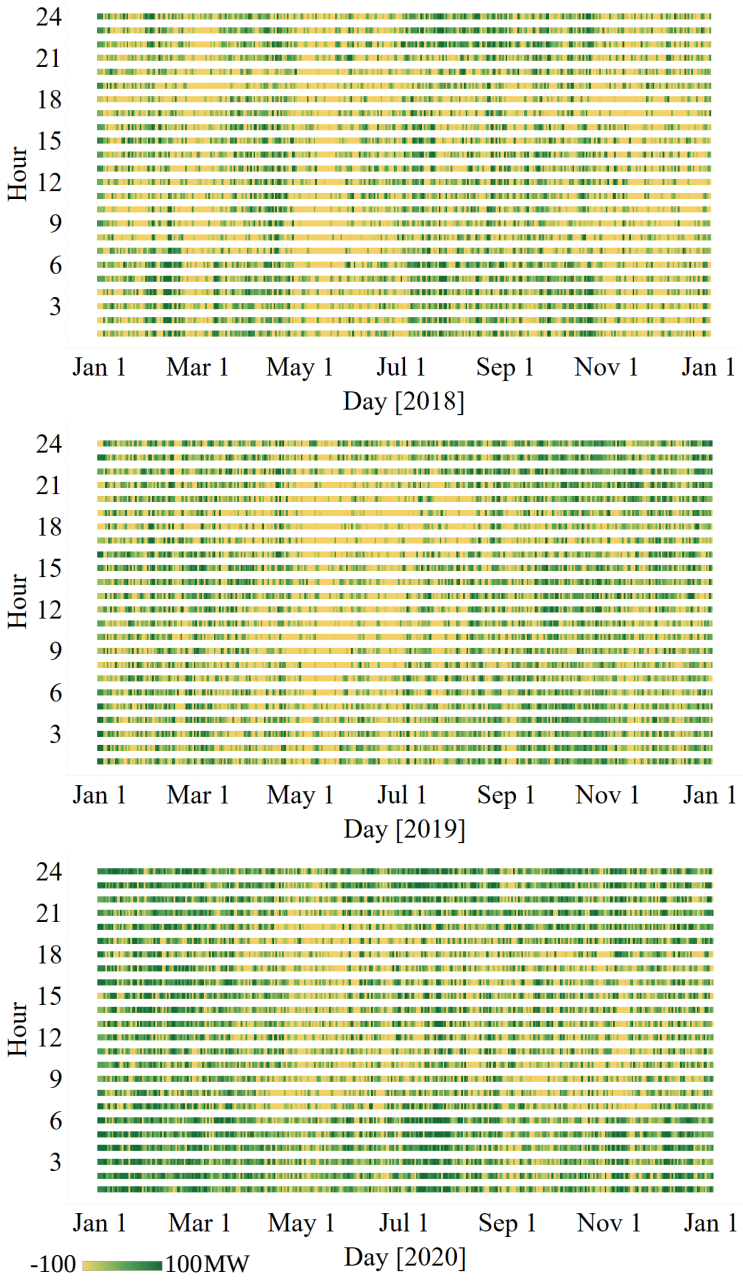

Figure 3.2: hourly excess capacity or capacity shortage due to the difference between market demand and power supply for three years of 2018, 2019, and 2020.

Figure 3.3: Annual frequency distribution of excess power (upper), and power shortage (lower) in Ontario for three years of 2018, 2019, and 2020.

- *Excess Power and Power Shortage Frequency of Occurrence*

  Figure 3.3 depicts the occurrence frequency (in %) of the power requirement to identify the level of excess or required power in Ontario based on available hourly data for the three years of 2018, 2019, and 2020. These graphs can be utilized to rapidly estimate the required capacity (compressor and expander sizes) for most events (charging and discharging) based on the desired percentage of frequency of occurrence. However, these bar graphs do not provide any details about the charging or discharging coverage of CAES, as larger components size does not necessarily result in a higher coverage. Additionally, sizing the CAES system to cover all events will be inefficient as the compressor and expander are operating at part load for most events. Based on the graphs of Figure 3.3, the maximum sizes of the compressor and expander for a CAES system in Ontario are 225 MW and 300 MW (based on the average of frequency of occurrence for three years of 2018, 2019, and 2020), respectively - this is based on the rapid visual observation of few to no events above these values, respectively (less than 1%). The maximum component sizes of the compressor and expander will be used as an input (upper limits) in the coverage-percentage method presented in Section 3.2.2.

- *Excess Energy and Energy Shortage Frequency of Occurrence*

  The same as finding the maximum required power for the compressor and expander (using Figure 3.3), the maximum air reservoir capacity can be determined by the method of frequency of occurrence (analyzing the excess energy or energy shortage (these terms are defined in section 3.2.1) frequency of occurrences). To accomplish this, consecutive excess power or power shortage values are summed to find excess energy or energy shortage in charge and discharge events (as the time interval is 1 hour, 1 KW power is 1 KWh energy). Then, these storing or delivering energy events are categorized into intervals of 50 MWh to identify the frequency of occurrence of events as illustrated in Figure 3.4. Figure 3.4 also depicts the cumulative frequency of occurrence (in %) for both charging and discharge events. Based on the graphs of Figure 3.4, the maximum reservoir size for a CAES system in Ontario is determined to be 300 MWh, in which it can cover around 80% of charging contingencies, while a capacity of 950 MWh is required to cover around 80% of discharging events (based on the average of cumulative frequency of occurrence for three years of 2018, 2019, and

2020). Therefore, the capacity of 950 MWh is considered for Ontario. The maximum reservoir size will be used as an input (upper limits) in the coverage-percentage method presented in Section 3.2.2.

3.2.2 Coverage-percentage Method

The CAES sizing criteria must be determined based on its applications, such as response timing (for spinning and non-spinning reserve services), utilization rates, and coverage rates. This study mainly focuses on the size a CAES system based on the desired charging and discharging coverage percentages, as described in Equations 3.1 and 3.2.

$$\text{Charging coverage percentage} = \frac{A}{B} \times 100 \tag{3.1}$$

$$\text{Discharging coverage percentage} = \frac{C}{D} \times 100 \tag{3.2}$$

where A is total storable energy in CAES during a given period, and B is total excess energy during the same period; and where C is total released energy by CAES during a given period, and D is total energy shortage during the same period. It is worth mentioning that the total storable or released energy (as defined in section 3.2.1) in Equations 3.1 and 3.2 can be limited by the compressor or expander sizes, and the maximum or minimum of air pressure inside the pressure vessel, respectively.

Figure 3.5 depicts a flowchart of the coverage-percentage method. In figure 3.5, based on the power mode (excess or shortage) at each time step (1 hour), the CAES system can operate in charging mode (during excess power), discharging mode (during power shortage), or no action is taken when energy demand and energy supply are matched or when the charging or discharging events cannot occur due to the maximum or minimum pressure constraints in pressure vessel.

At each time step, the air mass and air pressure inside the reservoir (at the end of time step) are calculated. If the mass of air or the air pressure is more than the maximum of upper value or less than the minimum of lower value, the charging or discharging event will only continue as long as the constraints are met (the event will be less than 1 hour in these cases). Accordingly, the compressor or expander running time and its load can be calculated. Then, the extracted heat from the hot compressed air (due to compression) as well as the required heat to heat up the low-temperature compressed air (prior to expansion) are calculated. It is important to mention that the size of double-tank thermal

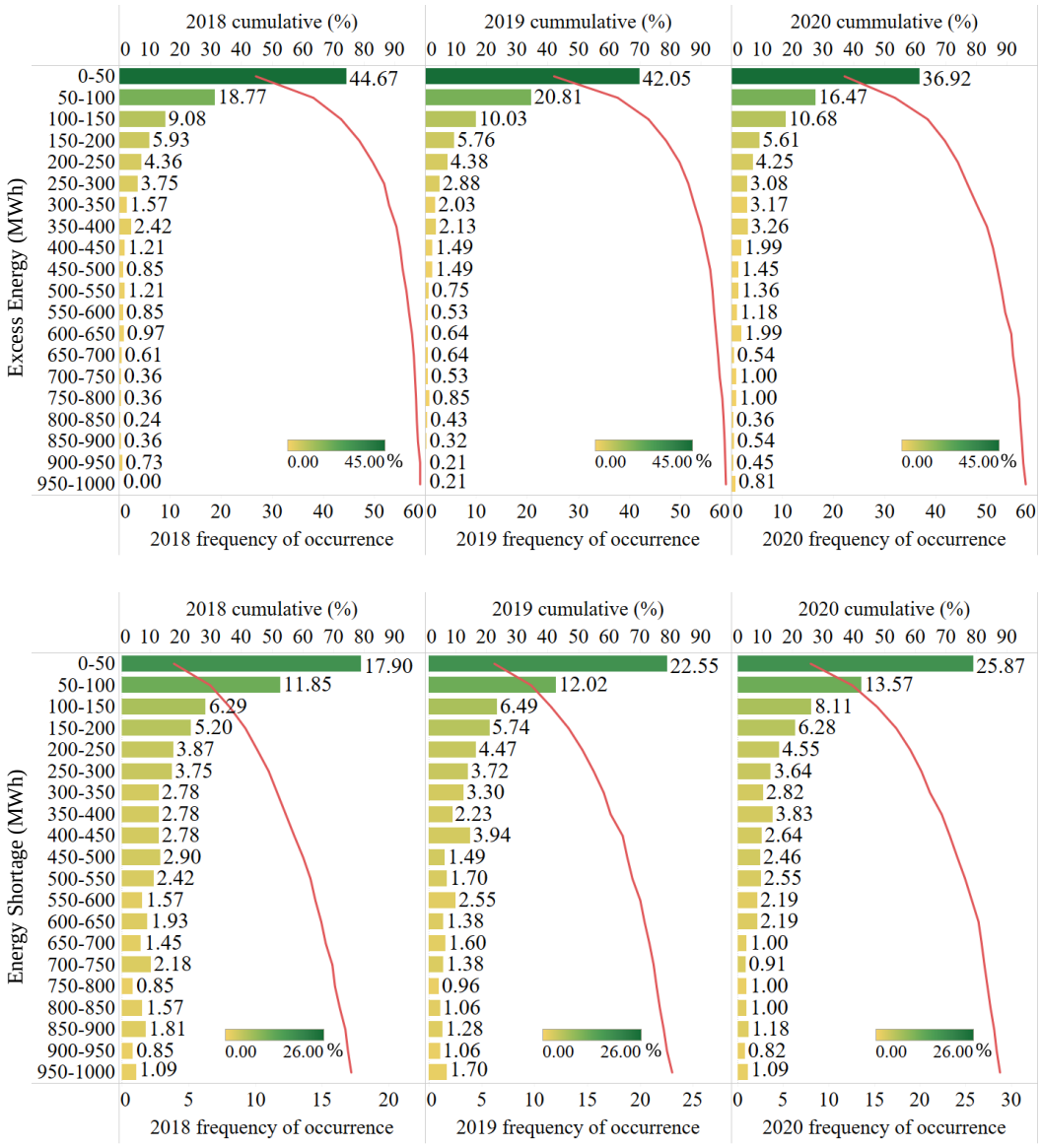

Figure 3.4: Annual frequency distribution of capacity requirement for excess power (upper), and power shortage (lower) in Ontario for three years of 2018, 2019, and 2020. The red lines depict the cumulative frequency of occurrence (%).

Figure 3.5: Flowchart of the coverage-percentage method.

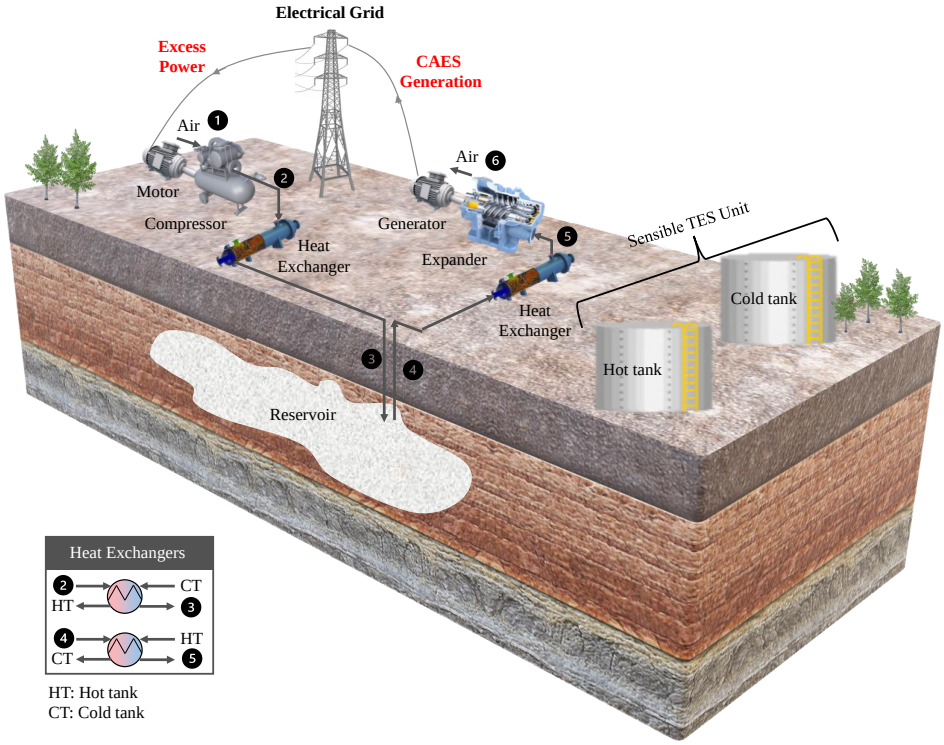

Figure 3.6: CAES system with double-tank heat exchange fluid heat storage.

energy storage is calculated based on known thermal fluid properties and heat exchanger effectiveness.

Applying the coverage-percentage method to three-year electrical data provides useful results on reasonable (not necessarily the optimum, but an appropriate value) sizing of CAES components based on the desired charging and discharging coverage percentages (Equations 3.1 and 3.2). Section 3.2.3 summarizes the thermodynamic equations and models used for the proposed sizing approach.

3.2.3 Thermodynamic modeling

This section presents a thermodynamic analysis of a CAES system and the parameters that can limit system operation (Figure 3.6). For this purpose, the operation of each component, including its thermodynamic formulas, assumptions, and operational limits are reviewed.

- *Compressor*

  The ideal air (compressibility factor=1) is assumed to be compressed from the atmospheric pressure in a single-stage compressor and through an actual process as presented in Equation 3.3 [156].

$$\dot{W}_c = \frac{\dot{m}_c C_p T_{c,in}}{\eta_c}\left[\left(\frac{P_{c,out}}{P_{c,in}}\right)^{\frac{\gamma-1}{\gamma}} - 1\right] \tag{3.3}$$

  where $\dot{m}_c, T_{c,in}, P_{c,in}, P_{c,out}$, and η_c are the rate of mass flow of air, inlet temperature, inlet pressure, outlet temperature, and the compressor isentropic efficiency, respectively. γ represents the heat capacity ratio ($\frac{C_p}{C_v}$), and Specific heat capacities are assumed constant (1006 and 719 $\frac{J}{kg-K}$ at 300 K, respectively). The compressor's output pressure ($P_{c,out}$) and temperature ($T_{c,out}$) can also be calculated using Equations 3.4 and 3.5.

$$P_{c,out} = PR \times P_{c,in} \tag{3.4}$$

$$T_{c,out} = T_{c,in} + \frac{T_{c,in}}{\eta_c}\left[\left(\frac{P_{c,out}}{P_{c,in}}\right)^{\frac{\gamma-1}{\gamma}} - 1\right] \tag{3.5}$$

  It is worth mentioning that the compressor power (compressor size) is a design parameter which can affect the sizing process, and limit the excess power stored during off-peak periods. In this case, Equation 3.6 has been utilized to limit the power which can be stored during charging mode. If compressor power and excess power are labeled by CP and EP respectively, then,

$$\text{Storable power} = \begin{cases} \text{CP} & \text{EP} \geq \text{CP} \\ \text{EP} & 0 < \text{EP} < \text{CP} \\ 0 & \text{EP} = 0 \end{cases} \tag{3.6}$$

  In Equation 3.6, when excess power is greater than compressor power, the compressor can maximally run at full load and compress air at compressor rated power. It means that some part of excess power is lost due to the compressor size (which is EP$-$CP). When excess power is less than compressor power, the compressor runs under part load conditions and no available excess power is lost due to the component sizing limitation. Equation 3.7 shows the compressor load during charging mode and under different conditions.

$$\text{Compressor load} = \begin{cases} 100\% & \text{EP} \geq \text{CP} \\ \frac{\text{EP}}{\text{CP}} \times 100\% & 0 < \text{EP} < \text{CP} \\ 0 & \text{EP} = 0 \end{cases} \tag{3.7}$$

- *Pressure Vessel Charge and Discharge*

  The first law of thermodynamics is applied to a pressure vessel through an open-system isochoric process. It is assumed that the uniform ideal air is entering or exiting the pressure vessel under transient condition while the changes in kinetic and potential energies are negligible [97]. By the aforementioned considerations, the following equations can be applied to the pressure vessel during charging or discharging mode. In the charging mode, $\dot{m}_{out}$ is zero, while $\dot{m}_{in}$ is zero in the discharging mode.

$$\frac{d\rho(t)}{dt} = \frac{\dot{m}_{in} - \dot{m}_{out}}{V} \tag{3.8}$$

$$C_v V \frac{d(\rho(t)T(t))}{dt} = \dot{m}_{in}[h_{in} - h(t) + RT(t)] - \dot{m}_{out}[RT(t)] + \dot{Q} \tag{3.9}$$

$$P(t)V = m(t)RT(t) \tag{3.10}$$

  The mass flow rates of air entering and exiting the pressure vessel, $\dot{m}_{in}$ and $\dot{m}_{out}$, are used in Equation 3.8 to calculate the air density, ρ. In Equation 3.9, T and h are the air temperature and enthalpy in the reservoir (h_{in} is specific enthalpy of injected air). In Equation 3.10, P, V, m, and R, are the air pressure at time t, closed volume of air, total air mass in pressure vessel at time t, and specific gas constant for air, respectively. $\dot{Q}$ can be calculated by Equation 9 in [156].

  The air pressure calculated by Equation 3.10 ($P(t)$) is another design parameter which influences sizing, and limits excess power stored during off-peak periods (capacity of the air storage reservoir) [171]. In other words, the air pressure inside the pressure vessel cannot be higher or lower than the maximum or minimum admissible pressure inside the reservoir, determined by reservoir material and location (if the reservoir is salt cavern). Pressure inside the pressure vessel should be lower than the lowest compressive stress at the pressure vessel wall [35]. Moreover, the deviatoric stress exceeds the strength of the pressure vessel wall and collapse happens, if air pressure goes lower than the minimum allowable pressure [171]. Therefore, in this study

the maximum or minimum permissible pressure limits the charging or discharging events. Equation 3.11 depicts how this restriction is applied to the model.

$$P(t) = \begin{cases} P_{max} & , \quad t_{ch,n} = \frac{m_n - m_{n-1}}{\dot{m}_{in}} & \text{P}\geq P_{max} \\ P & , \quad t_{chordisch,n} = \text{time interval} & P_{min} < P < P_{max} \\ P_{min} & , \quad t_{disch,n} = \frac{m_n - m_{n-1}}{\dot{m}_{out}} & \text{P}\leq P_{min} \end{cases} \tag{3.11}$$

According to equation 3.11, when the pressure at time interval n exceeds the maximum pressure, the charging mode stops and the fraction of time interval over which the system operates is calculated. If the pressure never exceeds the maximum pressure or falls short of the minimum pressure, the system operates during the entire time interval. System operation during the discharging mode stops if the pressure falls to the lower pressure limitation. In this case, the fraction of the time interval that the system operates can be calculated.

- *Expander*

  The actual expansion work, $\dot{W}_e$, can be determined from the first law of thermodynamics [80] by considering a single-stage expander with efficiency of η_e (Equation 3.12).

$$\dot{W}_e = \dot{m} C_p T_{in} \eta_e (PR^{\frac{\gamma-1}{\gamma}} - 1) \tag{3.12}$$

The expander output pressure ($P_{e,out}$) and temperature ($T_{e,out}$) are calculated by Equations 3.13 and 3.14.

$$P_{e,in} = \frac{P_{e,out}}{PR} \tag{3.13}$$

$$T_{e,out} = T_{e,in} + T_{e,in}\eta_e (PR^{\frac{\gamma-1}{\gamma}} - 1) \tag{3.14}$$

Same as the compressor power, the expander power (expander size) is a design parameter which sets an upper limit for the released power during on-peak periods, and can impact the sizing process. Equation 3.15 can be utilized to limit the power which can be released during discharging mode. If expander power (with positive sigh) and power shortage (with negative sigh) are labeled by EXP and PSH respectively, then,

$$\text{Releasable power} = \begin{cases} -\text{EXP} & \text{PSH} \leq -\text{EXP} \\ \text{PSH} & -\text{EXP} < \text{PSH} < 0 \\ 0 & \text{PSH} = 0 \end{cases} \tag{3.15}$$

In Equation 3.15, if the power shortage magnitude ($-PSH$) is greater than expander power, the expander can maximumly expand air at expander rated power. In other words, the expander is unable to release all the required power even if the power is available in the storage vessel due to expander size limits. Also, when power shortage magnitude is less than expander power, the expander operates under part load conditions and generates the power needed for the electrical grid (if the power is available in the reservoir). Equation 3.16 provides the expander load during discharging mode and under different conditions.

$$\text{Expander load} = \begin{cases} 100\% & \text{PSH} \leq -\text{EXP} \\ \frac{-\text{PSH}}{\text{EXP}} \times 100\% & \text{-EXP} < \text{PSH} < 0 \\ 0 & \text{PSH} = 0 \end{cases} \tag{3.16}$$

- *Thermal Energy Storage (TES)*

  The thermal energy increase from compression for A-CAES can be stored in an insulated pressure reservoir (not the case here), in an external thermal energy storage (TES) system, or in the thermal mass of the pressure vessel. As this study is focused on sizing a salt cavern-based A-CAES system for Ontario with an operating temperature range of 20 to 40 $^{\circ}C$ [17], an external double-tank heat exchange TES system has been sized to store the compression-generated thermal energy. The double-tank TES includes two tanks: a cold tank and a hot one. The thermal fluid (could be water, oil, or molten salt) extracts the compression heat through an indirect contact heat exchanger and is then stored in an insulated tank (hot tank). During the power release mode, the thermal fluid goes through another heat exchanger and the heat of the thermal fluid is extracted to heat up the compressed air, and the thermal fluid is then stored in a low-temperature tank (cold tank). It is worth mentioning even though a TES has been used in this study, the proposed model also applies to a CAES system without TES and to any king of pressure reservoir with any temperature and pressure limitations. The following set of equations (Equations 3.17 to 3.23) has be utilized to find the required volume of the TES tanks based on the number of transfer units (NTU) method [69].

$$C_{min} = Min\Big[\frac{\dot{m}_{in} \times \text{Compressor load} \times C_p}{100}, \dot{m}_c \times C_{p,c}\Big] \tag{3.17}$$

$$C_{max} = Max\Big[\frac{\dot{m}_{in} \times \text{Compressor load} \times C_p}{100}, \dot{m}_c \times C_{p,c}\Big] \tag{3.18}$$

$$q_{actual} = \frac{\dot{m}_{in} \times \text{Compressor load} \times C_p}{100} \times (T_{c,out} - T_{inj}) \tag{3.19}$$

$$q_{max} = C_{min} \times (T_{c,out} - T_c) \tag{3.20}$$

$$\epsilon_{HX} = \frac{q_{actual}}{q_{max}} \tag{3.21}$$

$$Q_{TES} = \dot{m}_c \times C_{p,c} \times (T_{c,out} - T_{c,in}) \times \text{Compressor running time} \tag{3.22}$$

$$Q_{TES,acc} = \sum Q_{TES} \tag{3.23}$$

Where, $\dot{m}_c$, $C_{p,c}$, T_c, and ρ_c are the mass flow rate, specific heat of constant pressure, initial temperature, and density of thermal fluid. C_{Min} and C_{Max} represent the minimum and maximum of heat capacity rates (i.e., mass flow rate multiplied by specific heat) of two fluids in heat exchanger. T_{inj}, q_{actual}, and q_{max} in Equations 3.19 and 3.20 are the air injection temperature to the reservoir and the actual and maximum heat that could be transferred between the fluids per unit time, respectively. The heat exchanger effectiveness (ϵ_{HX}) can be calculated from the ratio of actual to maximum heat transfer rate as shown in Equation 3.21. To size the volume of the cold and hot tanks (both the same size), first the heat that should be stored in each charging time step is calculated (matrix of Q_{TES} is calculated). Then, the accumulated heat due to the consecutive charging events is calculated (matrix of $Q_{TES,acc}$).

- *Simulation of CAES Operation*

  To depict the effects of operating parameters and their limitations on the performance of a CAES system and to size the system, an A-CAES is modeled under 65,550 different scenarios with the following considerations:

  1. The system includes a single-stage compressor and expander, a salt cavern as a reservoir (in Ontario), and a double-tank heat exchange TES.

  2. The system operation is limited by the maximum or minimum pressure limits in the salt cavern as well as components sizing.

  3. The cavern behaves as a thermal energy reservoir (TER) with constant wall temperature and constant convective heat transfer coefficient [179].

Table 3.1: Assumed operating parameters in this study.

Parameter	**Value**	**Unit**
Maximum/Minimum pressure in cavern	14/5	[MPa]
Maximum/Minimum temperature in cavern	40/20	[°C]
Maximum/Minimum cavern volume	1360/130,000	$[m^3]$
Compressor and expander pressure ratio	150	[Unitless]
Compressor inlet temperature $T_{in,c}$	300	[K]
Maximum compressor size	230	[MW]
Maximum expander size	300	[MW]
Maximum cavern size	950	[MWh]
Compressor efficiency	0.86	[Unitless]
Expander efficiency	0.92	[Unitless]
Air injection temperature	313.15	[K]
Thermal fluid inlet temperature	293.15	[K]
Thermal fluid heat capacity	4180	[J/kg.K]

4. The cavern capacity is specified in units of energy (MWh), but this capacity is directly proportional to fixed cavern volume.

5. Air acts as an ideal gas.

3.3 Results and Discussions

The main focus of this chapter is to illustrate how the sizing of different components (compressor, expander, and reservoir) of a CAES system affects its coverage percentages, utilization percentages, and system performance. The results indicate that an increase in the components size does not necessarily improve the coverage and utilization percentages. This means that a small-scale CAES system with much smaller components that are required to meet the Ontario electrical grid needs may have the same coverage and utilization percentages as a large-scale CAES, which can cover all charging or discharging events. Moreover, the presented results clearly confirm that consideration of design parameters such as the maximum or minimum pressure limits inside the pressure vessel (salt cavern here) can greatly impact the correct sizing of a CAES system. In other words, the method of frequency of occurrence proposed by [150] overestimates the coverage percentage of a CAES. A more accurate coverage percentage in the design of a CAES system is achieved using the new coverage percentage method presented in this chapter (Sections 3.3.1 to

3.3.7).

3.3.1 Power Utilization

As defined in section 3.2.1, power utilization is the percentage of hours the CAES system is operating in either charging or discharging mode. For example, the charging power utilization can never be 100 % because at some point the CAES system must discharge, however, the sum of the charging power utilization and the discharging utilization will be 100 % if the CAES system never rests and is always charging or discharging. In short, the power utilization does not indicate the coverage of available power (to be stored or released), however, it can easily illustrate that the components' size should be determined based on the grid requirements in any location. Figure 3.7 depicts the density of charging and discharging power utilization vs. components sizes for 65,550 scenarios (23 different compressor sizes with an interval of 10 MW and starting from 10 to 230, 30 different expander sizes with the interval of 10 MW and starting from 10 to 300, and 95 different cavern sizes with the interval of 10 MWh and starting from 10 to 950) based on three years real grid electrical data from 2018 to 2020 (26,304 hours). The dark green areas on the graphs show a higher density of values which reveals locations where both small and large components have nearly the same percentage of utilization, and thus, if cost is monotonic with component size, for lower cost economic reasons the smaller components would be preferred. Figure 3.8 displays the influence of compressor, expander, and cavern sizes on power utilization. Figure 3.8 observations are as follows:

- For a cavern and a constant 50 MW compressor size, the charging power utilization increases by increase in expander size and remains fairly constant after 100 MW (the size of majority of power shortage in Ontario based on data visualization results (Figure 3.2)). However, the discharging power utilization decreases by an increase in expander size and remains fairly constant for expanders greater than 100 MW. That is, the larger the expander, the greater the decrease in the state-of-charge (SOC) percentage, and the more opportunity to store power and to do so faster if the excess power is available.

- For a cavern and a constant 50 MW expander size, the charging power utilization decreases by increase in compressor size and remains fairly constant after 100 MW (the size of majority of excess power in Ontario based on data visualization results (Figure 3.2)). However, the discharging power utilization increases by an increase in compressor size and remains fairly constant for compressors greater than 100 MW.

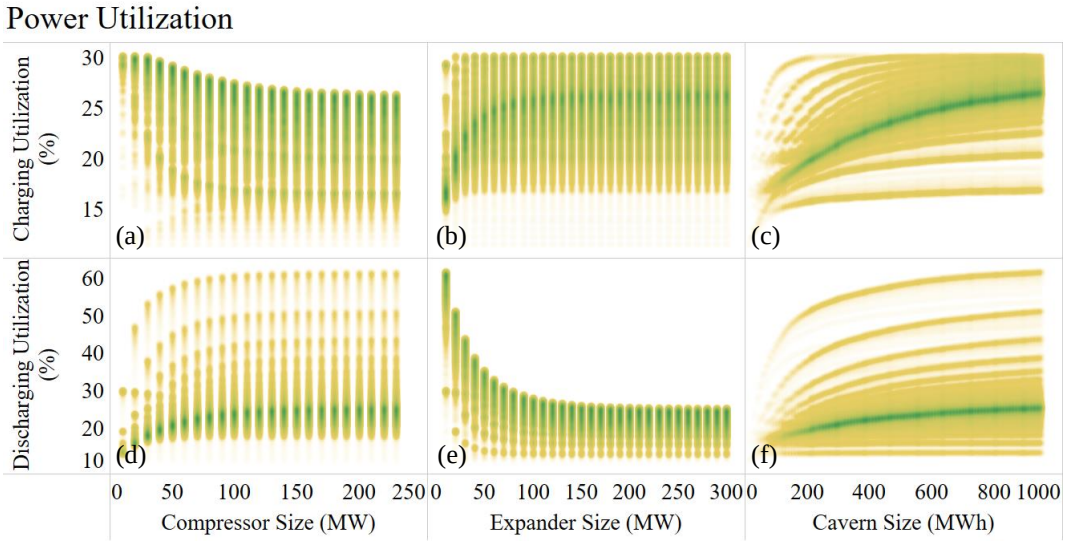

Figure 3.7: Density of charging and discharging power utilization of a CAES system vs. component's sizing for 65,550 scenarios (upper: charging operations, and lower: discharging operations; dark green shows higher density).

That is, the larger the compressor, the greater the increase in the state-of-charge (SOC) percentage, and the more opportunity to release power

- For both constant compressor and expander sizes, both charging and discharging power utilization increase with increasing cavern size.

It is informative to understand why the shading in Figure 3.7 is not continuous, an observation most evident in Figures 3.7(c) and 3.7(f). The source of the apparent lines and striped patterns in Figure 3.7 are an artifact of the necessarily finite number of scenarios are run. For example, in Figure 3.7(f) the striping above the dark green line occurs between discrete jumps in the expander sizes with each line corresponding to a given expander size, while other parameters are varied in the scenarios analyzed to give the line their width. Corollary, the white space implies that the utilization in these regions is very sensitive to expander size for the smaller expanders (10 MW to 40 MW). As a second example, in Figure 3.7(c) the apparent lines towards the bottom of the graph are the result of the discrete nature of expander sizes (for the smaller expanders of 10 MW to 40 MW), but the lines in the upper left are the result of the discrete nature of the compressor sizes (for the smaller compressors 10 MW to 30 MW).

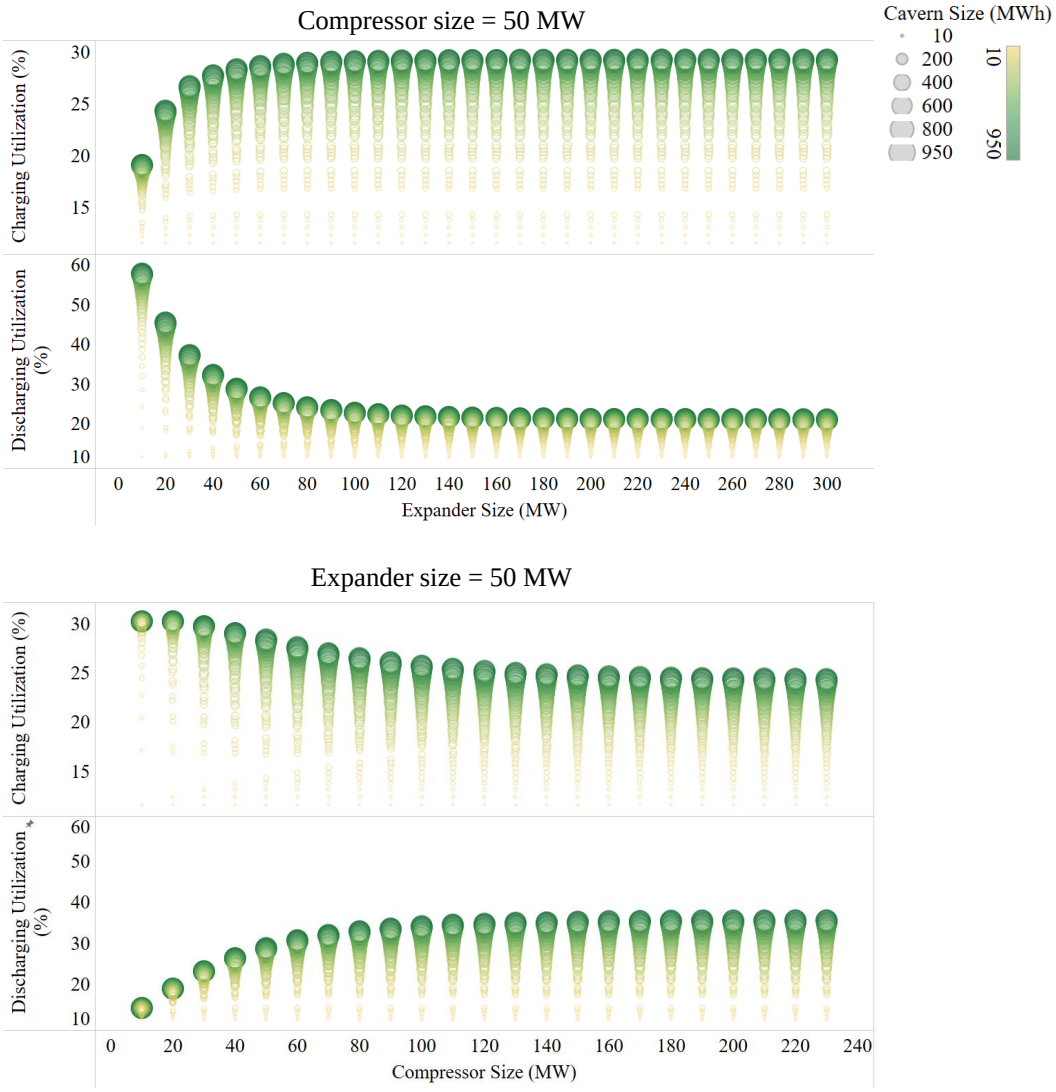

Figure 3.8: The effect of components sizing on the power utilization (bigger circles display bigger cavern size).

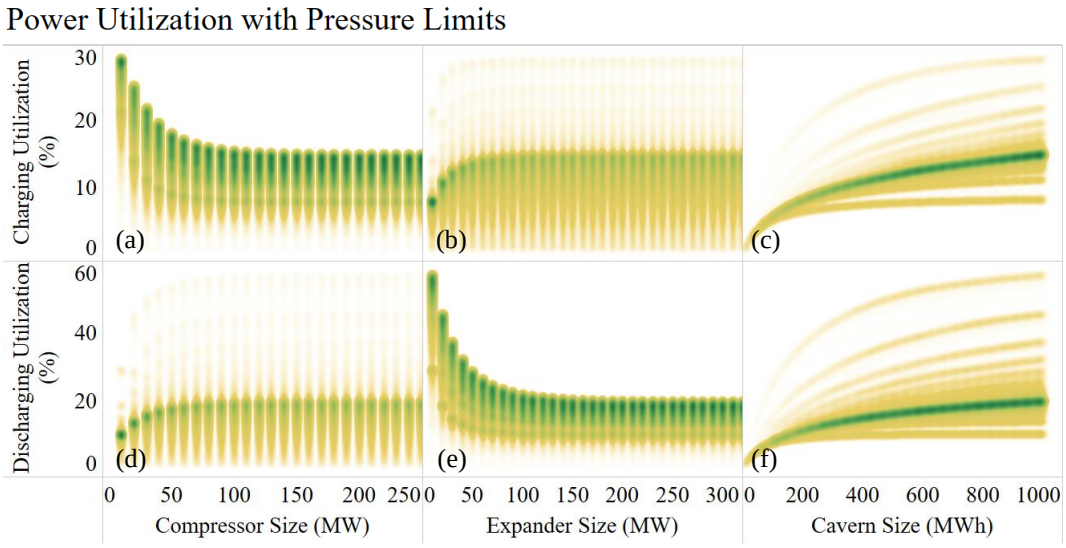

Figure 3.9: Power utilization of CAES system with maximum or minimum pressure limits vs. component's sizing for 65,550 scenarios (upper: charging operations, and lower: discharging operations; dark green shows higher density).

3.3.2 Power Utilization with Maximum or Minimum Pressure Limits

The air pressure inside the cavern is limited to minimum and maximum values, depending on the cavern material and location, to prevent wall collapse. This pressure limitation restricts CAES system operation even if excess power is available to be stored, or if there is a power shortage in need of CAES energy. Figure 3.9 illustrates the density of charging and discharging power utilization by considering the pressure limitations inside the salt cavern for 65,550 scenarios as described in section 3.3.1. Comparing the results of Figures 3.7 and 3.9 reveals the following:

- Cavern maximum and minimum pressure limits decrease charging and discharging power utilization, respectively. This decrease is larger for larger component sizes.
- The change in density distribution from Figure 3.7 to Figure 3.9 is a direct result of applying the pressure limits, in which the lowest charging and discharging power utilization percentages drop by 89% and 84%, respectively. Therefore, even though the compressor and expander are large enough to cover or release power, the system is not operating due to the cavern pressure limitations.

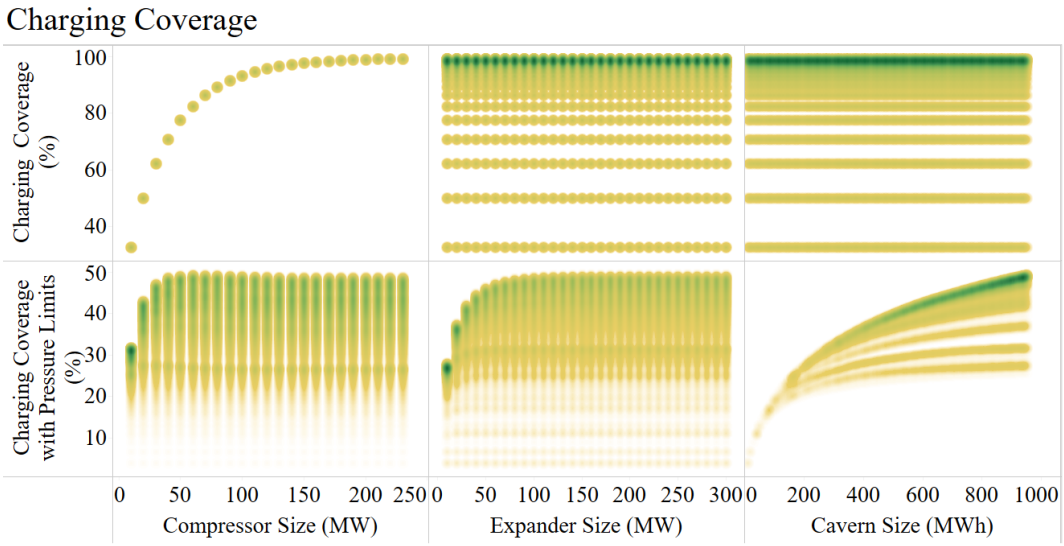

Figure 3.10: Density of charging coverage percentage for a CAES system vs. component's sizing for 65,550 scenarios (upper: without cavern pressure limits, and lower: with cavern pressure limits; dark green shows higher density).

- The patterns for power utilization with pressure limits vs. compressor size, expander size, and cavern size follow the same trends as shown in Figure 3.8, described in section 3.3.1.

3.3.3 Charging and Discharging Coverage Percentages

Although power utilization graphs for a CAES system provide insights into the the percentage of total hours that the system is operating, it does not give any information about the system coverage and the percentage of excess power that can be stored during off-peak periods (or what percentage of required power can be released by the CAES system during on-peak periods). Therefore, Equations 3.1 and 3.2 presented in section 3.2.2 are used to evaluate the system viability, and then to size the system as small as possible for anticipated economic savings. Figures 3.10 and 3.11 illustrate the density of charging and discharging coverage percentages for 65,550 scenarios, respectively. Figures 3.12, and 3.13 display the influence of compressor, expander, and cavern sizes on the charging and discharging coverage percentage as well. Comparing the results of Figures 3.10 and 3.12, as well as Figures 3.11 and 3.13, reveals the following observations:

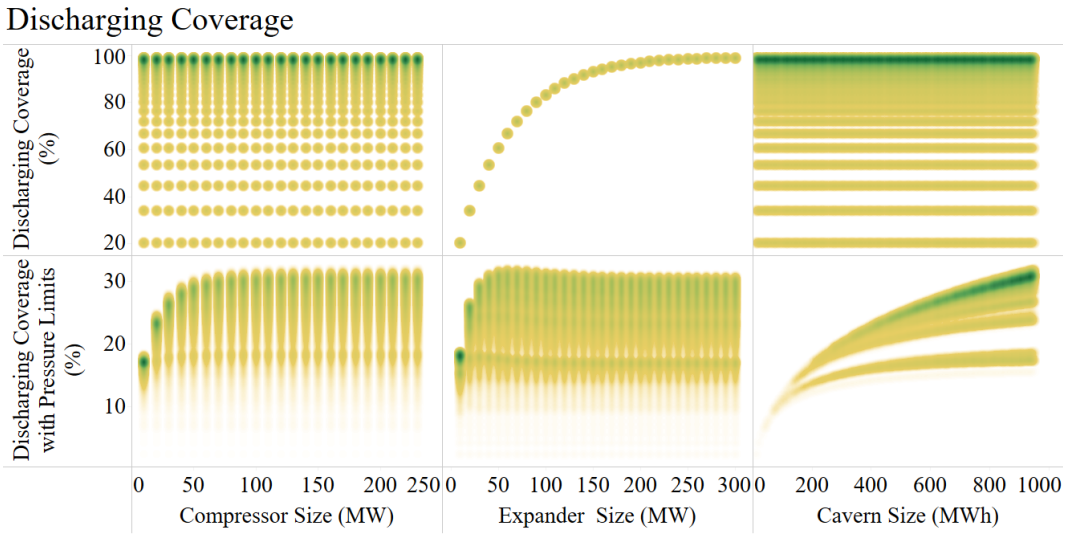

Figure 3.11: Density of discharging coverage percentage for a CAES system vs. component's sizing for 65,550 scenarios (upper: without cavern pressure limits, and lower: with cavern pressure limits; dark green shows higher density).

- For a cavern and a constant 50 MW compressor size, the charging coverage percentage is not dependent on the expander and cavern sizes if the air pressure limitations are not considered, in CAES modeling. However, the results reveal that the charging coverage percentage increases exponentially, approximately, when the compressor size increases, and approaches 100 % when the compressor size exceeds 100 MW.

- For a cavern and a constant 50 MW expander size, the discharging coverage percentage is not dependent on the compressor and cavern sizes if the air pressure constraints inside the cavern are not taken into account in CAES modeling, but the discharging coverage percentage exponentially increases when the expander size increases, and approaches 100 % when the expander size exceeds 100 MW.

- For both constant 50 MW compressor and expander sizes, both charging or discharging coverage percentages increase by increasing cavern size if the pressure limits are considered.

- For a cavern and a constant 50 MW compressor size, the charging and discharging coverage percentages increase by increasing the expander size where they respectfully approach 49% and 29.4%. Therefore, applying pressure limitations can decrease the

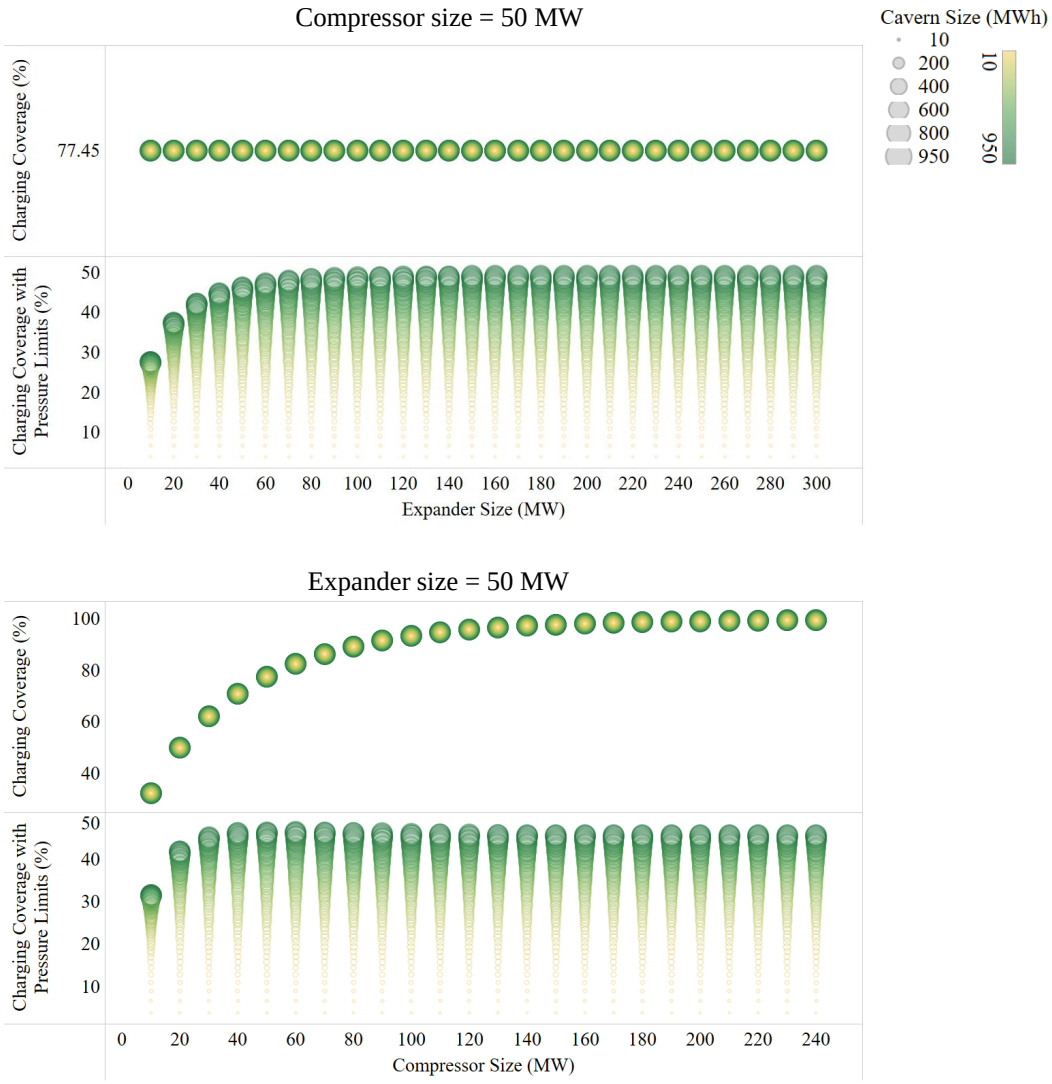

Figure 3.12: The effect of components sizing on the charging coverage percentage (upper: without cavern pressure limits, and lower: with cavern pressure limits).

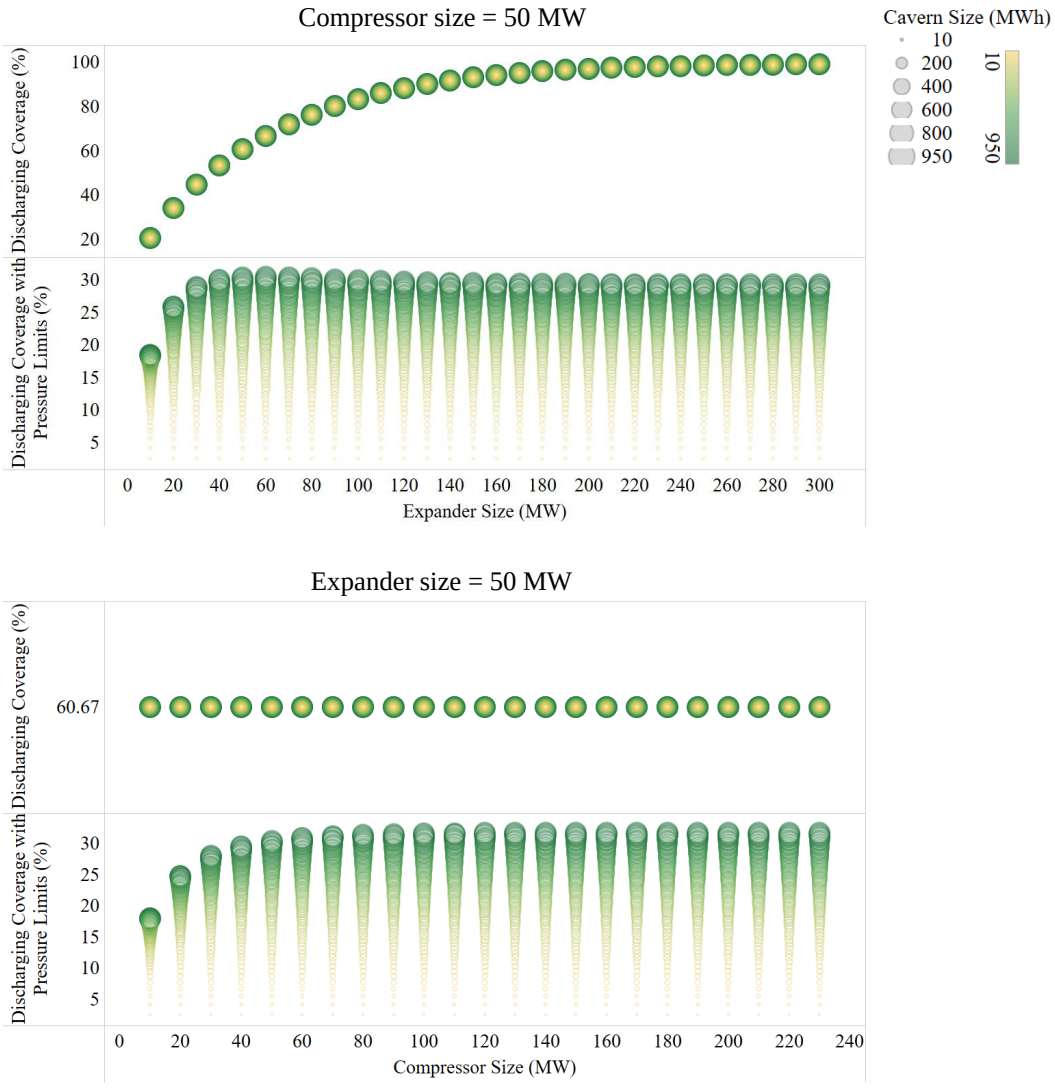

Figure 3.13: The effect of components sizing on the discharging coverage percentage (upper: without cavern pressure limits, and lower: with cavern pressure limits).

charging percentage of coverage up to 51% and the discharging percentage of coverage up to 70.6%. It should be mentioned that the charging coverage is dependent on expander size, as bigger expanders increase the opportunity of CAES charging modes in the next excess power events.

- For a cavern and a constant 50 MW expander size, the charging and discharging coverage percentages increase by increasing the compressor size where they respectfully approach 45% and 32%. Therefore, applying pressure limitations can decrease the charging percentage of coverage up to 65% and the discharging percentage of coverage up to 68%. It should be mentioned that the discharging coverage is dependent on compressor size, as bigger compressors increase the amount of SOC in cavern, and therefore the opportunity to discharge all required energy during on-peak periods.

3.3.4 Compressor and Expander Loads

Given that compressor and expander efficiencies drop at part load (the reason being leakage loss at low rotational speeds [42]), for example the efficiency decrease from full to half load can be 40% [38], the compressor and expander load are key parameters to be considered when a CAES system is designed. Figure 3.14 depicts the density of average compressor load (upper graphs) and the percentage of total hours that the compressor is running at full load (lower graphs) vs. components sizes for a CAES system based on three years electrical grid data and for 65,550 defined scenarios (see section 3.3.1). Figure 3.15 shows the impact of compressor, expander, and cavern sizes on compressor load. Based on Figure 3.15, the following observations are revealed:

- For a cavern and a constant 50 MW compressor size, both compressor average load and the full load operation hours (in percentage, compared to the total hours) increase as the expander size increases until an upper limit of 100 MW (see Section 3.2.1). As the expander size increases it becomes possible for the cavern to discharge more quickly creating the opportunity for the system to experience more charging events until all events can be fully accommodated.

- For a cavern and a constant 50 MW expander size, the compressor average load gradually drops as the compressor size increases, and when the compressor is larger than 100 MW (100 MW being the size that captures the majority of Ontario's excess power, see section 3.2.1 and Figure 3.2) the compressor always operates at less than half-load. The summation of hours that the compressor runs at full load (in percentage, compared to the total hours) also decreases.

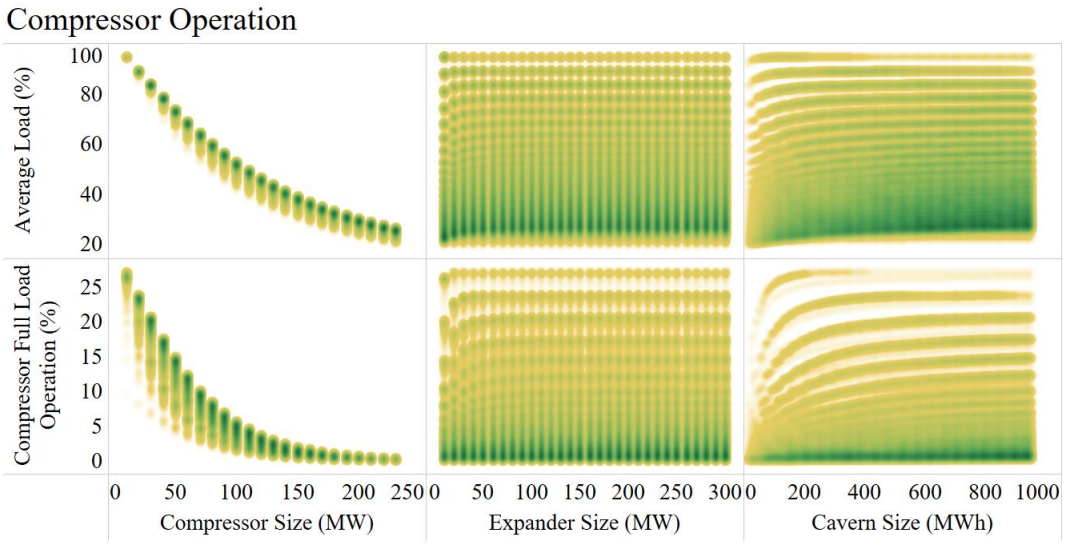

Figure 3.14: Density of compressor average load and total hours of full load operation vs. component's sizing for 65,550 scenarios (dark green shows higher density).

- For constant compressor and expander sizes, both compressor average load and full load operation hours percentage go up as the cavern size increases.

The expander behavior is similar to the compressor as follows:

- For a cavern and a constant 50 MW compressor size, both expander average load and the full load operation hours (in percentage, compared to the total hours) gradually drops as the expander size increases, and when the expander is larger than 100 MW the expander always operates at less than half-load.
- For a cavern and a constant 50 MW expander size, both expander average load and the full load operation hours (in percentage, compared to the total hours) increase as the compressor size increases until an upper limit of 100 MW. As the compressor size increases it becomes possible to store more excess power during charging contingencies creating the opportunity for the system to cover a greater proportion of discharging events.
- For both constant compressor and expander sizes, both expander average load and full load operation hours percentage go up as the cavern size increases.

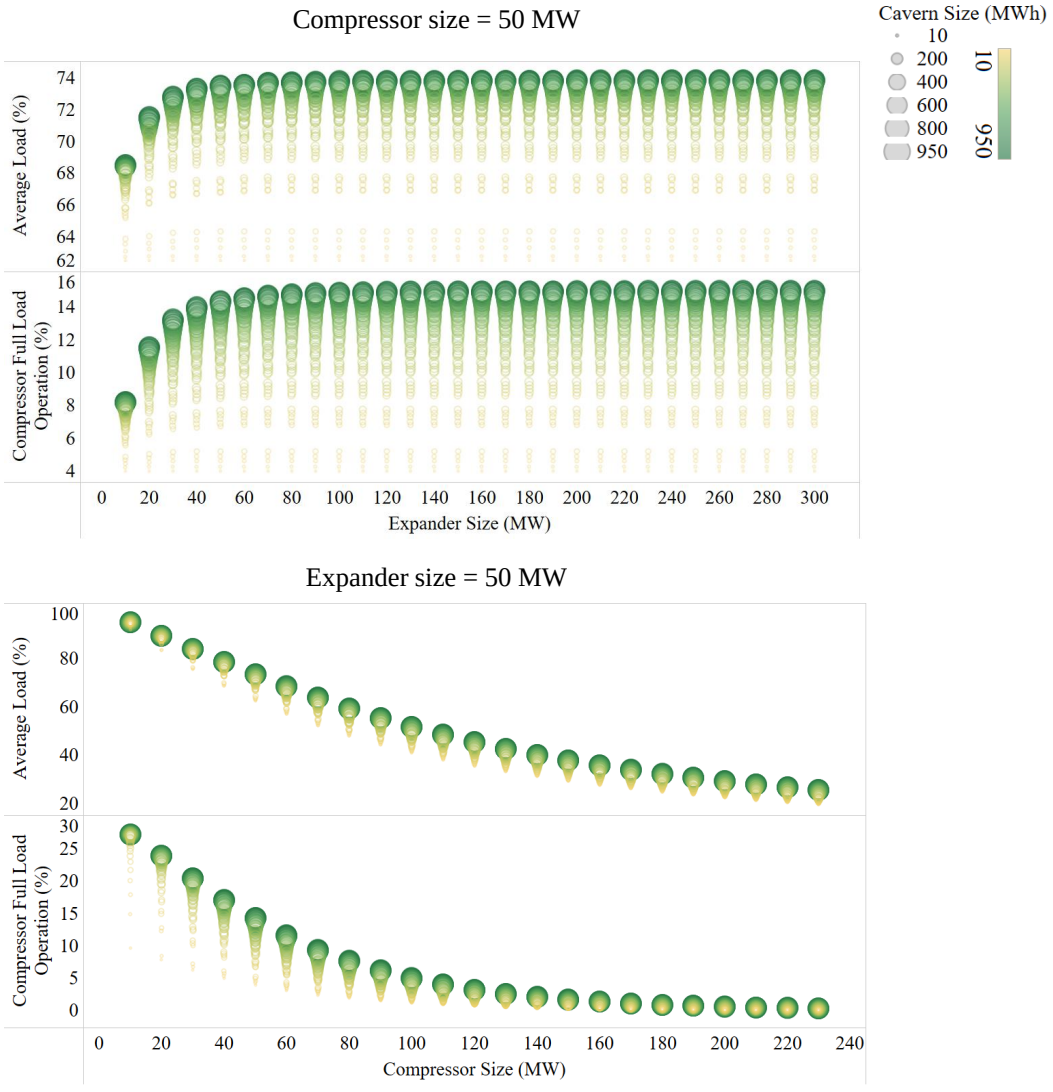

Figure 3.15: The effect of components sizing on the compressor load and its operation.

Figure 3.16: Evaluation of a CAES system performance by change of components sizing (dark green shows higher density).

3.3.5 CAES System Performance and Sensitivity Analysis

Figure 3.16 depicts CAES performance (according to the charging and discharging coverage percentages of a CAES system, as described in section 3.3.3), in Ontario, based on an analysis of the electrical grid data from 2018 to 2020. Graph (a) in Figure 3.16 illustrates the density distribution of discharging coverage vs. charging coverage for 65,550 scenarios where the highest performance point on the graph is obtained by finding the maximum in the summation of the charging and discharging coverage percentages. In 3.16 (a) the maximum sum is 81.3%; this comes from the sum of 49.7% and 31.6% for the charging and discharging coverages percentages, respectively, and this highest performance point is shown in Figure 3.16 (a). Lines corresponding to average and maximum values for both the charging and discharging coverage percentages are also shown in Figure 3.16, with the overlap region identified by the red outlined box corresponding to the acceptable range for charging and discharging coverage percentages in this research. The average coverage percentage is selected as a lower limit as a soft consideration for the economics, i.e., at lower coverage percentages the storage benefits would be lower for larger capital costs. Graphs (b), (c), and (d) in Figure 3.16 display the relation of components sizing with system performance. Observations revealed from Figure 3.16 are as follows:

- Based on the range of component sizes (23 different compressor sizes at 10 MW intervals from 10 to 230 MW, 30 different expander sizes at 10 MW intervals from 10 to 300 MW, and 95 different cavern sizes at 10 MWh intervals from 10 to 950 MWh as determined in Section 3.2.3, the best charging coverage percentage (total available power that can be stored in CAES during the 3 years of 2018-20 considered) does not exceed 50%, while the discharging coverage does not exceed 33%.

- Graphs (b) and (c) in Figure 3.16 clearly depict that charging coverage percentage can be obtained with very small compressor and expander sizes. Further, the charging coverage percentage is more sensitive to cavern size than the charging coverage percentage.

- A larger cavern size does not necessarily result in higher performance (see red points in Figure 3.16). Moreover, a larger compressor or expander size cannot solely improve system performance (see blue points in Figure 3.16, when the compressor size is more

Figure 3.17: Overall coverage variation of a CAES system by change of components sizing (dark green shows higher density).

than 200 MW). As a result, CAES components must be jointly considered to improve performance and coverage percentage.

- The main advantage of the coverage-percentage method is that the scenarios that yield the same (or close to the same) system performance can be visually seen and compared. For example, the black points (scenario I) and gray points (scenario II) in Figure 3.16 both have that same charging coverage and differ by only 4% in their discharging coverage, however, the component sizes involved, which affects capital cost economics, differ by much more. Specifically, the compressor and cavern in Scenario II are larger than that in Scenario I by 9%, and 17% respectively, while the expander in Scenario II is smaller than that in Scenario I by 33%.

Graphs (a) to (f) in Figure 3.17 depict how compressor, expander, and cavern sizes affect overall coverage percentage. Data is limited to the acceptable range for charging and discharging coverage percentages identified in Section 3.3.5 (Figure 3.16). Data is further constrained by requiring the overall coverage percentage to be above 55%, and constrained by the maximum component sizes indicated at the top of each Figure 3.17 graph. Observation of Figure 3.17 are as follows:

- These graphs quickly reveal visually the approximate compressor and expander optimal sizes for a given cavern size, where it is assumed smaller size and larger coverage improve the economics of the CAES system. That is, the optimum is considered that configuration that balances a search for the smallest compressor and expander with the largest overall coverage.

- Again comparing graphs (a), (b), (d), and (e) in Figure 3.17, but this time recognizing that Figure 3.17 plots density maps. Therefore, in the region near each data point location, there are many compressor, expander, and cavern sizes scenarios. Focusing on the small region in Figures 3.17 (d) and 3.17 (e) where the compressor and expander overall coverage no longer increase for increasing component size one can quickly locate a combination of the smallest component sizes that yields an overall coverage at or very near the maximum overall coverage possible. That is, one can quickly locate a combination of minimum-sized compressor and expander with

a near maximum overall coverage for an optimum CAES system (where optimum is defined as in the previous bullet). For example, the black data points in Figure 3.17 (e) were quickly located to identify minimum compressor (60 MW) and minimum expander (70 MW) sizes corresponding to a maximum overall coverage of 64.5 % at the maximum cavern size of 500 MWh.

- Figure 3.17 (d) and (e) reveal that the overall coverage percentage increases as the compressor and expander sizes increase until an upper limit of around 100 MW, which means that a compressor or an expander larger than 100 MW cannot increase the CAES coverage percentage (or gently increases as these two graphs have a vertical asymptotic). However, focusing on graphs (d) and (f) in Figure 3.17, although CAES performance becomes insensitive to further increases in compressor or expander size after around 100 MW size, there remains a strong sensitivity to cavern size up to 750 MWh and beyond. Additional scenarios using a 100 MW sized compressor and expander while increasing cavern size reveal that further increases in CAES performance ends around a cavern size of 6000 MWh. Therefore, a trade-off between the CAES system performance enhancement by increase of the cavern size, and the capital cost to enlarge the cavern could result in sizing a CAES system that is economically feasible.

3.3.6 CAES Components Sizing for Ontario

This section aims to propose some feasible (not optimum) CAES plants for Ontario based on its electrical grid requirements. Feasible CAES plants are those that have a high overall coverage but are not optimal because the economics of the various compressor, expander, and cavern sizes combinations that can yield near the same high overall coverage have not been fully taken into account - the only economic consideration in this feasibility work is that smaller compressor and expander sizes combinations, that yield approximately the same coverage, are considered more economical.

Feasible compressor, expander, and cavern size combinations are limited to those with a charging coverage between 43% to 45%, a discharge coverage between 26% to 29%, and an overall coverage percentage of around 70%. An overall coverage percentage of around 70% corresponds to a maximum for the smaller compressor and expander sizes. Overall coverage percentages up to 85% can be achieved but with much larger compressor, expander, and cavern sizes which for this work were deemed to likely be less economical.

Table 3.2 summarizes the components size, and the coverage percentages for the suggested CAES plants (P_1 to P_6). As seen in Table 3.2, a compressor and an expander with

Table 3.2: The proposed CAES plants for Ontario based on its electrical grid requirements.

CAES Plants	$\mathbf{P}_1$	$\mathbf{P}_2$	$\mathbf{P}_3$	$\mathbf{P}_4$	$\mathbf{P}_5$	$\mathbf{P}_6$
Compressor (MW)	30	40	40	60	60	70
Expander (MW)	60	40	70	50	90	80
Cavern (MWh)	770	760	670	670	630	630
Charging coverage (%)	43.5	42.4	43.4	42.2	43.1	42.8
Discharging coverage (%)	26.5	27.5	26.6	27.8	27	27.2
Overall coverage (%)	70	69.9	70	70	70.1	70

Figure 3.18: The difference in coverage percentage between the frequency-of-occurrence method and the coverage-percentage method for CAES system sizing.

a size of less than 100 MW (as also concluded by electrical grid data analysis in section 3.2.1) can cover the majority of charging or discharging events and result in an acceptable coverage percentage. The results also reveal that the required cavern size, to reach the desired coverage percentage in this study, should be between 600 to 800 MWh. However, it must be noted that the cavern size is also very dependent on the lower and upper cavern pressure limits; for this work, these limits were 5 MPa and 14 MPa, respectively. It is also worth mentioning that according to the kind of thermal fluid and its properties, the required volume of heat exchanger tanks can be calculated, as described in Chapter 4.

3.3.7 Difference in Coverage Percentage between the Frequency-of-occurrence Method and the Coverage-percentage method

Histogram (graph (a)) in Figure 3.18 depicts the probability distribution of difference in CAES overall coverage percentage (OCP: summation of charging coverage percentage and discharging coverage percentage) between the frequency-of-occurrence method and coverage-percentage method for the studied scenarios (65,550 different scenarios). The x-axis in Figure 3.18(a), which shows the difference in CAES overall coverage percentage calculated by two methods of frequency-of-occurrence and coverage-percentage, is determined by Equation 3.24.

$$\text{Coverage percentage difference} = \frac{OCP_{\text{f}} - OCP_{\text{c}}}{OCP_{\text{f}}} \times 100 \tag{3.24}$$

where subscript f and c denote the frequency-of-occurrence method and the coverage-percentage method, respectively. Each histogram bar in Figure 3.18(a) shows the number of scenarios in the given x-axis interval (the interval is 10%). The coverage percentage calculated by the frequency-of-occurrence method always overestimates the overall coverage percentage as it does not consider pragmatic constraints in CAES operation (e.g. pressure limitations in the reservoir). For the studied scenarios, this overestimation is concentrated at the 40 to 50% interval, while for a few scenarios, the overestimation can be up to 70 to 80 %.

Graphs (b) to (d) in Figure 3.18 display the range of CAES component (compressor, expander, or cavern) sizes that contribute to the overestimation of each interval. These results reveal that the overall coverage percentage difference between the frequency-of-occurrence method and the coverage-percentage method decreases as the cavern size increases. That is, the smaller the cavern, the greater the increase in overall coverage percentage overestimation, and the more sensitivity to pressure limitations inside the reservoir. Moreover, scenarios with larger compressors (more than 100 MW, which can cover the majority of excess power in Ontario) result in higher coverage percentage differences. That is, the greater the compressor size, the greater the probability of overall coverage percentage overestimation. In contrast, an overestimation in overall coverage percentage is not sensitive to expander size.

3.4 Verification

As no experimental data is available to practically assess the coverage-percentage method (available experimental data for existing CAES systems only include the CAES efficiency, and its operating properties, such as temperature and pressure), this method is theoretically verified in three steps, listed as follows:

- Step 1: The CAES overall coverage percentage obtained for the studied years is compared with the overall coverage percentage of the same CAES plant for another full-year real grid data to examine if the coverage-percentage method results in similar coverage.
- Step 2: The CAES charging and discharging coverage percentages over a twenty-year operation period (175,200 hours) are determined by both the frequency-of-occurrence method and the coverage-percentage method for different random data sets (each random data set includes random numbers between -100 MW and 100 MW as excess

Figure 3.19: Verification of the coverage-percentage method by comparison of the overall coverage percentage for four different scenarios during the studied years (2018 to 2021).

and shortage events) to display the ability of the coverage-percentage method code developed in this work to provide similar magnitude and pattern results, but with some small differences due to the random temporal variations in excess and shortage grid power (I.e., CAES system demands).

- Step 3: The CAES charging and discharging coverage percentages during a short (24 hours) and a long (one year) operation period are determined by both the frequency-of-occurrence method and the coverage-percentage method for correlated excess and shortage data. As shown and explained in Appendix A, the charging and discharging coverage percentages behave as expected reaching a steady-state spread.

To accomplish step 1, the overall CAES coverage percentage obtained by studying the Ontario electrical grid data during the three years of 2018, 2019, and 2020 are compared with the overall coverage percentage of 2021 in Ontario for four different scenarios. Figure 3.19 displays the comparison of overall coverage and the percentage of deviation for selected scenarios (each scenario specifies a CAES plant; the first scenario: compressor of 30 MW, expander of 30 MW, and cavern of 250 MWh, the second scenario: compressor of 50 MW, expander of 50 MW, and cavern of 500 MWh, the third scenario: compressor of 100 MW, expander of 100 MW, and cavern of 750 MWh, and the fourth scenario: compressor of 230 MW, expander of 300 MW, and cavern of 950 MWh). Based on Figure 3.19 all four scenarios based on Ontario data for 2018, 2019, and 2020 were able to provide similar overall coverage percentages to that in 2021 with a maximum deviation of plus 8.5%. In other words, by sizing a CAES system based on available electrical grid data is expected to still be applicable in future years barring any dramatic change to the electrical grid energy supply or demand.

In step 2, three different random data sets are employed to check how the frequency-of-occurrence and the coverage-percentage methods behave and compare for a CAES system operating over twenty years. This comparison shown in Figure 3.20 and is summarized as follows:

- The charging vs. discharging coverage percentage graphs of Figure 3.20(a) and (b) follow the same pattern, while the frequency-of-occurrence method results also follow a similar pattern but as expected with an overestimation of the CAES coverage percentages.

Figure 3.20: Evaluation of a CAES coverage percentages for 250 different scenarios (each marker (square, triangle, or cross) shows one scenario; scenarios cover 5 different compressor sizes from 10 to 50 MW in 10 MW intervals, 5 different expander sizes from 10 to 50 MW in 10 MW intervals, and 10 different cavern sizes from 10 to 100 MWh in 10 MWh intervals), and for three different random excess and shortage data set, ranged between -100 and 100 for duration of twenty years; (a) frequency-of-occurrence method, and (b) coverage-percentage method.

- The general pattern and magnitude of the charging vs. discharging coverage percentages in Figure 3.20(b) do not change for different sets of random surplus and shortage further supporting the expectation that sizing a CAES system based on available electrical grid data is expected to still be applicable reasonably far into future. Figure 3.20(a) and (b) also explain why the CAES coverage percentage obtained by the Ontario electrical grid data during the three years of 2018, 2019, and 2020 is not exactly the same as the coverage percentage in 2021 (different excess and shortage patterns result in different coverage percentages but of similar magnitude).
- The patterns that can be observed in the distribution of data points in Figure 3.20(a) and (b) are a result of the pattern used in the selection of the scenarios (for example, compressor sizes were systematically increased by in 10 MW steps).

3.5 Summary of Chapter

This chapter proposes a new method, referred to as the coverage-percentage method, to size a CAES system. Coverage percentage, in brief, is a measure of the ability of a CAES system to use the energy available for CAES energy storage, or the energy demand requests from energy storage. The coverage-percentage method is based on actual observed or predicted (hourly) data and improves upon the frequency-of-occurrence approach proposed by Rouindej e al. [150]. These improvements enhance the accuracy of CAES sizing by adding considerations for time-dependent operation, usability, and component limitations. Operation limitations considered include cavern pressure and temperature limits, while component limitations considered include compressor, expander, and cavern sizes (component sizes can restrict charging or discharging events, and affect the coverage and utilization of a CAES power plant). A major disadvantage of the frequency-of-occurrence method is that it overestimates the coverage percentage whereas a more accurate coverage

percentage is provided by the coverage-percentage method. The main contributions and findings of this chapter are as follows:

- Based on 2018 to 2020 Ontario hourly electrical grid data and using the frequency-of-occurrence approach of Rouindej et al. [150], a compressor and an expander of 230 MW and 300 MW, respectively, can capture the majority ($> 90\%$) of Ontario's excess power and power shortage if one ignores cavern size or pressure limits. Furthermore, using the frequency-of-occurrence approach a cavern size of 950 MWh can store in excess of 80% of excess energy, and in excess of 80% of the energy shortage. The key note here is that the frequency-of-occurrence approach uses only power considerations to size the compressor and expander, and only energy considerations to size the cavern. In contrast, via the coverage-percentage method introduced in this chapter, a cavern of 950 MWh can actually only cover 50% of Ontario's charging potential and only 33% of Ontario's discharging potential. The reason for this dramatic decrease from the 80% coverage determined using the frequency-of-occurrence approach is due to the pressure limits (5 MPa to 14 MPa) for an Ontario based salt cavern. Furthermore, to capture this 50% and 33% charging and discharging coverage percentages, respectively, the compressor and expander can be reduced to 70 MW or even less from 230 MW and 300 MW respectively. In brief, a CAES system based on the frequency-of-occurrence approach provides an overly optimistic cavern size and overly cautious compressor and expander sizes, while the coverage-percentage method provides more accurate size determinations and reveals a need to introduce economic considerations if one is not to oversize components of a CAES system.

- The link between compressor and cavern size (MWh), or expander and cavern sizes (MW), only exists when cavern pressure limits are considered. That is, a cavern of any size (m3) can hold any amount of energy (MWh) if there is no pressure limit. It is valuable to note that in this study an upper cavern volume size of 130,000 m^3 ($\sim$950 MWh) was selected enabling pressure limits to have an impact on how much energy can be stored or discharged. Though cavern pressure limits are considered in the coverage-percentage method presented in this chapter, it is worth noting that the compressor and expander were still considered ideal without friction, without speed-load-efficiency considerations, and without pressure ratio-efficiency considerations.

- Coverage-percentage method determined charging and discharging coverage percentages remain sensitive to cavern size beyond the frequency-of-occurrence determined maximum cavern size of about 950 MWh, while charging and discharging coverage percentages peak for compressor and expander around 100 MW. In contrast, this is

below the frequency-of-occurrence determined compressor and expander sizes of 230 MW and 300 MW, respectively.

- A larger cavern, compressor, or expander does not solely result in a higher CAES utilization and coverage percentages. As a result, CAES components must be jointly considered to improve CAES performance, or coverage percentage.

- Based on the coverage-percentage method applied to Ontario electrical grid data from the years 2018 to 2020, and based on a cavern pressure limits between 5 MPa and 14 MPa, it was found that compressors sized between 30 MW to 70 MW, expanders sized between 40 MW to 90 MW, and cavern energy capacities between 630 MWh and 770 MWh can capture at least 42% and 26% of charging and discharging capacity, respectively.

Chapter 4

Performance Improvement and Operational Mode Optimization of Adiabatic CAES Systems[1]

4.1 Introduction

As of 2023, the reported efficiencies of commercial CAES systems operating worldwide do not exceed 60%: the utility-scale Germany Huntorf (480 MWh) and USA McIntosh (2000 MWh) conventional CAES plants have reported efficiencies of around 42% and 54% [59], respectively, while the more recent Canadian Goderich (7 MWh) and Chinese Feicheng (300 MWh) adiabatic CAES plants (A-CAES) have reported efficiencies around 60% [104, 167]. It is worth mentioning that these reported efficiencies are not identified if they are averages, medians, or maximums, or whether they come from short-term or long-term CAES operations. Though CAES can be commercially viable at these low efficiencies in specific situations, its commercial viability would increase substantially if round-trip efficiencies of 80% or greater could be achieved [34]. As a result, there is much literature on various configurations and applications aimed at improving round-trip efficiency, but no known literature considers the impact of CAES operation (e.g., cycling profiles, turbomachine transient start-up, or thermal energy storage (TES) temperature transients) on efficiency improvements, and the subsequent impact such operation considerations have

[1]This chapter is based on the following journal article:
Sarmast, S., Rouindej, K., Fraser, R., and Dusseault, M., (2023), Optimizing near-adiabatic compressed air energy storage (NA-CAES) systems: sizing and design considerations. *Applied Energy* [158].

on CAES design/configuration. In other words, numerous studies on A-CAES have only predicted the round-trip efficiency, typically in the range of 50 to 70%, using numerical thermodynamic models ([130, 34, 119, 28], while a significant number of experimental projects have failed due to inappropriate size and design, and/or an actual efficiency lower than the predicted [30]. This study hypothesizes that possible reasons behind these failures could be as follows:

1. Components of A-CAES systems are modeled using generic thermodynamic equations, which generally do not consider operational limitations and/or design challenges such as start-up lag, pressure and temperature limits, and size limits [56, 116, 181]. Of particular note is that other works model with unbalanced heat exchangers (see Section 4.2.1.3 in this chapter for a discussion of CAES heat exchanger balance).

2. Modeled A-CAES systems are mostly not grid-connected which yields misunderstandings of CAES operational coverage percentages, and leads to disparity between the sizes of the modeled components and the actual required component sizes. Such approaches do not follow user-centered design [149, 157].

3. Heat losses in the TES and air reservoirs are neglected [79], or these units are modeled using pre-determined, constant, efficiencies[142, 55, 108].

4. A-CAES systems are generally not correctly designed [30] to achieve the highest performance under optimized operation. As an example, A-CAES systems are modeled with a mirrored compression-expansion design (same number of compressor and expander units, with same pressure ratios) which does not yield the maximum A-CAES system efficiency (see Section 4.2.1.3 for a detailed explanation).

Considering the aforementioned reasons, this chapter aims to improve the design of near-A-CAES systems by addressing the four shortcomings in previous near-A-CAES models - Important Note: many initially apparent A-CAES studies actually present near-A-CAES systems as they still involve some small amount of external heating to compensate for inefficiencies and TES heat loss by using a supplementary electric heater or combustion chamber [56, 55, 142, 137, 113].

This chapter starts with improving the coverage-percentage method (presented in Chapter 3), by considering additional CAES operation limits, including the desired minimum load for turbomachines (as the efficiency of compressor and expander fall at part-load operation), and the acceptable minimum time that a compressor and expander should run (start-up time). It means that if the load of a turbomachine or the time that it runs by available power is less than an acceptable minimum value, the CAES system should not be operating the turbomachine. This chapter is later followed by temperature limitations in TES design (e.g., minimum and maximum temperature for TES medium), heat exchanger

mass flow rates during charging and discharging of the TES medium, and the TES size impact on CAES system operation and performance. Therefore, the main contribution of this chapter is to enhance the coverage-percentage method [157] for CAES sizing and design, using a more pragmatic considerations inclusive framework created to include these additional limit considerations, and by addressing the shortcomings in previous research on CAES sizing and design (reasons 1 to 4 listed above), to identify a feasible operation for a diabatic CAES system in Ontario, and to also design a near adiabatic CAES system for Ontario that adds a sensible thermal energy storage system with operational limitations.

The contributions and novelties of the present chapter can be outlined as follows:

- Analyze Ontario's hourly power grid data to determine the supply-demand trend and to calculate excess power and power shortage during the full year of 2022.
- Determine the percentage of charging and discharging coverage by the coverage-percentage method (proposed in Chapter 3) to size the CAES components for Ontario by the 2022 power grid data and to verify the consistency of the coverage-percentage method in CAES components sizing.
- Compare a wide range of CAES coverage percentages to find an optimum range of sizes for a CAES system in Ontario.
- Size a sensible TES system for the proposed D-CAES system (based on the selected components size), and propose different configurations for A-CAES in Ontario that best increase the system efficiency.
- Perform a thermodynamic analysis (energy analysis) that considers operational restrictions (e.g., minimum turbomachines loads, minimum turbomachine run times, pressure and temperature limitations in the reservoir, as well as TES operating temperature) enabling the identification of system inefficiencies.
- Perform both local and global sensitivity analysis to identify the impact of different operational parameters on the NA-CAES performance and optimize the operational modes to maximize the system efficiency and minimize the TES volume (TES size).
- Find the charging/idle/discharging cycling profiles (for the reservoir and TES) for a near adiabatic CAES system sized for Ontario.

4.2 Method

NA-CAES system modeling is divided into two main sub-processes as follows and as illustrated in Figure 4.1:

Sub-process 1: Sizing and Design: One full year (2022) of observed Ontario electrical grid data is visualized and statistically analyzed to determine reservoir and turbomachines size using the coverage-percentage method [157]. In this step, three different NA-CAES configurations (plant A: constant-volume reservoir with throttling valve for discharging mode, plant B: constant-volume reservoir with a variable-pressure-ratio expander, and plant C: constant-pressure reservoir) are suggested for Ontario.

Sub-process 2: NA-CAES Performance and TES Operation: The performance and the round-trip efficiency of NA-CAES systems shown in Figure 4.8 are evaluated over one full-year operation (2022), and CAES and TES cycling profiles, and the impact of operational limits on CAES performance is determined in details over a period of two months (Aug 1, 2022, to Sep 30, 2022). Additionally, the CAES system operational modes as well as TES size are optimized to maximize the system round-trip efficiency and to minimize the required TES size, respectively.

More specifically, and in brief, a full year of electrical grid data for Ontario (from 2022 [7]) is initially visualized as a heat map using Tableau [12] in order to identify grid electricity excess and shortage patterns giving a sense as to the charging and discharging frequencies for the CAES system. Following visualization, a statistical analysis is employed following the frequencies-of-occurrence method as described in Chapter 3, but not to find the size of system components as proposed by [150], but to set practical limits to the range of scenarios analyzed using the coverage-percentage method (introduced in Chapter 3 to size the CAES system) based on the 2022 power grid data. Upon completion of the coverage-percentage method scenario mapping a CAES system with compressor, expander, and reservoir sizes suitable for Ontario is identified. This step is undertaken to verify the consistency of the coverage-percentage method (introduced in Chapter 3) in CAES component sizing and serves as the foundation for NA-CAES design. Subsequently, an appropriately sized thermal energy storage system is identified (see section 4.3.2) based on the frequency of occurrence of TES heat capacity during charging and discharging events. This TES size provides insight into the TES tanks' size limits (upper bound of TES size) for the optimization in the next step. In other words, the identified TES size represents the practical limit for the TES tank size constraints. In the TES sizing step, CAES operational restrictions (e.g., minimum turbomachine loads as well as minimum turbomachine run times) are included in the thermodynamic modeling so as not to oversize the TES as these realistic restrictions decrease CAES operation time and hence the thermal energy available.

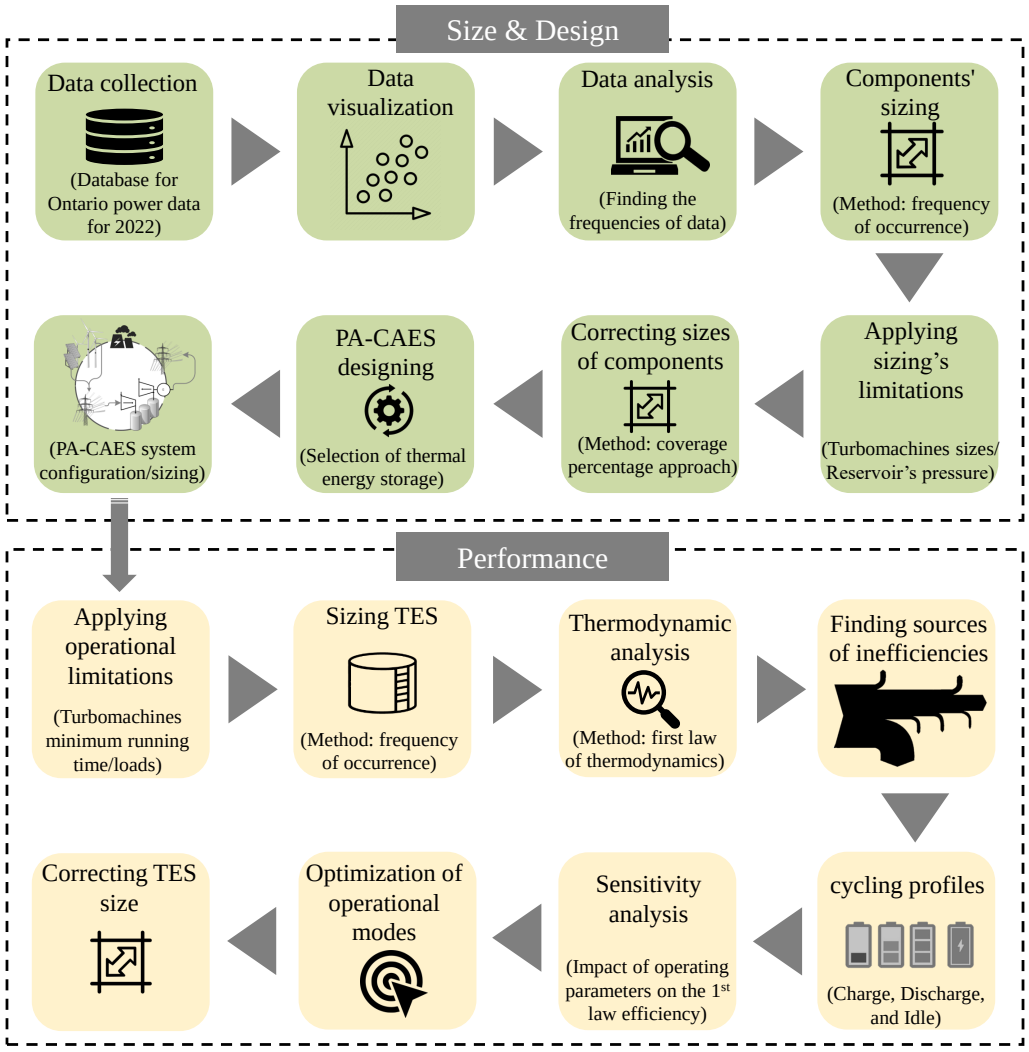

Figure 4.1: Schematic of NA-CAES sizing-design, and performance sub-processes.

Following sizing a CAES system for Ontario based on 2022 data, its performance is investigated for the purpose of investigating the sensitivity of a given CAES system to realistic variations in electricity grid supply and demand. Additionally, a sensitivity analysis is done to assess the impact of independent operating parameters on system efficiency and to specify what operating parameters have a greater impact on the system performance. Then, a multi-objective global optimization (using the differential evolution (DE) algorithm) is performed to find a set of operating parameters (as defined in section 4.2.1.3) that maximize the NA-CAES system efficiency, and to minimize the required TES size.

4.2.1 Sub-Process 1: Sizing and Design

The only input for the sizing and design sub-process is the Ontario hourly electrical grid data (in 2022, 8760 hours) collected from the IESO, and includes imports and exports, market demand, and power supply. The data matrix is composed of six columns (date, time, actual imports, actual exports, market demand, and power supply) and 8760 rows, equal to the total hours in 2022. Excess power and power shortage on the grid are calculated by subtracting market demand from supply. Excess power is characterized by a positive difference and indicates the available energy for charging a CAES system, while a negative value indicates that there is insufficient electricity to meet demand, i.e., a power shortage, which provides an opportunity for a CAES system to supply energy through reservoir air discharge. Section 4.2.1.1 presents the results of data visualization and the statistical analysis used to size and design the CAES system. These results include excess and shortage capacities and the magnitude, frequency, and duration of these capacities.

4.2.1.1 Heat Map and Statistical Data Analysis

This section applies the frequency-of-occurrence method to determine the excess power (as well as excess energy) or power shortage (as well as energy shortage) probability of distributions that will be used by the subsequent coverage-percentage sizing method.

- *Excess Power and Power Shortage - Frequency-of-Occurrence*

  The full-year distribution for 2022 of excess power and power shortage in Ontario is illustrated in Figure 4.2. This figure indicates how much power cannot be fed into the grid (excess, darker colors) or how much power is required to meet the market demand (shortage, lighter colors) at any given hour. The values in Figure 4.2 are limited between -150 to 150 MW, as this spans the majority of the observed excesses

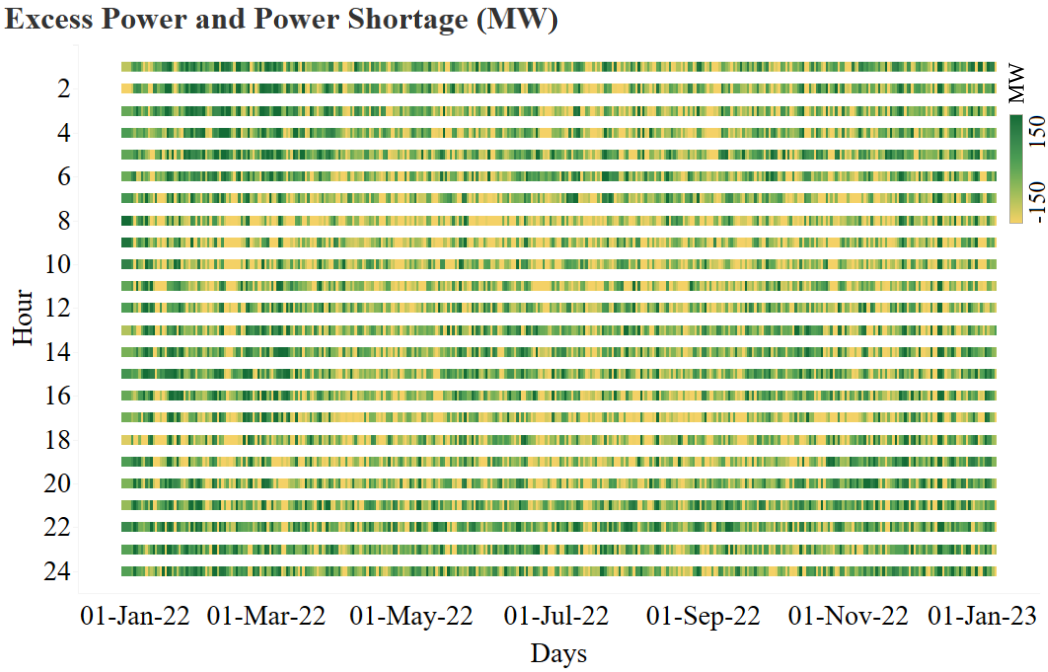

Figure 4.2: Excess power or power shortage in Ontario in 2022.

and shortages (spans 83.4% and 69.3% of excess and shortage, respectively), and for color map purposes this enables better contrast for visualization. Note that when values greater than 150 MW and less than -150 MW occur they are represented by the same color used for 150 MW or -150 MW, respectively.

The histogram graphs in Figure 4.3 depict the frequency of occurrence (in %) for excess power (upper) as well as power shortage (lower), alongside the cumulative values shown by line graphs in 2022 for intervals of 25 MW. This figure is beneficial to rapidly identify the level of power excess or shortage below which the majority of hourly events reside in Ontario. In the frequency-of-occurrence method, this histogram is used to identify, somewhat arbitrarily, a maximum excess or shortage power level to which the CAES system will be sized with the intent of fully capturing the majority of events while avoiding extremes that have low additional benefit compared to the additional cost. According to Figure 4.3, the majority of excess power during the off-peak periods is less than 175 MW (capturing close to 90% of events), while slightly more than 50% of events happens with excess power of less than 75 MW. In addition, the frequency of occurrence of excess power capacity greater than 250 MW

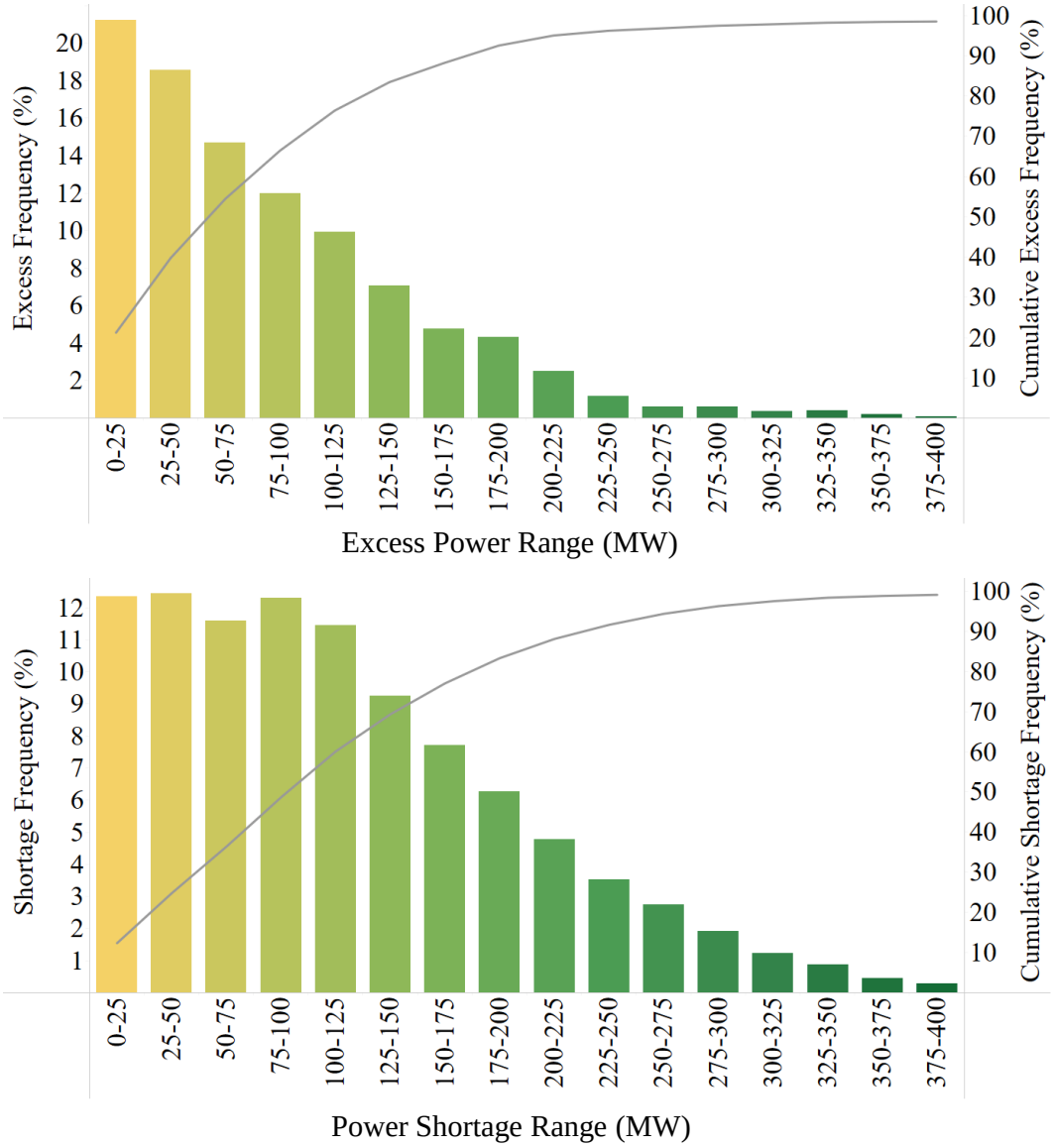

Figure 4.3: Annual frequency distribution of excess power (upper), and power shortage (lower) in Ontario for 2022.

is less than 1%. Regarding the expander size, only 25 % of power shortage events are less than 50 MW, and to reach the percentage of 90% an expander capacity of 250 MW is required. Moreover, less than 1% of power shortage capacity is greater than 325 MW. Therefore, the frequency-of-occurrence method maximum required sizes for the compressor and expander covering 99 % of events are 250 and 325 MW, respectively. It is important to note that these maximum required sizes for the compressor and expander determined by the frequency-of-occurrence only have the potential to capture 99 % of the excess or shortage events, however in reality system limitations (will be discussed in section 4.2.1.2) significantly limit system operation to lower coverage percentages. In other words, the frequency-of-occurrence method overestimates a CAES system's coverage percentage. Furthermore, larger components size does not necessarily result in higher coverage percentages. Therefore, frequency-of-occurrence selected maximum sizes for the compressor and expander represent an upper limit to their sizes with the coverage-percentage method refining these sizes downward to a more economically pragmatic size.

- *Excess Energy and Energy Shortage - Frequency-of-Occurrence*

  Similar to how the compressor and expander sizes are determined from the frequency-of-occurrence method as outlined above, the reservoir size is selected to capture a majority of events. In this study, 80 % is selected as the percentage that captures a majority of events. In contrast, the compressor size is determined from the power excess, and the expander size from the power shortage, however, the reservoir size must accommodate 'both' the energy excess and shortage. That is, the reservoir needs to be sized to the larger need in the energy excess or shortage. Figure 4.4 illustrates the frequency of occurrence for energy excess and shortage in Ontario for 2022 in intervals of 50 MWh (the cumulative values are shown by line graphs). According to the 4.4 frequency-of-occurrence distributions, 80 % of charging events corresponds to a frequency-of-occurrence reservoir capacity of less than 350 MWh, while for discharging events this 350 MWh capacity can only cover 52 % of events. According to Figure 4.4, in 2022 the discharging events control the frequency-of-occurrence method reservoir size determination. In order to cover 80 % of shortage or storage events, a reservoir capacity of 1000 MWh is required.

4.2.1.2 CAES Components Size by the Coverage-Percentage Method

Section 4.2.1.1 sized a CAES system (compressor, expander, and reservoir) for Ontario using the frequency-of-occurrence method proposed by Rouindej et al. [150]. However, the

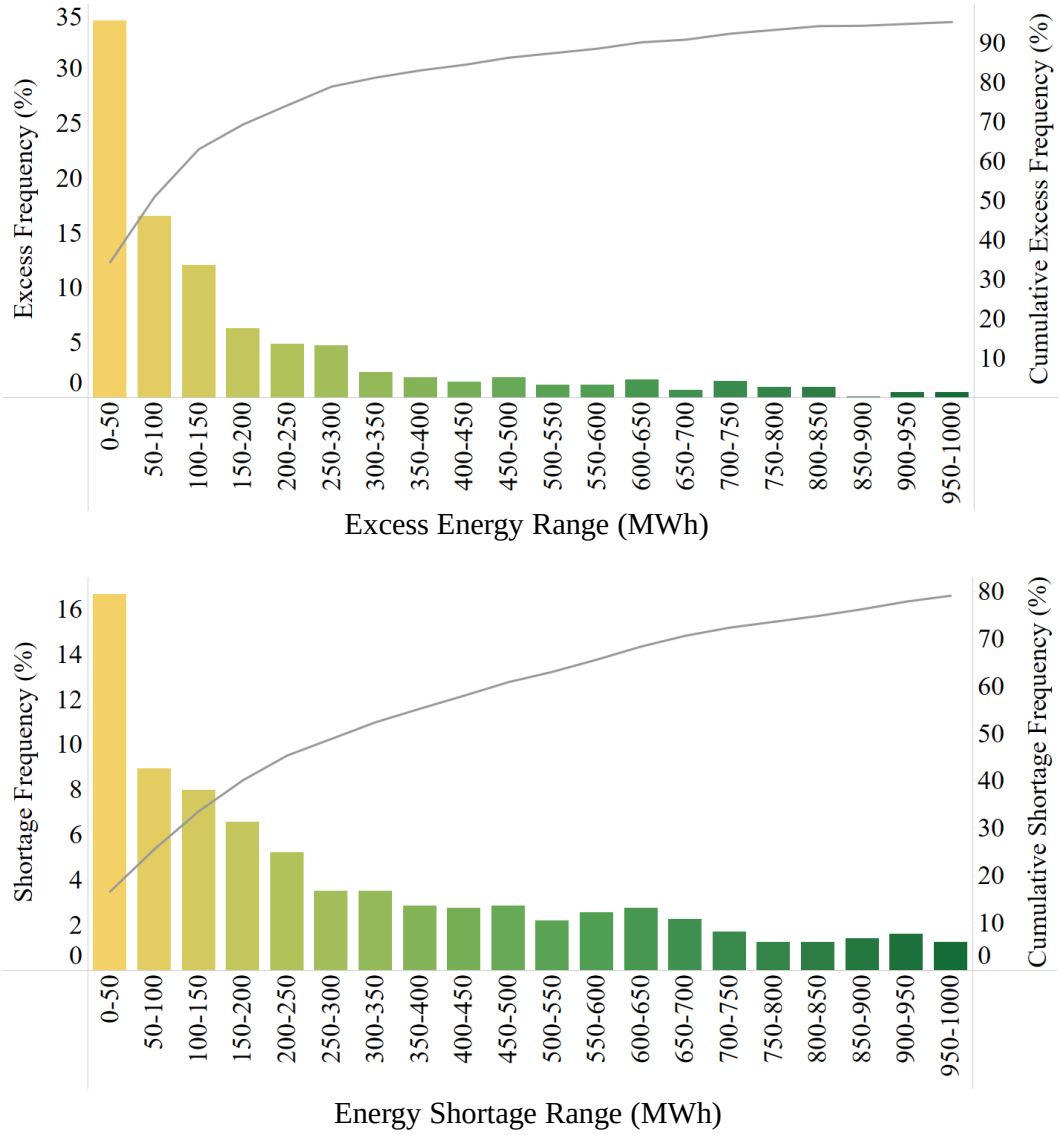

Figure 4.4: Annual frequency distribution of excess energy (upper) and energy shortage (lower) events in Ontario for 2022.

frequency-of-occurrence method fails to inform on the actual operation coverage percentage and system utilization, as discussed in Chapter 3 (both Charging and discharging coverage percentages are defined in Section 3.2.2 in Chapter 3.

When sizing an energy storage system the economics are important which in turn makes coverage percentage and utilization important criteria. Coverage percentage can be thought of as the percentage of the charging and discharging opportunities or events that are actually taken advantage of, and utilization is thought of as the amount of time the system is operating. Economically there is a trade-off or balance to be had between maximizing taking advantage of opportunities and the rising marginal costs associated with taking advantage. Consequently, coverage percentage becomes a criterion of interest as it indicates how well the system is taking advantage of opportunities, while system component size increases will increase marginal costs. Utilization brings in similar economic considerations, for example, an idle system is not generating revenue. In order to bring coverage percentage and utilization considerations into the sizing of a CAES system not only must the electrical grid excess and shortages be considered as per the frequency-of-occurrence method, but how the system operates needs to be considered as the operation puts constraints on CAES system capabilities. In particular, the coverage-percentage method developed in Chapter 3 necessarily incorporates CAES system operational limitations of reservoir pressure limits and components size. The main focus of the coverage-percentage method is to reach the desired (or maximum) coverage percentage for a CAES system using the smallest, most economical, components.

Figure 4.5 is the flowchart detailing the steps and logic of the coverage-percentage method (Figure 4.5 in Chapter 3), including the link between the coverage-percentage method and the CAES system additional operational limitations (applying the minimum load and start-up time constraints in CAES modeling). The steps shown in Figure 4.5 are repeated for each sizing configuration of CAES to be considered. Each configuration, or scenario, has inputs of electrical grid data (actual power supply and actual demand), and the components sizes that define a given scenario. A scenario is therefore defined by its corresponding thermodynamic properties of pressure and temperature limitations for the air inside the reservoir and by the compressor's and expander's size limits. In this chapter, the time step is 1 hour. As detailed in section 4.2.2.9, 82,500 different scenarios are considered.

4.2.1.3 NA-CAES system configuration

To design an adiabatic CAES system that operates without any external supplemental heat source (all compression heat can be recovered), the compression and expansion pro-

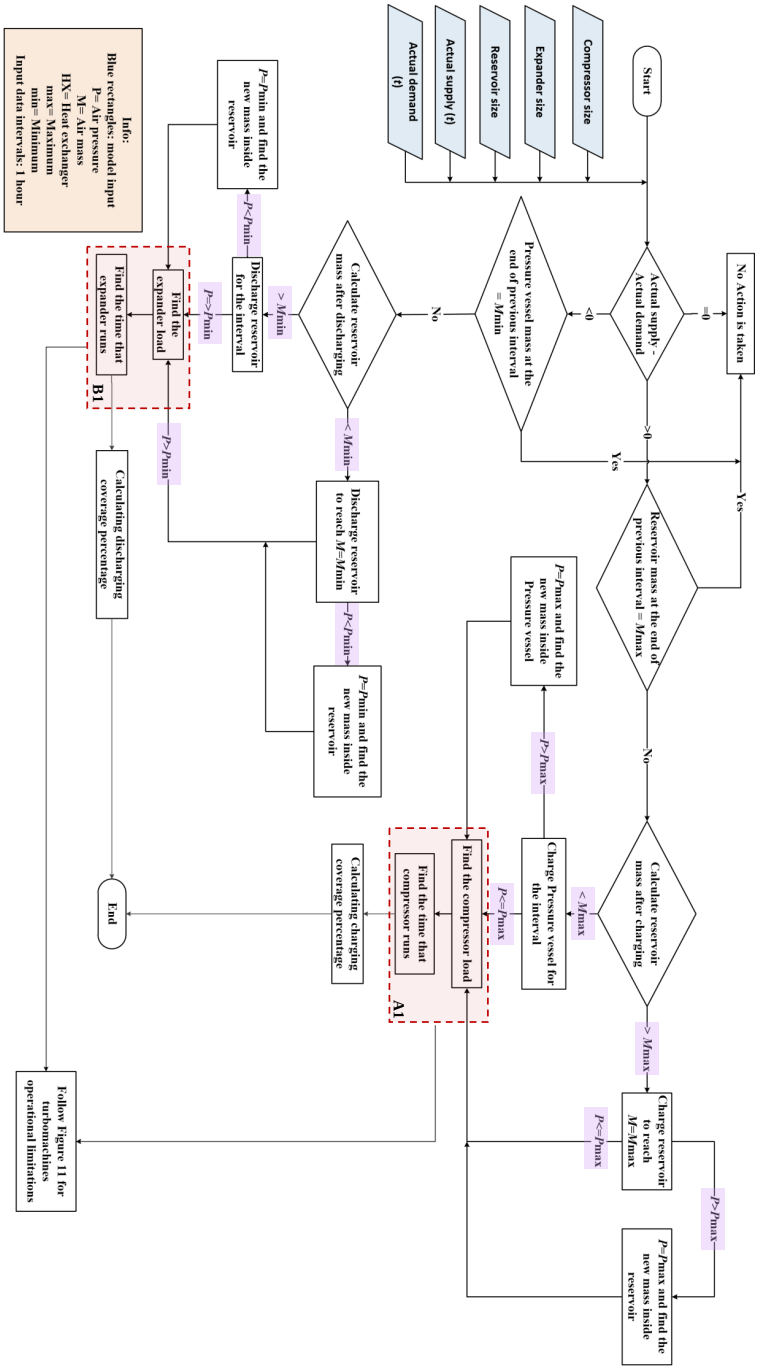

Figure 4.5: Flowchart of the coverage-percentage method (blue rectangles are the model inputs, purple rectangles are the system limitations examination, and red dashed boxes are linked to Figure 4.9).

cesses should be coupled, which means that the compression process is mirrored during discharging mode, and the expander inlet temperature is equal to the compressor outlet temperature [29]. If a fully adiabatic system can be designed, staging the compression unit and internally placing intercoolers to cool the compressed air temperature to the ambient temperature between any two stages leads to the minimum required work to reach a given cavern pressure. The same can be applied to the expansion unit (staging the expansion process and internally placing interheaters to heat up the air temperature from ambient temperature to the expander inlet temperature between any two stages results in the maximum generated work). Therefore, an A-CAES system performance can approach the internally isothermal CAES (I-CAES) by increasing the compression and expansion stages to infinity (the word "internally" refers to not using any external heat exchangers or thermal energy storage).

Considering the layout of an I-CAES system, recent research has focused on conceptually designing A-CAES systems by staging compression-expansion processes (attempting to be close to mirrored compression-expansion), and considering external heat exchangers and a sensible/latent TES system. However, paradoxically, approaching I-CAES with external intercooling/interheating yields a lower efficiency for an A-CAES system. The reason behind this paradox is explicitly explained in this section, and illustrated by Figures 4.6 and 4.7, where it is shown that staging the compression unit results in lower outlet temperature after each compression stage, less exergy captured by the TES, and less useful work extracted by a low-exergy thermal energy source. In other words, the expansion process in a CAES system can be simulated as a heat engine in which thermal energy storage is an energy source to be transformed into useful work. Figure 4.6 represents the performance of the A-CAES system based on different configurations and thermal energy storage temperature from the highest (internally isothermal concept) to the lowest (externally isothermal concept) performance.

As shown in Figure 4.6, the discharging process of the A-CAES system can be considered as a heat engine, in which the expansion unit receives heat from a high-temperature source (Q_h) and converts some percent of it to useful work while the rest is rejecting to a cold-temperature source (Q_c). If the performance of the expansion unit is evaluated based on the temperature of the hot source using the Carnot heat engine efficiency ($\eta_{Carnot} = 1 - \frac{T_{cold}}{T_{h_i}}$) (the temperature of the cold source is held constant), the efficiency increases as the hot source temperature increases. The Carnot efficiency indicates that the hot source temperature in the TES unit is an important factor in determining the CAES efficiency. However, some researchers claim that the A-CAES round-trip efficiency is not governed by the Carnot efficiency [176], and the heat losses in the entire cycle can be managed if the thermal energy storage temperature is designed in the range of 95 to 200°. In this study,

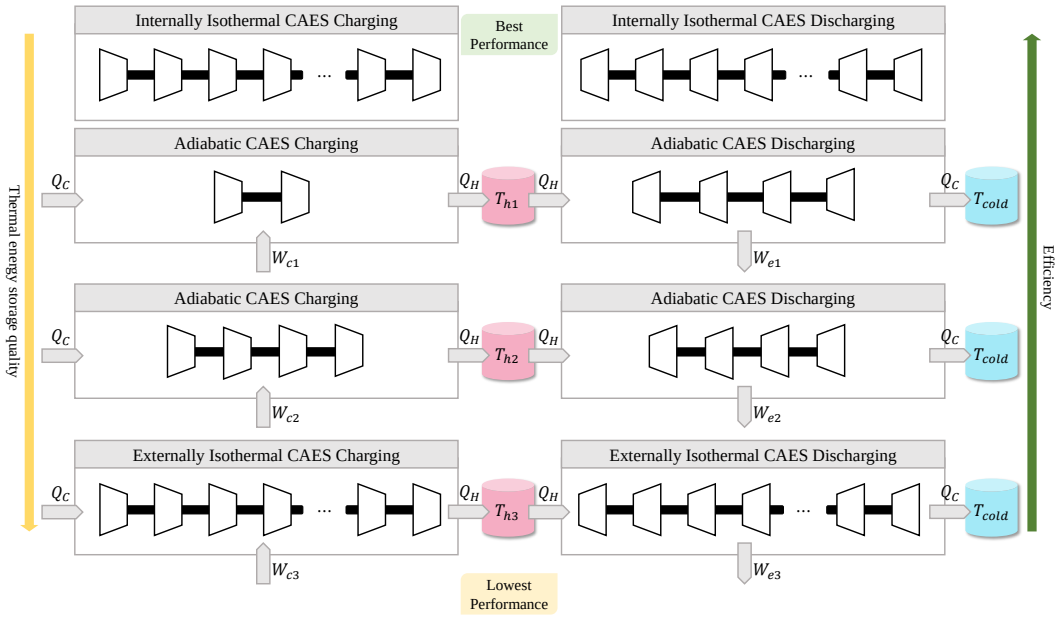

Figure 4.6: Performance of A-CAES system based on different configurations and thermal energy storage temperature ($T_{h1} > T_{h2} >> T_{h3}$).

the author agree with this claim up to a point. It is true that the A-CAES system efficiency is not completely governed by the Carnot cycle efficiency, but the quality of energy (i.e., TES temperature) is an essential factor in TES designing. The energy quantity in all three adiabatic CAES systems in Figure 4.6 are the same, but the last configuration (externally isothermal) has the lowest energy quality as low-temperature TES systems have a lower potential to produce work (electricity). The temperature (and therefore the quality) of the thermal energy storage is important as only a fraction of heat can be converted to work. Additionally, storing heat at low temperature by staging the compression and expansion units cannot result in a medium to high round-trip efficiency considering the available industrial heat exchangers (the outlet temperature of thermal fluid after the heat exchanger (TES temperature) is always lower than the compressor outlet temperature in charging mode, and the expander inlet temperature is always lower than the TES temperature). In other words, keeping the TES temperature (high-temperature source) close to or lower than the expander inlet temperature results in a lower round-trip efficiency.

To conclude, increasing the compression stages yields a higher efficiency in diabatic CAES systems when intercooling is used to dump heat to the environment (for example, the Germany Huntorf has 26 compression stages [29]) as this reduces the work input to

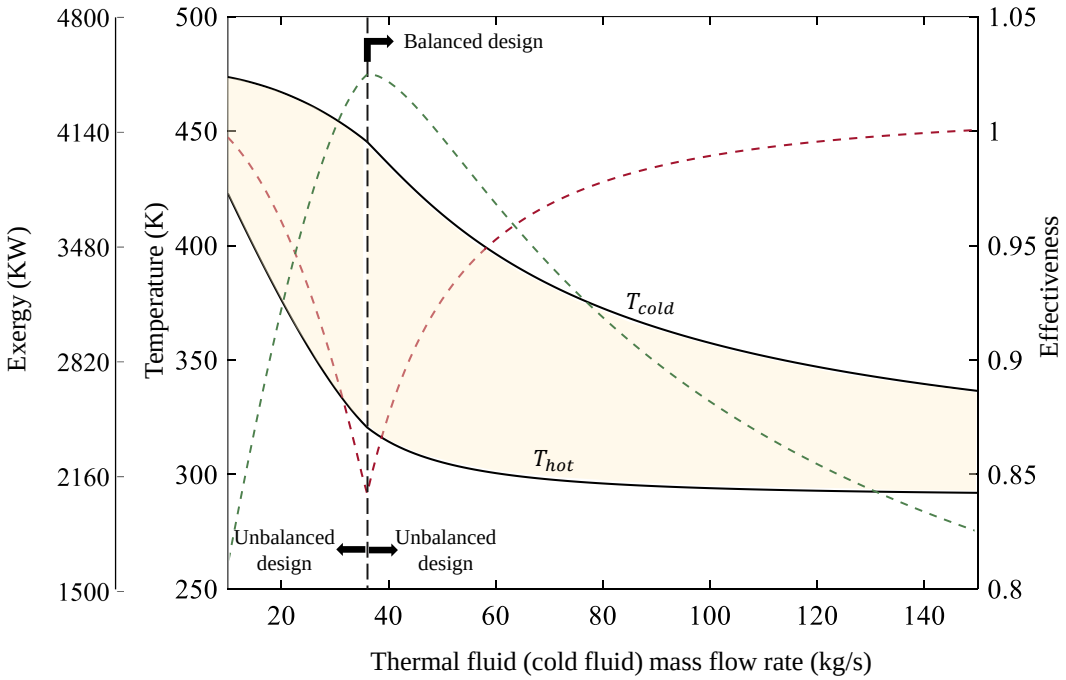

Figure 4.7: Heat exchanger operation under balanced and unbalanced conditions (black lines: temperature, red dashed line: effectiveness, green dashed line: thermal fluid exergy).

reach a given high pressure, and the lost thermal energy from intercooling is replaced by the combustion chamber. Given the desire for fewer stages when an A-CAES TES is used, and more stages with a D-CAES system, it is deceptive to think a D-CAES system can easily be converted to an A-CAES system by simply adding a TES without reengineering the entire system configuration. Furthermore, the paradox shown in Figure 4.6 where the internally isothermal (inherently adiabatic) system has a higher efficiency than the externally isothermal (externally adiabatic via TES) system is the result of the internally isothermal system not being subject to the entropy production or exergy destruction associated with the heat transfer from and to the system.

Another challenge that arises in designing a coupled compression-expansion A-CAES system is associated with heat exchangers. Heat exchangers can be sized and designed for balanced ($C_{min} = C_{max}$, where C_{min} and C_{max} can be found by Equations 4.8, and 4.9 in Table 4.2) or unbalanced operations ($C_{min} << C_{max}$). Figure 4.7 depicts the variation of thermal fluid (cold fluid) temperature (T_{cold}), compressed air (hot fluid) temperature (T_{hot}), heat exchanger effectiveness (red dashed line), as well as the exergy of the thermal fluid (green dashed line, which indicates the quantity of energy available to be stored in thermal energy storage system) by changing the thermal fluid mass flow rate (when the air mass flow rate is constant (150 kg/s), and the cold and hot fluids inlet temperatures into the heat exchanger are 293 K and 473, respectively). As shown in Figure 4.7, the heat exchanger can operate under a balanced condition (vertical black dashed line), where any increase or decrease in thermal fluid mass flow rate leads to unbalanced operation where the unbalanced region is shown by the yellow area in Figure 4.7. In a D-CAES system, heat exchangers should operate under unbalanced conditions in which the thermal fluid mass flow rate is high enough to decrease the air temperature to the ambient temperature after each compression stage with a normal heat exchanger surface area. The heat exchangers' effectiveness under the unbalanced condition is usually higher than 0.9 [29]. In an unbalanced heat exchange process, the cold thermal fluid experiences a small temperature increase which has no potential to generate work during the CAES system's discharge mode. A balanced heat-exchange process should be employed to achieve a high-temperature TES system with a temperature close to the compressor outlet temperature while the air temperature is low enough for the next compression stage. Balanced heat exchangers preserve the greatest amount of exergy while corresponding to the lowest effectiveness. By preserving exergy a balanced heat exchanger is closer to being reversible [29]. Additionally, placing several heat exchangers after each compression unit to store the compression heat in various-temperature TES systems (each heat exchanger is sized and designed for a balanced operation) can improve the CAES system performance, as the system can store a considerable part of the compression heat during charging mode.

A near adiabatic CAES system has an arrangement in which the compression heat is stored in a multi-tank sensible thermal energy storage unit and then is used during the expansion process to increase the CAES round-trip efficiency, and to minimize fuel use (due to a heat storage temperature restriction or TES size, some thermal energy during compression may be dumped to the environment). Figure 4.8 illustrates the proposed NA-CAES configuration during charging and discharging mode. Sensible double-tank heat exchange fluid heat storage (hot and cold tanks) has been widely studied for adiabatic CAES systems [190]. In the present work, a multi-tank heat exchange fluid TES operating with a sensible thermal fluid is utilized due to its low cost, high efficiency, ability to be brought to a high operating temperature (based on the selected thermal fluid and its pressure in TES tanks), and its simplicity [190]. The proposed charging configuration for the NA-CAES system, as shown in Figure 4.8, includes two compression units each followed by three heat exchangers (the number of heat exchangers after each compression unit could be decreased/increased based on its compression ratio and the compression outlet temperature). A combustion chamber is placed before each expander to heat up the compressed air if the air temperature is lower than the expander inlet temperature during discharging mode (is not shown in Figure 4.8). Additionally, a heat exchanger with water as the thermal fluid is placed before the cavern to decrease the compressed air temperature to the air injection temperature if any further temperature decrease is required. The thermal energy from this just before cavern heat removal by water is assumed to be dumped into the environment.

4.2.2 Sub-Process 2: NA-CAES Performance and TES Operation

Three different plants A, B, and C as described in section 4.2, which have the same configuration but are operated differently (with a throttling valve, variable-pressure-ratio expander, and constant-pressure reservoir, respectively), are suggested for the province of Ontario. This section provides the model for these plants, much of which is common due to these plants being of the same configuration.

The primary performance parameter for a CAES system is its round-trip efficiency. Economic costs and opportunity wise important performance metrics are coverage percentage and utilization. In Sub-Process 1, i.e., Sizing and Design, the coverage percentage was used to size the compressor, expander, and reservoir. In this section, the required thermal energy storage is sized first by the frequency-of-occurrence method. In the frequency-of-occurrence, the required hourly TES heat capacity during charging and discharging events

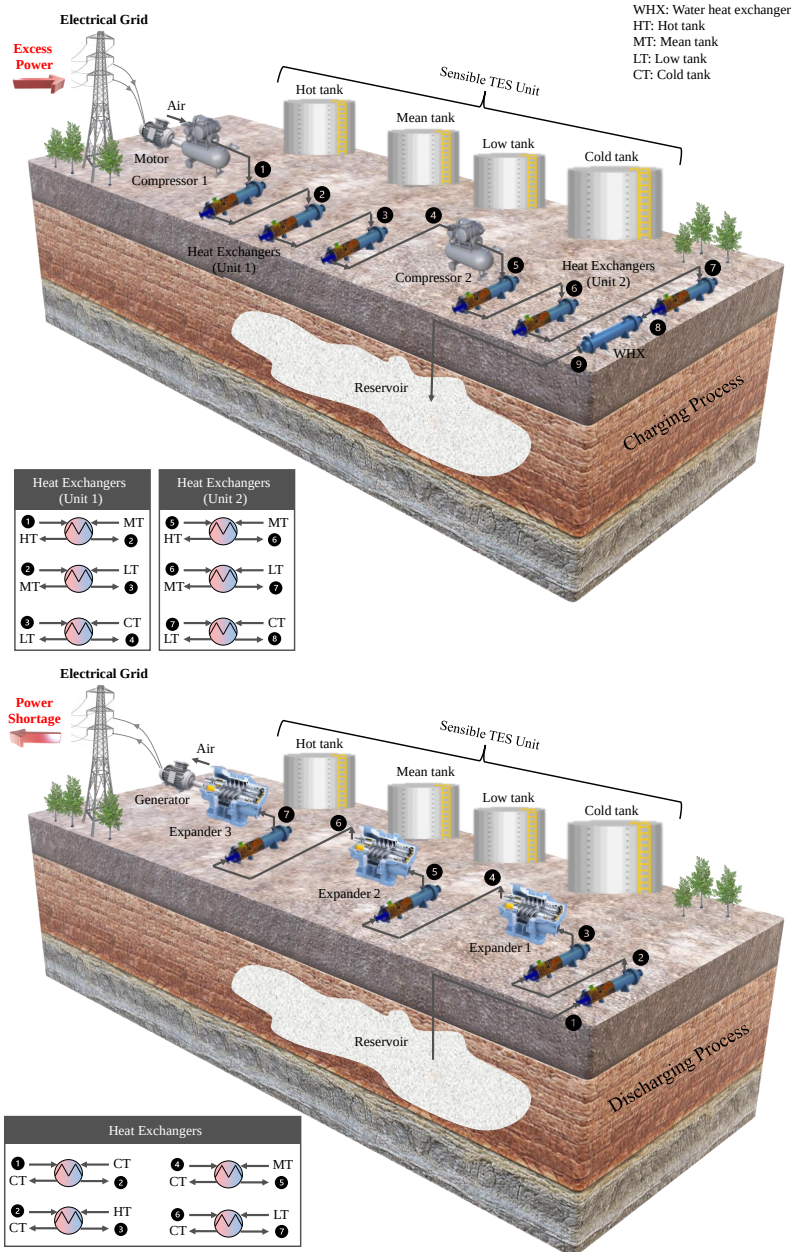

Figure 4.8: Suggested configuration for charging (upper) and discharging (lower) processes of a NA-CAES system with sensible thermal energy storage.

is statically analyzed and an appropriate TES size (as an initial assumption, and an upper bound of TES size) is selected using a box diagram as described in section 4.3.2. Afterward, a thermodynamic model is employed to assess the NA-CAES performance of plants A, B, and C via their first-law efficiency, and to find sources of inefficiencies. The model will also yield illustrative information on system operation (e.g., time-varying state-of-charge of the cavern, charging/idle/discharging events duration). This section then incorporates a sensitivity analysis to examine which operational parameters (see section 4.2.2.10) have the greatest impact on system performance, and finds the correlation between each operational parameter along with the first-law efficiency. In the end, a multi-objective optimization (first-law efficiency and the TES volume (TES size) are the fitness and cost functions, respectively) is used to identify plants A, B, and C's operational parameters that result in the best NA-CAES system operation and performance (see section 4.2.2.11).

The following subsections present the fundamental thermodynamic equations for the different components of the NA-CAES system (including motor, compressor, heat exchangers and TES tanks, reservoir, combustion chamber, pump, expander, and generator) as shown in Figure 4.8, system operation limitations (load limits, start-up time), a sensitivity analysis, and the global optimization method used in this study. The following assumptions have been applied to the thermodynamic analysis of all components.

- Air acts as an ideal gas (compressibility factor=1).
- Uniform air temperature and pressure in the cavern.
- Potential and kinetic energy changes are negligible [97].
- No chemical reactions or phase change.
- Operation of all components, except the salt cavern, are modeled at steady state.

4.2.2.1 Compressor

During the off-peak period, the compressor units consume electric power to pressurize ambient air. The compressor units are assumed to have constant isentropic efficiency (η_c) calculated by Equation 4.2 [105], while the compression ratio is considered constant. For this isentropic efficiency, the air temperature always increases as the air is compressed to a higher than atmospheric pressure. The specific compression work (KJ/kg), and the compressor's output temperature ($T_{c,2}$) and pressure ($P_{c,2}$), can respectively be determined by Equations 4.1, 4.3, and 4.4 as presented in Table 4.1, where $\dot{W}_c$ is the specific compressor

Table 4.1: Energy calculation for the compressors in a NA-CAES system.

Component	Equations	
Compressor [156, 105, 78]	$\dot{W}_c = \frac{\dot{m}_c C_p T_{c,1}}{\eta_c}\left[\left(\frac{P_{c,2}}{P_{c,1}}\right)^{\frac{\gamma-1}{\gamma}} - 1\right]$	(4.1)
	$\eta_c = 0.91 - \frac{\frac{P_{c,2}}{P_{c,1}} - 1}{300}$	(4.2)
	$T_{c,2} = T_{c,1} + \frac{T_{c,1}}{\eta_c}\left[\left(\frac{P_{c,2}}{P_{c,1}}\right)^{\frac{\gamma-1}{\gamma}} - 1\right]$	(4.3)
	$P_{c,2} = \mathrm{PR} \times P_{c,1}$	(4.4)
	$\text{Storable power} = \begin{cases} \mathrm{CP} & \mathrm{EP} \geq \mathrm{CP} \\ \mathrm{EP} & 0 < \mathrm{EP} < \mathrm{CP} \\ 0 & \mathrm{EP} = 0 \end{cases}$	(4.5)
	$\text{Load} = \begin{cases} 100\% & \mathrm{EP} \geq \mathrm{CP} \\ \frac{\mathrm{EP}}{\mathrm{CP}} \times 100\% & 0 < \mathrm{EP} < \mathrm{CP} \\ 0 & \mathrm{EP} = 0 \end{cases}$	(4.6)
	$\text{running time} = \frac{\text{Storable power} \times \Delta M}{\frac{\text{minimum load}}{100} \times \mathrm{CP} \times \dot{m}_c \Delta t_{\text{interval}}}$	(4.7)

power consumption (kW/kg), and $\dot{m}_c, T_{c,1}, P_{c,1}$, and γ are the air mass flow rate, the inlet temperature and pressure, and the specific heat ratio for air($\frac{C_p}{C_v} = 1.4$ @300 K; assumed constant), respectively.

As the compressor size can restrict the amount of excess power which can be stored during charging mode, the storable power can be limited as determined by Equation 4.5. When the compressor power (CP) is less than excess power (EP) in an event, some part of excess power is lost (EP−CP) while the compressor operates at full load. Equations 4.6 and 4.7 also determine the compressor load and time of run at different conditions (where ΔM represents the difference in cavern mass between two consecutive intervals). The compressor (or expander) efficiency can drop by over 40% [38] from its peak efficiency if it operates at part load due to leakage loss at low rotational speeds [42]). In other words, turbomachines are designed for high efficiency at full-load operation which means they operate best running at maximum capacity (rated load) and pressure ratio. However,

most of the time, a compressor (or expander) in a CAES plant runs at off-design operating conditions (e.g., reduced load), if throttling has been introduced to maintain pressure ratio, or if excess power is less than the compressor size (or power requirements in the electrical grid are lower than the expander size). Additionally, the compressor (or expander) cannot run for a duration which is lower than its startup time (the required time for the turbomachine to reach its rated capacity after being turned on). Therefore, a control strategy for CAES turbomachines can be designed to determine whether the CAES system can operate or if no action will be taken due to turbomachines inefficiencies. In this study, both the compressor and expander loads are limited by a lower value of 80%, while the compressor and expander have a minimum start-up time of 5 and 10 minutes, respectively.

Figure 4.9 illustrates the control unit (green dashed box) that restricts the turbomachine load and run-time operation based on cavern capacity, turbomachine load, and startup time limits. To apply the minimum load and start-up time constraints in CAES modeling, the suggested control unit starts with the turbomachines load and run time which are determined via the logic in Figure 4.5 (red dashed boxes of A_1 and B_1). Considering compressor operation as shown on the right-hand side of Figure 4.9, when the compressor load and run-time are determined at any given time (based on the flowchart presented in Figure 4.5), the load would be considered equal to the minimum load (stage A_2), and the running time corresponding to the minimum load is calculated (stage A_3). This step is done to verify whether the compressor can operate for a duration longer than the start-up time at a minimum load. In stage A_3, if the compressor running time falls short of the required minimum start-up time, the CAES system goes into idle mode, even when the cavern has sufficient capacity to store power. If the run-time calculated in stage A_3 exceeds the modeling time interval (1 hour), the compressor run time will consider the entire time interval (1 hour, stage A_4), and an updated compressor load will be determined (stage A_5). The same methodology can be applied to the expander operations, starting from the left-hand side of Figure 4.9.

4.2.2.2 Heat Exchangers (HXs) and Multiple-tank Thermal Energy Storage (TES)

The set of equations (Equations 4.8 to 4.14) presented in Table 4.2 is used to estimate the counter-flow heat exchangers effectiveness based on the number of transfer units (NTU, ranges between 0 and 5) and the thermal capacity ratio ($\frac{C_{min}}{C_{max}}$) [25], where A_1 to D_4 are tuned coefficients and can be found in [25]. In Equations 4.8 and 4.9, C_{Min} and C_{Max} are the minimum and maximum heat capacity rates for the two fluids in the heat exchanger (Air and thermal fluid). When C_{Min} is equal to C_{Max} the heat exchanger is said to be

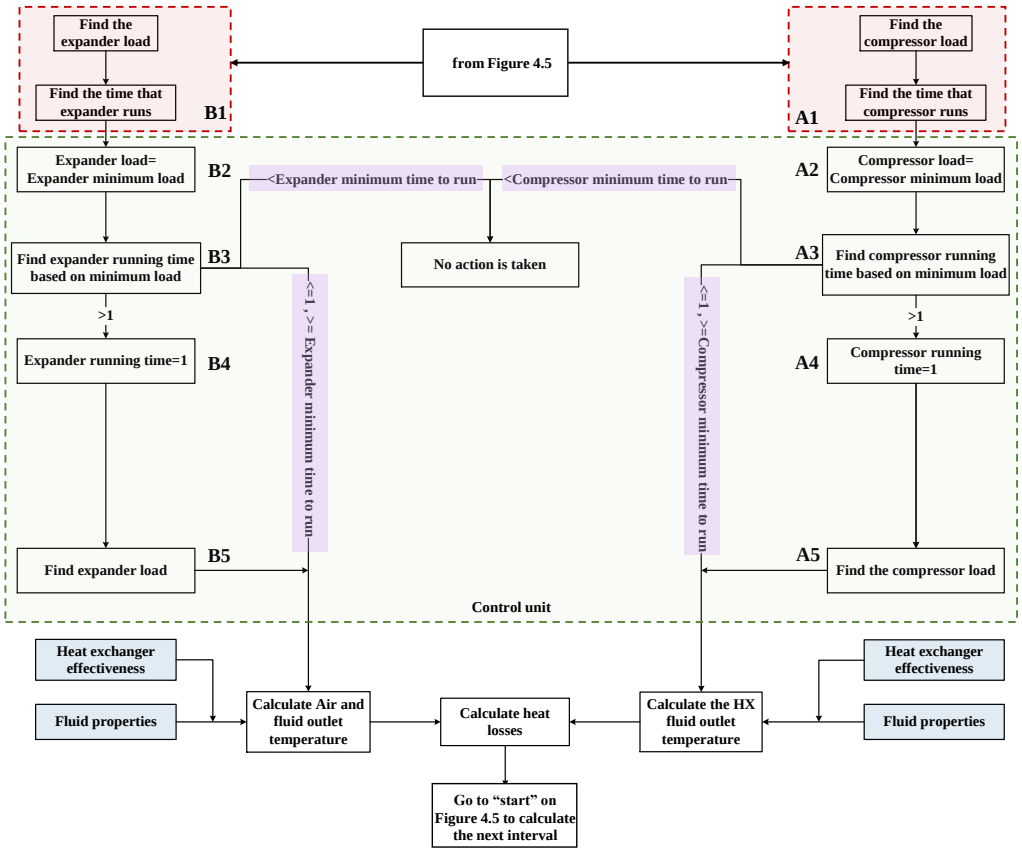

Figure 4.9: Applying the minimum load and start-up time constraints in CAES modeling (this flowchart is executed after Figure 4.5; see red dashed boxes in Figure 4.5).

balanced. $\dot{m}_{tf}$, $C_{p,tf}$, $T_{tf,1}$ and $T_{tf,2}$ are the mass flow rate, constant pressure specific heat, and the inlet and outlet temperature of thermal fluid. q_{max} and q_{actual} in Equations 4.15 and 4.16 represent the maximum and actual transferred heat between the air and thermal fluid per unit of time, respectively. Equations 4.17 and 4.18 can be employed to find the outlet temperature of thermal fluid and compressed air after heat exchanging, respectively. Equations 4.8 to 4.16 can be used for discharging process while the compressor load, $\dot{m}_c$, $T_{c,2}$, and $T_{tf,1}$ will be replaced by expander load, expander mass flow rate ($\dot{m}_e$), thermal energy storage temperature, and storage temperature (T), respectively. Similarly, Equations 4.17 and 4.18 can also be rewritten for the discharge process. It is worth mentioning that the pressure of compressed air drops when it goes through the heat exchangers, and the pressure losses are calculated by an empirical equation (Equation 4.19), where P_{in} is the air inlet pressure into heat exchanger.

During CAES charging, discharging mode, and idle periods, the thermal fluid inside the thermal energy storage tanks (vertical-cylindrical tanks with domed roofs) cools down due to heat loss to the environment. No heaters are considered in this modeling to keep the TES tanks' temperature constant, as results show that the risk of freezing is very low with daily charging/discharging. For this research, the walls and bottoms of the hot and cold tanks are assumed to be insulated with a layer of alumina silicate fiber (thickness of 350 mm) [186] and firebrick (thickness of 500 mm) [169], respectively. Equations 4.20 to 4.23 in Table 4.2 present the fundamental governing equations for the thermal storage tanks [186, 169, 184, 114], where M_{tf}, u_{tf}, α_{ins}, A_{ins}, T_{tank}, and T_{amb} are the thermal fluid mass inside the tank, internal energy of the thermal fluid inside the tank, insulation thermal conductivity (Equation 4.21), area of heat transfer, TES tank temperature, and ambient temperature, respectively. For safety the minimum and maximum of thermal fluid mass can be also calculated by Equations 4.22 and 4.23, in which a 10% tank volume is considered as freeboard (above the thermal fluid free surface level) and a 10% of maximum mass inside the tank is considered as a heal (the residual mass (or volume) of thermal fluid at the bottom of the tank for pump suction head) [122]. It is worth mentioning that in this study homogeneous temperature distribution is assumed for all heat storage tanks.

4.2.2.3 Pump

In this study, centrifugal pumps are modeled to move the thermal fluid through the heat exchangers, and TES tanks. The approximate pump power required during charging or discharging operations can be calculated by Equation 4.24, where η_P and η_M are respectively the pump and electric motor efficiencies, and P_{Pump}, g, and H are the pump power (in Watt), gravity acceleration, and pump head (height of fluid in meter) [125].

Table 4.2: Energy calculation for the heat exchangers and TES in a NA-CAES system.

Component	Equations
HXs and TES [69, 25, 174, 114, 186, 169]	$C_{\min} = \text{Min}\big[\frac{\dot{m}_c \times \text{Compressor load} \times C_p}{100}, \dot{m}_{tf} \times C_{p,tf}\big]$ (4.8)
	$C_{\max} = \text{Max}\big[\frac{\dot{m}_c \times \text{Compressor load} \times C_p}{100}, \dot{m}_{tf} \times C_{p,tf}\big]$ (4.9)
	$\epsilon_{\text{HX}} = a + b(\text{NTU}) + c(\text{NTU})^2 + d(\text{NTU})^3$ (4.10)
	$a = A_1 + B_1(\frac{C_{\min}}{C_{\max}}) + C_1(\frac{C_{\min}}{C_{\max}})^2 + D_1(\frac{C_{\min}}{C_{\max}})^3$ (4.11)
	$b = A_2 + B_2(\frac{C_{\min}}{C_{\max}}) + C_2(\frac{C_{\min}}{C_{\max}})^2 + D_2(\frac{C_{\min}}{C_{\max}})^3$ (4.12)
	$c = A_3 + B_3(\frac{C_{\min}}{C_{\max}}) + C_3(\frac{C_{\min}}{C_{\max}})^2 + D_3(\frac{C_{\min}}{C_{\max}})^3$ (4.13)
	$d = A_4 + B_4(\frac{C_{\min}}{C_{\max}}) + C_4(\frac{C_{\min}}{C_{\max}})^2 + D_4(\frac{C_{\min}}{C_{\max}})^3$ (4.14)
	$q_{\max} = C_{\min} \times (T_{c,2} - T_{tf,1})$ (4.15)
	$q_{\text{actual}} = \epsilon_{\text{HX}} q_{\max}$ (4.16)
	$T_{tf,2} = T_{tf,1} + \frac{q_{\text{actual}}}{\dot{m}_{tf} \times C_{p,tf}}$ (4.17)
	$T_{c,3} = T_{c,2} - \frac{q_{\text{actual}}}{\frac{\dot{m}_c \times \text{Compressor load} \times C_p}{100}}$ (4.18)
	$\Delta P = \big(\frac{0.0083\epsilon_{\text{HX}}}{1-\epsilon_{\text{HX}}}\big) P_{in}$ (4.19)
	$\frac{d}{dt}\big(M_{tf} u_{tf}\big) = \dot{m}_{tf} C_{p,tf} T_{tf} - \alpha_{\text{ins}} A_{\text{ins}} (T_{\text{tank}} - T_{\text{amb}})$ (4.20)
	$\alpha_{\text{ins}}(W/m.K) = \begin{cases} 0.034 + 0.0002 T_{tf} & \text{Alumina silicate fiber} \\ 0.61 + 0.00058 T_{tf} & \text{Firebrick} \end{cases}$ (4.21)
	$M_{tf,max} = \rho_{tf}(0.9 V_{\text{tank}})$ (4.22)
	$M_{tf,min} = 0.1 M_{tf,max}$ (4.23)

Table 4.3: Energy calculation for the pump in a NA-CAES system.

Component	Equations	
Pump [125]	$P_{\text{Pump}} = \frac{\dot{m}_{tf} g H}{\eta_P \eta_M}$	(4.24)

4.2.2.4 Reservoir

The first-law of thermodynamics, as presented in Equation 4.25 [156], is applied to the high-pressure reservoir (which is a salt cavern in this study), where M, u, T, R, and h are the air mass inside the reservoir at time t, air internal energy at time t, air temperature at time t, air specific gas constant, and specific enthalpy (h_{in} is the specific enthalpy of injected air), and $\dot{Q}$ can be calculated by Equation 4.26 (h_R and A_R in Equation 4.26 are the convective heat transfer coefficient and reservoir area, respectively). $\dot{m}_{in}$ and $\dot{m}_{out}$ are the entering and exiting mass flow into or from the reservoir. If the wall temperature (T_{wall}) and heat transfer coefficient (h_R) are known, then the solution to the ordinary differential Equation 4.25 for the reservoir air temperature is given by Equation 4.30. Otherwise heat conduction to the surrounding rock, Equation 4.28, along with the boundary conditions given in Equation 4.29, and Equations 4.25 and 4.26, are employed to find both air and wall temperatures; where, ρ_{surr}, $C_{p_{surr}}$, T_{surr}, and k_{surr} are respectively density, constant pressure specific heat, temperature, and thermal conductivity of surrounding rocks, and T_0 is the initial temperature of rock. Equation 4.30 is a unified and simplified solution to predict the thermodynamic properties within a CAES reservoir without experiencing the computational complexity of seeking an analytical solution [109, 179]. The wall temperature can be reasonably assumed constant, as the air temperature variation inside the salt cavern reservoir is small (the air temperature only varies between 20 to 40 degrees) [179]. Moreover, the heat transfer coefficient can be estimated by Equation 4.27 [156, 140], where a and b empirical values. Given the air temperature is calculated by Equation 4.30, the air pressure ($P(t)$, for a constant-volume reservoir) or the reservoir volume ($V(t)$, for a constant-pressure reservoir) can be calculated by the ideal gas law (Equation 4.33).

The air pressure inside the constant-volume reservoir can effectively limit the operation of a CAES system, its coverage percentage, and the required size of components. In other words, it is crucial to ensure that the air pressure remains within the acceptable range determined by the salt cavern depth, as exceeding the maximum or falling below the minimum pressure is not permissible. For salt caverns in Southwestern Ontario, the maximum and minimum pressure are 14 and 5 MPa, respectively. Equation 4.34 illustrates how this constraint is incorporated into the thermodynamic model. According to Equation

Table 4.4: Energy calculation for the reservoir in a NA-CAES system.

Component	Equations
Reservoir [156, 179]	$\frac{d(M(t)u(t))}{dt} = \dot{m}_{\text{in}}[h_{\text{in}} - h(t) + RT(t)] - \dot{m}_{\text{out}}[RT(t)] + \dot{Q}$ (4.25)
	$\dot{Q} = h_R(t)A_R(t)\big(T_{wall}(t) - T(t)\big)$ (4.26)
	$h_R = a + b\lvert\dot{m}_{\text{in}} - \dot{m}_{\text{out}}\rvert^{0.8}$ (4.27)
	$\rho_{surr}C_{p_{surr}}\frac{dT_{surr}}{dt} = \frac{1}{r}\frac{d}{dr}(k_{surr}r\frac{dT_{surr}}{dr})$ (4.28)
	$T_{surr} = \begin{cases} h_R(T(t) - T_{wall}(t)) = -k_{surr}\frac{dT_{surr}}{dr} & r = r_R \\ T_0 & r \to \infty \end{cases}$ (4.29)
	$T(t) = (T_0 + \alpha)e^{\beta(t-t_0)} - \alpha$ (4.30)
	$\alpha = \begin{cases} \frac{\dot{m}_{in}C_pT_ih_R(t)A_R(t)T_{wall}(t)}{\dot{m}_{in}(R-C_p)-h_R(t)A_R(t)} & \text{Charging mode} \\ -T_{wall}(t) & \text{Idle mode} \\ \frac{h_R(t)A_R(t)T_{wall}(t)}{\dot{m}_{out}R-h_R(t)A_R(t)} & \text{Discharging mode} \end{cases}$ (4.31)
	$\beta = \begin{cases} \frac{\dot{m}_{in}(R-C_p)-h_R(t)A_R(t)}{\rho(t)V(t)C_v} & \text{Charging mode} \\ \frac{-h_R(t)A_R(t)}{\rho(t)V(t)C_v} & \text{Idle mode} \\ \frac{\dot{m}_{out}R-h_R(t)A_R(t)}{\rho(t)V(t)C_v} & \text{Discharging mode} \end{cases}$ (4.32)
	$P(t)V(t) = m(t)R_{\text{air}}T(t)$ (4.33)
	$P(t) = \begin{cases} P_{\max} \quad , \quad t_{ch,n} = \frac{m_n - m_{n-1}}{\dot{m}_{in}} & \text{P}\geq P_{\max} \\ P \quad , \quad t_{ch/disch,n} = \Delta t_{\text{interval}} & P_{\min} < P < P_{\max} \\ P_{\min} \quad , \quad t_{disch,n} = \frac{m_n - m_{n-1}}{\dot{m}_{out}} & \text{P}\leq P_{\min} \end{cases}$ (4.34)

Table 4.5: Energy calculation for the combustion chamber in a NA-CAES system.

Component	Equations	
Combustion chamber [106, 31]	$\dot{Q}_{\mathrm{NG}} = \dot{m}_{NG}\mathrm{LHV}_{\mathrm{NG}}$	(4.35)
	$\dot{m}_{\mathrm{NG}} = \dfrac{\dot{m}_{out}C_p(T_{e,1} - T(t))}{\mathrm{LHV}_{\mathrm{NG}} \times \eta_{\mathrm{cc}}}$	(4.36)

4.34, if the air pressure reaches the maximum pressure during the charging mode within a given time interval, the charging process ceases, and the system only operates for a partial duration of that 1-hour interval. The same restriction applies during the discharging mode if the pressure drops and reaches the lower pressure limit. Consequently, the system can complete an entire interval of operation only when the pressure remains within the acceptable range, neither exceeding the maximum pressure nor falling below the minimum pressure. If the reservoir is a constant-pressure reservoir, CAES operation is restricted by the minimum and maximum volume, allowing Equation 4.34 to be reformulated based on the cavern volume.

4.2.2.5 Combustion Chamber

Due to the heat losses that occur at different locations (e.g., heat exchangers, TES, and the cavern) and during different stages of operation, a combustion chamber (CC) is used to provide additional heat as needed to heat up the compressed air before the air expander. Heating is needed to optimize the efficiency performance of a chain of expanders, but may also be needed to avoid ice formation. Equation 4.35 in Table 4.5 displays the amount of heat provided by burning natural gas (NG) in the combustion chamber, where LHV stands for the lower heating value of fuel. The fuel mass flow rate can also be determined by Equation 4.36, where $T_{e,1}$ and η_{cc} are respectively the expander inlet temperature and combustion chamber efficiency.

4.2.2.6 Expander

During discharging mode, the compressed air is released generating power ($\dot{W}_e$) using an air expander. The expansion work, output pressure, and temperature can be determined by equations 4.37 to 4.39 (in Table 4.6), where $P_{e,2}$, $T_{e,2}$, and PR are the output pressure

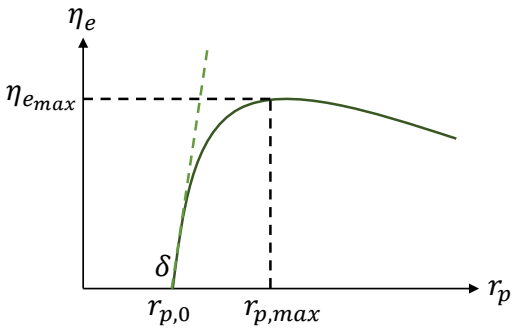

Parameters	Definition
$\eta_{e_{max}}$	Maximum efficiency
$r_{p,0}$	r_p-intercept of the efficiency curve
$r_{p,max}$	Optimal pressure ratio
δ	Slope of the efficiency curve at $r_{p,0}$

Figure 4.10: Significant parameters in analytical modeling of a variable-pressure expander.

and temperature at time t, and expander pressure ratio, and η_e is the expander efficiency. The efficiency and performance of an expander varies with pressure ratio and rotational speed. In this research rotational speed variations are not considered as the expanders only operate close to full-load (i.e., 80 % load or higher) and at a constant rotational speed [46].

If a NA-CAES system operates with a constant-volume reservoir and a throttling valve for its discharging mode (plant A), or operates with a constant-pressure reservoir (plant C), the high-pressure expander pressure ratio is constant ($\frac{P_{e,1}}{P_{e,2}}$=constant), and the expander efficiency can be calculated by the empirical expression presented in Equation 4.40 [78]. For the thermodynamic modeling of a NA-CAES system operating with a variable-pressure-ratio expander ($\frac{P_{e,1}}{P_{e,2}}$=variable), the high-pressure expander efficiency can be estimated by the second expression in Equation 4.40 which is an empirically derived analytical model for an expander - the analytical model follows the same shape as that of the empirical efficiency-pressure ratio curve as shown in Figure 4.10. In Equation 4.40, ξ is the shape factor that controls the shape of the efficiency curve. In this study, $\eta_{e_{max}}$ is considered to be 0.9, while other parameters are chosen from [46].

A similar approach to that applied to the compressor in Section 4.2.2.1 is applied to the expansion process restricting the amount of power generated and delivered to the power grid. The restriction is the fixed expander size/power. Equation 4.43 represents the amount of releasable power for different situations. If the power shortage magnitude (-PSH) is greater than the expander-rated maximum power, the CAES system will not be able to generate all the power the grid requires. If the power shortage is less than the size of the expander, it can operate at part load as long as there is available power in the reservoir. Equations 4.44 and 4.45 also determine the expander load and start-up time at different conditions.

Table 4.6: Energy calculation for the expander in a NA-CAES system.

Component	Equations
Expander [156, 78, 46]	$\dot{W}_e = \dot{m}_e C_p T_{e,1} \eta_e (\mathrm{PR}^{\frac{\gamma-1}{\gamma}} - 1)$ (4.37)
	$P_{e,1} = \frac{P_{e,2}}{\mathrm{PR}}$ (4.38)
	$T_{e,2} = T_{e,1} + T_{e,1}\eta_e (\mathrm{PR}^{\frac{\gamma-1}{\gamma}} - 1)$ (4.39)
	$\eta_e = \begin{cases} 0.9 - \frac{\frac{P_{e,1}}{P_{e,2}}-1}{250} & \frac{P_{e,1}}{P_{e,2}} = \mathrm{Cte} \\ \eta_{emax} \sin\left(\xi \arctan\left(B(r_p - r_{p,0})\right.\right. & \\ -E\big(B(r_p - r_{p,0}) - \arctan\left(B(r_p - r_{p,0})\right)\big)\big) & \frac{P_{e,1}}{P_{e,2}} = \mathrm{Var} \end{cases}$ (4.40)
	$B = \frac{\delta}{\xi \eta_{emax}}$ (4.41)
	$E = \frac{B(r_{p,max} - r_{p,0}) - \tan(\frac{\pi}{2\xi})}{B(r_{p,max} - r_{p,0}) - \arctan(B(r_{p,max} - r_{p,0}))}$ (4.42)
	$\text{Releasable power} = \begin{cases} -\mathrm{EXP} & \mathrm{PSH} \leq -\mathrm{EXP} \\ \mathrm{PSH} & \text{-EXP} < \mathrm{PSH} < 0 \\ 0 & \mathrm{PSH} = 0 \end{cases}$ (4.43)
	$\text{Load} = \begin{cases} 100\% & \mathrm{PSH} \leq -\mathrm{EXP} \\ \frac{-\mathrm{PSH}}{\mathrm{EXP}} \times 100\% & -\mathrm{EXP} < \mathrm{PSH} < 0 \\ 0 & \mathrm{PSH} = 0 \end{cases}$ (4.44)
	$\text{start-up time} = \frac{\text{Releasable power} \times \Delta M}{\frac{\text{minimum load}}{100} \times \mathrm{EXP} \times \dot{m}_e \Delta t_{\text{interval}}}$ (4.45)

4.2.2.7 Electrical Motor and Generator

The electrical motor and generator are not modeled in detail in this study, and their efficiencies are taken as the same as in [56].

4.2.2.8 First-law Efficiency

The round-trip efficiency of a NA-CAES system (η_{cycle}) can be calculated by Equation 4.46:

$$\eta_{\text{RTE}} = \frac{W_{\text{el-out}}}{W_{\text{el-in}} + Q_{\text{required}}} \tag{4.46}$$

where, $W_{\text{el-in}}$, and $W_{\text{el-out}}$ are the total input electrical work into the system (compressors and pumps), and the total electrical work output of the CAES system (expanders), respectively (see Equations 4.47 and 4.48, where, η_M and η_G are the DC motor and the generator efficiencies, respectively.). Q_{required} is the amount of heat required to heat up the air before entering the expander if the thermal energy storage cannot provide all the heat needed.

$$W_{\text{el-in}} = \frac{W_c + P_{pump}}{\eta_M} = \frac{\int_0^{t_{charge}} (\dot{W}_c + \dot{P}_{pump}) dt}{\eta_M} \tag{4.47}$$

$$W_{\text{el-out}} = W_e \times \eta_G = \eta_G \times \int_0^{t_{discharge}} \dot{W}_e dt \tag{4.48}$$

4.2.2.9 Operating Parameters of NA-CAES System

Table 4.7 summarizes the CAES system operating parameters in this study. To size a NA-CAES system that minimizes component size for a desired coverage percentage, and given temperature and pressure operation limits, 82,500 different scenarios are considered as shown in Figure 4.11.

Table 4.7: Assumed operating parameters in this study.

Parameter	**Value**	**Unit**
Maximum/Minimum pressure in cavern [157]	14/5	[MPa]
Maximum/Minimum temperature in cavern [157]	313/333	[K]
Compressors unit pressure ratio	12.5	[Unitless]
Compressor inlet temperature	300	[K]
Expander outlet temperature (last stage only)	300	[K]
Maximum size of compressor	250	[MW]
Maximum size of expander	330	[MW]
Maximum size of cavern	1000	[MWh]
Compressor efficiency	variable	[Unitless]
Minimum compressor load	80%	[Unitless]
Minimum compressor start-up time	10	[minute]
Expander efficiency	variable	[Unitless]
Minimum expander load	80%	[Unitless]
Minimum expander start-up time	5	[minute]
Combustion chamber efficiency [106]	97%	[Unitless]
Electrical motor efficiency [56]	94%	[Unitless]
Generator efficiency [56]	94%	[Unitless]
Pump efficiency [125]	70%	[Unitless]
Air injection temperature	293.15	[K]
Sensible TES tanks initial temperature	293.15	[K]

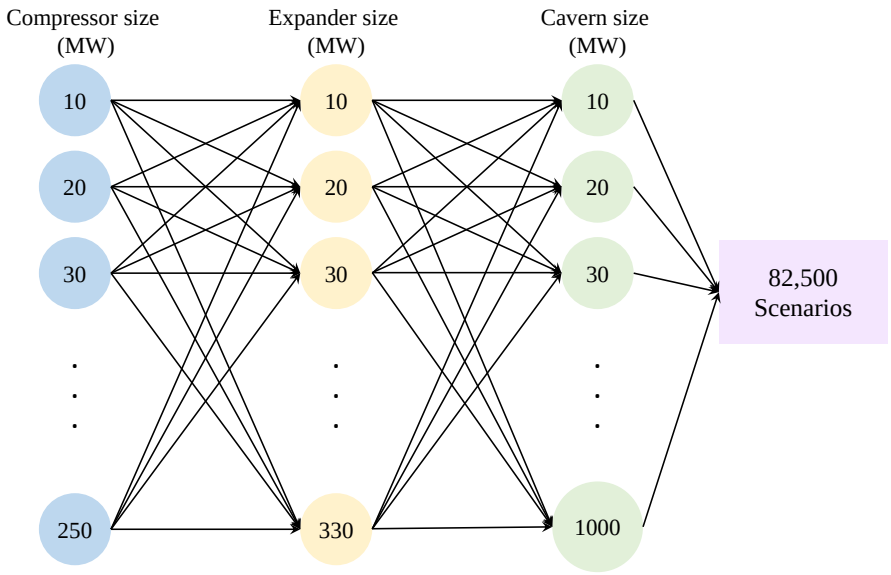

Figure 4.11: Different scenarios to size and examine the NA-CAES system performance in Ontario.

4.2.2.10 Sensitivity Analysis: Determining the Effective Parameters

The aim of sensitivity analysis (SA) is to assess the impact of independent parameters (referred to as factors in SA) on the first-law efficiency (referred to as a response in SA) and to simplify the optimization process by eliminating insignificant parameters/factors. There are two different approaches to investigating which factors have a larger impact on the response: local and global [133]. Local sensitivity analysis (LSA) studies the impact of changes around a single factor on response values. Global sensitivity analysis (GSA) assesses the impact of a single factor on the response by changing the factor in question as well as changing the values of other factors. LSA and GSA may rank the sensitivity of the response to studied factors differently. Therefore, performing both LSA and GSA methods is beneficial (and could be necessary) to ensure that the most significant design factors are not being neglected in the optimization process. In this study, both LSA and GSA are employed to rank the factors with the negligible impact factors being identified and not varied in the optimization process.

- *Global Sensitivity Analysis: Morris Method*

  The Morris method for global sensitivity analysis is utilized due to its simplicity and its low computational cost when several input factors may impact response [27].

The Morris method consists of several repetitions (defined by the user) and it is a GSA technique as all factors vary over their entire domain at each repetition. The procedure of the Morris method is given in [154].

- *Local Sensitivity Analysis*

  The LSA method used follows that of [154] and [81]. Like the Morris method a sensitivity coefficient is defined, but unlike the Morris method only one factor is changed at a time.

Table 4.8 summarizes the studied independent factors and their range for the three suggested plants (Plants A, B, and C).

4.2.2.11 Optimization of the NA-CAES System

This research uses the hierarchical two-objective optimization approach of Differential Evolution (DE) [101] to determine the optimal operational parameters of the NA-CAES system. A two-objective hierarchical optimization method constitutes a systematic strategy for optimizing the two objectives of maximizing efficiency and minimizing TES size with the relative importance of each objective specified by a user-defined weighting factor.

In summary, first, the objective function with the highest level of importance (the system's first-law efficiency) undergoes optimization in the first iteration, while the second objective function (the TES size, indicated by its volume and calculated by the summation of the high-temperature, mean-temperature, and low-temperature tanks) is ignored. The optimal solution for the first iteration is denoted as $X^1_{optimal}$. Subsequently, the optimization process follows by optimizing the TES size (the second objective, denoted by f_2), subject to a supplementary constraint imposed on the first objective function as depicted in Equation 4.49. The hierarchical optimization algorithm's outcomes will yield a Pareto optimal solution by manipulating the values of ϵ_i [101].

$$f_1(X) \geq (1 - \frac{\epsilon_i}{100}) f_1(X^{i-1}_{opimal}) \tag{4.49}$$

4.3 Results and Discussions

To assess the accuracy of the thermodynamic model used for the salt cavern reservoir, the results of mathematical modeling are compared with available experimental air temperature and pressure data from the Huntorf power plant [179]. The comparison is presented in

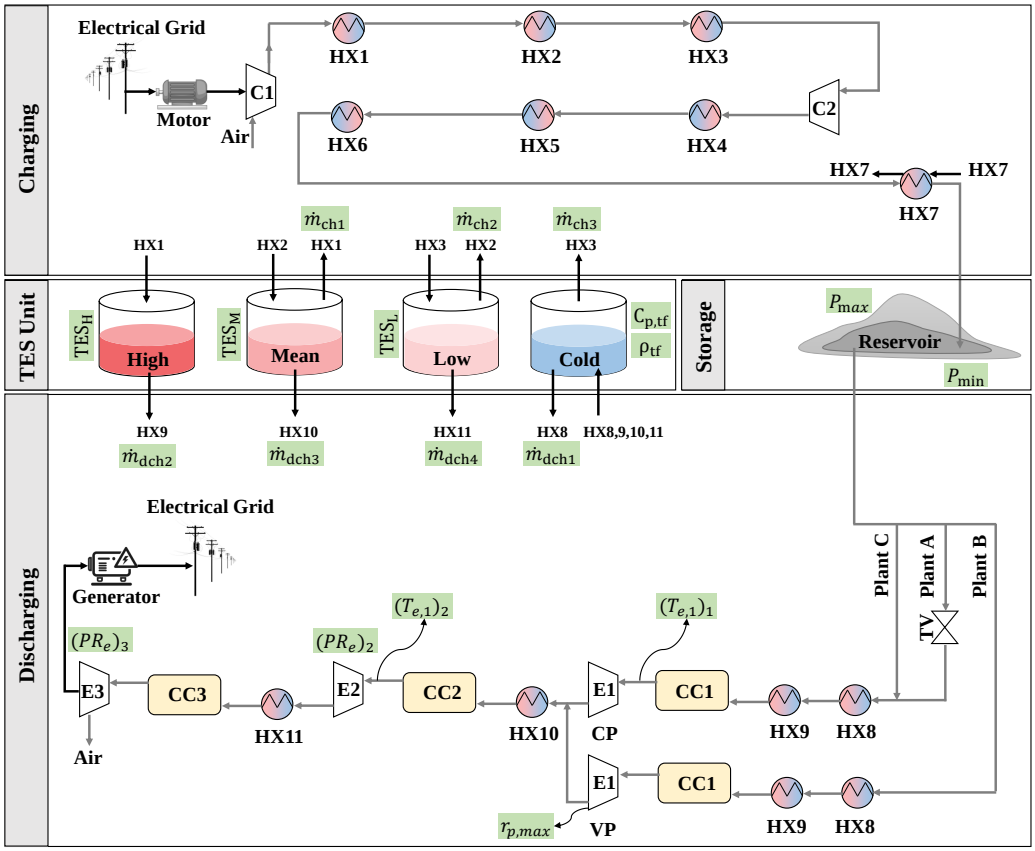

Figure 4.12: Studied independent parameters in the sensitivity analysis (highlighted by a green rectangle box); C: compressor, E: expander, CP: constant-pressure, VP: variable pressure, CC: combustion chamber, HX: heat exchanger, Cold: cold-temperature tank, Low: low-temperature tank, Mean: mean-temperature tank, and High: high-temperature tank.

Table 4.8: Studied independent parameters in sensitivity analysis for Plants A, B, and C (parameters in highlighted rectangle boxes in Figure 4.12).

Parameter	**Symbol**	**Range**	**Unit**
Thermal fluid mass flow rate during charging process (from mean-temperature to high-temperature tank)	$\dot{m}_{\text{ch1}}$	[10-300]	[kg/s]
Thermal fluid mass flow rate during charging process (from low-temperature to mean-temperature tank)	$\dot{m}_{\text{ch2}}$	[10-300]	[kg/s]
Thermal fluid mass flow rate during charging process (from cold-temperature to low-temperature tank)	$\dot{m}_{\text{ch3}}$	[10-300]	[kg/s]
Thermal fluid mass flow rate during discharging process (from cold-temperature to cold-temperature tank)	$\dot{m}_{\text{dch1}}$	[10-300]	[kg/s]
Thermal fluid mass flow rate during discharging process (from high-temperature to cold-temperature tank)	$\dot{m}_{\text{dch2}}$	[10-300]	[kg/s]
Thermal fluid mass flow rate during discharging process (from mean-temperature to cold-temperature tank)	$\dot{m}_{\text{dch3}}$	[10-300]	[kg/s]
Thermal fluid mass flow rate during discharging process (from low-temperature to cold-temperature tank)	$\dot{m}_{\text{dch4}}$	[10-300]	[kg/s]
Size of high-temperature tank	$(TES)_H$	[10-500]	[m^3]
Size of mean-temperature tank	$(TES)_M$	[10-500]	[m^3]
Size of low-temperature tank	$(TES)_L$	[10-500]	[m^3]
Thermal fluid density	ρ_{tf}	[800-1600]	[kg/m^3]
Thermal fluid heat capacity	$C_{p,tf}$	[800-4500]	[J/kg.K]
Reservoir upper pressure	P_{max}	[11-14]	[MPa]
Reservoir lower pressure	P_{min}	[5-10]	[MPa]
Expander 1 inlet temperature	$(T_{e,1})_1$	[390-700]	[K]
Expander 2 inlet temperature	$(T_{e,1})_2$	[370-600]	[K]
Expander 1 optimal pressure ratio	$(PR_e)_{1,opt}$	[3-9]	[Unitless]
Expander 2 pressure ratio	$(PR_e)_2$	[3-7]	[Unitless]
Expander 3 pressure ratio	$(PR_e)_3$	[2-6]	[Unitless]

Appendix B. Excellent agreement is observed, with the standard deviation of the difference between experiment and measurement being 0.58°C for a cavern temperature swing over a day of 20.1 °C (i.e., 25.7 to 45.8°C), and 0.07 MPa for a cavern pressure swing over a day of 1.3 MPa (4.7 to 6 MPa).

4.3.1 Sizing a CAES System for Ontario

The objective of this section is to establish economically viable component sizes for CAES systems in Ontario using the coverage-percentage method (refer to section 4.2.1.2 and the study by Sarmast et al. [157] for the definitions of coverage percentages). To accomplish this, a comprehensive assessment involving 82,500 distinct scenarios (as depicted in Figure 4.11) was undertaken to compare the coverage percentages of CAES across various components sizes (a compressor of 10 to 250 MW, an expander of 10 to 330 MW, and a cavern of 10 to 1000 MWh).

Figure 4.13 illustrates the distribution of discharging coverage versus charging coverage through the use of box plots, presenting a visual summary of the studied scenarios. These visualizations are instrumental in identifying scenarios that exhibit acceptable coverage percentages for both charging and discharging events, as well as identifying any outliers. Each box plot in Figure 4.13 features a rectangular box representing the interquartile range, with the lower and upper quartiles (Q_1 and Q_3, respectively) clearly displayed. The median (Q_2) of the data is denoted within the box. The lines extending from the rectangular box, known as lower and upper whiskers, are calculated as $Q_1 - 1.5(Q_3 - Q_1)$ and $Q_3 + 1.5(Q_3 - Q_1)$, respectively.

In this study, any scenario in Figure 4.13 with a charging or discharging coverage percentage falling below the lower whisker is classified as an outlier. Specifically, charging coverage percentages below 18% and discharging coverage percentages below 13% (indicated by the black outlined box in Figure 4.13) are deemed outliers. Conversely, the region outlined in red in Figure 4.13, representing charging and discharging coverage percentages exceeding the median values, is considered an acceptable range. Another significant observation revealed by Figure 4.13 is that the maximum charging coverage percentage does not exceed 48%, while the maximum discharging coverage percentage does not surpass 36% throughout the entirety of 2022. These observations are based on the selected range of component sizes.

Figure 4.14 exclusively presents graphs showcasing scenarios within the acceptable range, as defined in Figure 4.13. Additionally, these scenarios adhere to a limitation of 100 MW for both the compressor and expander sizes, which is an additional consideration

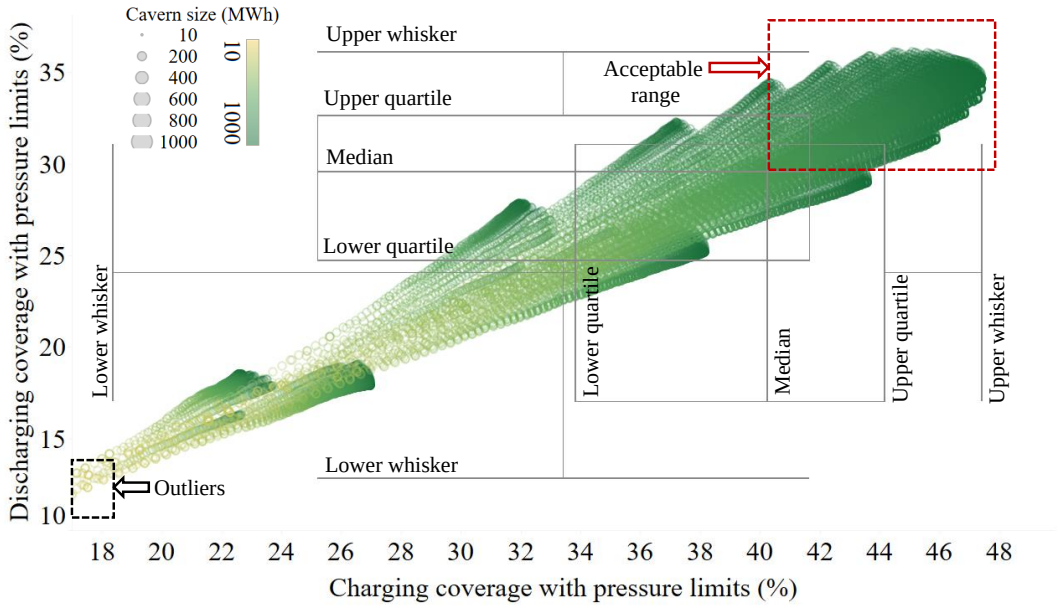

Figure 4.13: The distribution of coverage percentages for studied scenarios.

for economic feasibility. The data in Figure 4.14 are categorized based on compressor size. The observations can be summarized as follows:

- In order to size and design a CAES system for Ontario it is necessary to have a compressor with a minimum size of 30 MW (according to graph (a)) and an expander with a minimum size of 40 MW (according to graph (b)) to achieve an acceptable coverage percentage. Additionally, the salt cavern should have a minimum energy storage capacity of 640 MWh.

- Graphs (a) to (b) in Figure 4.14 provide a quick visual representation of the range of charging and discharging coverage percentages for various sizes of compressors and expanders. For instance, a 50 MW compressor, in combination with other component sizes, can yield a charging coverage ranging from 40.2% to 46.8%, while a CAES system with a 50 MW expander will not exceed a discharging coverage of 35.4%.

- Graphs (a) and (b) demonstrate that the charging and discharging coverage percentages increase as the sizes of the expander and compressor, respectively, are enlarged. For a given compressor size, this means that larger expanders allow for a greater decrease in the state-of-charge percentage of the cavern, providing more opportunities

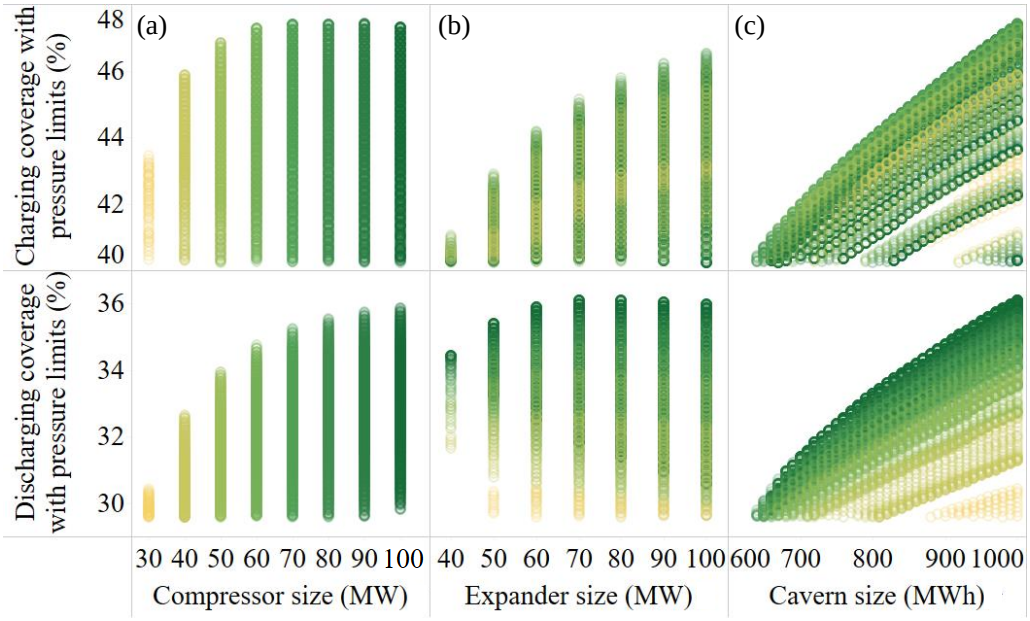

Figure 4.14: Coverage percentages variation of a CAES system by change of components sizing (data is categorized based on the compressor size from 30 (yellow) to 100 MW (dark green)).

Table 4.9: Proposed CAES systems for Ontario.

CAES Plants	$\mathbf{P}_1$	$\mathbf{P}_2$	$\mathbf{P}_3$	$\mathbf{P}_4$	$\mathbf{P}_5$	$\mathbf{P}_6$
Compressor (MW)	50	60	70	80	90	100
Expander (MW)	60	70	80	90	90	90
Cavern (MWh)	920	860	830	820	820	810
Charging coverage (%)	43.1	43.1	43.4	43.4	43.5	43
Discharging coverage (%)	33.1	33.1	33	33.1	33.1	33.1

for power storage. Conversely, for a given expander size, larger compressors result in a greater increase in the state-of-charge percentage, enabling a greater release of power. However, it should be noted that there exists an optimal size for both the compressor and expander to achieve the highest charging and discharging coverage percentages. The decrease in coverage percentages after reaching the optimal size is a direct consequence of applying the upper and lower pressure limits.

- Each data point in graphs (a) to (c) represents a potential candidate for a feasible CAES plant in Ontario, characterized by a charging coverage percentage of approximately 52.5% and a discharging coverage percentage of around 29.1%. Opting for CAES component combinations that meet the desired charging and discharging coverage percentages while utilizing the smallest possible component sizes proves to be a more economically advantageous approach. By prioritizing such combinations, the overall cost-effectiveness of the CAES system can be maximized.

As depicted in Table 4.9, achieving the desired coverage percentages necessitates employing a compressor and an expander within the range of 60 to 100 MW, along with a salt cavern possessing an energy capacity of 810 to 920 MWh. Moreover, it can be concluded that different CAES components sizes can yield identical coverage percentages. Conducting a cost analysis to investigate the size of the components (which falls beyond the scope of this study) can aid in determining the most cost-effective scenario. For the remainder of this chapter, we have used the Plant P_3 components sizes, which entail a 70 MW compressor, an 80 MW expander, and an 830 MWh salt cavern.

4.3.2 Design a NA-CAES System for Ontario: Sizing a TES

In section 4.3.1 a D-CAES system (i.e., no TES) was sized for the province of Ontario based on the desired coverage percentages for both charging and discharging events considering

the power grid's historic excess/shortage size and patterns, and considering air reservoir upper and lower pressure limitations.

This section aims to design a NA-CAES system for Ontario by sizing the TES. A small combustion unit is also added to provide make-up heat because the TES will not be able to capture all the exergy of compression heat, and the TES will also experience some heat loss. The need for this combustion unit is why this is not an A-CAES system, but a NA-CAES system. A multi-tank TES is considered due to its ability to capture a greater percentage of the compression heat exergy (refer to section 4.2.1.3). In other words, the implementation of a multi-tank thermal energy storage (TES) system, which operates at various temperatures, enables the efficient capture of compression heat at a temperature higher than that of the expander inlet. The determination of the optimal number of TES tanks falls beyond the purview of this work. Nonetheless, as part of this work, it has been observed that the optimal number of tanks correlates with the number of expansion units. In this study, three high-temperature tanks are employed to align with the use of three expansion units, as each tank can supply the required heat to an expansion unit at a specific temperature.

Several criteria, including cost, feasibility, storage temperature, duration, and size, necessitate consideration during the evaluation and design of a thermal energy storage (TES) system to ensure its successful implementation. In this study, the design of a TES system incorporates sizing and thermal storage temperature as factors. Proper sizing of a TES system in the context of compressed air energy storage power plants can contribute to enhanced plant profitability and efficiency, while an oversized TES system can have a detrimental impact on capital costs. To avoid the issues of over-sizing and under-sizing the TES system an optimization process is employed (as described and presented in Section 4.3.3.2)). However, an estimation of the TES size can be achieved by determining its hourly heat capacity through the CAES operation. However, estimating the size of the thermal energy storage (TES) can be accomplished by determining its hourly heat capacity based on the operation of the compressed air energy storage (CAES) system. This process is depicted in Figure 4.15. In Figure 4.15, the operation of the D-CAES plant is first simulated at each interval, denoted as interval i. During interval i, if the CAES plant engages in the charging action, the thermal energy storage undergoes the charging process, and its capacity is determined by aggregating the compression heat generated during interval i with the TES heat capacity from the previous interval, $i-1$ (assuming that only 95% of the compression heat can be effectively stored in the TES, while the remaining portion is dissipated through the heat exchangers. Similarly, only 95% of the TES heat capacity at any interval is available and 5% is assumed subject to dissipation). Conversely, in the case of discharging, the TES heat capacity at interval i decreases and can be computed

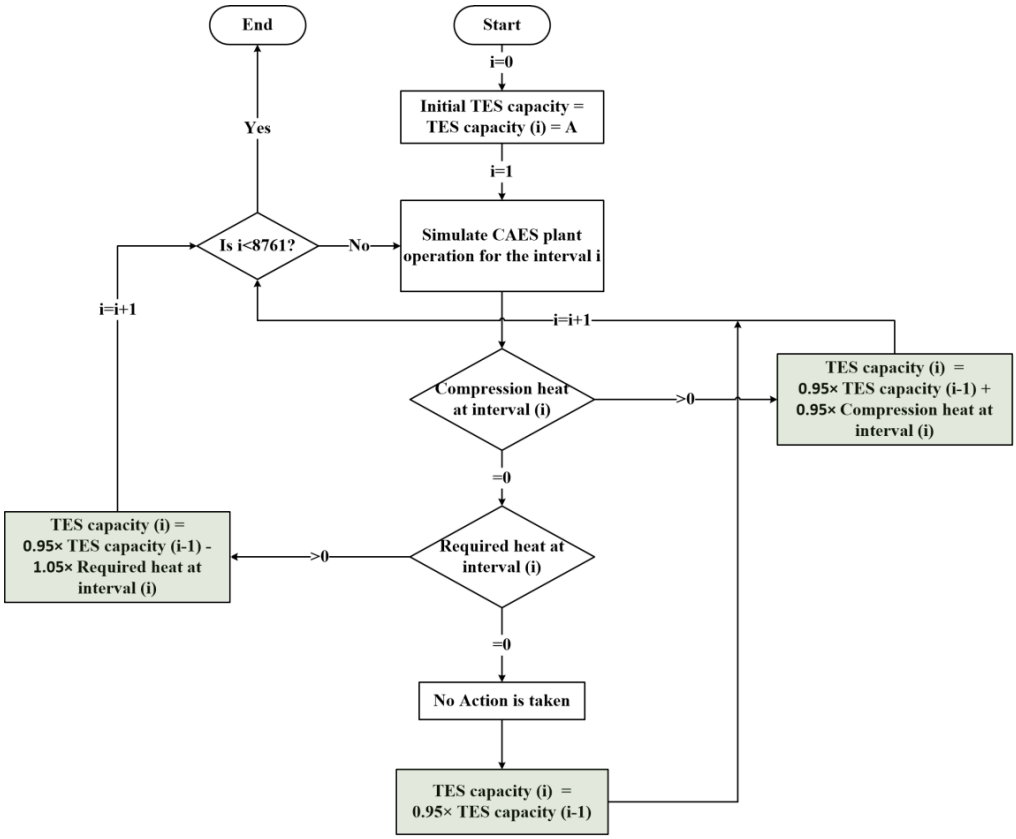

Figure 4.15: Workflow of the TES sizing method (A is the initial TES heat capacity).

by subtracting the required heat for the discharging event during interval i from the TES heat capacity in the previous interval, $i-1$ (again 95% of the TES heat capacity at any interval is available, and 5% more heat is taken due to the inefficiencies of discharging heat exchangers). In the event of an idle situation, no specific action is undertaken, apart from acknowledging that 5% of the TES heat capacity is dissipated due to insulation ineffectiveness of the TES tanks. The workflow process continues as long as $i < 8761$, corresponding to an hourly CAES operation spanning a full year.

Figure 4.16 provides a visual representation of the hourly heat capacity of the TES based on the CAES system operation in 2022. In Figure 4.16, any data point exceeding the upper whisker represents an outlier, indicating heat capacities greater than 1073 GJ. Sizing a thermal energy storage system based on the maximum required heat capacity may lead to higher initial costs, longer payback periods, larger installation space requirements,

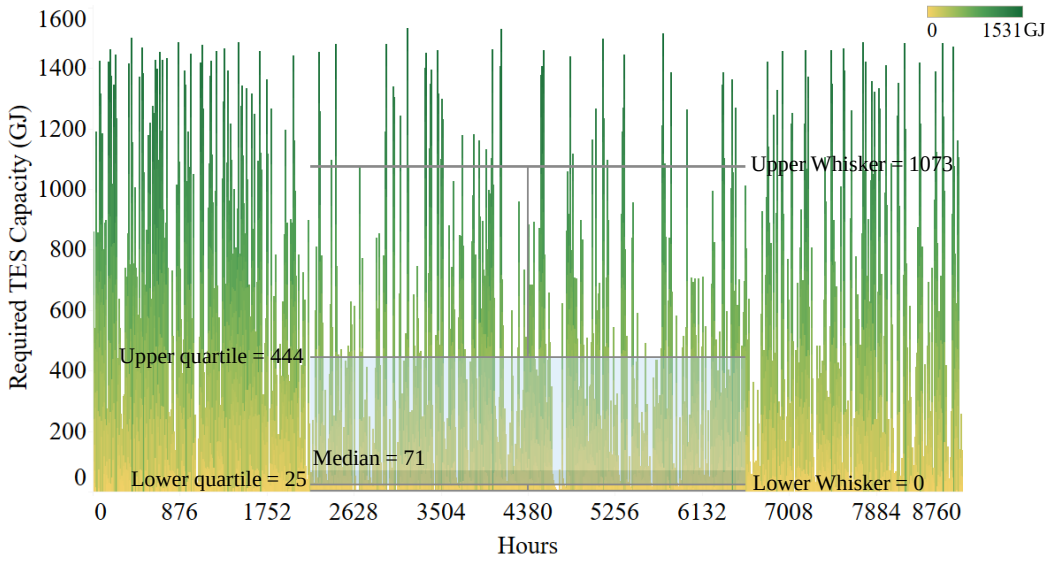

Figure 4.16: Hourly heat capacity of thermal energy storage obtained by Frequency-of-occurrence method for the CAES plant in Ontario by the 2022 grid data.

and reduced efficiency due to heat dispersion over a larger volume. According to the box plot depicted in Figure 4.16, the TES system in the majority of hours has a heat capacity of approximately 1000 GJ (upper whisker) or lower. This capacity is equivalent to storing the compression heat generated by a 70 MW compressor operating at full load for four hours. It is noteworthy to mention that this assumption serves as an initial estimation, and both oversized and under-sized TES systems will be evaluated during the optimization process. Figure 4.16 serves as a valuable resource for determining the overall size of TES heat capacity for the D-CAES system sized and designed in section 4.3.1. The size of each TES tank (high-temperature, mean-temperature, and low-temperature tanks) depends on various factors, including the temperature of the tank, and the thermal properties of the fluid, such as density and heat capacity. Therefore, The size and heat capacity of individual tanks will be determined through the optimization process, as outlined in section 4.3.3.2.

4.3.3 Performance of a NA-CAES System in Ontario

In this section, the results of global and local sensitivity analyses are presented. This analysis finds the strength of the correlation between the input parameters (factors) and the first-law efficiency (response) allowing the input parameters to be ranked from most

to least impact (see section 4.3.3.1). After conducting a thorough sensitivity analysis and deciding which parameters qualify for removal within the optimization process, the system is optimized to get the maximum efficiency with the lowest TES size (see section 4.3.3.2). Following this section, the NA-CAES system cycling profile (including charging, storage, and discharging), the salt cavern, and TES state-of-charge, in addition to the determination of the number of ramp-up (discharging) and ramp-down (charging) events, all of which are expounded upon in section 4.3.3.4 is illustrated. Sources of inefficiencies for the three different studied and optimized plants (Plants A to C, as described in section 4.2) are also presented and compared in section 4.3.3.5.

To this end, the input electrical grid data used for the thermodynamic model and optimization is restricted solely to the months of August and September 2022. This limitation is implemented for the purpose of conveniently displaying the results of the thermodynamic simulation. Figure 4.17 (a) visually represents the surplus power (depicted by green data points) and power shortage (represented by red data points), with a maximum value of 335 MW for excess power and 500 MW for power shortage. Any value below -500 MW or above 335 MW is indicated using the same color (excess green, shortage red) as -500 MW or 335 MW, respectively. Furthermore, Figure 4.17 (b) portrays the quantity of power that can be stored or released, taking into account the compressor and expander sizes, which are 70 MW and 80 MW respectively.

4.3.3.1 Parameters Identification for Plant A, B, and C in Ontario

Figure 4.18 provides a comprehensive overview of the influence of the examined parameters (as indicated in Figure 4.12) concerning both the quality (ranking) and quantity (magnitude) aspects. It also presents a comparative analysis of the outcomes obtained from global and local sensitivity techniques. The key discoveries resulting from the sensitivity analyses can be summarized as follows:

- The results of the global sensitivity analysis revealed that the parameters under investigation can be categorized into two distinct groups: primary and secondary. The primary parameters encompass those that exhibit the most significant impact, ranked from 1st to 5th. This includes variables such as the minimum and maximum pressure within the salt cavern, as well as the pressure ratio of the expanders. Conversely, the remaining parameters are referred to as secondary, as they display considerably lower magnitudes in terms of sensitivity indices. These secondary parameters are denoted by the red box in the analysis and are normalized after excluding the primary parameters from consideration.

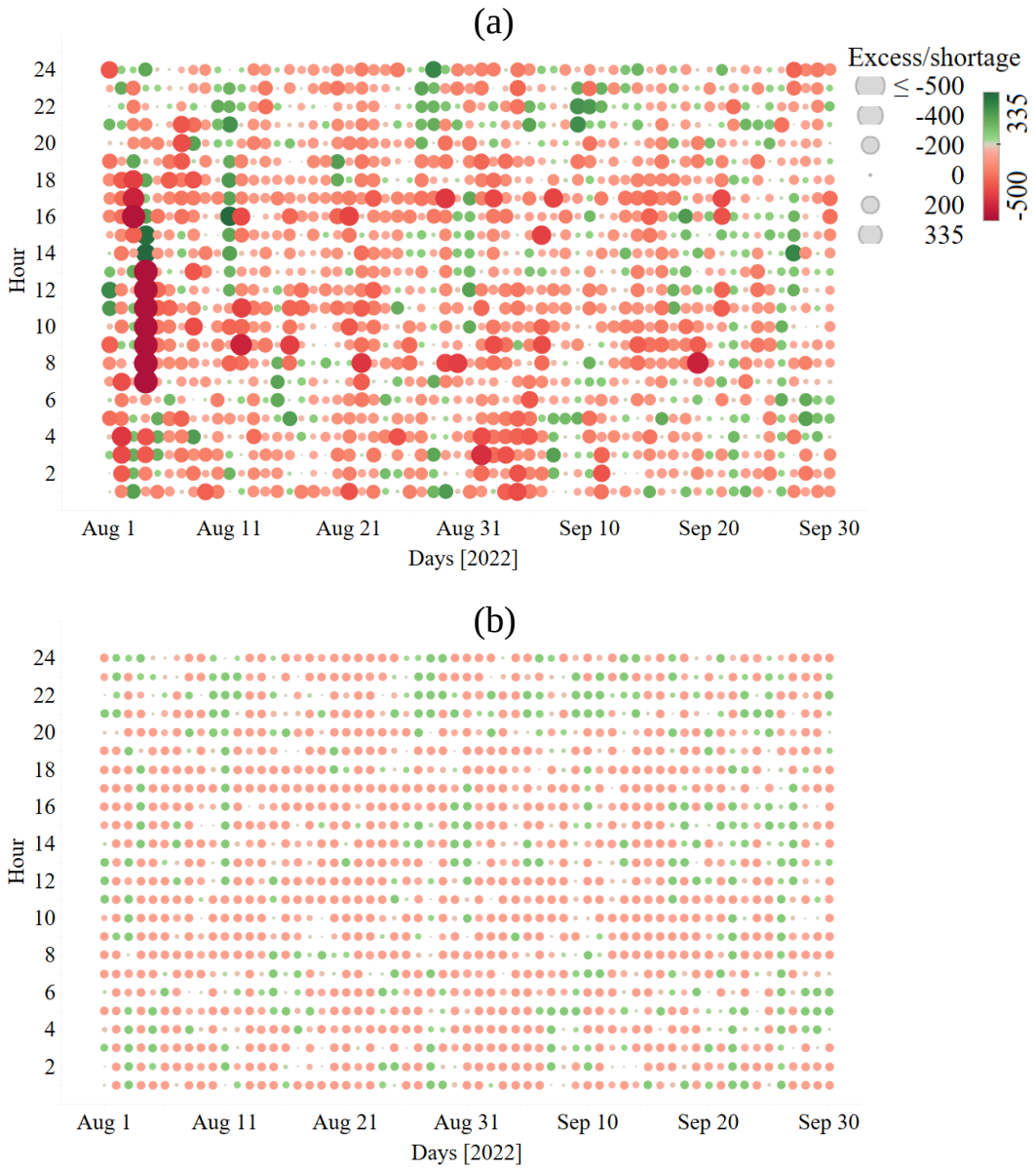

Figure 4.17: (a) Excess power (CAES charging opportunities) and power shortage (CAES discharging opportunities) in Ontario from August 1 to September 30, 2022, (b) Storable and releasable power due to the selected compressor and expander sizes.

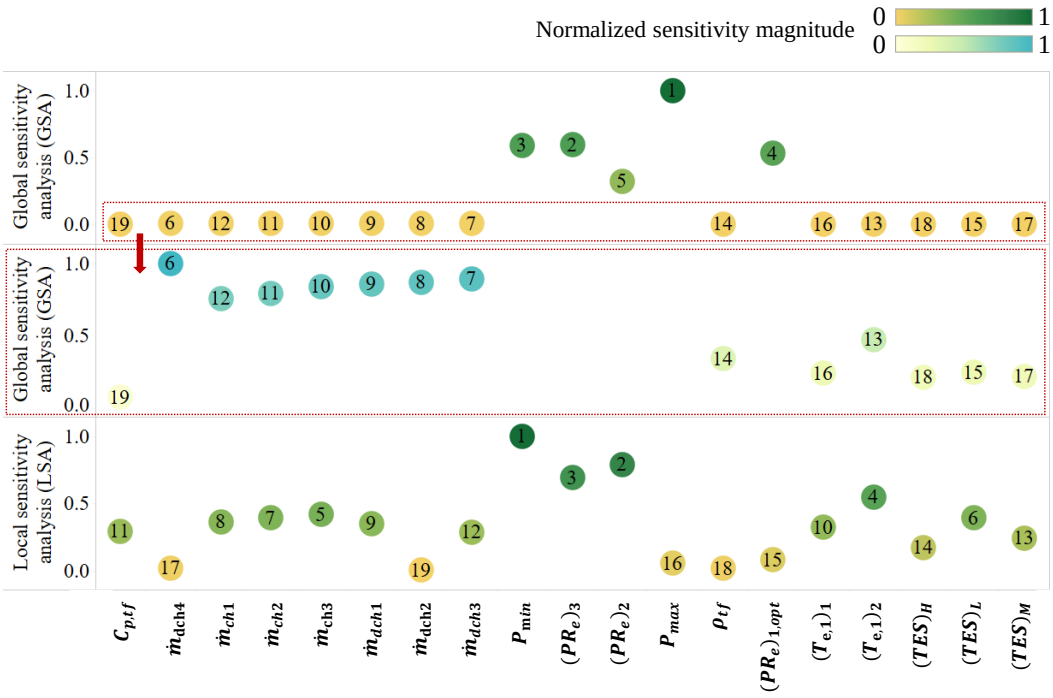

Figure 4.18: Comparison of sensitivity analysis results using the suggested local and global methods (the factors are ranked based on their effectiveness (rank 1st has the highest impact on the response), and to compare the local and global sensitivity analysis indices, normalized sensitivity magnitude is computed).

- The outcomes of the local sensitivity analysis (LSA) diverge from those of the global sensitivity analysis (GSA) due to the dissimilarity in their methodologies. However, there is a consensus between the GSA and LSA in ranking three parameters as primary factors. In LSA, these parameters hold ranks 1, 2, and 3, while in GSA, they occupy ranks 2, 3, and 5. The LSA method does not rank the maximum pressure inside the cavern and the pressure ratio of the variable-pressure-ratio expander as primary parameters; this is attributed to their complex interactions with other variables preventing their identification as primary factors. The results of the LSA method suggest that the expanders' inlet temperature can also be regarded as a primary parameter.

- The secondary parameters can be classified into two distinct groups: (1) the parameters related to TES charging and discharging mass flow rates, and (2) the inlet temperature of the expanders, as well as the temperature of TES tanks. These parameters can be identified as the TES sizing and temperature parameters, respectively, primarily influencing the TES size (the secondary objective in the optimization process). However, it is worth noting that these parameters can still have some influence on the system efficiency, particularly if the sensitivity analysis is conducted within a narrow range of intervals. As an illustrative example, the TES tanks charging mass flow rates can have a considerable influence on the TES temperature, thereby impacting the system efficiency, as explicated in section 4.2.1.3.

Upon analyzing both LSA and GSA in the context of a NA-CAES system, certain key parameters have been identified as primary factors that significantly contribute to enhancing the system's efficiency. These parameters include the expanders' pressure ratio, the upper and lower pressure levels within the reservoir, and the expanders' inlet temperature. In addition to these primary factors, there are other parameters that have been studied as part of sensitivity analysis, referred to as secondary factors. These secondary parameters may have a noteworthy to moderate impact on the efficiency of the NA-CAES system and therefore should not be completely disregarded. Their effects become more apparent when the NA-CAES system approaches optimal performance while minimizing the TES size.

To visually demonstrate the influence of these uncertain parameters on the behavior of the first-law efficiency, Figure 4.19 provides a graphical representation. The green dots, along with their corresponding curve fit, represent the outcomes obtained through the local sensitivity approach, where the impact of individual parameter variations is examined. On the other hand, the yellow dots depict the system's efficiency when any parameter is altered, considering variations in all other factors simultaneously, which is known as

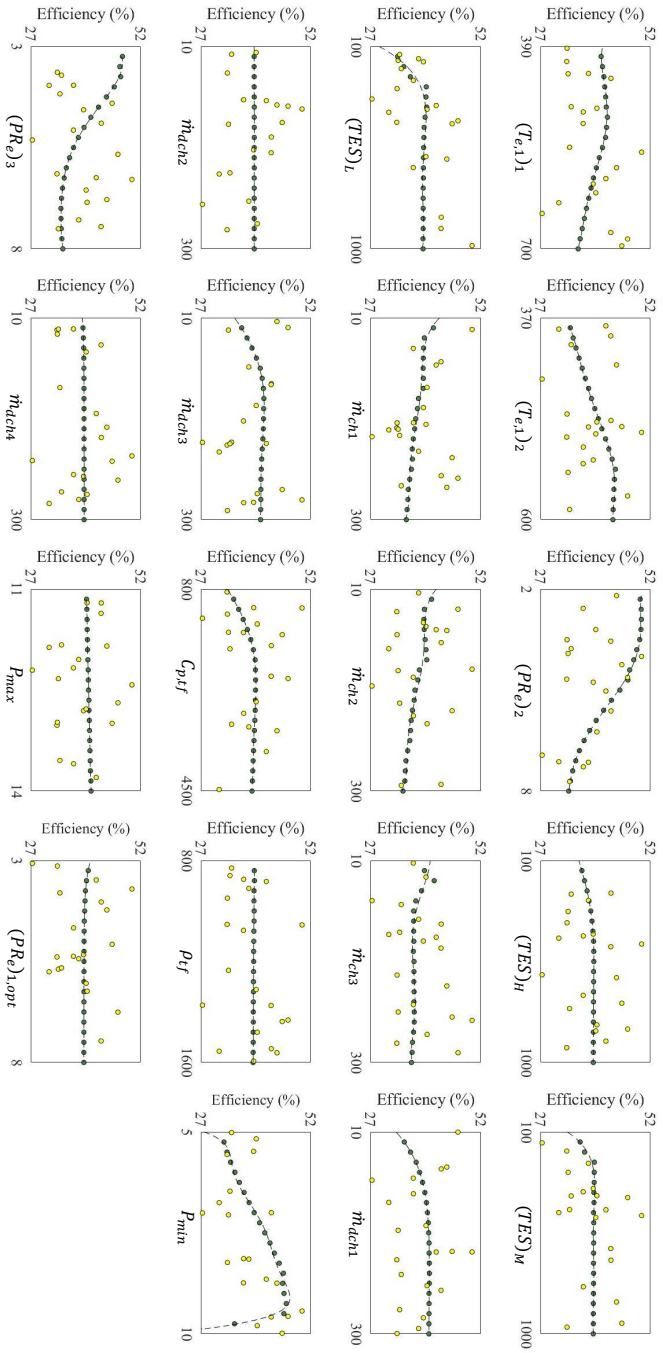

Figure 4.19: Impact of uncertain parameters on the NA-CAES efficiency. Green dots with the curve fitting (third-degree polynomial): LSA, yellow dots: GSA.

the global sensitivity approach. This visual representation helps to illustrate the overall sensitivity and interdependencies of these parameters in relation to the system's efficiency.

Overall, the sensitivity analysis highlights the importance of the primary factors and acknowledges the significance of the secondary factors in optimizing the efficiency of the NA-CAES system, providing valuable insights for its design and operation.

4.3.3.2 Operational Modes Optimization

The graphs (a) to (c) presented in Figure 4.20 demonstrate the convergence curves of the CAES round-trip efficiency (the first objective function) and thermal energy storage (TES) volume (the second objective function) based on the weighting factor of zero (ϵ_i=0 in Equation 4.49). This implies that the operational parameters resulting from the optimization process are associated with a system that achieves the highest efficiency with the smallest TES size. In other words, in the initial stage of the optimization process, the system considers efficiency as the sole criterion for optimization, and subsequently, the system undergoes an additional optimization stage with the aim of attaining the minimum size of thermal energy storage. This implies that all the operational parameters shown in Table 4.10 are adjusted and optimized to maximize the efficiency of the system, with the minimum required TES size.

The findings illustrate that the constant-pressure reservoir CAES system (Plant C) surpasses the efficiency of both the CAES system with a constant-volume reservoir with the variable-pressure-ratio expander (Plant B) and the constant-pressure-ratio expander (Plant A) in terms of efficiency. However, this enhancement is not regarded as significant as the optimization results for Plant A (constant-volume reservoir) demonstrate a mere 1.3 MPa disparity between the minimum and maximum air pressure values within the cavern. This discovery suggests that the system undergoes limited charging or discharging, as it strives to maintain the air pressure within a restricted range, approximating a constant-pressure CAES operation. The primary factor contributing to the superior efficiency of a constant-pressure CAES system is its relatively stable reservoir pressure, which enhances turbine performance. In contrast, a constant-volume CAES system with substantial pressure variation within the cavern experiences notable temperature and pressure fluctuations, resulting in energy losses and reduced efficiency.

Furthermore, the results for the efficiencies of Plants A to C are 60.5%, 61.05%, and 61.5%, respectively. Table 4.10 summarizes the optimal operational modes of the NA-CAES system for all three investigated configurations (Plants A to C). Upon comparing the outcomes of Plants A, B, and C in terms of TES size it is evident that a larger TES

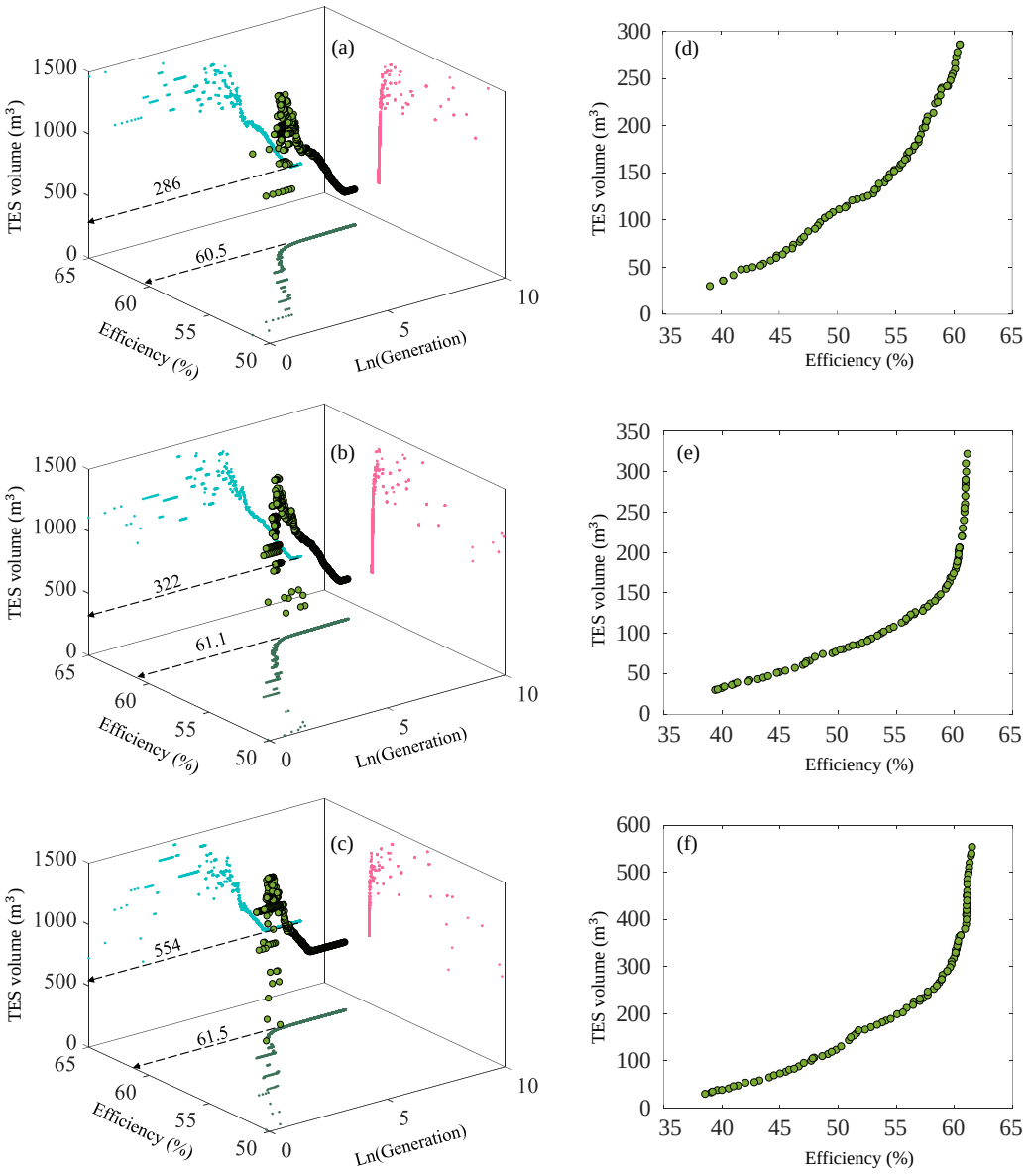

Figure 4.20: Convergence curves and their projections for NA-CAES round-trip efficiency and TES volume for (a) plant A, (b) plant B, and (c) plant C. Pareto front curves corresponding to each plant are shown in graphs (d) to (f).

size is chosen in the constant-pressure cavern scenario (Plant C) to attain maximum efficiency within the optimization process, without considering any weighting factor for TES size. However, there should be a trade-off between the size of the thermal energy storage system and the desired system efficiency. Hence, Pareto-front graphs (d) to (f) depicted on the right-hand side of Figure 4.20 provide a set of solutions and offer insights into the CAES sizing-design procedure enabling decision-making based on design priorities and requirements. It is important to note that graphs (d) to (f) in Figure 4.20 exclusively feature non-dominated solutions, where each solution represents a favorable scenario in terms of at least one objective (higher efficiency or lower TES size). This selection criterion ensures that only solutions offering improved performance in one or both aspects are included in the graphical representations. Graphs (d) to (f) in Figure 4.20 also demonstrate that increasing the size of the thermal energy storage system does not invariably result in higher CAES efficiency. There does exist an optimal size for the TES system beyond which further enlargement fails to enhance performance. Thus, during the design phase of a NA-CAES system, it is imperative to consider the optimal trade-off between the size of the thermal energy storage system and the desired system efficiency. In summary, the optimization outcomes for Plants A to C can be described as yielding an approximate efficiency of 61%, with a TES volume of 300 m^3 derived from the optimized values of TES thermal fluid density and heat capacity ($C_{p,tf}$). Section 4.3.3.3 delves into an analysis of the influence of three prevalent thermal fluids commonly employed in high-temperature and large-scale TES systems (compressed water, mineral oil, and molten salt) on TES sizing and temperature, and the NA-CAES efficiency.

4.3.3.3 TES Thermal Fluid Selection and Optimized Temperature

In Section 4.3.3.2, the optimization process was employed to ascertain the efficiency of the NA-CAES system and determine the TES size, without explicitly specifying a particular thermal fluid for operation. The outcomes derived from the optimization process (i.e., maximum efficiency, minimum TES size), as explicated in Section 4.3.3.2, demonstrate that optimal values for the TES thermal fluid density and heat capacity are at their upper range ($\rho_{tf} = 1600$, $C_{p,tf} \approx 4300$). Nevertheless, selecting a thermal fluid possessing both high density, such as molten salts, and high heat capacity, like water, is not without challenges. The selection of a specific thermal fluid relies on the specific requirements of the application, compatibility with the materials employed in the system, safety considerations, and various other influencing factors. In this study, the NA-CAES performance is analyzed for three widely adopted and mature thermal fluids employed in large-scale TES systems, comprising compressed water, mineral oil, and molten salt. The specifications of the selected TES

Table 4.10: Optimized operational parameters of the NA-CAES system under different scenarios.

Parameter	**Plant A**	**Plant B**	**Plant C**
$\dot{m}_{ch1}$	10	10	12
$\dot{m}_{ch2}$	20	20	21.3
$\dot{m}_{ch3}$	30.5	30	34.7
$\dot{m}_{dch1}$	33	32.6	32
$\dot{m}_{dch2}$	33	32.6	32
$\dot{m}_{dch3}$	34.6	32.6	37
$\dot{m}_{dch4}$	300	300	300
$(TES)_H$	67.6	68	90
$(TES)_M$	93.5	95.4	275.7
$(TES)_L$	125.6	158.3	188.2
ρ_{tf}	1600	1600	1600
$C_{p,tf}$	4384	4392	4500
P_{max}	11	11	11
P_{min}	9.7	9.7	11
$(T_{e,1})_1$	531	531	531
$(T_{e,1})_2$	481	476	480
$(PR_e)_{1,\text{opt}}$	NA	8	NA
$(PR_e)_2$	5.17	4.3	5.5
$(PR_e)_3$	3.1	3.14	3.15

Table 4.11: TES thermal fluid specifications [18, 57, 64, 138, 47, 65].

Thermal fluid	**Tank pressure (bar)**	**Density (kg/m^3)**	**Heat capacity (J/kg.K)**	**Melting point(°C)**	**Boiling point(°C)**
Compressed water	$\approx 90-100$	≈ 730	≈ 4900	≈ 0	≈ 330
Mineral oil	1	≈ 770	≈ 1966	≈ 10	≈ 350
Molten salt	1	≈ 1992	≈ 1447	≈ 110	≈ 550

thermal fluids are summarized in Table 4.11. Additionally, Table 4.12 presents the NA-CAES performance, and the TES volume requirements for each thermal fluid, while also highlighting their respective advantages and disadvantages. The graphs (a) to (c) presented in Figure 4.21 depict the convergence curves of the CAES round-trip efficiency and TES volume. These graphs demonstrate that plant A, representing the aforementioned system, achieves an approximate efficiency of 60.5% across all chosen thermal fluids. Notably, the TES volume varies in ascending order, with compressed water, molten salt, and mineral oil, owing to the distinctions in their respective density and heat capacity properties. Figure 4.22 illustrates the optimized temperature of TES tanks (for mineral oil as the TES thermal fluid) over the studied period, from August 1 to September 30, 2022. It is worth noting that the average temperature of tanks is regarded as the optimized temperature (red dashed line in Figure 4.22). The TES tank' temperature is independent of the type of thermal fluid utilized. Within the framework of the optimization process, the selection of thermal fluid mass flow rates for charging and discharging processes, as well as TES tank size, is contingent upon attaining the optimized TES tank temperature, which is determined by the expanders' inlet temperature.

4.3.3.4 NA-CAES Cycling Profiles

This section studies the NA-CAES cycling profiles, including charging, discharging, and idle modes, along with the state of charge (SOC) of the cavern and the thermal energy storage tanks. The SOC of the cavern is calculated by determining the ratio of the difference between instantaneous cavern mass and minimum cavern mass to the difference between the maximum and minimum of cavern mass on an hourly basis (SOC=100% signifies that the mass of the cavern is equivalent to its maximum value, whereas SOC=0% corresponds to situations wherein the cavern attains its minimum mass). Figure 4.23(a) presents the cavern SOC profile in Ontario for two months from August 1 to September 30, 2022, considering an initial SOC value of 0%. Furthermore, Figure 4.23(a) provides a graphical

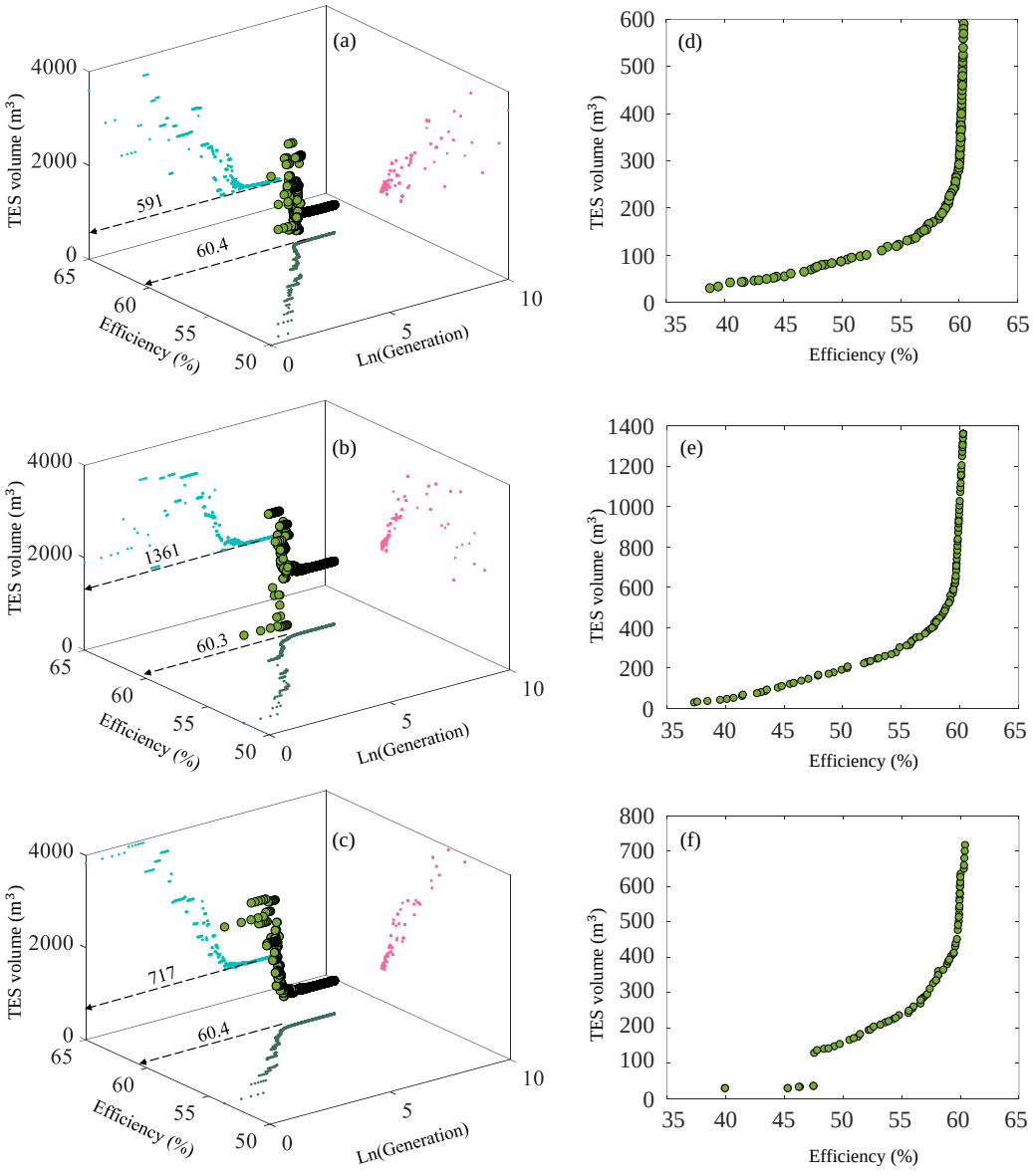

Figure 4.21: Convergence curves and their projections for NA-CAES round-trip efficiency and TES volume for (a) compressed water, (b) mineral oil, and (c) molten salt. Pareto front curves corresponding to each thermal fluid are shown in graphs (d) to (f).

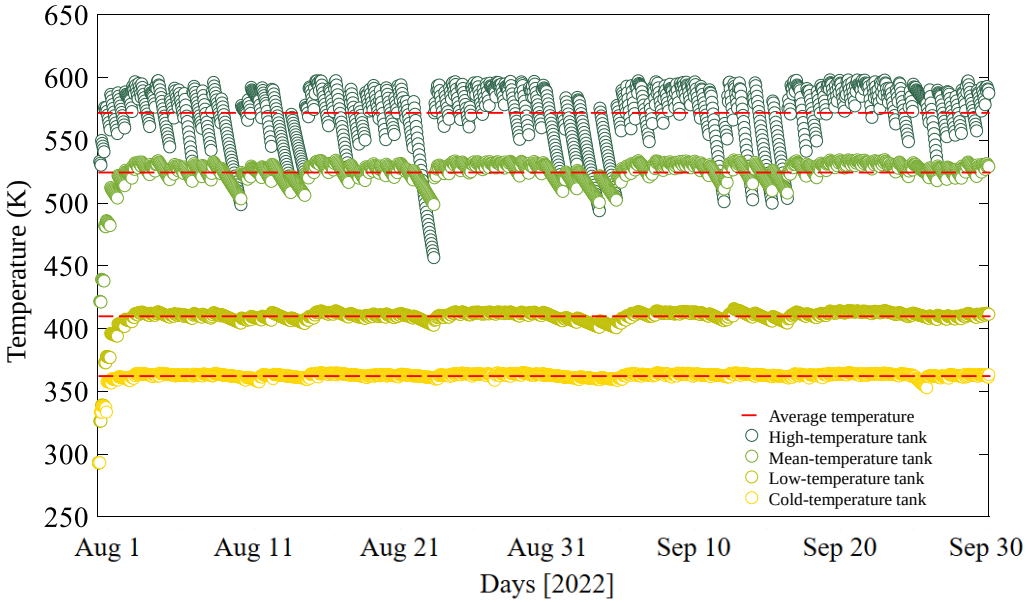

Figure 4.22: TES tanks temperature (for mineral oil as the TES thermal fluid) over the studied period, from August 1 to September 30, 2022; the red dashed line shows the average temperature.

Table 4.12: Comparison of NA-CAES efficiency and TES Size for different TES thermal fluids.

Thermal fluid	**NA-CAES efficiency (%)**	**TES volume(m^3)**
Compressed water	60.4	591
Advantages:	High thermal stability and heat capacity, relatively low cost, abundant, minimal environmental impact.	
Disadvantages:	Limited temperature range compared to other storage mediums, requires very high-pressure (>90 bar) systems to maintain the water in the compressed state, lower energy density.	
Mineral oil	60.3	1361
Advantages:	Wider temperature range compared to water, non-corrosive and chemically stable, suitable for medium to large-scale applications, high energy density.	
Disadvantages:	Lower heat capacity compared to water, limited availability, higher cost, require additional safety measures due to flammability properties.	
Molten salt	60.4	717
Advantages:	High thermal stability and heat capacity, widely used in large-scale TES systems, wide temperature range.	
Disadvantages:	High melting point, corrosive nature, high capital and maintenance costs.	

representation of the CAES system's operation, illustrating the occurrence of charging, discharging, and idle modes at any given hour. By analyzing the power data for this two-month period in Ontario (Figure 4.17) in conjunction with the CAES cycling profile depicted in Figure 4.23(a), a noteworthy observation arises. Contrary to the prevailing assumption of storing power once per day and generating power once per day in CAES designing and performance improvements[58, 89], the cavern undergoes multiple charging and discharging cycles throughout the day, adapting to the demand-supply pattern of the power grid.

To gain further insights into the system dynamics, Figure 4.23(b) displays the state of charge of the TES system, consisting of a triple-tank configuration for the studied period. The TES SOC is defined as the ratio of the instantaneous TES capacity to the maximum TES capacity (in GJ). An examination of cycling profiles (a) and (b) presented in Figure 4.23 unveils a striking correlation: the thermal energy storage system implemented in a NA-CAES configuration aligns with the cavern events in its entirety. To provide a quantitative analysis, Table 4.13 presents the number and duration of ramp-up and ramp-down events for plants A (constant-volume reservoir) and C (constant-pressure reservoir). Additionally, the duration of CAES events per day is depicted in Figure 4.24 for a constant-pressure reservoir. These findings hold significant importance in CAES sizing-design process for several reasons.

First, a CAES system with a constant-pressure reservoir exhibits higher utilization than a constant-volume reservoir due to its inherent ability to accommodate variable air volumes during charging and discharging processes. By maintaining a consistent pressure level, the constant-pressure CAES affords enhanced flexibility in storing varying amounts of compressed air, thereby enabling longer durations for charging and discharging operations without reaching the system's maximum pressure limit (as can be seen in Table 4.13). In contrast, a constant-volume reservoir possesses a fixed air volume, thereby imposing limitations on storage capacity. Once the constant-volume reservoir reaches its minimum or maximum pressure, it becomes incapable of accommodating any operation, leading to constrained utilization time for the system. Consequently, the utilization advantages of the constant-pressure reservoir in a CAES system lie in its capacity for accommodating variable air volumes, thereby enabling more efficient and extended operation periods for charging and discharging, rendering it a preferred choice for energy storage applications. However, a constant-pressure CAES system necessitates the implementation of complex control systems to effectively regulate and sustain the desired pressure level throughout the charging and discharging phases. These systems are often combined with pumped hydro storage to ensure pressure constancy despite fluctuations in storage volume, albeit this integration may introduce certain geological limitations and environmental impacts.

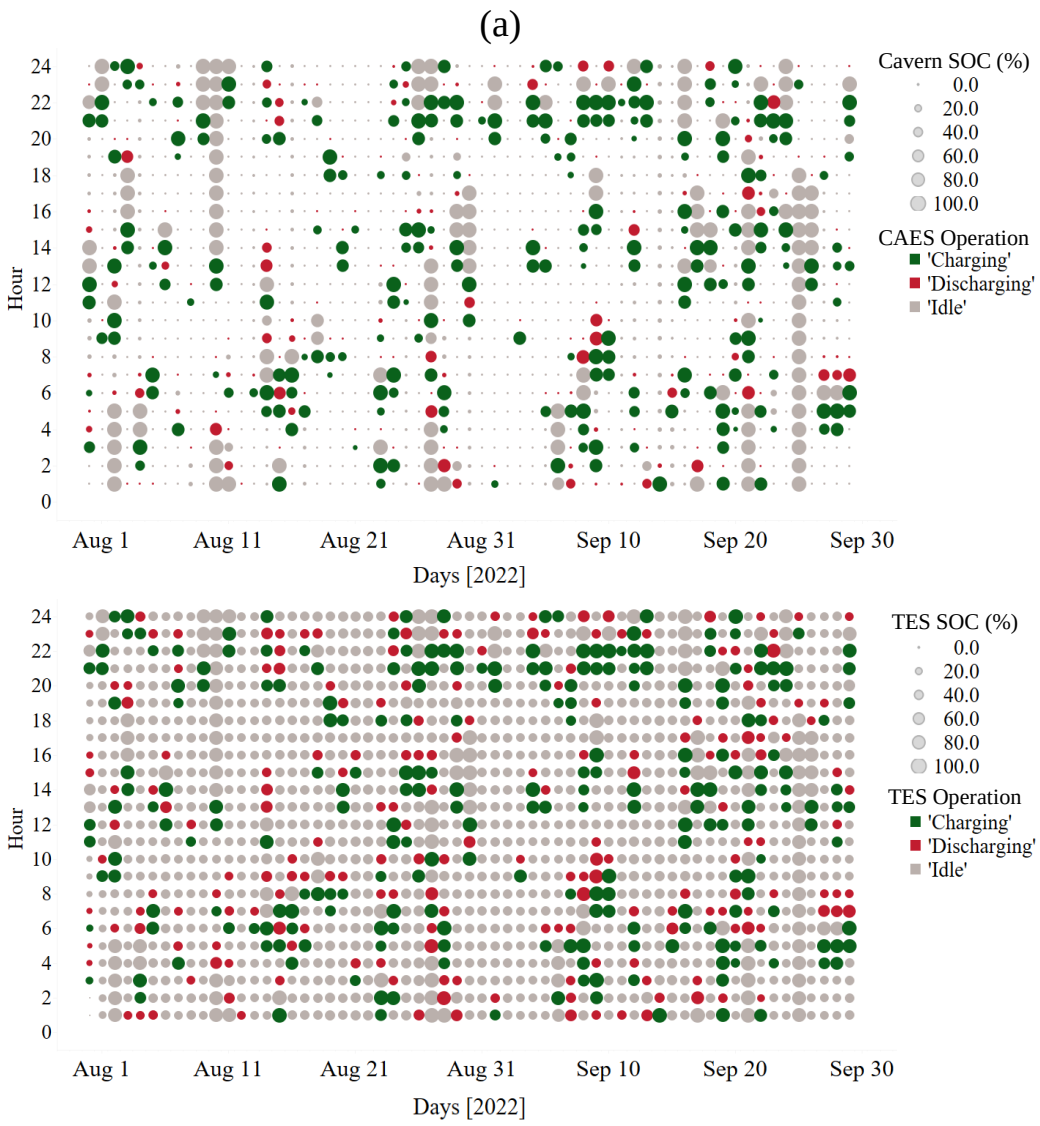

Figure 4.23: (a) Cavern state-of-charge, and (b) TES state-of-charge in Ontario from August 1 to September 30, 2022.

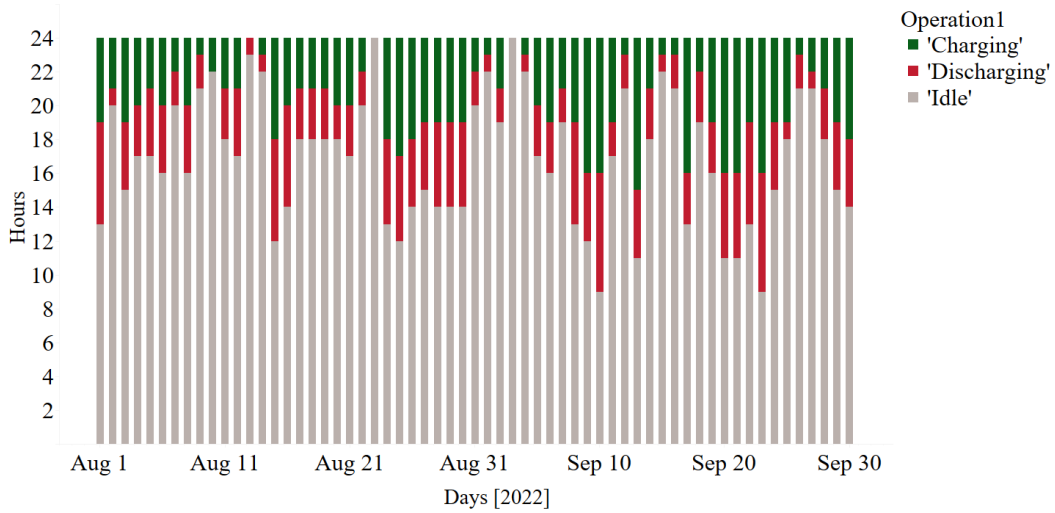

Figure 4.24: NA-CAES events duration per day in Ontario for the studied period.

Second, understanding the NA-CAES cycling profiles, cavern SOC, and TES tank SOC enables a comprehensive understanding of the system's behavior and performance. By recognizing the occurrence of multiple charging and discharging cycles throughout the day, rather than a single daily cycle as previously assumed operators can optimize the system's operation to better match the dynamic demand-supply patterns of the power grid. This knowledge aids in refining the system design and sizing of TES capacity to ensure optimal performance and cost. The presented data on the duration and frequency of ramp-up and ramp-down events further contributes to system planning, maintenance, and decision-making processes.

4.3.3.5 NA-CAES Sources of Inefficiencies

Figure 4.25 provides a visual representation of the various sources of inefficiency within the NA-CAES system, along with their respective percentages during the operational period spanning August and September 2022. Notably, the dissipation of energy in the cavern, relative to the other sources of inefficiencies, can be deemed negligible due to the assumption that the temperature of the compressed air injection matches that of the cavern walls. Furthermore, the contribution of the electrical pump work has been omitted from the diagram, as it accounts for a negligible proportion in relation to the total input work. Based on the insights derived from Figure 4.25, it can be determined that the first-law efficiency of the NA-CAES system stands at 60.4%.

Table 4.13: NA-CAES cycling metrics in Ontario for plants A and C during the studied period.

Parameter	Plant A	Plant C
Number of charging events (Ramp-Down)	166	239
Number of discharging events (Ramp-up)	165	196
Total duration of charging events (Ramp-Down)	119.6 hours	157.6 hours
Total duration of discharging events (Ramp-up)	72.7 hours	105.1 hours
Total duration of idling	1271.7 hours	1201.3 hours
Average duration of charging per day (Ramp-Down)	2 hours	2.6 hours
Average duration of discharging per day (Ramp-Up)	1.2hours	1.7 hours
Average duration of idling per day	20.8 hours	19.7 hours

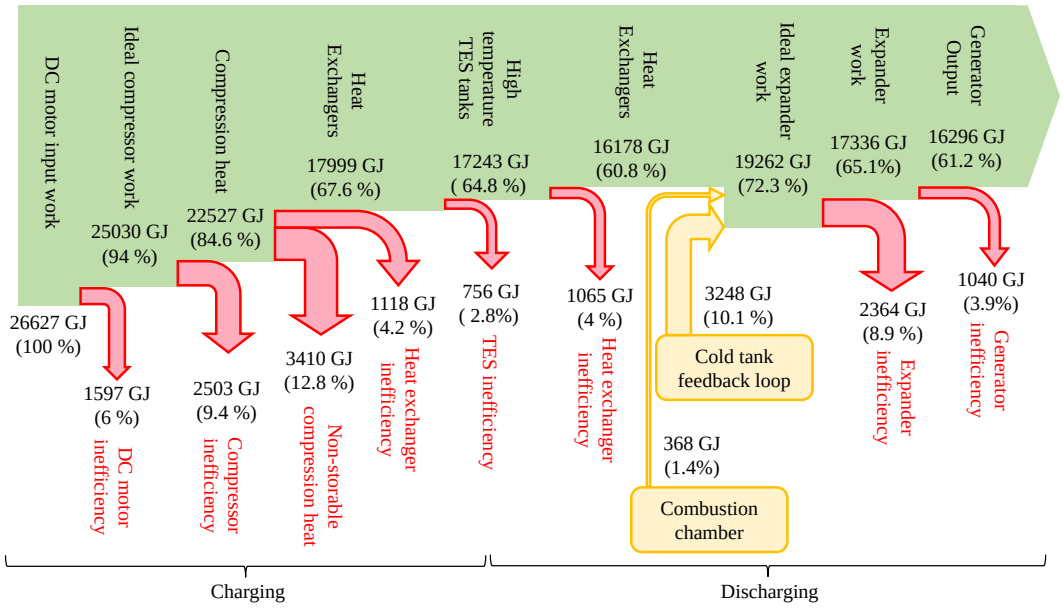

Figure 4.25: Inefficiency sources of the proposed NA-CAES system.

It is essential to highlight that the NA-CAES system undergoes several charging and discharging throughout a single day. Consequently, it can be inferred that the air leakage from the cavern is negligible. In the case of a CAES system charged once per day for a few hours, the air leakage during each cycle amounts to merely 0.004% (or 0.4% after 100 cycles) [178]. With several charging and discharging events occurring daily, the percentage of air leakage diminishes further due to reduced idling durations.

4.4 Summary of Chapter

This chapter provides a comprehensive analysis of the factors contributing to the reported ([29]) low operational efficiency of adiabatic CAES systems as compared to experiments. The identified factors include oversimplified heat management system modeling, neglected heat losses throughout the system components, the substitution of a diabatic CAES combustor with a TES without significant design modifications, the utilization of low-fidelity single-cycle modeling, the adoption of a mirrored compression-expansion design, and potential limitations in defining efficiency. Accounting for these factors, and in particular the heat management modeling issues, this research also presents an A-CAES system design case study for Ontario with a particular focus on maximizing the work potential (i.e., exergy) stored in a TES system and maximizing exergy transfer through balanced heat exchangers.

This chapter also identifies the need to be particularly concerned with the impact of external factors (e.g., operation cycle, power grid shortage, and excess patterns), component operation and performance limits (e.g., pressure and temperature limits, minimum compressor and expander load, and start-up time and compressor and expander power-efficiency relationships) and design configuration issues (e.g., heat exchanger and TES tank numbers and sizing for balanced heat exchange) when designing and optimizing an A-CAES system.

The key findings of this research are as follows:

- Optimal component sizes for a CAES system in Ontario were determined through a comprehensive assessment involving 82,500 scenarios and by employing the coverage-percentage method. It was observed that larger compressor and expander sizes increase charging and discharging coverage percentages, respectively, up to an optimal point.

- The chosen component sizes for the CAES system in this study are a 70 MW compressor, an 80 MW expander, and an 830 MWh salt cavern. These sizes yield a charging coverage percentage of approximately 52.5% and a discharging coverage percentage of around 29.1%. These coverage percentages can be increased if a larger maximum cavern size is considered, however, there are advantages to distributed energy storage, i.e., multiple A-CAES systems in Ontario.

- A multi tank thermal energy storage system is recommended for efficiently capturing compression heat in a NA-CAES system design in Ontario.

- The optimal number of TES tanks, aligns with the number of expansion units. Moreover, the size and heat capacity of each TES tank, including high-temperature, mean-temperature, and low-temperature tanks, require an optimization process considering factors such as tank temperature and fluid properties

- A CAES system with a constant-pressure reservoir has higher efficiency compared to that one operating with a constant-volume reservoir with a variable-pressure-ratio expander, and a constant-pressure-ratio expander, with maximum efficiency values of 61.5%, 61.05%, and 60.5%, respectively, under optimal condition.

- The optimal temperature of TES tanks is independent of thermal fluid, but highly dependent on the expanders' inlet temperature, and can be achieved by optimizing the TES thermal fluid charging and discharging mass flow rates, and TES tanks' size.

- A CAES system with a constant-pressure reservoir exhibits higher utilization and flexibility compared to a constant-volume reservoir, arising from variable air volumes during charging and discharging, enabling longer and more efficient operation periods without reaching the cavern maximum pressure limits.

Chapter 5

Adaptive hybrid energy system for remote Canadian communities[1]

5.1 Introduction

Remote Canadian communities encounter energy challenges due to their geographical isolation and limited access to power grid infrastructure [22, 87]. These communities heavily rely on diesel generators as their primary electricity source, leading to high costs and environmental degradation. To address these pressing issues, and align with the global shift towards sustainable energy solutions, the development of hybrid renewables-diesel systems that integrate renewable energy sources with diesel-based generators becomes imperative [153]. Wind energy presents a promising opportunity to mitigate the carbon footprint associated with diesel fuel consumption in remote areas. Nonetheless, implementing a standalone wind-diesel power plant without integrating energy storage entails several inherent limitations[87, 72, 175]. Primarily, the system must be designed on an oversized scale to ensure the provision of electricity even during periods of low wind speeds, which consequently results in substantial curtailment. This curtailment arises from the surplus generation capacity when the wind turbine is perpetually dimensioned to meet the demand under adverse wind conditions. Secondly, the absence of an energy storage system prevents the effective utilization of excess wind energy to offset future diesel usage. Instead, the ex-

[1]This chapter is based on the following journal article:
Sarmast, S., Séjourné, S., Wigston, A. Fraser, R., and Dusseault, M., (2023), Adaptive hybrid energy system for remote Canadian communities: optimizing wind-diesel systems integrated with adiabatic compressed air energy storage. *Energy Conversion and Management* [159].

cess wind energy must be curtailed during instances of abundant availability, impeding the optimal utilization of renewable resources. Lastly, the absence of energy storage renders it unfeasible to entirely eliminate the reliance on diesel fuel, as it becomes indispensable during periods of wind scarcity, ensuring continuous power supply.

In response to the aforementioned challenges, the integration of battery and flywheel energy storage technologies with wind-diesel systems has been the subject of extensive investigation and analysis in various studies[99, 14, 118, 161, 141]. Batteries are often preferred due to their ease of implementation, modular design, and high efficiency. However, their high cost and limited lifespan impose financial burdens [21]. Additionally, batteries are sensitive to weather and temperature fluctuations, which can decrease efficiency and damage the system, introducing uncertainty regarding reliability [139]. Flywheels provide quick response times and high-power output but encounter large standby losses, high self-discharge rates, and safety concerns [107, 43].

Compressed Air Energy Storage (CAES) has emerged as a highly promising alternative to batteries and flywheels for facilitating the implementation of adaptive hybrid energy systems in remote areas [86, 88, 84]. The increasing interest in CAES can be attributed to its notable characteristics, including its long-term energy storage capacity, reliability, and scalability. However, determining the most suitable option among battery, flywheel, and CAES technologies presents a challenge in the absence of specific information regarding the requirements and constraints of the wind-diesel system, thereby emphasizing the need for careful consideration of various factors based on the specific application. For instance, the duration of power shortage in a given region may vary from minutes to a few hours, necessitating a storage system with rapid response rather than long-term storage capacity. Conversely, if the power shortage duration extends over a few days to months, a long-term storage technology may be preferred.

The recent literature (2010 to 2023) predominantly focuses on demonstrating the potential integration of CAES into wind-diesel systems, emphasizing its capability to enhance diesel engine performance and reduce fuel consumption in remote communities [88, 120, 32, 87].

The objective of this Chapter is to evaluate the appropriateness and viability of deploying a CAES system in a Northern Canadian community into a wind-diesel hybrid system. CAES is a reliable storage technology [59], however, there is a need for a more comprehensive approach to address various aspects of sizing, design, operation, and viability when applied to small communities.

The contributions and novelties of the present chapter can be outlined as follows:

- Comprehensive analysis of power supply-demand patterns for the full year of 2021, and analysis of the duration and frequency of excess and shortage events.
- Determination of optimal sizing and operation configuration for CAES systems in the selected community.
- Proposal for an optimization-based sizing strategy for the adaptive hybrid energy system in remote areas.
- Evaluation of the long-term operating performance of hybrid wind-diesel CAES systems in terms of efficiency, diesel fuel reduction, and cost functions.

5.2 Method

This section provides a summary of the statistical data analysis and the sizing-design approach conducted for an adaptive hybrid energy system in the village of Kangirsuk. The primary objective is to demonstrate the potential of a hybrid wind-diesel adiabatic compressed air energy storage (H-WD-A-CAES) system in augmenting the utilization of wind energy to meet the electricity demand of this off-grid community. By implementing optimized operational strategies, the H-WD-A-CAES system can substantially reduce the reliance on diesel fuel, resulting in significant cost savings. In order to comprehend the behavior of the hybrid system, the power data is subjected to a comprehensive statistical analysis to determine the suitability of a CAES system to meet the community's power consumption requirements. These requirements are assessed based on the magnitude and duration of excess and shortage events, considering two different scenarios: one wind turbine and two wind turbines. Subsequently, this study proposes a configuration for a H-WD-A-CAES power plant tailored to the selected community and introduces an optimized-based sizing-design method that aims to minimize diesel fuel consumption while utilizing the smallest possible components (compressor, expander, reservoir, and TES) to reduce capital costs. To accomplish these objectives, a mathematical model is employed to evaluate the performance of the H-WD-PA-CAES system in accordance with the principles of the first law of thermodynamics. Figure 5.1 illustrates a mindmap diagram that outlines the process of sizing, designing, optimizing, and estimating the performance of a H-WD-A-CAES system. The subsequent sections (sections 5.2.1 through 5.2.4) delve into the details of each branch in the mindmap, providing a comprehensive explanation for each.

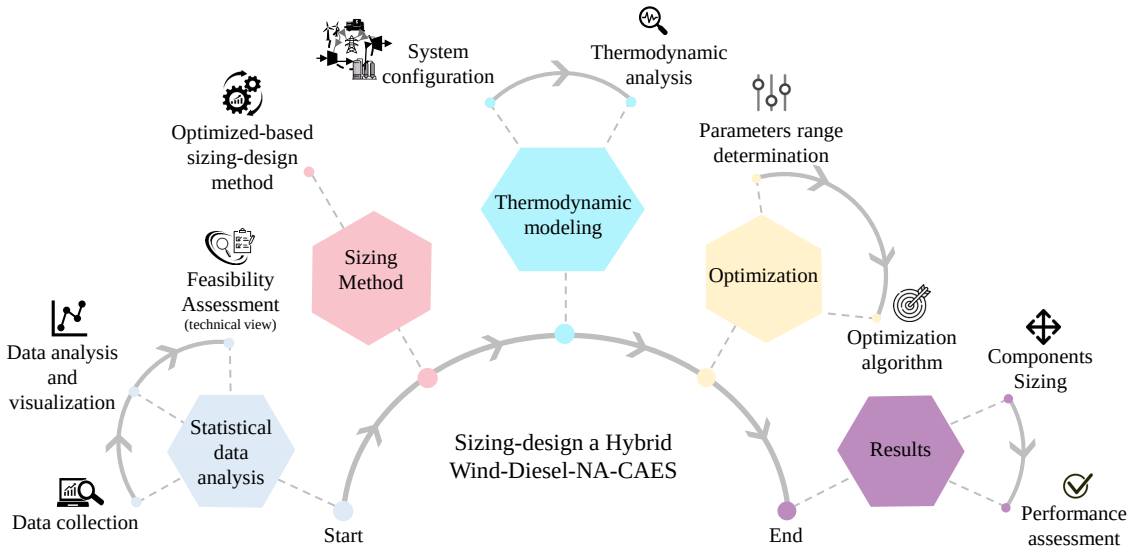

Figure 5.1: Mindmap diagram for sizing, design, and performance optimization of a H-WD-PA-CAES system.

5.2.1 Statistical Data Analysis

The data analysis in this study includes an examination of the meteorological time data (wind speed and ambient air temperature), the power generation of wind turbines, and the load demand of the community's diesel generators. These data were collected and are visually presented in Sections 5.2.1.1 and 5.3.1, respectively, providing a foundation for the CAES viability analysis (Sections 5.3.2) and sizing strategy.

5.2.1.1 Data Collection

The data presented in this section is for the village of Kangirsuk, a representative example of numerous remote communities in Canada's northern region. Kangirsuk is noteworthy due to its lack of connection to the national grid providing readily accessible year-long electrical load data for analysis. Additionally, the subsidized price of fuel ($ per liter) at this location is significantly higher compared to that of most other northern communities ($1.4 per liter compared to an average of $0.87 per liter [1]). These factors contribute to the selection of Kangirsuk as an ideal candidate for studying the implementation of energy storage systems and increasing the utilization of renewable energy sources as alternatives to diesel fuel.

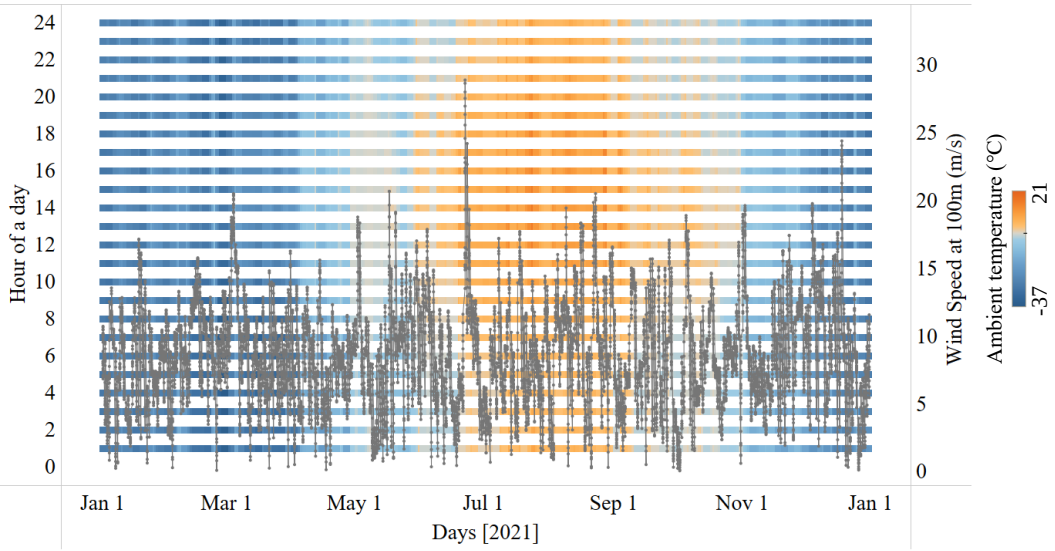

Figure 5.2: Hourly ambient temperature (heat map with y-axis on the left) and the wind speed (line graph with y-axis on the right) for the village of Kangirsuk during the year 2021 (data is extracted from [10]); wind speed is calculated at an altitude of 100 meters and the ambient temperature is recorded at a height of 2 meters above ground level.

- Meteorological Data

  Hourly meteorological time data for wind speed at altitudes of 10 and 50 meters, as well as ambient air temperature at an elevation of 2 meters in Kangirsuk, were collected for the year 2021 from the NASA Langley Research Center (LaRC) POWER Project [10]. In order to correct the wind speed at an altitude of 100 meters (which corresponds to the altitude of the wind turbine rotor at the studied location), the wind profile power law was employed. The correction was derived using a Hellman exponent of 0.197 [163], which was determined to be the best fit for adjusting the wind speed from 10 meters to 50 meters. The annual wind speed (line graph) and temperature heat map (where the x-axis shows different days, and the y-axis shows hours; the color bar shows the ambient temperature) can be seen in Figure 5.2 for the year 2021.

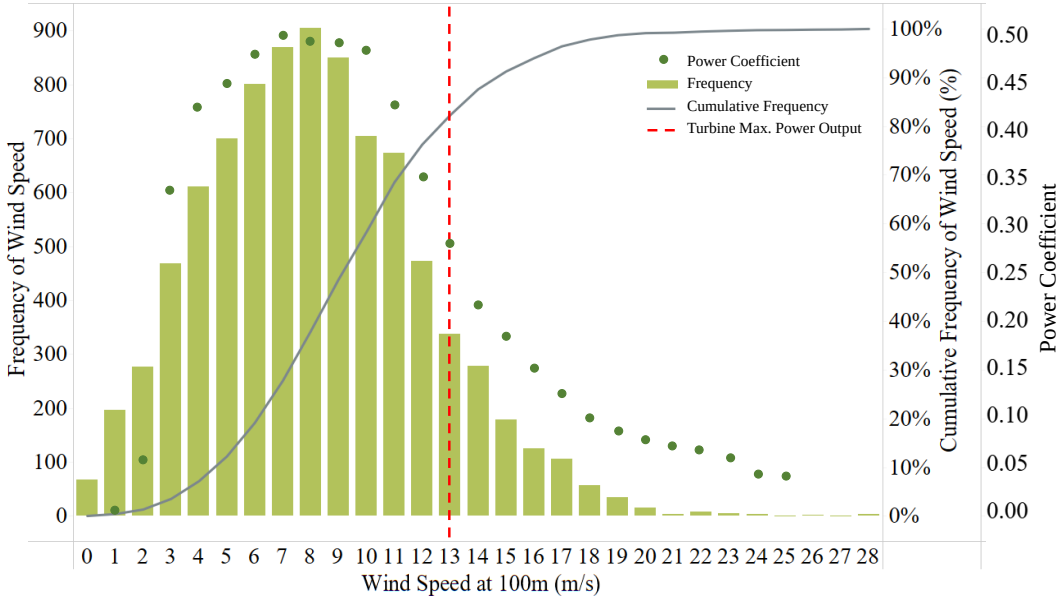

Figure 5.3: Annual frequency distribution of wind speed in Kangirsuk for the year 2021, The grey line depicts the cumulative frequency of occurrence (%), green dots show the wind turbine power coefficient, and red dashed line corresponds to the wind speed that results in the turbine maximum power output.

- Wind Turbine

  The Enercon E-53 [5] wind turbine has been selected in this study. This choice is based on its suitability for a wind-diesel hybrid power plant project being considered in another Nunavik community as noted in the work by Pike and Kummert [134]. The maximum power output of the Enercon E-53 turbine is 800 kW (rated power), which can be achieved with wind speeds between 13 and 25 m/s [5].

  According to the local wind profile analysis as depicted in Figure 5.3, the wind speed in Kangirsuk is found to be below the maximum power wind speed range for the turbine approximately 82.3% of the time during the reference year of 2021 (7209 hours from 8760 hours). As can also be seen in Figure 5.3 the wind speed frequency profile matches the turbine power coefficient (the ratio of the electric power generated by a wind turbine to the total power present in the wind passing through its area [83]) profile both reaching maximums in the 7 to 9 m/s range. If the wind turbine were to operate at full capacity for the entire year it would produce 7,096 MWh/yr. Using the observed hourly wind history for Kangirsuk in 2021 and the manufacturer-

reported turbine power coefficient [5] the energy produced would be 3678 MWh/yr (see Appendix C) for a capacity factor of 0.52. However, the actual energy the wind turbine would have produced will in general be lower than 3678 MWh/yr although in certain situations it could be higher. Factors that lower the actual energy produced include wind direction transients (i.e., yaw); using average wind speeds (i.e., turbine power varies as the cube of wind speed; not linearly); topology impacts on the atmospheric boundary layer wind speed profile (e.g. if turbine location is at the bottom of a hill); possible icing; etc. Factors that can increase the actual energy produced include topology impacts (e.g. if the turbine location is at the top of a hill) and wind speed transients (i.e., gustiness). Furthermore, extrapolation errors from known hourly wind speeds at 10 and 50 meters to the wind turbine hub height may provide either over or under predictions of the wind energy produced.

Considering the factors just identified, it is assumed that the actual wind energy produced is below the manufacturer provided power coefficient determined production of 3678 MWh/yr. This assumption of lower wind energy production is both common reality and means that the results reported in this study are more likely to be conservative in nature. By being conservative in nature then the likelihood of overstating diesel fuel reduction benefits is minimized. A base case energy decrease of 15% is assumed for the majority of results reported in this chapter.

- Diesel Generators

  To satisfy the electricity demand for Kangirsuk (for non-heating purposes), the community currently employs three generators with capacities of 450 kW, 450 kW, and 560 kW, respectively, all powered by Artic diesel fuel. The load data available for Kangirsuk (electricity generated by diesel fuel) was last updated in 2015 and sourced from the Hydro-Québec Distribution database [51]. To estimate the total electrical load for the community in 2021 this dataset was extrapolated using a constant growth rate of 1.4%, which is based on the 2019-2029 forecast provided in a Hydro-Québec report [51].

  In the present study, the electric output of the wind turbine is prioritized for use to reduce the electrical load of the community with excess being stored, however, for power reliability reasons at least one of the 450 kW diesel generators is always operating at least 30% load (135 kW), even the wind or storage systems provide 100% of the energy needs. Refer to Appendix D for a visual representation of the hourly community's remaining diesel load profile after prioritizing the use of wind energy. Appendix D also presents a visual representation of the surplus wind power for a single wind turbine for the year 2021.

5.2.2 Sizing Method

In Section 5.2.1, a comprehensive analysis was conducted to evaluate the power generation and load demand in the village of Kangirsuk and to assess the viability of implementing a hybrid wind-diesel CAES system. Furthermore, the frequency-of-occurrence method was employed to establish the upper and lower bounds of CAES components size based on the results of the data analysis. This section demonstrates the application of a CAES components sizing process, referred to as the optimization-based sizing approach (OBSA). The main objective of OBSA is to determine the optimal hybrid wind-CAES component sizes that maximize the reduction of Kangirsuk's dependency on diesel fuel through the integration of wind energy while minimizing the associated capital costs.

5.2.2.1 CAES Optimization-based Sizing Approach

The primary objective function in the optimization process is to maximize the percentage of diesel fuel reduction during the year 2021. This objective function, referred to as the "Diesel Reduction Function," is mathematically defined by Equation 5.1, and serves as a quantitative measure to guide the optimization process and steer it towards reducing diesel fuel reliance. In Equation 5.1, A represents the overall net community diesel consumption in the absence of any wind turbines and energy storage systems. Meanwhile, B, C, and D denote the quantities of directly utilized wind power, CAES power generation, and CAES heat requirements by diesel (during discharging mode), respectively. Notably, the diesel reduction function takes into account both the diesel fuel consumption by the community and any supplementary heat requirements associated with the CAES system (such as additional heat to heat up the compressed air before the air expanders if the TES does not have enough capacity, or to avoid ice formation in air expanders). Therefore, the optimization process in the sizing method does not treat efficiency as a separate objective function. This is due to the inherent relationship between CAES performance improvements, particularly in terms of efficiency, and reductions in diesel fuel consumption. Enhancements in CAES efficiency allow for an operation that is more closely aligned with an adiabatic CAES system, resulting in lower diesel fuel requirements.

$$\text{Diesel Reduction Function} = \frac{A - B - C + D}{A} \times 100 \tag{5.1}$$

$$\text{Components Cost Function} = \sum Z_i \tag{5.2}$$

Another important factor addressed within the optimization method is associated with the capital cost of the hybrid wind-CAES system. This includes determining the optimal total volume of thermal energy storage and the minimum size of the compressor, expander, and reservoir. This sizing process enables the CAES system to achieve maximum diesel reduction while employing the minimum feasible TES and components capacity. This second objective function, denoted as the "Components Cost Function" is mathematically defined by Equation 5.2, which represents the summation of components capital cost (Z_i); where i is the CAES component index. The cost function of CAES components is presented in Table 5.1; where the cost functions derive from [94]. However, these cost functions are chosen as representatives to compare the case studies in this paper, and a more comprehensive cost analysis is required to examine the viability of a hybrid wind-diesel CAES system in northern Canadian communities. To visualize the sequential steps involved in the sizing of CAES system components, refer to Figure 5.4.

Figure 5.4 illustrates a flowchart utilized in this study to guide the OBSA methodology. The process and logic employed for CAES system operation are similar to those developed in Chapter 3. However, the sizing process undergoes optimization to accurately size the CAES system components based on the optimal objective functions. In Figure 5.4, the process initiates with the optimization of the first generation (G=1; each generation is a population of individuals). Following this, a comparison is made between the community load ($L(t)$) and the available wind power ($W(t)$) to determine the presence of an excess event (charging mode) or a shortage (discharging mode). The charging mode becomes active when there is surplus power available ($W(t) - L(t) > 0$), while the discharging mode is engaged when demand surpasses the power supply ($W(t) - L(t) < 0$). Furthermore, a no-action mode comes into play when the actual demand matches the power supply, or when operational constraints like reservoir pressure limits, minimum load of turbomachines, or start-up time prevent the CAES system from responding. The logical flow of the charging and discharging processes is illustrated in Figure 5.5 (A1 and A2, respectively). The time interval shown in Figure 5.4 represents one hour. After completing the simulation for all time steps (8760 hours; year 2021) of the first generation (G=1), these computations will be reiterated for subsequent generations. This cycle continues until the simulation reaches the maximum number of generations in order to determine the optimal sizing of CAES components.

Figure 5.5 depicts the control unit (represented by the green box) responsible for constraining the operational parameters of the CAES reservoir (red dashed box, including the reservoir mass and pressure limits) and turbomachines (blue dashed box, including the

[2]The reservoir cost used in this study is an average cost for caverns. The cost of other CAES reservoirs, such as cased wellbores or pressure vessels, would be more expensive.

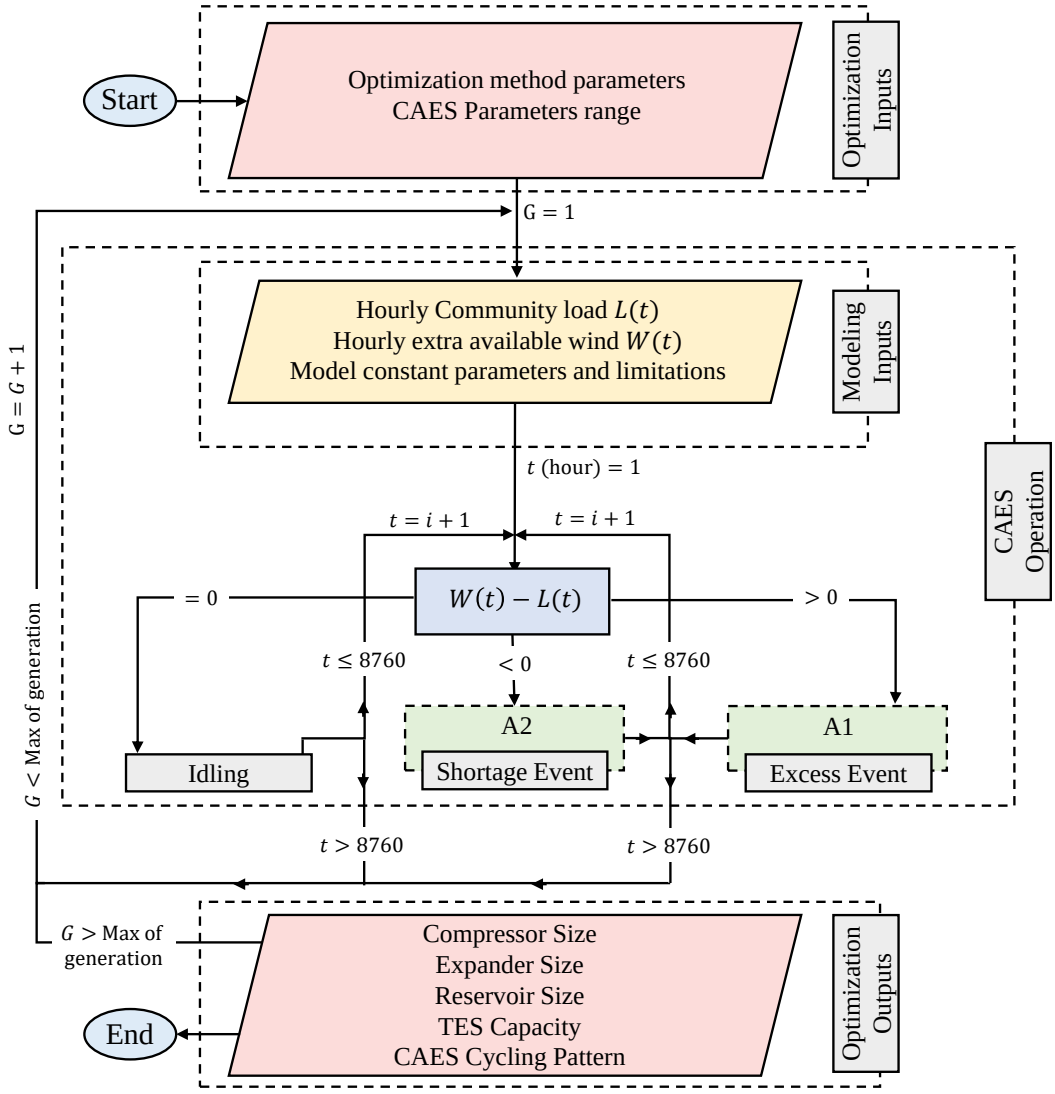

Figure 5.4: Optimization-based sizing approach (OBSA).

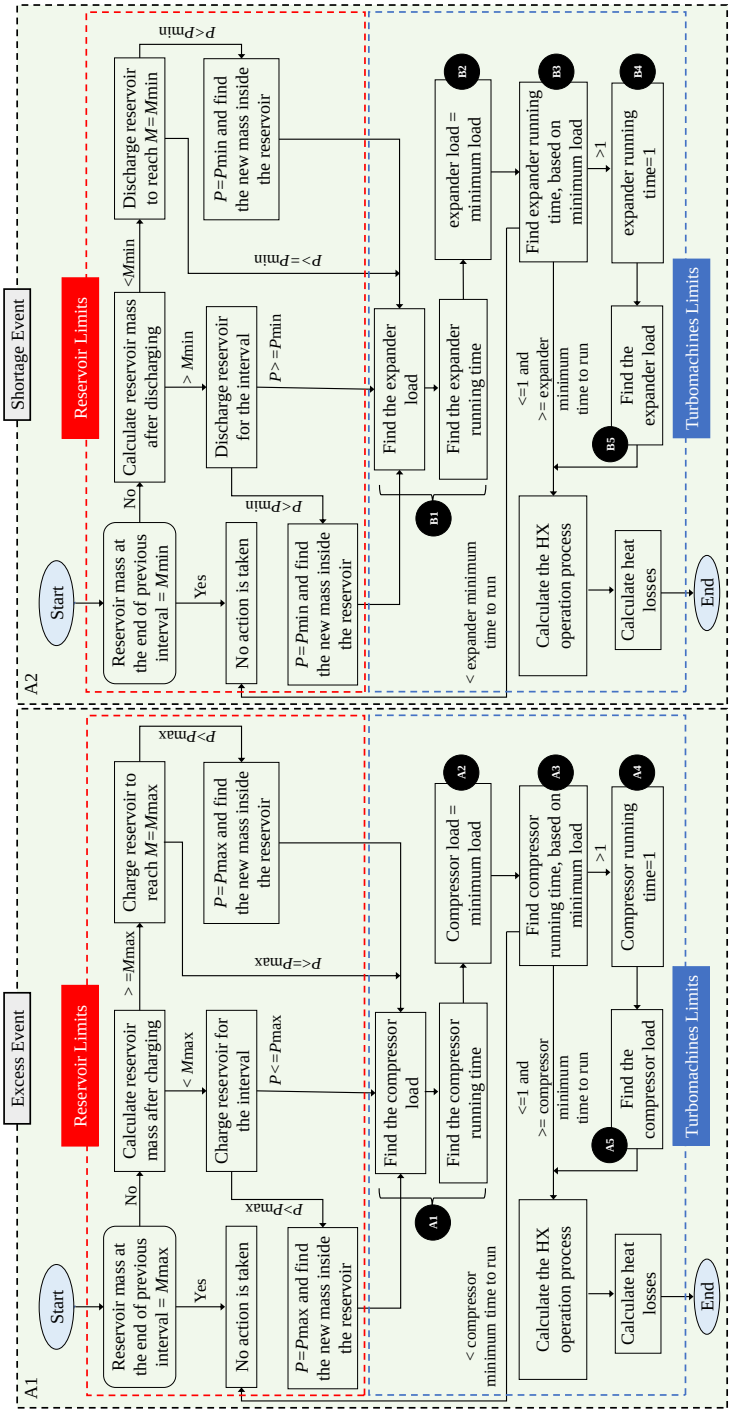

Figure 5.5: CAES charging (excess) and discharging (shortage) processes; considering the system limitations examination.

Table 5.1: Capital investment cost functions for different CAES components and wind turbine (CAD) [94, 134].

Component	Cost function symbol	Cost function value
Compressor	$Z_{compressor}$	\$730/KW
Expander	$Z_{expander}$	\$435/KW
Reservoir[2]	$Z_{reservoir}$	\$37/KWh
Thermal storage	Z_{TES}	$0.25(Z_{compressor} + Z_{expander})$
Wind turbine	$Z_{Wind-turbine}$	$4,010,000$

turbomachine load, and startup time limits). In instances of surplus power occurrence, an evaluative comparison will be conducted between the reservoir mass and pressure, in relation to the upper mass and pressure thresholds. This assessment serves the purpose of determining the system's viability for commencing the charging process. Similarly, the identical control mechanism is employed for the discharging process, wherein a comparison is drawn between the reservoir mass and pressure, and the lower mass and pressure thresholds. The objective here is to determine the system's capacity to effectively respond to a shortage event. If the system is unable to operate for the entire interval due to restrictions in mass or pressure, it will function partially within the interval to align with the operational limitations. These limitations are referred to as the reservoir limits (red dashed box in Figure 5.5).

Figure 5.5 also shows the control unit for the turbomachinery performance (highlighted by a blue dashed box), which limits the minimum load and runtime of the turbomachinery. To include the requirements of minimum load and start-up time in the modeling of the CAES system, the recommended control unit begins by deciding the turbomachine load and runtime for a specific period (represented by A_1 and B_1). For the compressor operation, as seen on the left side of Figure 5.5, after calculating the runtime for a given time step (step A_1), the load is adjusted to meet the minimum load (called stage A_2). Then, the corresponding runtime for this minimum load is calculated (known as stage A_3). This calculation confirms if the compressor can operate for a duration beyond the minimum start-up time. If the calculated runtime at stage A_3 is not enough for the required minimum start-up time, the CAES system goes into idle mode, even if the reservoir has enough capacity for power storage. If the runtime obtained in stage A_3 exceeds the modeling time interval (which is 1 hour), the compressor's runtime is set to the entire interval (1 hour) in stage A_4, and a new compressor load is calculated (shown in stage A_5). The same approach can be applied to the expander operations (steps B_1 to B_5).

5.2.3 Thermodynamic Modeling

This section illustrates the configuration of a hybrid wind-diesel CAES system and provides an overview of the mathematical formulation employed in this study to assess the CAES system's performance and quantify the reduction in diesel fuel consumption for the selected community.

5.2.3.1 Hybrid Wind-Diesel Partially A-CAES (H-WD-PA-CAES) System Configuration

The hybrid wind-diesel partial adiabatic compressed air energy storage (H-WD-PA-CAES) system integrates wind turbines and a diesel generator with a PA-CAES system designed to capture surplus wind energy. The PA-CAES technology includes a compressed air energy storage system with thermal energy storage to capture the heat generated during the compression phase. However, this approach requires the incorporation of a combustion chamber positioned before each expansion unit to raise the temperature of compressed air if it falls below the required inlet temperature of the expansion unit during the discharge phase, despite the utilization of the stored compression heat. The rationale behind this choice arises from the inherent heat losses occurring at various system parts, including heat exchangers, thermal energy storage, and the reservoir, throughout different operational stages. As a result, a combustion chamber (CC) is introduced to provide supplementary heat when necessary, ensuring that the compressed air reaches the required temperature before entering the air expander. This discharge procedure holds great significance in optimizing the efficiency performance of a chain of expanders and is also imperative to prevent the formation of ice.

The current study introduces an innovative configuration (depicted in Figure 5.6) wherein an advanced heat exchange system is integrated to enhance energy conversion efficiency during both compression and expansion stages. This configuration aims to optimize the utilization of renewable wind energy, minimize diesel consumption, and enhance the overall reliability of the hybrid power generation system.

As illustrated in Figure 5.6, the PA-CAES system is structured such that the heat generated during compression is stored within a multi-tank sensible thermal energy storage unit. Subsequently, this stored heat is employed during the expansion process to enhance the efficiency of the CAES cycle and minimize fuel usage. However, due to limitations imposed by the heat storage temperature or the size of the thermal energy storage unit, a portion of the thermal energy generated during compression may be dissipated into the environment. A dual-tank sensible heat exchange fluid storage system (consisting of hot

and cold tanks) has been extensively investigated for its application in adiabatic CAES systems [190]. In this research, a multi-tank heat exchange fluid thermal energy storage unit operating with a sensible thermal fluid is adopted due to its cost-effectiveness, high efficiency, high operating temperature (based on the chosen thermal fluid and its pressure within the storage tanks), and its inherent simplicity [190].

The suggested charging configuration for the PA-CAES system, as depicted in Figure 5.6, includes two compression units, each followed by three heat exchangers (with the count of heat exchangers after each compression unit subject to modification based on the compression ratio and outlet temperature). To address instances where the compressed air temperature falls below the inlet temperature of the expander during discharge, a combustion chamber is positioned prior to each expander for the purpose of thermal elevation (not depicted in Figure 5.6). Additionally, a heat exchanger is positioned before the reservoir, intended to further reduce the temperature of the compressed air to the desired injection temperature. The thermal energy extracted through this heat exchange process, just prior to reaching the reservoir, is assumed to be dumped into the environment.

5.2.3.2 Thermodynamic Analysis

The thermodynamic equations corresponding to various elements of a PA-CAES system (such as the compressor, heat exchangers, TES tanks, reservoir, combustion chamber, pump, and expander) have been provided in Tables 4.1 to 4.6 of chapter 4. The thermodynamic analysis of all components is based on the following assumptions [97]:

- The air behaves as an ideal compressible gas (compressibility factor of 1).
- Uniform temperature and pressure of the air within the reservoir.
- Negligible changes in potential and kinetic energy.
- Absence of chemical reactions or phase changes.
- All components, except for the reservoir, are assumed to operate at steady-state conditions.

5.2.4 Optimization

This study utilizes a hierarchical two-objective optimization approach based on the differential evolution (DE) technique [101] to determine the optimal operational parameters of

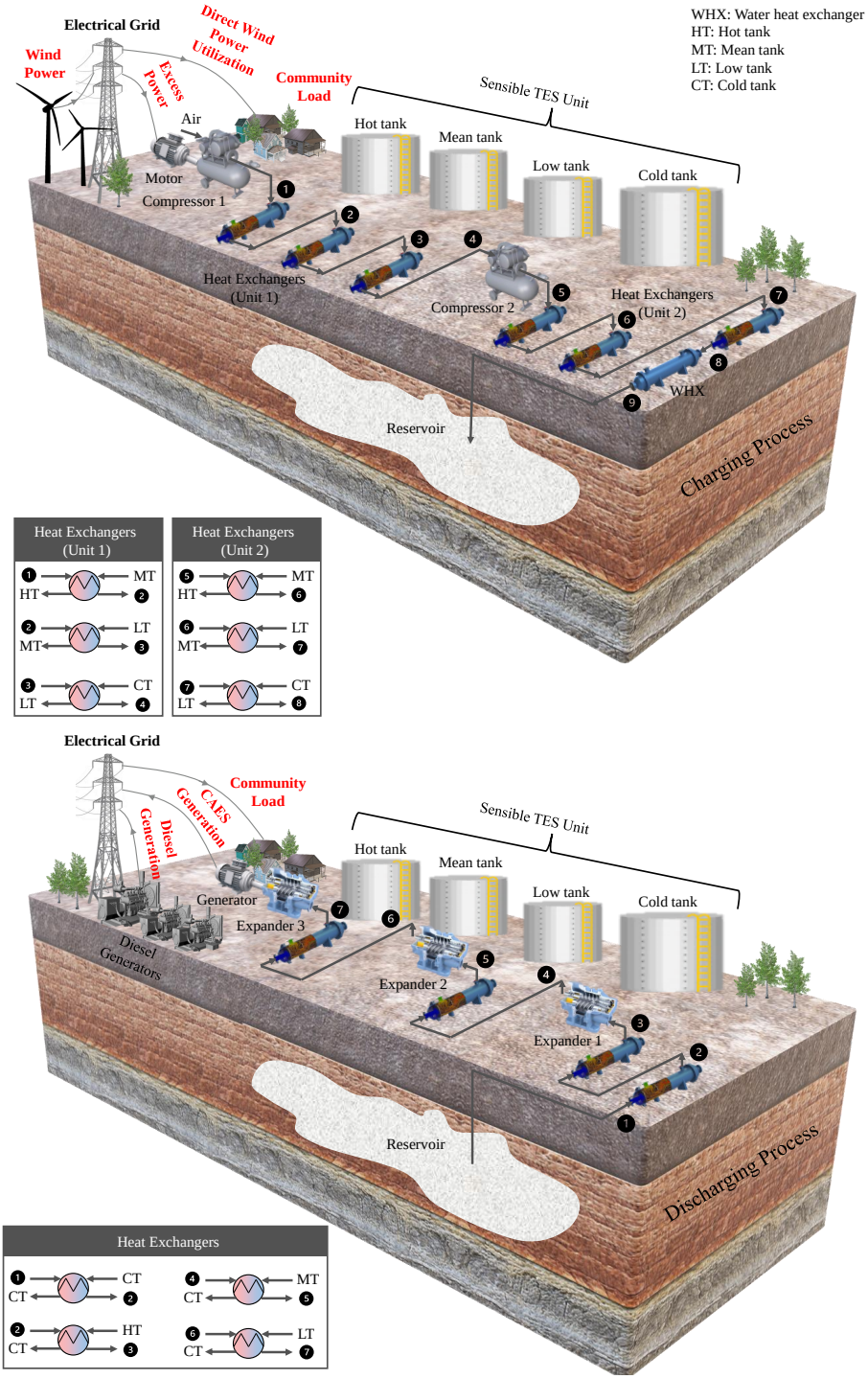

Figure 5.6: Suggested configuration for charging (upper) and discharging (lower) processes of a hybrid wind-diesel PA-CAES system. 141

the PA-CAES system. The determination of system parameter ranges and the explanation of the optimization algorithm are provided in Sections 5.2.4.1 and 5.2.4.2, respectively.

5.2.4.1 Parameters Range Determination

Table 5.2 summarizes the PA-CAES independent parameters and their range for the optimization process.

5.2.4.2 Optimization Algorithm

A hierarchical optimization method is employed as a systematic approach to reduce Kangirsuk's dependency on diesel fuel (evaluated by the diesel reduction function defined by Equation 5.1), while minimizing the cost of energy storage components (assessed by the components cost function defined by Equation 5.2). The hierarchical optimization approach facilitates the assessment of the importance of each objective function, guided by a user-defined weighting factor. To elaborate, the optimization process unfolds in two stages. Initially, the foremost objective, prioritized due to its heightened significance (namely, the diesel reduction function labeled as f_1), undergoes optimization during the initial iteration, while the secondary objective (components cost function), is disregarded. The optimal solution obtained from this initial phase is denoted as $X^1_{optimal}$. Subsequent to this, the optimization proceeds by focusing on the components cost function as the secondary objective (labeled as f_2). However, this optimization is subject to an additional constraint placed upon the first objective, as expressed in Equation 5.3. The outcomes of this hierarchical optimization process yield a Pareto optimal solution through manipulation of ϵ_i, as outlined by Karim and Adeniran [101].

$$f_1(X) \geq (1 - \frac{\epsilon_i}{100}) f_1(X^{i-1}_{opimal}) \tag{5.3}$$

5.3 Results and Discussions

This section summarizes the results of the data analysis, hybrid CAES wind-diesel viability, and optimization.

Table 5.2: PA-CAES independent parameters and their range for the optimization process (scenario 1).

Parameter	**Symbol**	**Range**	**Unit**
Thermal fluid mass flow rate during charging process (from mean-temperature to high-temperature tank)	$\dot{m}_{\text{ch1}}$	[0.1-2]	[kg/s]
Thermal fluid mass flow rate during charging process (from low-temperature to mean-temperature tank)	$\dot{m}_{\text{ch2}}$	[0.1-2]	[kg/s]
Thermal fluid mass flow rate during charging process (from cold-temperature to low-temperature tank)	$\dot{m}_{\text{ch3}}$	[0.1-2]	[kg/s]
Thermal fluid mass flow rate during discharging process (from cold-temperature to cold-temperature tank)	$\dot{m}_{\text{dch1}}$	[0.1-2]	[kg/s]
Thermal fluid mass flow rate during discharging process (from high-temperature to cold-temperature tank)	$\dot{m}_{\text{dch2}}$	[0.1-2]	[kg/s]
Thermal fluid mass flow rate during discharging process (from mean-temperature to cold-temperature tank)	$\dot{m}_{\text{dch3}}$	[0.1-2]	[kg/s]
Thermal fluid mass flow rate during discharging process (from low-temperature to cold-temperature tank)	$\dot{m}_{\text{dch4}}$	[0.1-50]	[kg/s]
Size of high-temperature tank	$(TES)_H$	[10-100]	$[m^3]$
Size of mean-temperature tank	$(TES)_M$	[10-100]	$[m^3]$
Size of low-temperature tank	$(TES)_L$	[10-100]	$[m^3]$
Compressor size	W_c	[10-440]	[KW]
Expander size	W_e	[10-390]	[KW]
Reservoir size	E_{cav}	[10-20000]	[KWh]
Reservoir upper pressure	P_{max}	[9-15]	[MPa]
Reservoir lower pressure	P_{min}	[2-8]	[MPa]
Expander 1 inlet temperature	$(T_{e,1})_1$	[350-650]	[K]
Expander 2 inlet temperature	$(T_{e,1})_2$	[350-650]	[K]
Expander 2 pressure ratio	$(PR_e)_2$	[2-7]	[Unitless]
Expander 3 pressure ratio	$(PR_e)_3$	[2-6]	[Unitless]

5.3.1 Data Analysis and Visualization

To size and design an energy storage system for the village of Kangirsuk, a comprehensive understanding of energy production (energy supply; wind energy is the sole source of clean energy) and energy needs (energy demand; the community load) is essential [148, 157]. A community energy demand analysis helps to ensure that the energy storage system can provide energy shortage during on-peak periods. Additionally, the community's wind energy production is equally important as it helps prevent oversizing energy storage components, resulting in higher capital and maintenance costs. Conversely, undersizing results in an energy storage system that does not take the best advantage of clean wind energy to reduce the community's diesel fuel use. In the present study, two distinct scenarios are investigated to determine the appropriate size and design of a storage system for an adaptive hybrid system in Kangirsuk. The first scenario examines the installation of a single wind turbine, while the second scenario considers the installation of two wind turbines. Considering the power generated by wind without energy storage, the community stands to achieve diesel fuel savings of up to 48%, 56%, and 59 % with one, two, and three wind turbines, respectively. It is worth noting that the small increase in diesel fuel savings from two turbines to three turbines suggests that the installation of additional wind turbines beyond two, in the absence of energy storage, may not be economically feasible, i.e., increased diesel fuel savings may not be sufficient to provide third turbine payback. Furthermore, wind curtailment in the absence of energy storage is 1.3 (42%), 4.1 (66%), and 7.1 (76%) GWh/year with one, two, and three wind turbines, respectively. The percentages are calculated given a single wind turbine produces 3.1 GWh/year.

Box plots (a) and (b) in Figure 5.7 present a comprehensive summary of the diesel fuel savings per added wind turbine in kW and as a percentage of the community load for each hour throughout the year 2021 (with no energy storage). Within the box plots displayed in Figure 5.7, result pairs are shown for each month with the green-yellow column corresponding to the diesel savings associated with the installation of a single wind turbine, and the blue column corresponding to the additional savings by a second turbine. Each horizontal line within a given month represents an hour. The color bars featured in the plot serve to indicate the corresponding savings in diesel power per added turbine. These savings in diesel fuel are determined by Equations 5.4 and 5.5 for a single wind turbine and two wind turbines, respectively (where C denotes the community net load with no wind turbines and no energy storage system, DFS and DFS(%) respectively refer to the diesel fuel saving and diesel fuel saving as a percentage of the community net load, and X and Y represent the community's remaining diesel load after installation of a single wind turbine and two wind turbines, respectively). Also shown in the box plot of Figure 5.7 is

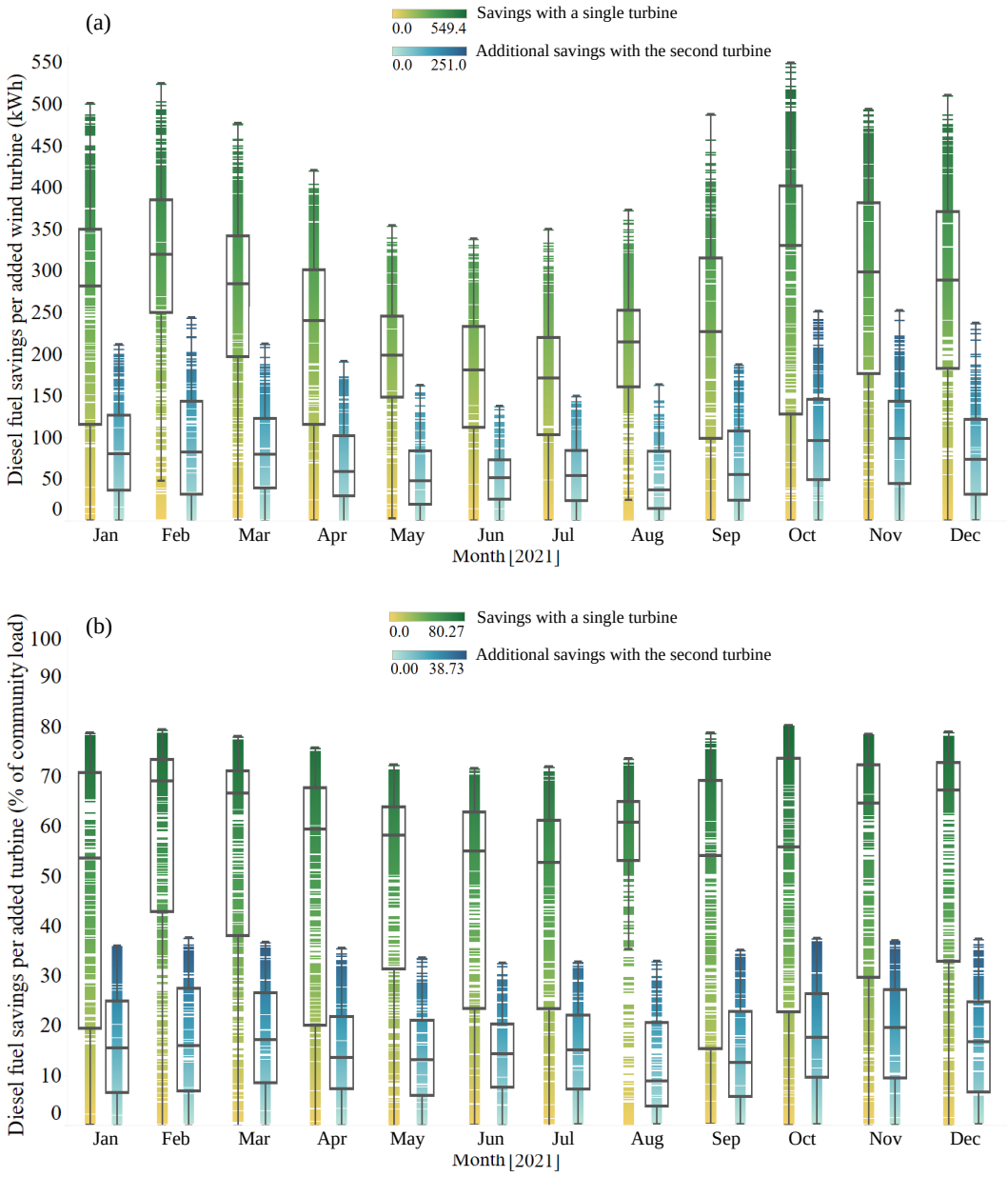

Figure 5.7: Without energy storage, (a) diesel fuel savings per added turbine (kWh), and (b) diesel fuel savings as a percent of hourly community load per added turbine

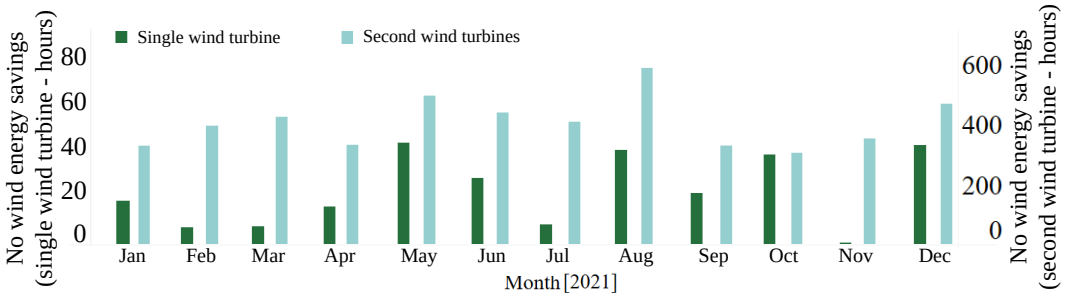

Figure 5.8: Number of hours no wind energy is produced by a given turbine with the difference between the second and single turbine hours being the hours of full curtailment of the second turbine. Note the different axes scales.

the interquartile range, clearly indicating the lower quartile (Q_1) and upper quartile (Q_3) values. The median (Q_2) of the data is denoted by a horizontal line positioned inside the box. Moreover, two lines known as the lower and upper whiskers extend from the box. These lower and upper whiskers are calculated using the formulas $Q_1 - 1.5(Q_3 - Q_1)$ or the minimum value, and $Q_3 + 1.5(Q_3 - Q_1)$ or maximum value, respectively. All whiskers are minimum or maximum values meaning by this criteria there are no outliers in the data indicating a well-dispersed distribution of the data around the median.

$$\begin{aligned} \text{DFS}_{\text{single wind turbine}} &= C - X \\ \text{DFS (\%)}_{\text{single wind turbine}} &= \frac{C - X}{C} \times 100 \end{aligned} \tag{5.4}$$

$$\begin{aligned} \text{DFS}_{\text{two wind turbines}} &= X - Y \\ \text{DFS (\%)}_{\text{two wind turbines}} &= \frac{X - Y}{C} \times 100 \end{aligned} \tag{5.5}$$

Figure 5.7(a) reveals greater diesel fuel savings are achieved during the cold winter months. Noting that these results are for a wind-diesel system with no energy storage, the greater diesel fuel savings in winter are due to a combination of two factors. First, there is the opportunity for less curtailment in winter due to the higher community load in winter (498 kW average winter community load versus 386 kW average summer community load; also see Figure D.1 in Appendix D). This decrease in curtailment is indeed observed (171 kW average curtailed in summer versus 116 kW average curtailed in winter). Second, there is greater wind energy potential in the winter (367 kW average wind energy available in winter October-March versus 346 kW average in summer April-September) to displace

the use of a greater amount of diesel fuel. Additionally, Figure 5.7(a) demonstrates that installing a second wind turbine in Kangirsuk allows the preservation of an additional 296 MWh/yr, equivalent to 8% of the community load. However, these smaller diesel savings due to the second turbine, when compared to employing a single turbine (1866 MWh savings, equivalent to 48% of the community load), suggest that increasing the number of wind turbines without an energy storage system may not be economically viable. This statement is further supported by Figure 5.9.

Figure 5.7(b) provides information on the diesel fuel savings achieved per added wind turbine as a percentage of the community load. It is important to note that the maximum percentage of fuel savings possible is 81% since diesel fuel is always consumed no matter how much wind energy is available as the system always has one diesel generator running at 135 kW. Also, note that the order of the horizontal lines (representative of a specific hour) is not correlated. Figure 5.8 illustrates the cumulative number of hours without wind energy savings for both wind turbines. It is important to note that, for the first wind turbine, the number of hours represents the duration in which no wind energy is produced. For the second wind turbine, the number of hours consists of the combined period of no wind energy production and the duration of 'full' curtailment in hours. Full curtailment is represented by the difference between the second and single turbine in Figure 5.8; do take note of the different axes scales. Furthermore, it is important to note that partial curtailment is not represented in Figure 5.8. The data presented in Figure 5.8 visually demonstrates that installing the second wind turbine in the village of Kangirsuk, without an energy storage system, results in thousands of hours (4613 hours) of full curtailment. This observation finds support in the data provided in Figure 5.9 where the individual green-yellow and blue lines depicted in Figures 5.7(a) and (b) are represented as circles on a two-dimensional diagram in Figures 5.9(a) and (b), respectively. While Figures 5.7(a) and (b) do not exhibit any correlation in the arrangement of lines, the circles in Figure 5.9(a) maintain identical positions to those in Figure 5.9(b). Furthermore, Figure 5.9(c) presents the cumulative diesel fuel savings obtained by summing the values from Figures 5.9(a) and (b).

Figures 5.9(a) and (b) also depict the regions of wind turbine curtailment for different wind power and community net load. In cases where the community's energy demand, reduced by 135 kW from the consistently operational diesel engine, equals or surpasses the energy harnessed by the wind turbine, there is no curtailment, resulting from full utilization of the wind-generated energy. Given that the community's energy requirements consistently exceed the 135 kW supplied by the continuously operational diesel engine, never a full curtailment happens in the presence of a single wind turbine (refer to Figure 5.9(a)). However, under circumstances where a single wind turbine satisfies the entire

community load, a full curtailment occurs for the second wind turbine (depicted in Figure 5.9(b)). Instances of partial curtailment arise either when the potential power output of a single wind turbine surpasses the community's load minus the 135 kW requirement (as depicted in Figure 5.9(a)), or when a single wind turbine alone cannot fulfill the community's load, but in conjunction with a second wind turbine, the cumulative power output surpasses the community's load requirement, thereby leading to partial curtailment (as shown in Figure 5.9(b)). It is noteworthy that Figure 5.9(b) also presents the possibility of no curtailment, occurring when the total potential power generated by two wind turbines is insufficient to meet the community's load less 135 kW requirement.

To evaluate the occurrence of excess and shortage power events within the community and to determine the appropriate size of a storage system in response to these events, a frequently employed approach involves the deduction of surplus wind power from the community's remaining diesel load (i.e., the load that still relies on diesel fuel after the installation of wind turbines) [157]. Positive values indicate an excess of power, whereas negative values indicate a power shortage.

Box plots (a) and (b) in Figure 5.10 illustrate the community's excess wind power (in green, charging events opportunities) and power shortage (in red, discharging events prospects) values for the installation of a single wind turbine and two wind turbines, respectively. In Figure 5.10, each column is representative of a month, while each horizontal green (hours of excess power; wind curtailment) or red line (hours of shortage; reliance on diesel fuel) within a column corresponds to an hour.

Figures 5.11(a) and (b) illustrate the frequency of occurrence for excess power and power shortage, along with their respective cumulative frequency of occurrence (expressed in %) for the scenario involving a single wind turbine. Additionally, Figures 5.11(c) and (d) depict the frequency of occurrence for excess energy and energy shortage, accompanied by their cumulative frequency of occurrence expressed in percentages, for the same scenario. To determine the excess energy and energy shortage, the consecutive values of excess power or power shortage are summed, resulting in the excess energy or energy shortage during charge and discharge events. For this study, the time interval is considered 1 hour (1 kWh of energy is equivalent to 1 kW of power for 1 hour). The frequency of occurrence graphs for the two turbines are similar and presented in Appendix E. The main observations derived from Figures 5.10 and 5.11 are as follows:

- The total hours of excess power during the spring and summer seasons are higher compared to the fall and winter as indicated by the median locating in the excess power region in the presence of a single wind turbine (Figure 5.10 (a)). This implies

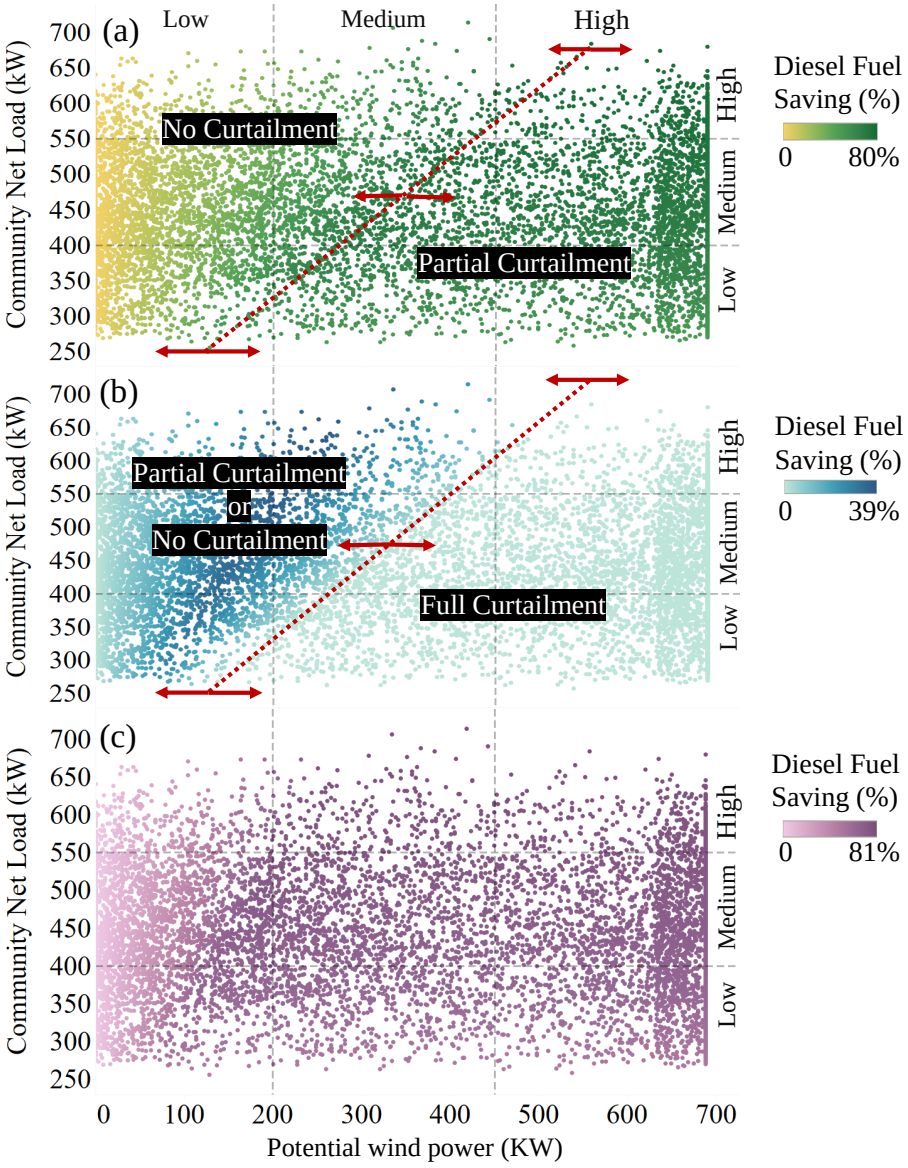

Figure 5.9: Without energy storage and considering no wind power cut off, (a) diesel fuel savings as a percent of hourly community load by a single wind turbine, (b) diesel fuel savings as a percent of hourly community load by a second wind turbine, and (c) total diesel fuel savings as a percent of hourly community load (the summation of graphs (a) and (b)). The color bars show the diesel fuel kW savings percentage. The apparent increased density band from about 638 kW to the maximum of 688 kW is an artifact of the manufacturer-reported turbine power curve, see Appendix Figure C.1.

(a) Excess power and Power Shortage with One Wind Turbine (KW)

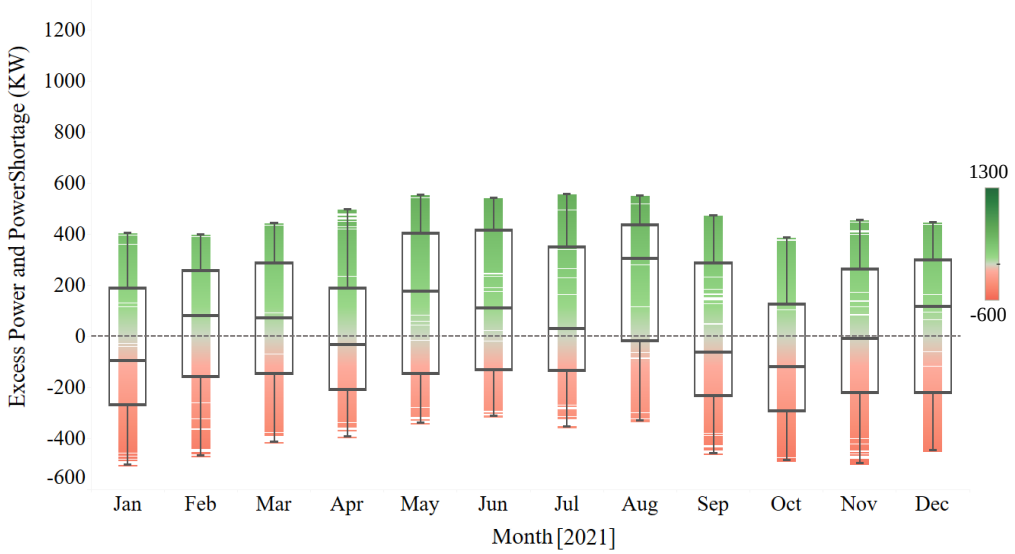

(b) Excess power and Power Shortage with Two Wind Turbines (KW)

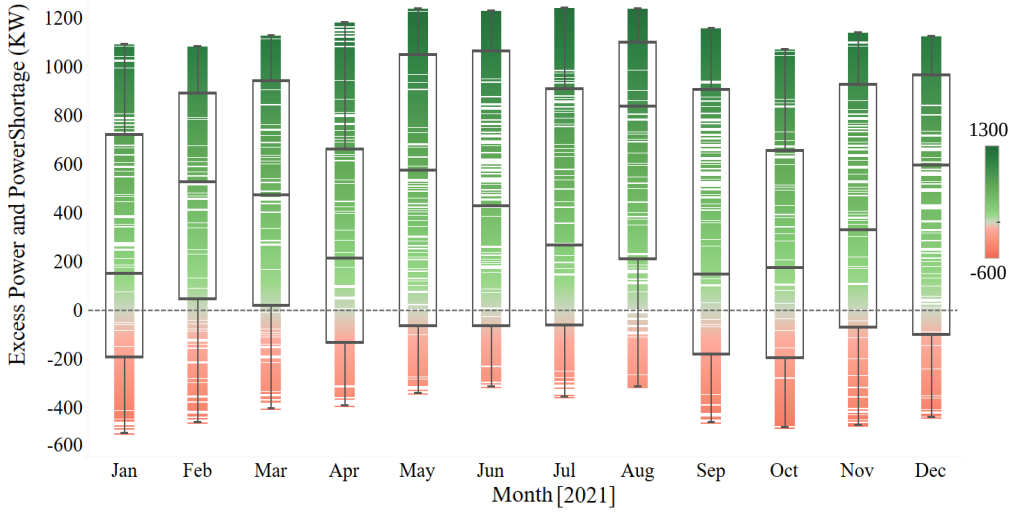

Figure 5.10: Monthly excess power and power shortage (box plot analysis) in the village of Kangirsuk in 2021; (a) in the presence of a single wind turbine, and (b) in the presence of two wind turbines. The grey dashed lines show the zero line.

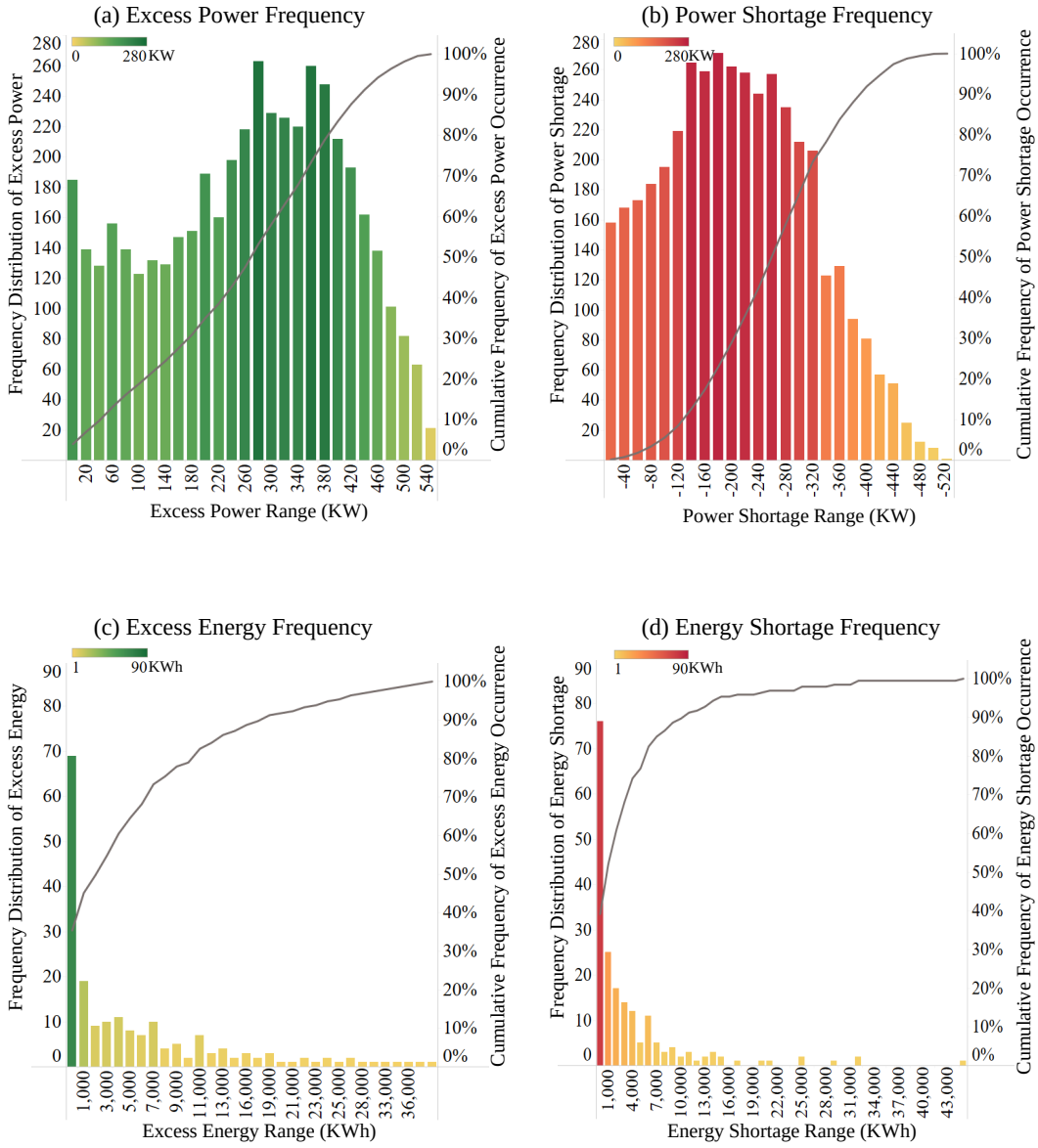

Figure 5.11: Annual frequency distribution of excess power (graph (a)) and power shortage (graph (b)), along with the corresponding cumulative frequency of occurrence (grey lines), and annual frequency distribution of excess energy (graph (c)) and energy shortage (graph (d)), along with the corresponding cumulative frequency of occurrence (grey lines) for considering a single wind turbine in the village of Kangirsuk in 2021.

that, during the months in which the village has been supplied with diesel fuel to cover the community's electrical needs for a full year, an energy storage system can be relied upon to a greater extent. This would enable the community to conserve diesel fuel for peak demands in the winter and reduce overall dependency on diesel. However, in the presence of two wind turbines in the community, a shift in the median occurs with its location consistently falling within the excess power region for all months (Figure 5.10 (b)). This indicates a substantial amount of wind curtailment in the absence of energy storage.

- In addition to the greater total hours of excess power observed during the spring and summer seasons compared to the fall and winter, the average amount of excess power in spring and summer is also higher. In fact, the maximum amount of excess power during these two seasons can reach up to 550 KW in the scenario of one wind turbine, while it does not exceed 470 KW in fall and winter (Figure 5.10 (a)). Nevertheless, the size of the box plots for each month suggests that there is a similar degree of variability in the data across all months, with the data points spread out around the median value. When considering the installation of two wind turbines, the pattern of excess power distribution across different months follows the same trend as depicted in Figure 5.10 (a) for a single wind turbine.

- The box graphs presented in Figure 5.10, denoted as (a) and (b), illustrate that no outliers were observed in terms of excess power and power shortage for both scenarios. This observation is supported by the alignment of the upper and lower whisker values with the maximum values of excess and shortage for each month. The absence of outliers can be attributed to the well-dispersed distribution of the data around the median. Therefore, it is reasonable to regard the maximum values of excess and shortage as the boundaries for determining the sizing requirements of the compressor and expander in a CAES power plant located in Kangirsuk. Specifically, these boundaries are determined as 555 KW and 505 KW for excess and shortage, respectively, in the case of a single wind turbine, and 1240 KW and 505 KW, respectively, for excess and shortage when considering two wind turbines. However, the frequency distribution of excess power and power shortage for a single wind turbine, graphs (a) and (b) in Figure 5.11, indicates that to cover 90% of the excess and shortage, a minimum compressor and expander sizes of around 440 and 390 KW is required (this sizing method is called frequency-of-occurrence [150]). In the scenario involving two wind turbines, the determined sizes for the compressor and expander, using the frequency distribution and considering a 90% coverage, are 1100 KW and 390 KW, respectively.

- Based on the data presented in Figure 5.11(c), it can be observed that an energy reservoir with a capacity of approximately 20,000 kWh is capable of addressing over 90% of excess energy occurrences for a single wind turbine. Moreover, the majority of energy shortage events are below 10,000 kWh (with 20,000 kWh being sufficient to cover 96% of shortage events). As a result, reservoir sizes exceeding 20,000 kWh may not significantly impact the integration of wind energy and the reduction of diesel fuel consumption in the presence of a single wind turbine. In the case of two wind turbines, an energy reservoir with a capacity of around 60,000 kWh is sufficient to address over 90% of excess energy occurrences. This reservoir size is more than enough to cover 100% of shortage events. However, these percentages are related to the event's frequency of occurrences, and it cannot be concluded that if a storage reservoir is able to respond to most events, it necessarily possesses an acceptable coverage percentage of excess energy or energy shortage events. Therefore, a more accurate metric is required to size a storage reservoir effectively.

- The optimal operational frequency for an energy storage system in Kangirsuk has the potential to range from hourly to monthly. Nevertheless, the data analysis findings suggest that employing a compressed air energy storage system with hourly operation and with an oversized reservoir could enhance wind energy integration into the community's local electricity generation. This conclusion is further supported by graphs shown in Figure 5.12, where all instances of excess and shortage events are illustrated for each month in terms of their magnitude (measured in kilowatt-hours) and duration (measured in hours) for the scenario including the installation of a single wind turbine (a similar graph for the installation of two wind turbines is presented in E). Additionally, a box plot is employed to identify any outliers. By excluding these outliers, which are deemed inconsequentially significant events, one can determine the appropriate capacity of a CAES system based on the frequency of excess and shortage occurrences, as previously explained. However, graphs in Figure 5.12 demonstrate how excess outliers can be effectively utilized to compensate for shortage events in the subsequent month (indicated by the grey dashed arrows). It is essential to note that the term "oversized reservoir" does not imply a reservoir capable of accommodating the maximum surplus energy. Rather, it signifies a reservoir that can store a portion of energy for short-term durations (such as hourly or daily charging/discharging) in summer, while also storing surplus wind-generated energy over longer-term durations to be utilized in winter.

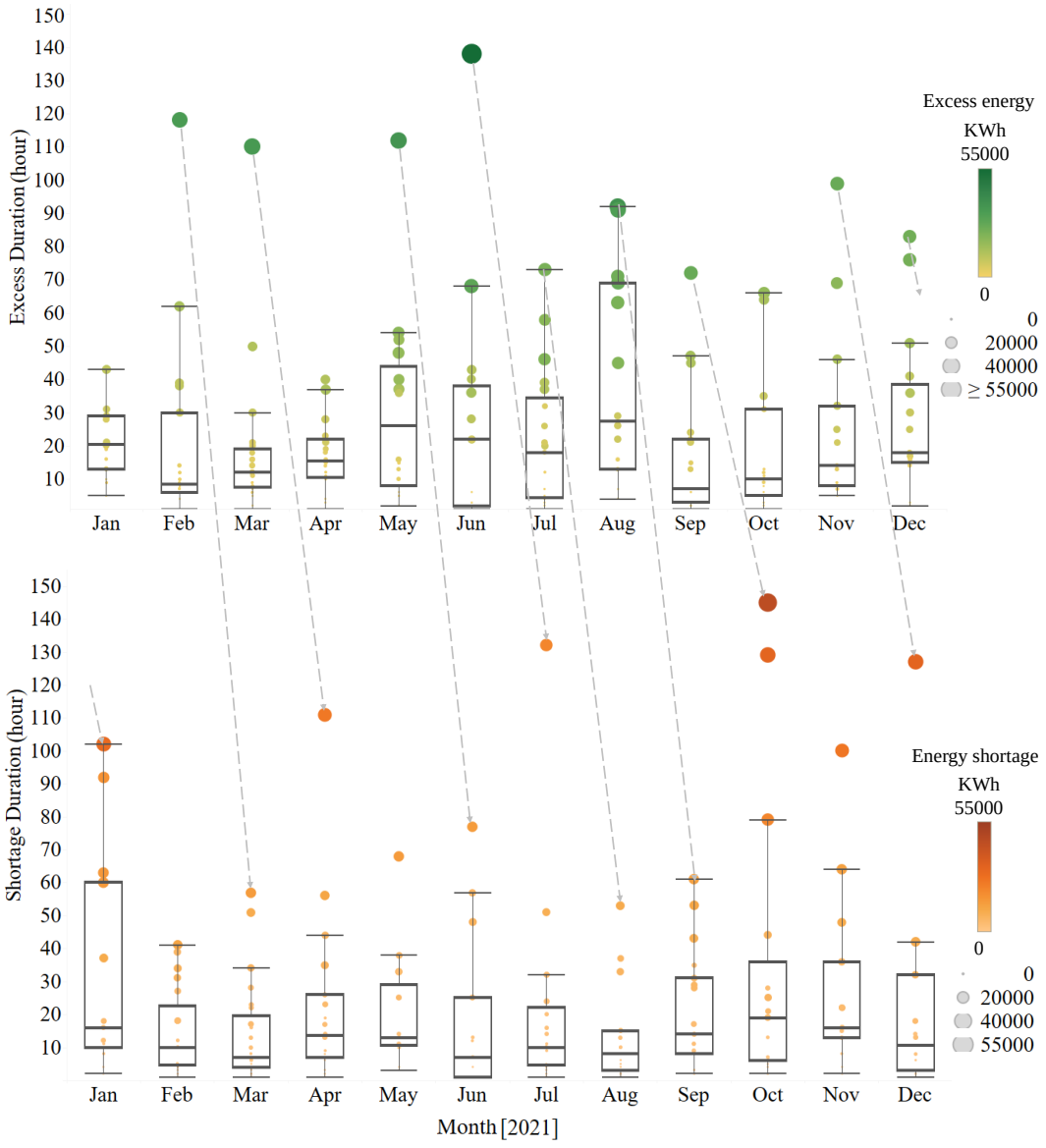

Figure 5.12: Duration of excess (upper graph) and shortage (lower graph) events for each month, considering a single wind turbine in the village of Kangirsuk in 2021; dashed grey lines depict how excess outliers can be utilized to cover shortage outliers.

5.3.2 Hybrid CAES Wind-Diesel Viability Analysis

The viability analysis of implementing a Hybrid wind-diesel CAES system in the Village of Kangirsuk holds great importance, given the power data analysis that indicates the necessity for an energy storage system capable of short- to medium-term operations (i.e., ranging from daily to monthly durations). Therefore, CAES emerges as a suitable option for the village of Kangirsuk, primarily owing to its cost-effectiveness in accommodating oversized energy storage systems and providing long-term storage capabilities. Nonetheless, to ensure the successful deployment of a CAES system in this small community, further comprehensive studies and detailed assessments are required to thoroughly evaluate the technical, economic, and environmental implications. These investigations are essential to understand the benefits and challenges associated with implementing a CAES system for Kangirsuk. However, these in-depth studies are beyond the scope of this chapter, highlighting the need for additional research to make well-informed decisions regarding the viability of Hybrid CAES Wind-Diesel integration for the Village of Kangirsuk.

5.3.3 Hybrid CAES Wind-Diesel Performance

This section provides an overview of the performance of the hybrid CAES wind-diesel system with regard to the reduction of diesel fuel consumption and capital cost. The main objective is to optimize the CAES operational modes (as listed in Table 5.2) to maximize the percentage of diesel fuel reduction (Equation 5.1) with the minimum capital cost (i.e., minimum components size, Equation 5.2). The findings outlined here relate to seven distinct cases as follows:

- Case 1 (C1): Diesel fuel reduction and capital cost for the installation of a single wind turbine.
- Case 2 (C2): Diesel fuel reduction, capital cost, and optimal solution for the installation of a single wind turbine, utilizing upper component size limits determined by the frequency of occurrence method.
- Case 3 (C3): Diesel fuel reduction, capital cost, and optimal solution for the installation of a single wind turbine, employing oversized upper limits for component sizes based on the maximum size method.
- Case 4 (C4): Diesel fuel reduction and capital cost for the installation of two wind turbines.

Table 5.3: Optimization results for cases 1 to 7, in terms of diesel fuel reduction and capital cost.

Case	**Number of wind turbine**	**Turbine loss (%)**	**Wind-diesel-CAES**	**Over-sized CAES**	**Diesel fuel reduction (%)**	**Capital cost ($CAD)**
C1	1	15	×	×	48	4,010,000
C2	1	15	✓	×	55	5,080,000
C3	1	15	✓	✓	56.7	6,120,000
C4	2	15	×	×	56	8,020,000
C5	2	15	✓	×	63.4	9,980,000
C6	2	15	✓	✓	65.3	13,520,000
C7	3	15	×	×	59	12,030,000

- Case 5 (C5): Diesel fuel reduction, capital cost, and optimal solution for the installation of two wind turbines, utilizing upper component size limits determined by the frequency of occurrence method.
- Case 6 (C6): Diesel fuel reduction, capital cost, and optimal solution for the installation of two wind turbines, employing oversized upper limits for component sizes based on the maximum size method.
- Case 7 (C7): Diesel fuel reduction and capital cost for the installation of three wind turbines.

It is worth noting that the utilization of a CAES system with oversized turbomachines and an oversized reservoir and TES is attributed to the data analysis findings that indicate how an oversized system could potentially reduce diesel fuel consumption within the community (refer to Figure 5.12). Table 5.3 presents the outcomes of these cases, including the results of optimizations concerning diesel fuel consumption reduction and capital expenditure. These results are also depicted in Figure 5.13. Further insights into the optimal operational modes for each case are available in Table 5.4.

The findings presented in Table 5.3 demonstrate the significant influence of integrating wind turbines with the CAES system. In Case 1, the installation of a single wind turbine resulted in a remarkable 48% reduction in diesel fuel consumption. This reduction highlights the capacity of wind power to displace a substantial portion of diesel fuel usage in the remote off-grid Kangirsuk. Furthermore, the incorporation of CAES led to further

Table 5.4: Optimized operational parameters of the hybrid CAES wind-diesel system under different cases.

Symbol	**C2**	**C3**	**C5**	**C6**
$\dot{m}_{\mathrm{ch1}}$	0.11	0.11	0.73	0.73
$\dot{m}_{\mathrm{ch2}}$	0.25	0.25	0.21	0.21
$\dot{m}_{\mathrm{ch3}}$	0.41	0.41	0.49	0.49
$\dot{m}_{\mathrm{dch1}}$	0.32	0.32	0.56	0.56
$\dot{m}_{\mathrm{dch2}}$	0.34	0.34	0.60	0.60
$\dot{m}_{\mathrm{dch3}}$	0.36	0.36	0.53	0.53
$\dot{m}_{\mathrm{dch4}}$	23	23	32	32
$(TES)_H$	60	101	101	160
$(TES)_M$	60	110	87	99
$(TES)_L$	67	133	100	170
W_c	310	360	400	620
W_e	210	230	290	360
E_{cav}	18500	44900	39000	128100
P_{max}	9.5	9.5	14.8	14.8
P_{min}	3	3	2.6	2.6
$(T_{e,1})_1$	455	455	475	475
$(T_{e,1})_2$	412	412	445	445
$(PR_e)_2$	3.6	3.6	5.8	5.8
$(PR_e)_3$	1.9	1.9	3.4	3.4

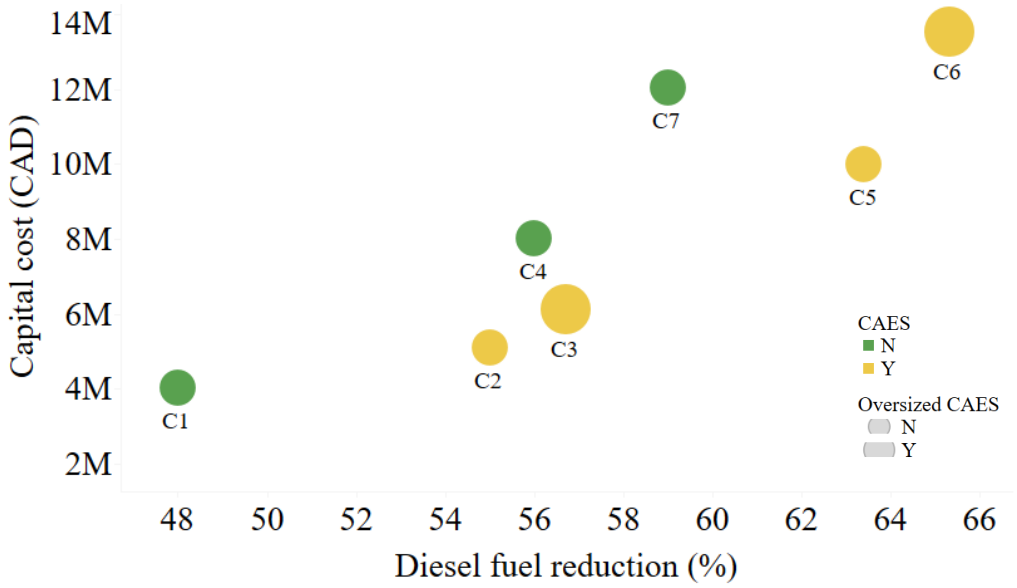

Figure 5.13: Diesel fuel reduction and capital cost for cases 1 to 7 (N: No, and Y: Yes).

enhancements in diesel fuel reduction. Specifically, Case 2 shows an impressive reduction of 55%, and in Case 5, a reduction of 63.4% is observed. These findings indicate the role of CAES in augmenting the reduction of diesel fuel consumption. However, it is worth noting that oversizing the CAES system to achieve greater diesel fuel savings is associated with an increased capital cost. Nevertheless, it is essential to evaluate these trade-offs within the broader context of long-term operational savings resulting from reduced diesel fuel consumption.

The capital costs required for the implementation of the hybrid CAES wind-diesel system can be a substantial investment. In Case 1, the installation cost for a single wind turbine was $4,010,000. As the study progressed to Cases 2 and 3, which involved the utilization of a single wind turbine, the capital costs escalated to $5,080,000 and $6,120,000, respectively, which are notably lower than the cost of deploying two wind turbines ($8,020,000). The results indicate that the implementation of two wind turbines, coupled with a CAES system that is not oversized, as in Case 5, is more efficient in harnessing wind energy to reduce diesel fuel consumption and entails a lower capital cost when compared to employing three wind turbines. However, the choice between Case 2 and Case 5 hinges on the project's priorities. If the primary objective is to maximize diesel fuel reduction and ensure long-term energy sustainability, Case 5 emerges as the preferred

option, notwithstanding the higher initial investment. On the other hand, if capital cost considerations take precedence, Case 2 represents a more cost-effective alternative while still delivering a substantial reduction in diesel fuel consumption.

Figure 5.14 provides a graphical representation of the hourly energy sources available to the village of Kangirsuk under two cases: case 2, which involves a single wind turbine with CAES, and case 5, which employs two wind turbines with CAES. In Figure 5.14(a), the net community load is depicted in olive, while the gray area within the community load graph represents the dependency on diesel fuel. Figure 5.14(b) illustrates CAES production, and Figure 5.14(c) demonstrates the utilization of wind power for the community. These simulations are grounded in energy data from 2021. According to the data of 2021, a CAES system could contribute 274,000 kWh and 367,000 kWh to the community load under the single wind turbine and two wind turbine scenarios, respectively. Additionally, the longest continuous activity periods were 33 hours and 64 hours, respectively.

5.4 Summary of Chapter

This study has conducted a comprehensive investigation into the appropriateness and viability of integrating an adaptive energy storage system, integrating a CAES system into a wind-diesel setup for a remote Canadian community. The primary objective was to address critical gaps in existing research by thoroughly examining various aspects of CAES system deployment, including sizing, design, operation, and overall viability in small, isolated communities. The contributions in this chapter are multifaceted:

- Comprehensive power data analysis: A comprehensive analysis of power supply-demand patterns for the entire year 2021 was carried out, providing an in-depth understanding of energy dynamics in the Kangirsuk community. This analysis is pivotal for evaluating the feasibility (in terms of excess and shortage events durations, and quantity) of CAES integration into wind-diesel hybrid systems.
- Optimal sizing and operation strategies: Optimal sizing and operation configurations for CAES systems within the selected community were identified. These strategies are essential for achieving maximum diesel fuel reduction with the minimum energy storage size and minimum number of wind turbines.
- Sizing strategy proposal: An innovative optimization-based sizing strategy for the integration of A-CAES into a wind-diesel power plant was introduced, utilizing Kan-

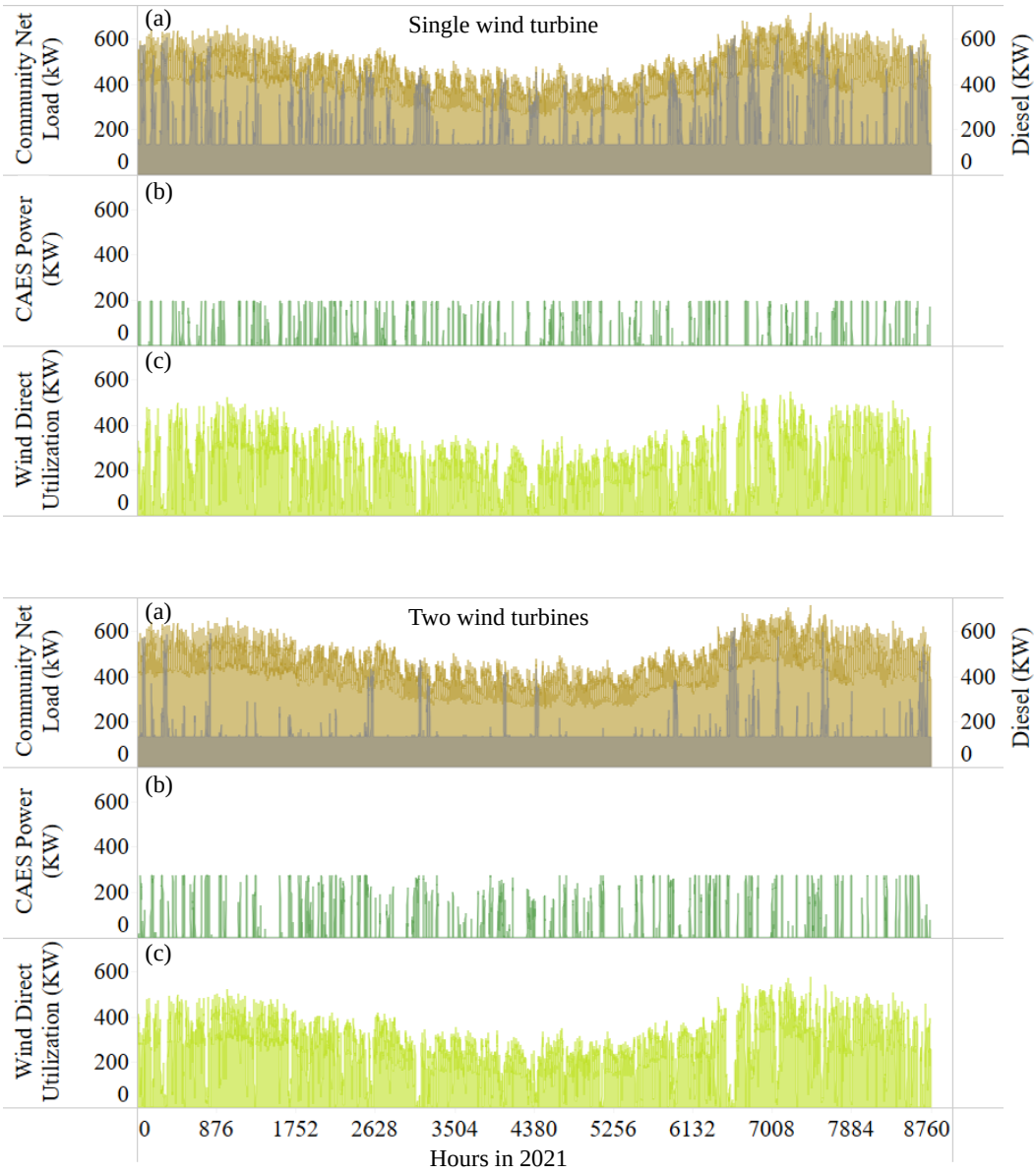

Figure 5.14: Hourly energy sources available to the village of Kangirsuk in the presence of a single wind turbine with CAES (Case 2), and two wind turbines with CAES (Case 5). Graph (a) illustrates the net community load (in olive), while the gray area in the community load is dependent on diesel fuel. Simulations are based on available energy data from 2021.

girsuk as a case study. This strategy has the potential to substantially reduce diesel consumption, thus enhancing energy sustainability in remote, off-grid regions.

- A full-year performance assessment: The long-term operating performance of hybrid wind-diesel CAES systems was assessed, considering critical factors such as efficiency, diesel fuel reduction, and cost functions. The findings highlight the capacity of CAES to serve as a reliable backup during periods of low wind energy production or heightened electricity demand.

In conclusion, the integration of CAES holds promise for reducing diesel fuel dependency and advancing energy sustainability in remote regions. However, to fully assess the feasibility of CAES implementation in such communities, comprehensive studies are necessary, encompassing technical, economic, and environmental factors. Notably, the findings from this research (refer to Table 5.3) indicate that Case 2 (a CAES with a compressor of 310 KW, an expander of 210 KW, and a reservoir of 18500 KWh) achieves a 55% reduction in diesel fuel consumption, offering a cost-effective solution for Kangirsuk with a capital cost of $5,080,000. Conversely, Case 5 (a CAES with a compressor of 400 KW, an expander of 290 KW, and a reservoir of 39000 KWh) achieves a higher reduction of 63.4% but requires a greater initial investment ($9,980,000), making it the preferred choice for long-term energy sustainability, provided that capital costs can be managed.

Chapter 6

Conclusions, Publications, and Future Works

This chapter provides a summary of the main contributions and conclusions of the thesis, lists publications resulting from this research, and outlines potential directions for future studies.

6.1 Conclusions

In the growing pursuit of sustainable and low-carbon energy systems, the integration of renewable energy sources into the electrical grid presents both immense potential and considerable challenges. The intermittent nature of renewable resources, such as wind and solar power, has led to a pressing need for effective grid-scale electrical energy storage (EES) systems. Among the various EES technologies, compressed air energy storage (CAES) has emerged as a promising candidate. However, the recent advent of adiabatic CAES (A-CAES) has highlighted the need for advancements in this field to address CAES' low efficiency and operational limitations.

This thesis aimed to address important gaps in the study of CAES systems, with a particular focus on A-CAES. The initial chapters provided a comprehensive examination of existing literature and highlighted limitations in previous research, notably the absence of a comprehensive understanding of external factors, the need to consider operational limits, and the challenges observed in A-CAES modeling. It was evident that many prior models relied on generic thermodynamic models, lacked power grid analysis, and overlooked

key design and operational considerations. In response, this research aimed to bridge these gaps and propose solutions through the design of a near-A-CAES (NA-CAES) system.

In Chapter 3, the first objective of this thesis was achieved with the introduction of the coverage-percentage method, a novel CAES sizing approach that enhanced the accuracy of component sizing. By considering time-dependent operational constraints, component limitations, and pressure constraints within the cavern, the method was applied to Ontario's electrical grid data, yielding optimal compressor, expander, and reservoir sizes. This highlighted the importance of economic considerations to avoid oversizing components. The chapter highlighted the need to move beyond the overly optimistic estimates provided by the frequency-of-occurrence approach, offering a more accurate method for determining coverage percentages and ultimately improving the operation and cost-effectiveness of CAES systems.

In Chapter 4, the second objective of this thesis was addressed through a comprehensive analysis that delved into the factors contributing to the gap between theoretical models and practical A-CAES experiments. Key contributors to the operational efficiency disparity were identified, including oversimplified heat management modeling, neglected heat losses, and several design issues. The chapter also presented a case study for designing an A-CAES system in Ontario, with a focus on maximizing exergy stored in thermal energy storage (TES) systems and optimizing heat exchanger configurations. The findings emphasized the importance of considering system operational limits, component limitations, and design configurations when optimizing A-CAES systems, ultimately improving their practical implementation. Specifically, this research resulted in the design of a NA-CAES system in Ontario with a round-trip efficiency exceeding 60%, highlighting significant efficiency improvements.

In Chapter 5, the third objective of this thesis was pursued, expanding the research scope to explore the integration of a partially A-CAES (PA-CAES) system with wind-diesel configurations in remote and isolated areas. Unlike previous studies that primarily focused on diesel engine efficiency, this chapter shifted emphasis to CAES system sizing, design, and operational feasibility in these challenging off-grid areas. The objective was to address a crucial question: can CAES technologies effectively contribute to the development of sustainable and reliable adaptive hybrid energy systems for remote Canadian communities? This chapter aimed to provide insights and solutions to enhance the viability and performance of CAES systems in such demanding off-grid environments.

In summary, this thesis has addressed significant research gaps and provided practical insights and methodologies for sizing, designing, and optimizing adiabatic CAES systems. These contributions have the potential to drive advancements in energy storage, benefiting

engineers, and researchers who aim to enhance the efficiency and feasibility of grid-scale energy storage systems.

6.2 Summary Conclusion of Sizing and Design a Near A-CAES System for Ontario (Chapters 3 and 4)

- The frequency-of-occurrence approach often overestimates the coverage percentage, while the coverage-percentage method provides a more accurate means of sizing CAES components, aligning system design with actual operational constraints, and economic considerations.
- Cavern pressure limits significantly impact the charging and discharging coverage percentages.
- The recommended sizes for CAES components in Ontario, determined by the coverage-percentage method, are as follows: a compressor and expander sized between 30 MW to 70 MW, with cavern energy capacities between 630 MWh and 770 MWh, capturing at least 42% of charging and 26% of discharging capacity.
- A constant-pressure reservoir offers higher efficiency and greater flexibility compared to a constant-volume reservoir, further enhancing the practicality of A-CAES systems.
- A multi-tank thermal energy storage (TES) system is suitable for efficiently capturing compression heat in a near-adiabatic compressed air energy storage (NA-CAES) system.
- Under optimal operational modes, the NA-CAES system can achieve an efficiency of above 60%, demonstrating the potential for highly efficient energy storage and utilization.

6.3 Summary Conclusion of Sizing and Design Adaptive Hybrid CAES Wind-diesel Systems for Remote Communities (Chapters 5)

- The integration of CAES holds promise for reducing diesel fuel dependency and advancing energy sustainability in remote regions.
- The findings from this research (refer to Table 5.3) indicate that a CAES with a compressor of 306 KW, an expander of 207 KW, and a reservoir of 18550 KWh achieves a 55% reduction in diesel fuel consumption, offering a cost-effective solution for Kangirsuk with a capital cost of $5,088,000.
- A CAES with a compressor of 400 KW, an expander of 290 KW, and a reservoir of 39028 KWh can achieve a higher reduction of 63.4% but requires a greater initial investment ($9,987,000), making it the preferred choice for long-term energy sustainability, provided that capital costs can be managed.

6.4 Overall Conclusion

This research delves deeply into the processes involved in sizing and designing adiabatic compressed air energy storage (CAES) systems and explores the design challenges inherent to CAES, emphasizing the absence of a universally applicable solution. Building upon two distinct case studies conducted within the scope of this thesis, it becomes evident that the sizing and design of such systems necessitate an approach that takes into account the array of external factors influencing system operation. It is important to recognize that the project's overarching objectives, whether optimizing efficiency, coverage percentage, utilization percentage, capital costs, or achieving diesel fuel savings, should guide the CAES design process.

For example, the Ontario case study placed supreme importance on achieving high system efficiency. Consequently, the CAES system was designed to operate at lower utilization rates, thereby maintaining reservoir pressure within a narrow range. This strategy ensured consistent and efficient performance. In contrast, the case study in remote communities prioritized minimizing diesel fuel dependency, a crucial objective given the geographical isolation of these areas. To attain this goal, the CAES system was designed for high utilization, despite the reduction in overall system efficiency.

These findings highlight the need for a context-dependent approach in the design and sizing of CAES systems. There is no one-size-fits-all solution, as the unique demands of each project dictate the appropriate design parameters. It is crucial to recognize the complex interplay between system efficiency, utilization rates, costs, and overall project objectives. By adopting this adaptable approach and tailoring CAES designs to their specific targets and external constraints, the full potential of CAES technology can be harnessed, thereby contributing to a sustainable energy ecosystem. This research offers valuable insights that will guide future efforts in the field of CAES system design and application, facilitating the transition towards more efficient and eco-friendly energy solutions.

6.5 Publications

This section provides a list of peer-reviewed journal papers that have originated from the research conducted during this Ph.D. program.

Sarmast, S., Fraser, R., and Dusseault, M., (2021), Performance and cyclic heat behavior of a partially adiabatic Cased-Wellbore Compressed Air Energy Storage system. *Journal of Energy Storage* [156].

Sarmast, S., Rouindej, K., Fraser, R., and Dusseault, M., (2023), Sizing-design method for compressed air energy storage (CAES) systems: a case study based on power grid in Ontario. *Energy Conversion and Management* [157].

Sarmast, S., Rouindej, K., Fraser, R., and Dusseault, M., (2023), Performance improvement and operational mode optimization of near-adiabatic compressed air energy storage (NA-CAES) systems: sizing and design an NA-CAES system for Ontario. *Applied Energy* [158].

Sarmast, S., Séjourné, S., Wigston, A. Fraser, R., and Dusseault, M., (2023), Adaptive hybrid energy system for remote Canadian communities: optimizing wind-diesel systems integrated with adiabatic compressed air energy storage. *Energy Conversion and Management*, under revision [159].

6.6 Future Works

The following areas are recommended for further exploration and building upon the research outlined in this Ph.D. dissertation.

- **Economic analysis and optimization of a NA-CAES system, including capital costs, maintenance costs, and operational costs.** To gain insights into the financial aspects of implementing the NA-CAES system, a comprehensive techno-economical analysis is essential. This analysis is pivotal for informed investment decisions and is essential in transforming the NA-CAES system into a financially and environmentally sustainable energy storage solution.

- **Enhance the NA-CAES system performance through the inclusion of exergy in the optimization process.** Beyond energy efficiency and thermal energy storage cost, there is potential for optimizing the NA-CAES system using multiple criteria, including exergy analysis. Exploring exergy as one of the performance metrics can provide a more comprehensive insight into the system's overall efficiency and open up opportunities for further enhancements.

- **Conduct a comprehensive feasibility assessment and life cycle analysis.** In addition to optimizing performance metrics, a thorough feasibility assessment and life cycle analysis of the NA-CAES system are crucial. This research can explore the environmental, economic, and technical aspects across the system's entire life cycle, including the development, and operation phases. A comprehensive evaluation of its long-term feasibility and sustainability will offer valuable insights for potential stakeholders and decision-makers in the renewable energy sector.

- **Develop a dynamic control system to improve NA-CAES system efficiency through adaptive TES mass flow rates.** Instead of employing a static charging and discharging mass flow rate for each TES tank, designing a dynamic control system to adaptively control the charge and discharge mass flow rates of thermal fluid in real time can increase the overall system efficiency.

- **Consider deformation behavior of CAES systems in different rocks.** To further enhance the comprehensiveness of this study, the influence of mechanical deformations within the underground storage cavern during CAES operation can be taken into account.

- **Apply machine learning for performance prediction of hybrid CAES wind-diesel systems.** Machine learning techniques can be employed to estimate the performance of hybrid CAES wind-diesel systems involving factors such as CAES components size, the number of wind turbines, and other externalities affecting the system performance. These methods can provide insights into optimizing these systems for efficiency and reliability, thereby supporting the design of sustainable hybrid energy solutions.

References

[1] The atlas of canada - remote communities energy database. https://atlas.gc.ca/rced-bdece/en/index.html, Accessed: May 5, 2023.

[2] Canyon creek pumped hydro energy storage project. https://majorprojects.alberta.ca/Details/Canyon-Creek-Pumped-Hydro-Energy-Storage-Project/1975, Accessed: May 2, 2023.

[3] Capacity of pumped storage hydropower worldwide in 2022, by leading country. https://www.statista.com/statistics/689667/pumped-storage-hydropower-capacity-worldwide-by-country/, Accessed: Sep 10, 2023.

[4] Converting an old mine into a giant hydro battery. https://www.opg.com/projects-services/projects/energy-storage/marmora/, Accessed: Sep 18, 2023.

[5] Enercon product overview. https://pdf.directindustry.com/pdf/enercon/enercon-product-overview/20877-243513-_5.html, Accessed: May 8, 2023.

[6] Global energy review 2020. https://www.iea.org/reports/global-energy-review-2020/oil, Accessed: Oct 1, 2023.

[7] Ieso reports site. http://reports.ieso.ca/public, Accessed: Oct 30, 2023.

[8] Independant electricity system operator (ieso). https://ieso.ca/en, Accessed: Oct 30, 2023.

[9] Managing oversupply. https://www.caiso.com/informed/Pages/ManagingOversupply.aspx, Accessed: Oct 3, 2023.

[10] Nasa, 2023. solar and meteorological data. national aeronautics and space administration, langley research center (larc) power project funded through the nasa earth science/applied science program. https://power.larc.nasa.gov, Accessed: May 7, 2023.

[11] Pumped storage tracking tool. https://www.hydropower.org/hydropower-pumped-storage-tool, Accessed: Oct 8, 2023.

[12] Tableau 2021.3. https://www.tableau.com.

[13] Global renewable energy market analysis, market trends, growth, forecast, insights from 2020 to 2027, April 2020. https://www.shingetsuresearch.com/renewable-energy-market/, Accessed: Oct 8, 2023.

[14] Chad Abbey and Geza Joos. Sizing and power management strategies for battery storage integration into wind-diesel systems. In *2008 34th Annual Conference of IEEE Industrial Electronics*, pages 3376–3381. IEEE, 2008.

[15] R Al-Khoury and J Bundschuh. *Computational Models for CO2 Geo-sequestration & Compressed Air Energy Storage*. CRC Press, 2014.

[16] Seyed Mojtaba Alirahmi, Shadi Bashiri Mousavi, Amir Reza Razmi, and Pouria Ahmadi. A comprehensive techno-economic analysis and multi-criteria optimization of a compressed air energy storage (caes) hybridized with solar and desalination units. *Energy Conversion and Management*, 236:114053, 2021.

[17] RD Allen, TJ Doherty, and Arlo F Fossum. Geotechnical issues and guidelines for storage of compressed air in excavated hard rock caverns. 1982.

[18] Guruprasad Alva, Lingkun Liu, Xiang Huang, and Guiyin Fang. Thermal energy storage materials and systems for solar energy applications. *Renewable and Sustainable Energy Reviews*, 68:693–706, 2017.

[19] C Anierobi, K Bhattacharya, and C Canizares. Behind-the-meter compressed air energy storage feasibility and applications. *Electric Power Systems Research*, 189:106630, 2020.

[20] Chioma C Anierobi, Kankar Bhattacharya, and Claudio A Canizares. Behind-the-meter compressed air energy storage feasibility and applications. *Electric Power Systems Research*, 189:106630, 2020.

[21] LF Arenas, C Ponce De León, and FC Walsh. Engineering aspects of the design, construction and performance of modular redox flow batteries for energy storage. *Journal of Energy Storage*, 11:119–153, 2017.

[22] Mariano Arriaga, Claudio A Cañizares, and Mehrdad Kazerani. Northern lights: Access to electricity in canada's northern and remote communities. *IEEE Power and Energy Magazine*, 12(4):50–59, 2014.

[23] Ehsanolah Assareh, Seyed Sajad Mousavi Asl, Neha Agarwal, Mehrdad Ahmadinejad, Amin Jalali, and Moonyong Lee. A cogeneration-coupled energy storage system utilizing hydrogen and methane-fueled caes and orc with ambient temperature consideration enhanced by artificial neural network, and multi-objective optimization. *Thermal Science and Engineering Progress*, 46:102161, 2023.

[24] Beckwith Associates. Review of environmental studies and issues on compressed air energy storage. 1983.

[25] Alireza Bahadori. Simple method for estimation of effectiveness in one tube pass and one shell pass counter-flow heat exchangers. *Applied energy*, 88(11):4191–4196, 2011.

[26] S Balasubramanian and P Balachandra. Effectiveness of demand response in achieving supply-demand matching in a renewables dominated electricity system: A modelling approach. *Renewable and Sustainable Energy Reviews*, 147:111245, 2021.

[27] M. Balesdent, L. Brevaul, S. Lacaze, S. Missoum, and J. Morio. 8 - methods for high-dimensional and computationally intensive models. In Jérôme Morio and Mathieu Balesdent, editors, *Estimation of Rare Event Probabilities in Complex Aerospace and Other Systems*, pages 109–136. Woodhead Publishing, 2016.

[28] Edward Barbour, Dimitri Mignard, Yulong Ding, and Yongliang Li. Adiabatic compressed air energy storage with packed bed thermal energy storage. *Applied energy*, 155:804–815, 2015.

[29] Edward Barbour and Daniel L Pottie. Adiabatic compressed air energy storage technology. *Joule*, 5(8):1914–1920, 2021.

[30] Edward R Barbour, Daniel L Pottie, and Philip Eames. Why is adiabatic compressed air energy storage yet to become a viable energy storage option? *IScience*, 24(5):102440, 2021.

[31] Matheus B de A Barros, Daniel Rodriguez, and Jorge R Henriquez. Thermodynamic analysis of a compressed air energy storage system with constant volume storage considering different operating conditions for reservoir walls. *Journal of Energy Storage*, 32:101728, 2020.

[32] Tammam Basbous, Rafic Younes, Adrian Ilinca, and Jean Perron. Optimal management of compressed air energy storage in a hybrid wind-pneumatic-diesel system for remote area's power generation. *Energy*, 84:267–278, 2015.

[33] Elaheh Bazdar, Fuzhan Nasiri, and Fariborz Haghighat. An improved energy management operation strategy for integrating adiabatic compressed air energy storage with renewables in decentralized applications. *Energy Conversion and Management*, 286:117027, 2023.

[34] Elaheh Bazdar, Mohammad Sameti, Fuzhan Nasiri, and Fariborz Haghighat. Compressed air energy storage in integrated energy systems: A review. *Renewable and Sustainable Energy Reviews*, 167:112701, 2022.

[35] Pierre Bérest, Benoît Brouard, Mehdi Karimi-Jafari, and Arnaud Réveillère. Maximum admissible pressure in salt caverns used for brine production and hydrocarbon storage. *Oil & Gas Science and Technology–Revue d'IFP Energies nouvelles*, 75:76, 2020.

[36] BP Bp. Statistical review of world energy 2022, 2023.

[37] Carol Braester and Jacob Bear. Some hydrodynamic aspects of compressed-air energy storage in aquifers. *Journal of Hydrology*, 73(3-4):201–225, 1984.

[38] Joost JJ Brasz. Comparison of part-load efficiency characteristics of screw and centrifugal compressors. 2006.

[39] Stefano Briola, Paolo Di Marco, Roberto Gabbrielli, and Juri Riccardi. A novel mathematical model for the performance assessment of diabatic compressed air energy storage systems including the turbomachinery characteristic curves. *Applied Energy*, 178:758–772, 2016.

[40] Marcus Budt, Daniel Wolf, Roland Span, and Jinyue Yan. A review on compressed air energy storage: Basic principles, past milestones and recent developments. *Applied energy*, 170:250–268, 2016.

[41] Brian C Cheung, Rupp Carriveau, and David S-K Ting. Parameters affecting scalable underwater compressed air energy storage. *Applied Energy*, 134:239–247, 2014.

[42] M Chikano, Y Yanagase, M Matsunaga, and K Tojo. Development of high efficiency scroll compressor. In *7th Imeche International conference on compressors and their systems*, 2011.

[43] Subhashree Choudhury. Flywheel energy storage systems: A critical review on technologies, applications, and future prospects. *International Transactions on Electrical Energy Systems*, 31(9):e13024, 2021.

[44] Nicolas Courtois, Mostafa Najafiyazdi, Reza Lotfalian, Richard Boudreault, and Mathieu Picard. Analytical expression for the evaluation of multi-stage adiabatic-compressed air energy storage (a-caes) systems cycle efficiency. *Applied Energy*, 288:116592, 2021.

[45] V De Biasi. Fundamental analyses to optimize adiabatic caes plant efficiencies. *Gas Turbine World*, 39(5):26–28, 2009.

[46] Sébastien Declaye, Sylvain Quoilin, Ludovic Guillaume, and Vincent Lemort. Experimental study on an open-drive scroll expander integrated into an orc (organic rankine cycle) system with r245fa as working fluid. *Energy*, 55:173–183, 2013.

[47] María del Rocío Rodríguez-Laguna, Pedro Gomez-Romero, Clivia M Sotomayor Torres, Ming-Chang Lu, and Emigdio Chavez-Angel. Development of low-melting point molten salts and detection of solid-to-liquid transitions by alternative techniques to dsc. *Solar Energy Materials and Solar Cells*, 202:110107, 2019.

[48] Paul Denholm and Ramteen Sioshansi. The value of compressed air energy storage with wind in transmission-constrained electric power systems. *Energy Policy*, 37(8):3149–3158, 2009.

[49] Ghady Dib, Philippe Haberschill, Romuald Rullière, Quentin Perroit, Simon Davies, and Rémi Revellin. Thermodynamic simulation of a micro advanced adiabatic compressed air energy storage for building application. *Applied Energy*, 260:114248, 2020.

[50] Ibrahim Dincer and Marc Rosen. *Thermal energy storage: systems and applications*. John Wiley & Sons, 2002.

[51] Hydro Québec Distribution. Complément d'information du plan d'approvisionnement 2020-2029, 2019.

[52] Michael Doering. Assessment of storage options for reduction of yield losses in a region with 100% renewable electricity. *Energy Procedia*, 73:218–230, 2015.

[53] Mark Dooner and Jihong Wang. Compressed-air energy storage. In *Future Energy*, pages 279–312. Elsevier, 2020.

[54] Easan Drury, Paul Denholm, and Ramteen Sioshansi. The value of compressed air energy storage in energy and reserve markets. *Energy*, 36(8):4959–4973, 2011.

[55] Mehdi Ebrahimi, Rupp Carriveau, David S-K Ting, and Andrew McGillis. Conventional and advanced exergy analysis of a grid connected underwater compressed air energy storage facility. *Applied energy*, 242:1198–1208, 2019.

[56] Mehdi Ebrahimi, David S-K Ting, Rupp Carriveau, Andrew McGillis, and Davin Young. Optimization of a cavern-based compressed air energy storage facility with an efficient adaptive genetic algorithm. *Energy Storage*, 2(6):e205, 2020.

[57] S Egorov, V Nemtinov, Y Nemtinova, and E Egorov. Development of an online application for determination of thermo-physical properties of substances. In *Journal of Physics: Conference Series*, volume 1278, page 012016. IOP Publishing, 2019.

[58] Annette Evans, Vladimir Strezov, and Tim J Evans. Assessment of utility energy storage options for increased renewable energy penetration. *Renewable and Sustainable Energy Reviews*, 16(6):4141–4147, 2012.

[59] Aoife Foley and I Díaz Lobera. Impacts of compressed air energy storage plant on an electricity market with a large renewable energy portfolio. *Energy*, 57:85–94, 2013.

[60] Ann-Kathrin Fries, Friederike Kaiser, Hans-Peter Beck, and Roman Weber. Huntorf 2020-improvement of flexibility and efficiency of a compressed air energy storage plant based on synthetic hydrogen. In *NEIS 2018; Conference on Sustainable Energy Supply and Energy Storage Systems*, pages 1–5. VDE, 2018.

[61] AB Gallo, JR Simões-Moreira, HKM Costa, MM Santos, and E Moutinho Dos Santos. Energy storage in the energy transition context: A technology review. *Renewable and sustainable energy reviews*, 65:800–822, 2016.

[62] Mojtaba Jabbari Ghadi, Ali Azizivahed, Dillip Kumar Mishra, Li Li, Jiangfeng Zhang, Miadreza Shafie-khah, and João PS Catalão. Application of small-scale compressed air energy storage in the daily operation of an active distribution system. *Energy*, 231:120961, 2021.

[63] Bahram Ghorbani, Mehdi Mehrpooya, and Armin Ardehali. Energy and exergy analysis of wind farm integrated with compressed air energy storage using multi-stage phase change material. *Journal of Cleaner Production*, 259:120906, 2020.

[64] Antoni Gil, Marc Medrano, Ingrid Martorell, Ana Lázaro, Pablo Dolado, Belén Zalba, and Luisa F Cabeza. State of the art on high temperature thermal energy storage for power generation. part 1—concepts, materials and modellization. *Renewable and sustainable energy reviews*, 14(1):31–55, 2010.

[65] Dylan CP Grogan. Development of molten-salt heat transfer fluid technology for parabolic trough solar power plants-public final technical report. Technical report, Abengoa Solar, LLC, 2013.

[66] Chaobin Guo, Cai Li, Keni Zhang, Zuansi Cai, Tianran Ma, Federico Maggi, Yixiang Gan, Abbas El-Zein, Zhejun Pan, and Luming Shen. The promise and challenges of utility-scale compressed air energy storage in aquifers.

[67] Chaobin Guo, Lehua Pan, Keni Zhang, Curtis M. Oldenburg, Cai Li, and Yi Li. Comparison of compressed air energy storage process in aquifers and caverns based on the huntorf caes plant. *Applied Energy*, 181:342–356, 2016.

[68] Chaobin Guo, Keni Zhang, Lehua Pan, Zuansi Cai, Cai Li, and Yi Li. Numerical investigation of a joint approach to thermal energy storage and compressed air energy storage in aquifers. *Applied Energy*, 203:948–958, 2017.

[69] Cong Guo, Yujie Xu, Huan Guo, Xinjing Zhang, Xipeng Lin, Liang Wang, Yi Zhang, and Haisheng Chen. Comprehensive exergy analysis of the dynamic process of compressed air energy storage system with low-temperature thermal energy storage. *Applied Thermal Engineering*, 147:684–693, 2019.

[70] Cong Guo, Yujie Xu, Xinjing Zhang, Huan Guo, Xuezhi Zhou, Chang Liu, Wei Qin, Wen Li, Binlin Dou, and Haisheng Chen. Performance analysis of compressed air energy storage systems considering dynamic characteristics of compressed air storage. *Energy*, 135:876–888, 2017.

[71] Huan Guo, Yujie Xu, Lujing Huang, Jianting Sun, and Haisheng Chen. Optimization strategy using corresponding-point methodology (cpm) concerning finite time and heat conduction rate for caes systems. *Energy*, 266:126336, 2023.

[72] Li Guo, Zhouzi Yu, Chengshan Wang, Fangxing Li, Jean Schiettekatte, Jean-Claude Deslauriers, and Lingquan Bai. Optimal design of battery energy storage system for a

wind–diesel off-grid power system in a remote canadian community. *IET Generation, Transmission & Distribution*, 10(3):608–616, 2016.

[73] Tao Hai, Mohammad Zoghi, and Kourosh Javaherdeh. 4e analysis and optimization of a biomass-fired waste-to-energy plant integrated with a compressed air energy storage system for the multi-generation purpose. *Fuel*, 348:128457, 2023.

[74] Zhonghe Han, Senchuang Guo, Shan Wang, and Wei Li. Thermodynamic analyses and multi-objective optimization of operation mode of advanced adiabatic compressed air energy storage system. *Energy Conversion and Management*, 174:45–53, 2018.

[75] Zhonghe Han, Ye Sun, and Peng Li. Research on energy storage operation modes in a cooling, heating and power system based on advanced adiabatic compressed air energy storage. *Energy Conversion and Management*, 208:112573, 2020.

[76] N Hartmann, O Vöhringer, C Kruck, and L Eltrop. Simulation and analysis of different adiabatic compressed air energy storage plant configurations. *Applied Energy*, 93:541–548, 2012.

[77] Qing He, Guoqing Li, Chang Lu, Dongmei Du, and Wenyi Liu. A compressed air energy storage system with variable pressure ratio and its operation control. *Energy*, 169:881–894, 2019.

[78] Yang He, Haisheng Chen, Yujie Xu, Jianqiang Deng, et al. Thermodynamic research on compressed air energy storage system with turbines under sliding pressure operation. *Energy*, 222:119978, 2021.

[79] S Houssainy, M Janbozorgi, P Ip, and P Kavehpour. Thermodynamic analysis of a high temperature hybrid compressed air energy storage (hth-caes) system. *Renewable Energy*, 115:1043–1054, 2018.

[80] Sammy Houssainy, Mohammad Janbozorgi, and Pirouz Kavehpour. Thermodynamic performance and cost optimization of a novel hybrid thermal-compressed air energy storage system design. *Journal of Energy Storage*, 18:206–217, 2018.

[81] Yue Hu, Rui Guo, Per Kvols Heiselberg, and Hicham Johra. Modeling pcm phase change temperature and hysteresis in ventilation cooling and heating applications. *Energies*, 13(23):6455, 2020.

[82] S Huang. A new adiabatic compressed air energy storage system: Modeling, design, optimization, and experiments. Master's thesis, University of Waterloo, 2020.

[83] Mahmoud Huleihil and Gedalya Mazor. Wind turbine power: The betz limit and beyond. In *Advances in wind power*. IntechOpen, 2012.

[84] H Ibrahim, A Bourji, M Ghandour, and A Merabet. Optimization of compressed air storage's volume for a stand-alone wind-diesel hybrid system. In *2013 IEEE Electrical Power & Energy Conference*, pages 1–7. IEEE, 2013.

[85] Hussein Ibrahim, Karim Belmokhtar, and Mazen Ghandour. Investigation of usage of compressed air energy storage for power generation system improving-application in a microgrid integrating wind energy. *Energy Procedia*, 73:305–316, 2015.

[86] Hussein Ibrahim, Adrian Ilinca, Rafic Younes, Jean Perron, and Tammam Basbous. Study of a hybrid wind-diesel system with compressed air energy storage. In *2007 IEEE Canada Electrical Power Conference*, pages 320–325. IEEE, 2007.

[87] Hussein Ibrahim, Rafic Younès, Adrian Ilinca, M Dimitrova, and Jean Perron. Study and design of a hybrid wind–diesel-compressed air energy storage system for remote areas. *Applied Energy*, 87(5):1749–1762, 2010.

[88] Hussein Ibrahim, Rafic Younès, Adrian Ilinca, D Ramdenee, M Dimitrova, Jean Perron, M Adegnon, D Boulay, and C Arbez. Potential of a hybrid wind-diesel-compressed air system for nordic remote canadian areas. *Energy Procedia*, 6:795–804, 2011.

[89] Heidar Jafarizadeh, M. Soltani, and Jatin Nathwani. Assessment of the huntorf compressed air energy storage plant performance under enhanced modifications. *Energy Conversion and Management*, 209:112662, 2020.

[90] E Jannelli, M Minutillo, A Lubrano Lavadera, and G Falcucci. A small-scale caes (compressed air energy storage) system for stand-alone renewable energy power plant for a radio base station: A sizing-design methodology. *Energy*, 78:313–322, 2014.

[91] Mohammad Javidmehr, Fatemeh Joda, and Amin Mohammadi. Thermodynamic and economic analyses and optimization of a multi-generation system composed by a compressed air storage, solar dish collector, micro gas turbine, organic rankine cycle, and desalination system. *Energy conversion and management*, 168:467–481, 2018.

[92] Peng Jiang, Yee Van Fan, and Jiří Jaromír Klemeš. Impacts of covid-19 on energy demand and consumption: Challenges, lessons and emerging opportunities. *Applied energy*, 285:116441, 2021.

[93] Runhua Jiang, Zhuodi Cai, Kewen Peng, and Minlin Yang. Thermo-economic analysis and multi-objective optimization of polygeneration system based on advanced adiabatic compressed air energy storage system. *Energy Conversion and Management*, 229:113724, 2021.

[94] Verena Jülch. Comparison of electricity storage options using levelized cost of storage (lcos) method. *Applied energy*, 183:1594–1606, 2016.

[95] F Kaiser. Steady state analyse of existing compressed air energy storage plants. *Power and Energy Student Summit (PESS) 2015, January 13th-14th, Dortmund Germany*, 2015.

[96] Friederike Kaiser. Steady state analyse of existing compressed air energy storage plants. *Power and Energy Student Summit (PESS) 2015, January 13th-14th, Dortmund Germany*, 2015.

[97] Siddharth Atul Kakodkar. Extensible modeling of compressed air energy storage systems. Master's thesis, University of Waterloo, 2018.

[98] Siva Kalaiselvam and Rajagopalan Parameshwaran. *Thermal energy storage technologies for sustainability: systems design, assessment and applications*. Elsevier, 2014.

[99] JK Kaldellis. An integrated model for performance simulation of hybrid wind–diesel systems. *Renewable Energy*, 32(9):1544–1564, 2007.

[100] Morteza Saleh Kandezi and Seyed Mojtaba Mousavi Naeenian. Investigation of an efficient and green system based on liquid air energy storage (laes) for district cooling and peak shaving: Energy and exergy analyses. *Sustainable Energy Technologies and Assessments*, 47:101396, 2021.

[101] Asim Karim. Multi-objective optimization techniques, 2002.

[102] Hye Rim Kim and Tong Seop Kim. Investigation of synergistic integration and optimization in combining compressed-air energy storage and a gas turbine. *Applied Thermal Engineering*, page 120988, 2023.

[103] YM Kim, DG Shin, and D Favrat. Operating characteristics of constant-pressure compressed air energy storage (caes) system combined with pumped hydro storage based on energy and exergy analysis. *Energy*, 36(10):6220–6233, 2011.

[104] Marcus King, Anjali Jain, Rohit Bhakar, Jyotirmay Mathur, and Jihong Wang. Overview of current compressed air energy storage projects and analysis of the potential underground storage capacity in india and the uk. *Renewable and Sustainable Energy Reviews*, 139:110705, 2021.

[105] T Korakianitis and DG Wilson. Models for predicting the performance of brayton-cycle engines. 1994.

[106] Krzysztof Kosowski, Marian Piwowarski, Wojciech Włodarski, Paweł Ziemiański, and Gabriel Pawlak. Technical and economic analysis of energy storage in the compressed air technology with low capacity for the production plant. *Energy Conversion and Management*, 282:116872, 2023.

[107] Tarik Kousksou, Pascal Bruel, Abdelmajid Jamil, T El Rhafiki, and Youssef Zeraouli. Energy storage: Applications and challenges. *Solar Energy Materials and Solar Cells*, 120:59–80, 2014.

[108] Piotr Krawczyk, Łukasz Szabłowski, Sotirios Karellas, Emmanuel Kakaras, and Krzysztof Badyda. Comparative thermodynamic analysis of compressed air and liquid air energy storage systems. *Energy*, 142:46–54, 2018.

[109] R Kushnir, A Dayan, and A Ullmann. Temperature and pressure variations within compressed air energy storage caverns. *International Journal of Heat and Mass Transfer*, 55(21-22):5616–5630, 2012.

[110] R Kushnir, A Ullmann, and A Dayan. Compressed air flow within aquifer reservoirs of caes plants. *Transport in porous media*, 81(2):219–240, 2010.

[111] Fatemeh Lashgari, Seyed Mostafa Babaei, Mona Zamani Pedram, and Ahmad Arabkoohsar. Comprehensive analysis of a novel integration of a biomass-driven combined heat and power plant with a compressed air energy storage (caes). *Energy Conversion and Management*, 255:115333, 2022.

[112] Joseph CY Lee and M Jason Fields. An overview of wind-energy-production prediction bias, losses, and uncertainties. *Wind Energy Science*, 6(2):311–365, 2021.

[113] Ruixiong Li, Rui Tao, Erren Yao, Haoran Zhang, Yulei Niu, Lanning Ling, An Yan, and Huanran Wang. Decoupling heat-pressure potential energy of compressed air energy storage system: Using near-isothermal compressing and thermal energy storage. *Journal of Energy Storage*, 63:107017, 2023.

[114] Xiaolei Li, Ershu Xu, Shuang Song, Xiangyan Wang, and Guofeng Yuan. Dynamic simulation of two-tank indirect thermal energy storage system with molten salt. *Renewable Energy*, 113:1311–1319, 2017.

[115] Yaowang Li, Fuxing Yao, Shixu Zhang, Yuliang Liu, and Shihong Miao. An optimal dispatch model of adiabatic compressed air energy storage system considering its temperature dynamic behavior for combined cooling, heating and power microgrid dispatch. *Journal of Energy Storage*, 51:104366, 2022.

[116] Jin-Long Liu and Jian-Hua Wang. A comparative research of two adiabatic compressed air energy storage systems. *Energy conversion and management*, 108:566–578, 2016.

[117] Xueling Liu, Lisha Zhong, and Jiansheng Wang. The investigation on a hot dry rock compressed air energy storage system. *Energy Conversion and Management*, 291:117274, 2023.

[118] Shameem Ahmad Lone et al. Integrating a redox flow battery system with a wind-diesel power system. In *2006 International Conference on Power Electronic, Drives and Energy Systems*, pages 1–6. IEEE, 2006.

[119] Xing Luo, Jihong Wang, Christopher Krupke, Yue Wang, Yong Sheng, Jian Li, Yujie Xu, Dan Wang, Shihong Miao, and Haisheng Chen. Modelling study, efficiency analysis and optimisation of large-scale adiabatic compressed air energy storage systems with low-temperature thermal storage. *Applied energy*, 162:589–600, 2016.

[120] Sebastian C Manchester, Lukas G Swan, and Dominic Groulx. Regenerative air energy storage for remote wind–diesel micro-grid communities. *Applied Energy*, 137:490–500, 2015.

[121] Youssef Mazloum, Haytham Sayah, and Maroun Nemer. Exergy analysis and exergoeconomic optimization of a constant-pressure adiabatic compressed air energy storage system. *Journal of Energy Storage*, 14:192–202, 2017.

[122] Mark Mehos, Craig Turchi, Judith Vidal, Michael Wagner, Zhiwen Ma, Clifford Ho, William Kolb, Charles Andraka, and Alan Kruizenga. Concentrating solar

power gen3 demonstration roadmap. Technical report, National Renewable Energy Lab.(NREL), Golden, CO (United States), 2017.

[123] ShengWei Mei, JunJie Wang, Fang Tian, LaiJun Chen, XiaoDai Xue, Qiang Lu, Yuan Zhou, and XiaoXin Zhou. Design and engineering implementation of non-supplementary fired compressed air energy storage system: Ticc-500. *Science China Technological Sciences*, 58(4):600–611, 2015.

[124] Hui Meng, Meihong Wang, Olumide Olumayegun, Xiaobo Luo, and Xiaoyan Liu. Process design, operation and economic evaluation of compressed air energy storage (caes) for wind power through modelling and simulation. *Renewable energy*, 136:923–936, 2019.

[125] Seán Moran. Pump sizing: Bridging the gap between. *The Best of Equipment Series*, page 3, 2016.

[126] H Mozayeni, X Wang, and M Negnevitsky. Thermodynamic and exergy analysis of a combined pumped hydro and compressed air energy storage system. *Sustainable Cities and Society*, 48:101527, 2019.

[127] Hamidreza Mozayeni, Xiaolin Wang, and Michael Negnevitsky. Dynamic analysis of a low-temperature adiabatic compressed air energy storage system. *Journal of Cleaner Production*, 276:124323, 2020.

[128] Simone Mucci, Aldo Bischi, Stefano Briola, and Andrea Baccioli. Small-scale adiabatic compressed air energy storage: Control strategy analysis via dynamic modelling. *Energy Conversion and Management*, 243:114358, 2021.

[129] Natalia Naval, Jose M Yusta, Raul Sánchez, and Fernando Sebastián. Optimal scheduling and management of pumped hydro storage integrated with grid-connected renewable power plants. *Journal of Energy Storage*, 73:108993, 2023.

[130] AG Olabi, Tabbi Wilberforce, Mohamad Ramadan, Mohammad Ali Abdelkareem, and Abdul Hai Alami. Compressed air energy storage systems: Components and operating parameters–a review. *Journal of Energy Storage*, 34:102000, 2021.

[131] Iñigo Ortega-Fernández, Simone A Zavattoni, Javier Rodríguez-Aseguinolaza, Bruno D'Aguanno, and Maurizio C Barbato. Analysis of an integrated packed bed thermal energy storage system for heat recovery in compressed air energy storage technology. *Applied energy*, 205:280–293, 2017.

[132] Hao Peng, Yu Yang, Rui Li, and Xiang Ling. Thermodynamic analysis of an improved adiabatic compressed air energy storage system. *Applied energy*, 183:1361–1373, 2016.

[133] C. Pichery. Sensitivity analysis. In Philip Wexler, editor, *Encyclopedia of Toxicology (Third Edition)*, pages 236–237. Academic Press, Oxford, third edition edition, 2014.

[134] Annie Pike and Michael Kummert. District heating: a practical solution for reducing fossil fuel dependency in quebec's remote communities. In *Building Simulation 2021*, volume 17, pages 431–438. IBPSA, 2021.

[135] Andrew Pimm and Seamus D Garvey. Underwater compressed air energy storage. In *Storing Energy*, pages 157–177. Elsevier, 2022.

[136] Andrew J Pimm, Seamus D Garvey, and Maxim de Jong. Design and testing of energy bags for underwater compressed air energy storage. *Energy*, 66:496–508, 2014.

[137] Ali Piri, Cyrus Aghanajafi, and Ali Sohani. Enhancing efficiency of a renewable energy assisted system with adiabatic compressed-air energy storage by application of multiple kalina recovery cycles. *Journal of Energy Storage*, 61:106712, 2023.

[138] Justin W Raade and David Padowitz. Development of molten salt heat transfer fluid with low melting point and high thermal stability. 2011.

[139] Faizur Rahman, Shafiqur Rehman, and Mohammed Arif Abdul-Majeed. Overview of energy storage systems for storing electricity from renewable energy sources in saudi arabia. *Renewable and Sustainable Energy Reviews*, 16(1):274–283, 2012.

[140] Mandhapati Raju and Siddhartha Kumar Khaitan. Modeling and simulation of compressed air storage in caverns: A case study of the huntorf plant. *Applied Energy*, 89(1):474–481, 2012. Special issue on Thermal Energy Management in the Process Industries.

[141] Gazala Rashid, Shameem Ahmad Lone, and Mairaj Ud-Din Mufti. Modeling and performance assessment of an isolated wind-diesel system with flywheel energy storage system. *Wind Engineering*, page 0309524X221147601, 2023.

[142] Amir Reza Razmi and Majid Janbaz. Exergoeconomic assessment with reliability consideration of a green cogeneration system based on compressed air energy storage (caes). *Energy Conversion and Management*, 204:112320, 2020.

[143] Amirreza Razmi, M Soltani, Mohammad Tayefeh, M Torabi, and MB Dusseault. Thermodynamic analysis of compressed air energy storage (caes) hybridized with a multi-effect desalination (med) system. *Energy Conversion and Management*, 199:112047, 2019.

[144] Amirreza Razmi, M. Soltani, and M. Torabi. Investigation of an efficient and environmentally-friendly cchp system based on caes, orc and compression-absorption refrigeration cycle: Energy and exergy analysis. *Energy Conversion and Management*, 195:1199–1211, 2019.

[145] Arnaud Réveillère, Virginie Hamm, Hervé Lesueur, Elisabeth Cordier, and Patrick Goblet. Geothermal contribution to the energy mix of a heating network when using aquifer thermal energy storage: modeling and application to the paris basin. *Geothermics*, 47:69–79, 2013.

[146] A Rogers, A Henderson, X Wang, and M Negnevitsky. Compressed air energy storage: Thermodynamic and economic review. In *2014 IEEE PES General Meeting—Conference & Exposition*, pages 1–5. IEEE, 2014.

[147] Philipp Roos and Andreas Haselbacher. Analytical modeling of advanced adiabatic compressed air energy storage: Literature review and new models. *Renewable and Sustainable Energy Reviews*, 163:112464, 2022.

[148] K Rouindej. *Study of Electrical Grid Profile & Behavior and its Impact on Design and Operation of Adiabatic Compressed Air Energy Storage (A-CAES) Systems*. PhD thesis, 2019.

[149] Kamyar Rouindej, Ehsan Samadani, and Roydon A Fraser. Caes by design: A user-centered approach to designing compressed air energy storage (caes) systems for future electrical grid: A case study for ontario. *Sustainable Energy Technologies and Assessments*, 35:58–72, 2019.

[150] Kamyar Rouindej, Ehsan Samadani, and Roydon A Fraser. A comprehensive data-driven study of electrical power grid and its implications for the design, performance, and operational requirements of adiabatic compressed air energy storage systems. *Applied Energy*, 257:113990, 2020.

[151] Kamyar Rouindej, Ehsan Samadani, and Roydon A. Fraser. A comprehensive data-driven study of electrical power grid and its implications for the design, performance, and operational requirements of adiabatic compressed air energy storage systems. *Applied Energy*, 257:113990, 2020.

[152] Hossein Safaei and David W Keith. Compressed air energy storage with waste heat export: An alberta case study. *Energy Conversion and Management*, 78:114–124, 2014.

[153] Tapas Kumar Saha and Debaprasad Kastha. Design optimization and dynamic performance analysis of a stand-alone hybrid wind–diesel electrical power generation system. *IEEE Transactions on Energy Conversion*, 25(4):1209–1217, 2010.

[154] Andrea Saltelli, Stefano Tarantola, Francesca Campolongo, and Marco Ratto. *Sensitivity Analysis in Practice: A Guide to Assessing Scientific Models*. Wiley, 2004.

[155] Erwan Adi Saputro, Refat Al-Shannaq, and Mohammed M Farid. Performance of metal and non-metal coated phase change materials microcapsules when used in compressed air energy storage system. *Applied Thermal Engineering*, 157:113715, 2019.

[156] Sepideh Sarmast, Roydon A Fraser, and Maurice B Dusseault. Performance and cyclic heat behavior of a partially adiabatic cased-wellbore compressed air energy storage system. *Journal of Energy Storage*, 44:103279, 2021.

[157] Sepideh Sarmast, Kamyar Rouindej, Roydon A. Fraser, and Maurice B. Dusseault. Sizing-design method for compressed air energy storage (caes) systems: A case study based on power grid in ontario. *Energy Conversion and Management*, 277:116656, 2023.

[158] Sepideh Sarmast, Kamyar Rouindej, Roydon A Fraser, and Maurice B Dusseault. Optimizing near-adiabatic compressed air energy storage (na-caes) systems: Sizing and design considerations. *Applied Energy*, 357:122465, 2024.

[159] Sepideh Sarmast, Stephan Séjourné, Andrew Wigston, Roydon A. Fraser, and Maurice B. Dusseault. Adaptive hybrid energy system for remote canadian communities. *Energy Conversion and Management*, 2024.

[160] Adriano Sciacovelli, Yongliang Li, Haisheng Chen, Yuting Wu, Jihong Wang, Seamus Garvey, and Yulong Ding. Dynamic simulation of adiabatic compressed air energy storage (a-caes) plant with integrated thermal storage–link between components performance and plant performance. *Applied energy*, 185:16–28, 2017.

[161] R Sebastián and R Peña-Alzola. Control and simulation of a flywheel energy storage for a wind diesel power system. *International Journal of Electrical Power & Energy Systems*, 64:1049–1056, 2015.

[162] M Soltani, M. H Nabat, A. R Razmi, M. B Dusseault, and J Nathwani. A comparative study between orc and kalina based waste heat recovery cycles applied to a green compressed air energy storage (caes) system. *Energy Conversion and Management*, 222:113203, 2020.

[163] DA Spera and TR Richards. Modified power law equations for vertical wind profiles. In *Proceedings of the Conference and Workshop on Wind Energy Characteristics and Wind Energy Siting; 19-21 June 1979; Portland, Oregon (USA)*, pages 47–58, 1979.

[164] Lukasz Szablowski, Piotr Krawczyk, Krzysztof Badyda, Sotirios Karellas, Emmanuel Kakaras, and Wojciech Bujalski. Energy and exergy analysis of adiabatic compressed air energy storage system. *Energy*, 138:12–18, 2017.

[165] Michael J Tessier, Michael C Floros, Laziz Bouzidi, and Suresh S Narine. Exergy analysis of an adiabatic compressed air energy storage system using a cascade of phase change materials. *Energy*, 106:528–534, 2016.

[166] Vittorio Tola, Valentina Meloni, Fabrizio Spadaccini, and Giorgio Cau. Performance assessment of adiabatic compressed air energy storage (a-caes) power plants integrated with packed-bed thermocline storage systems. *Energy conversion and management*, 151:343–356, 2017.

[167] Zheming Tong, Zhewu Cheng, and Shuiguang Tong. A review on the development of compressed air energy storage in china: Technical and economic challenges to commercialization. *Renewable and Sustainable Energy Reviews*, 135:110178, 2021.

[168] G Venkataramani, P Parankusam, V Ramalingam, and J Wang. A review on compressed air energy storage–a pathway for smart grid and polygeneration. *Renewable and Sustainable Energy Reviews*, 62:895–907, 2016.

[169] Zhenjie Wan, Jinjia Wei, Mumtaz A Qaisrani, Jiabin Fang, and Nan Tu. Evaluation on thermal and mechanical performance of the hot tank in the two-tank molten salt heat storage system. *Applied Thermal Engineering*, 167:114775, 2020.

[170] Jidai Wang, Kunpeng Lu, Lan Ma, Jihong Wang, Mark Dooner, Shihong Miao, Jian Li, and Dan Wang. Overview of compressed air energy storage and technology development. *Energies*, 10(7):991, 2017.

[171] Tongtao Wang, Guoyin An, Shuai Xu, Jianchao Jia, Wenquan Wang, and Jaak JK Daemen. Minimum operating pressure for a gas storage salt cavern under an emergency: a case study of jintan, china. *Oil & Gas Science and Technology–Revue d'IFP Energies nouvelles*, 75:85, 2020.

[172] X Wang, C Yang, M Huang, and X Ma. Off-design performances of gas turbine-based cchp combined with solar and compressed air energy storage with organic rankine cycle. *Energy Conversion and Management*, 156:626–638, 2018.

[173] Zhiwen Wang, Wei Xiong, David S-K Ting, Rupp Carriveau, and Zuwen Wang. Conventional and advanced exergy analyses of an underwater compressed air energy storage system. *Applied energy*, 180:810–822, 2016.

[174] Zhiwen Wang, Wei Xiong, David S-K Ting, Rupp Carriveau, and Zuwen Wang. Comparison of underwater and underground caes systems for integrating floating offshore wind farms. *Journal of Energy Storage*, 14:276–282, 2017.

[175] Timothy M Weis and Adrian Ilinca. The utility of energy storage to improve the economics of wind–diesel power plants in canada. *Renewable energy*, 33(7):1544–1557, 2008.

[176] Daniel Wolf and Marcus Budt. Lta-caes–a low-temperature approach to adiabatic compressed air energy storage. *Applied Energy*, 125:158–164, 2014.

[177] Daniel Wolf, Marcus Budt, and HJ Prümper. Lta-caes low-temperature adiabatic compressed air energy storage. In *Proceedings of the 6th international renewable energy storage conference IRES*, pages 28–30, 2011.

[178] Di Wu, JG Wang, Bowen Hu, and Sheng-Qi Yang. A coupled thermo-hydro-mechanical model for evaluating air leakage from an unlined compressed air energy storage cavern. *Renewable Energy*, 146:907–920, 2020.

[179] Caichu Xia, Yu Zhou, Shuwei Zhou, Pingyang Zhang, and Fei Wang. A simplified and unified analytical solution for temperature and pressure variations in compressed air energy storage caverns. *Renewable Energy*, 74:718–726, 2015.

[180] Xiaojun Xue, Jiarui Li, Jun Liu, Yunyun Wu, Heng Chen, Gang Xu, and Tong Liu. Performance evaluation of a conceptual compressed air energy storage system coupled with a biomass integrated gasification combined cycle. *Energy*, 247:123442, 2022.

[181] Ke Yang, Yuan Zhang, Xuemei Li, and Jianzhong Xu. Theoretical evaluation on the impact of heat exchanger in advanced adiabatic compressed air energy storage system. *Energy conversion and management*, 86:1031–1044, 2014.

[182] Binxin Yin, Yaowang Li, Shihong Miao, Yujun Lin, and Haipeng Zhao. An economy and reliability co-optimization planning method of adiabatic compressed air energy storage for urban integrated energy system. *Journal of Energy Storage*, 40:102691, 2021.

[183] Behnam Zakeri and Sanna Syri. Electrical energy storage systems: A comparative life cycle cost analysis. *Renewable and sustainable energy reviews*, 42:569–596, 2015.

[184] Fritz Zaversky, Javier García-Barberena, Marcelino Sánchez, and David Astrain. Transient molten salt two-tank thermal storage modeling for csp performance simulations. *Solar Energy*, 93:294–311, 2013.

[185] Jianjun Zhang, Shengni Zhou, Shuaiqi Li, Wenji Song, and Ziping Feng. Performance analysis of diabatic compressed air energy storage (d-caes) system. *Energy Procedia*, 158:4369–4374, 2019.

[186] Xiaoming Zhang, Yuting Wu, Chongfang Ma, Qiang Meng, Xiao Hu, and Cenyu Yang. Experimental study on temperature distribution and heat losses of a molten salt heat storage tank. *Energies*, 12(10):1943, 2019.

[187] Pan Zhao, Yiping Dai, and Jiangfeng Wang. Design and thermodynamic analysis of a hybrid energy storage system based on a-caes (adiabatic compressed air energy storage) and fess (flywheel energy storage system) for wind power application. *Energy*, 70:674–684, 2014.

[188] Pan Zhao, Yiping Dai, and Jiangfeng Wang. Design and thermodynamic analysis of a hybrid energy storage system based on a-caes (adiabatic compressed air energy storage) and fess (flywheel energy storage system) for wind power application. *Energy*, 70:674–684, 2014.

[189] Pan Zhao, Mingkun Wang, Jiangfeng Wang, and Yiping Dai. A preliminary dynamic behaviors analysis of a hybrid energy storage system based on adiabatic compressed air energy storage and flywheel energy storage system for wind power application. *Energy*, 84:825–839, 2015.

[190] Qian Zhou, Dongmei Du, Chang Lu, Qing He, and Wenyi Liu. A review of thermal energy storage in compressed air energy storage system. *Energy*, 188:115993, 2019.

APPENDICES

Appendix A

Coverage-percentage Method Verification

Figures A.1(a) and (b) illustrate the charging and discharging coverage percentages over a 24-hour operation period for the initial conditions of an empty and a full cavern, respectively, and for a periodic pattern of excess and shortage power (MW). The pattern of excess and shortage is: +100, +100, -100, -100, +100, +100, -100, -100, ...; where positive and negative values indicate excess and shortage power, respectively. Figure A.1(c) includes data for both an initially empty and an initially full cavern while continuing the same two hour periodic +100 MW/-100 MW pattern, but now a full year (8760 hours) of operation is considered. Figure A.1(d) introduces a new random pattern with the excess and shortage power changing each hour to a random value ranging between -100 MW and 100 MW. All graphs in Figure A.1 depict results from 250 scenarios for each of the frequency-of-occurrence method and the coverage-percentage method. The scenarios cover 5 compressor sizes from 10 to 50 MW in 10 MW intervals, 5 expander sizes from 10 to 50 MW in 10 MW intervals, and 10 cavern sizes from 10 to 100 MWh in 10 MWh intervals.

It is observed, however, that these 250 scenarios yield far fewer than 250 distinct data points in Figures A.1(a), (b), and (c) as many results precisely overlap in the case of frequency-of-occurrence method, and very nearly overlap (i.e., not visually distinct) in the case of coverage-percentage method. In Figures A.1(a) and (b) this results in there being only 30 distinct frequency-of-occurrence method data points, and 24 visually distinct coverage-percentage method data points, per graph. When CAES operation is extended from 24 hours to 1 year (Figure A.1(c)) for the same periodic excess and shortage power pattern the data further collapses to fewer data points. Specifically, the frequency-of-occurrence method results collapse to 10 distinct data points and the coverage-percentage

method results collapse to 15 distinct data points. That the data collapses to fewer data points in Figure A.1(c) is as expected as the influence of the initial starting charge (empty or full) fades from importance. Next, by observing that upon switching from a periodic excess and shortage energy pattern (Figure A.1(a), (b) and (c)) to a random energy pattern (Figure A.1(d)) the results for both the frequency-of-occurrence and coverage-percentage methods no longer display the strong propensity to collapse to far fewer data points than scenarios analyzed. There remains, however, still some data collapse in the random energy pattern results of Figure A.1(d) as there are still fewer than 250 visually distinct data points for each of the frequency-of-occurrence and coverage-percentage methods. That there remains some close proximity (near overlap) between many scenarios in Figure A.1(d) is not unexpected given the number of degrees of freedom (three) in the scenarios exceeds the two degrees of freedom of the graphs, and given the systematic pattern in the scenarios run. In brief, most of the data collapse in Figure A.1 is from the 250 scenarios is due to correlations in the excess and shortage power pattern, and far less due to the selected initial cavern charge condition or the systematic scenario selection pattern for compressor, expander, and cavern sizes. Further, the coverage-percentage method involves two additional degrees of freedom given its use of cavern pressure and temperature limits. These two degrees of freedom where not varied but rather were fixed at lower and upper limits of 5 MPa and 14 MPa, and 20 C and 50 C, however, these limits are responsible for the coverage-percentage method data points that collapse together not precisely overlapping in Figures A.1(a) and (b). This is in contrast to the frequency-of-occurrence method collapsed data points in Figures A.1(a) and (b) that do precisely overlap.

The collapse of data to fewer data points due to the use of a periodic excess and shortage power pattern, as described and discussed above, is advantageous for the purpose of verifying the coverage-percentage method. Verification of the coverage-percentage method includes the following:

- The distribution of charging coverage percentage vs. discharging coverage percentage for an empty cavern which undergoes a periodic excess and shortage pattern over a short operation period (24 hours) consists of a diagonal line and some horizontal lines of dots (see A.1(a)). The horizontal lines are expected for a process that starts with an empty cavern and in which this empty cavern over a short period is still filling to its steady-state start-of-fill capacity (note: because of the periodic excess and shortage power pattern the amount of air filling and discharging into and from the cavern will also become periodic, however, initially it will not be periodic until the cavern has filled sufficiently). Correspondingly, the expectation over a longer period of time is for the horizontal lines to approach a point on the diagonal line until there is just

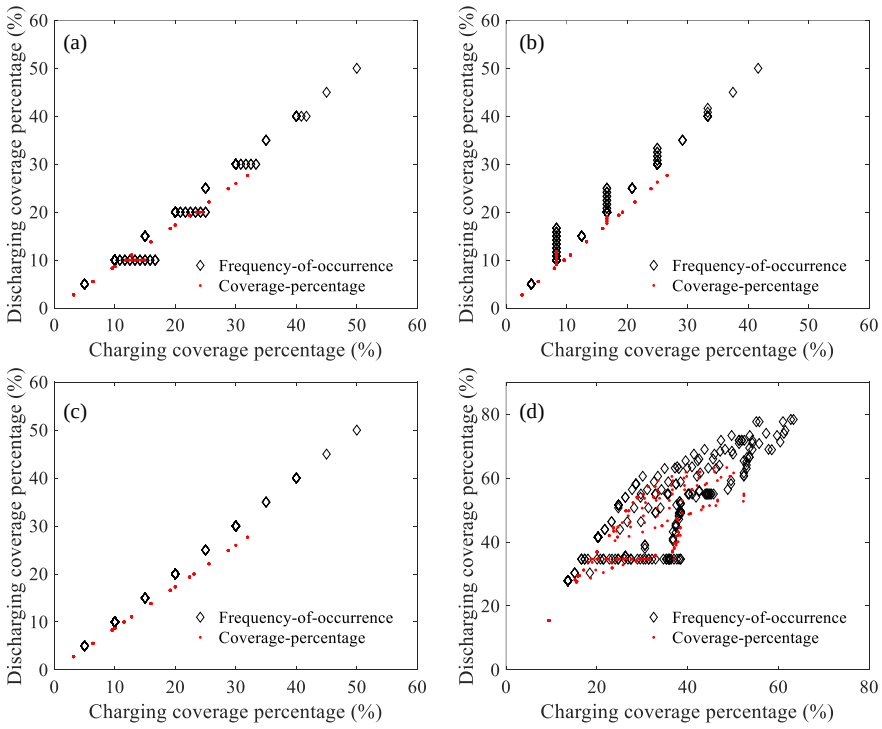

Figure A.1: CAES coverage percentages for 250 scenarios for each of frequency-of-occurrence (diamonds) and coverage-percentage (points) methods (scenarios cover 5 different compressor sizes from 10 to 50 MW in 10 MW intervals, 5 different expander sizes from 10 to 50 MW in 10 MW intervals, and 10 different cavern sizes from 10 to 100 MWh in 10 MWh intervals). Cases (a), (b), and (c) are based on a periodic excess and shortage power pattern of +100 MW and -100MW switching every two hours, while case (d) is based on a random excess or shortage power value ranging between -100 MW to +100 MW changing hourly. Further, the initial cavern charge and duration of operation are as follows: (a) initially empty cavern, 24 hours operation; (b) initially full cavern, 24 hours operation; (c) both initially empty and initially full cavern, 8760 hours or 1 year operation; and (d) initially empty cavern, 24 hours operation.

a diagonal line. This does indeed happen as shown in A.1(c) when the operation time for an initially empty cavern extends to 1 year (8760 hours). Similarly, when the cavern is initially filled (see A.1(b)) vertical lines are observed as expected over the short operation period of 24 hours while after a year all scenarios collapse to the diagonal line (see A.1(c)).

- When the excess and shortage pattern is random (ranged between -100 and 100 MW) instead of periodic, the distribution of charging coverage percentage vs. discharging coverage percentage no longer collapses to the diagonal line, but rather it is like a combination of the two studied cases in Figures A.1(a), and (b) which spreads the diagonal line both horizontally (initially empty cavern) and vertically (initially full cavern) as the cavern capacity never reaches a steady-state start-of-fill capacity. This behavior is seen in A.1(d) as expected. In other words, as the correlation between excess power and power shortage decreases, the spread in the charging and discharging coverage percentages distribution increases from the diagonal line. The patterns seen in A.1(d) are a result of the systematic pattern in the scenarios selected as similarly previously explained for Figure **??**.

Appendix B

Thermodynamic Modeling Validation

This Appendix presents a comparison between the results obtained from the developed mathematical model for the CAES reservoir and the experimental data sourced from the study by Xia et al. [179]. In order to validate the accuracy and reliability of the mathematical model, the air temperature and pressure variations within the reservoir of the Huntorf plant are analyzed. The graphical representations of these variations are illustrated in Figure B.1(a) for air temperature and Figure B.1(b) for air pressure. Comparing the mathematical and experimental results, it is evident that there is a good agreement between the mathematical results and the experimental data. The trends and patterns observed in both sets of data align well, indicating that the mathematical model successfully captures the essential dynamics of air temperature and pressure variations within the CAES reservoir during charging, discharging, and idle modes.

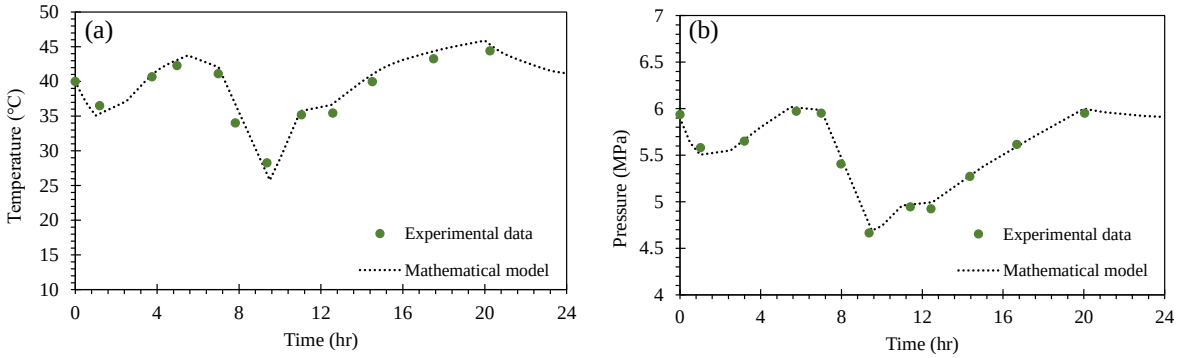

Figure B.1: The air temperature (a), and pressure (b) variations inside the Huntorf reservoir.

Appendix C

Technical Specifications of the E-53 Turbine

The detailed technical specifications and power output characteristics of the E-53 turbine have been obtained from the manufacturer's documentation [5]. This turbine is equipped with a cut-in mechanism designed to initiate operation at wind speeds as low as 2 m/s, ensuring optimal performance even in relatively mild wind conditions. Conversely, to safeguard the turbine and its components, a cut-out mechanism discontinues operation when wind speeds exceed 25 m/s, preventing potential damage and ensuring the longevity of the system. The turbine provides a consistent output of 810 kW beyond wind speeds of 13 m/s, as illustrated in Figure C.1.

To estimate the wind turbine's power output under different wind speeds, the equations presented in Table C.1 can be employed. These equations, derived from the information presented in Figure C.1, offer a systematic approach for predicting the turbine's performance across a spectrum of wind conditions.

Table C.1: Wind power output at different wind speeds without considering losses.

Power output	Wind speed
0	wind speed < 2
Slope $\times (v - v_0) + P_0$	$2 \leq$ wind speed < 13
810	$13 \leq$ wind speed ≤ 25
0	wind speed > 25

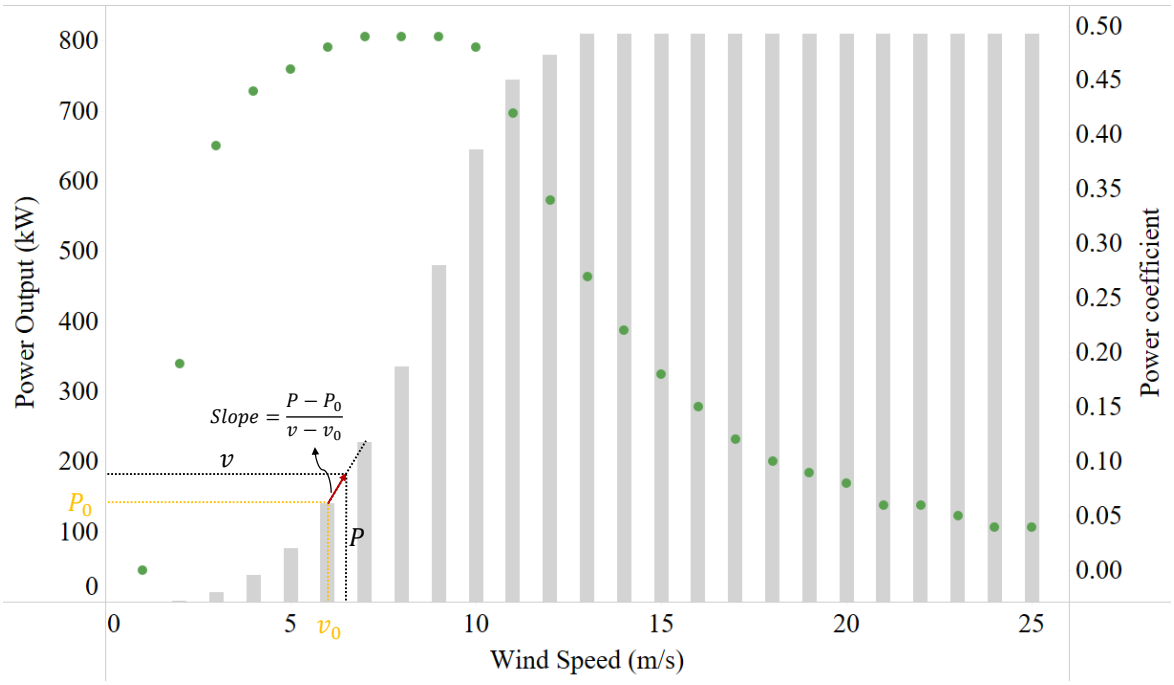

Figure C.1: Technical specifications and power output values of the E-53 turbine.

Appendix D

Community Diesel Load and Excess Wind Power in Kangirsuk

The graphical representation in Figure D.1(a) illustrates the hourly community diesel load within the village of Kangirsuk throughout the year 2021, with the installation of a single wind turbine. Figure D.1(b) depicts the surplus wind power generated as a consequence of the singular wind turbine installation.

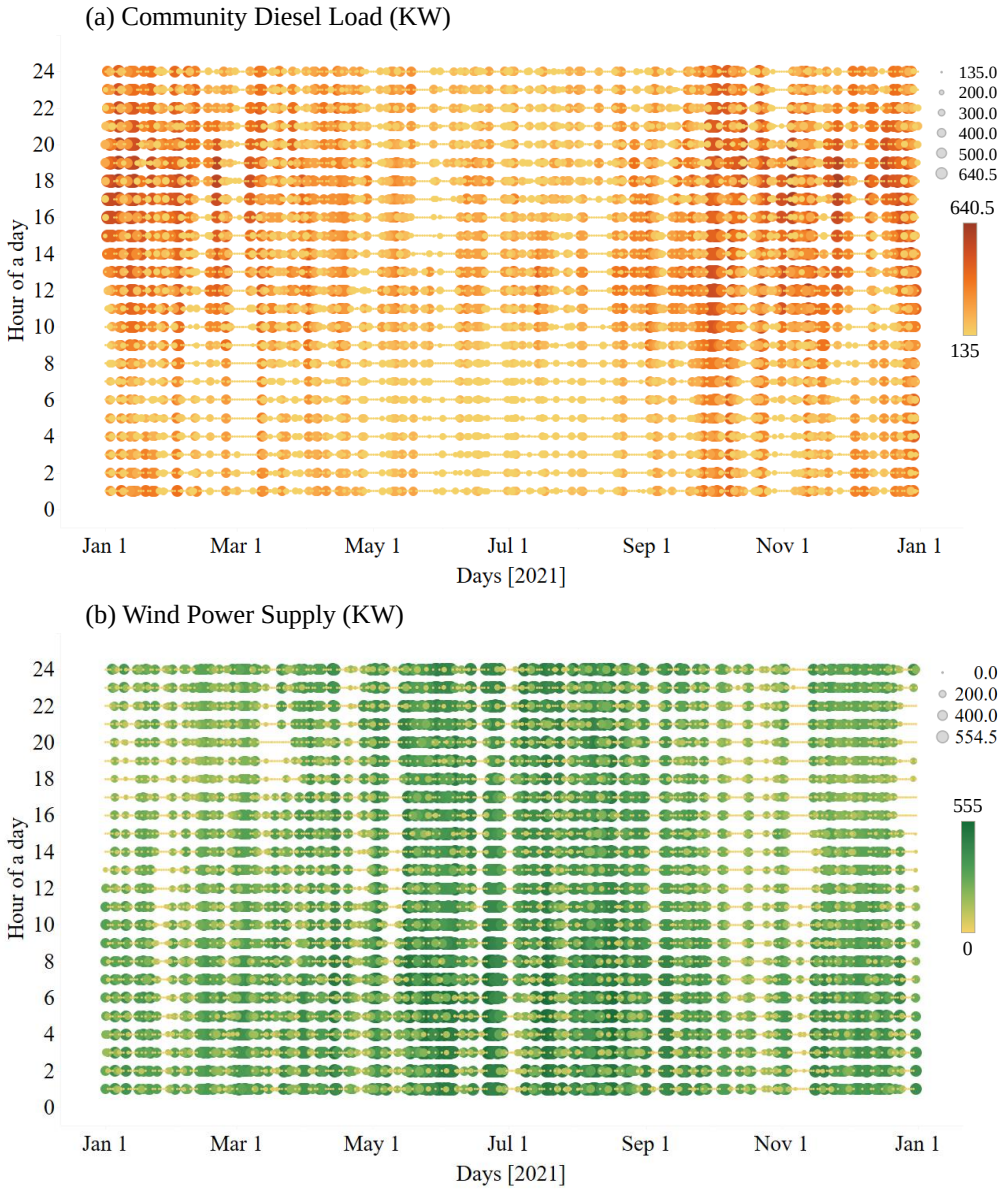

Figure D.1: Hourly remaining community load (net load minus the generated wind), and wind power generation surplus (one wind turbine) in the village of Kangirsuk in 2021; the color bars show the value, while the circle's diameter corresponds to magnitude.

Appendix E

Results of Utilization of Two Wind Turbines in Kangirsuk

Figures E.1(a) and (b) illustrate the frequency of occurrence for excess power and power shortage, along with their respective cumulative frequency of occurrence (expressed in %) for the scenario involving two wind turbines. Additionally, Figures E.1(c) and (d) depict the frequency of occurrence for excess energy and energy shortage, accompanied by their cumulative frequency of occurrence expressed in percentages, for the same scenario. Figure E.2 also depicts the duration of excess and shortage events for each month, considering two wind turbines in the village of Kangirsuk in 2021.

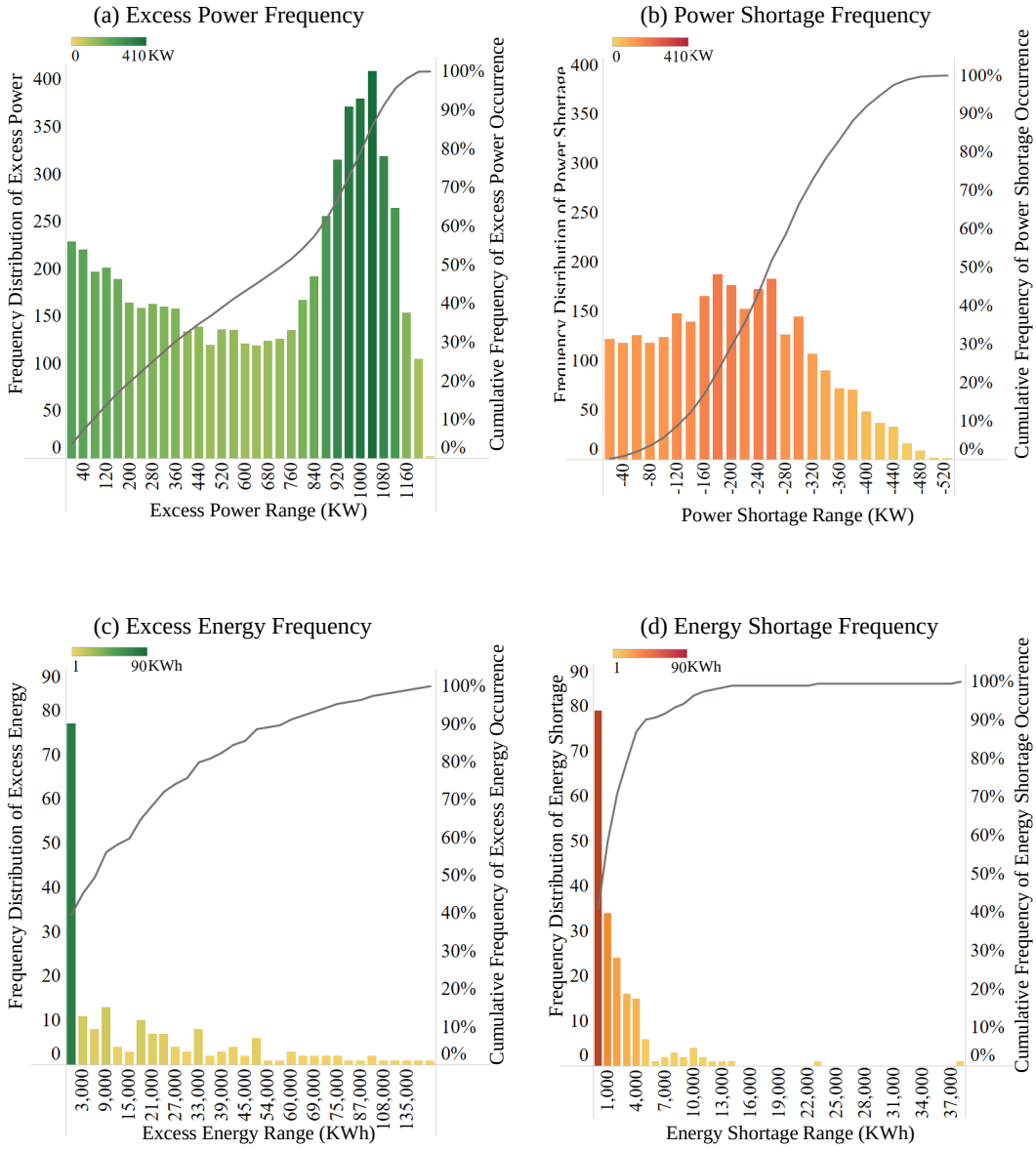

Figure E.1: Annual frequency distribution of excess power (graph (a)) and power shortage (graph (b)), along with the corresponding cumulative frequency of occurrence (grey lines), and annual frequency distribution of excess energy (graph (c)) and energy shortage (graph (d)), along with the corresponding cumulative frequency of occurrence (grey lines), considering two wind turbines in the village of Kangirsuk in 2021.

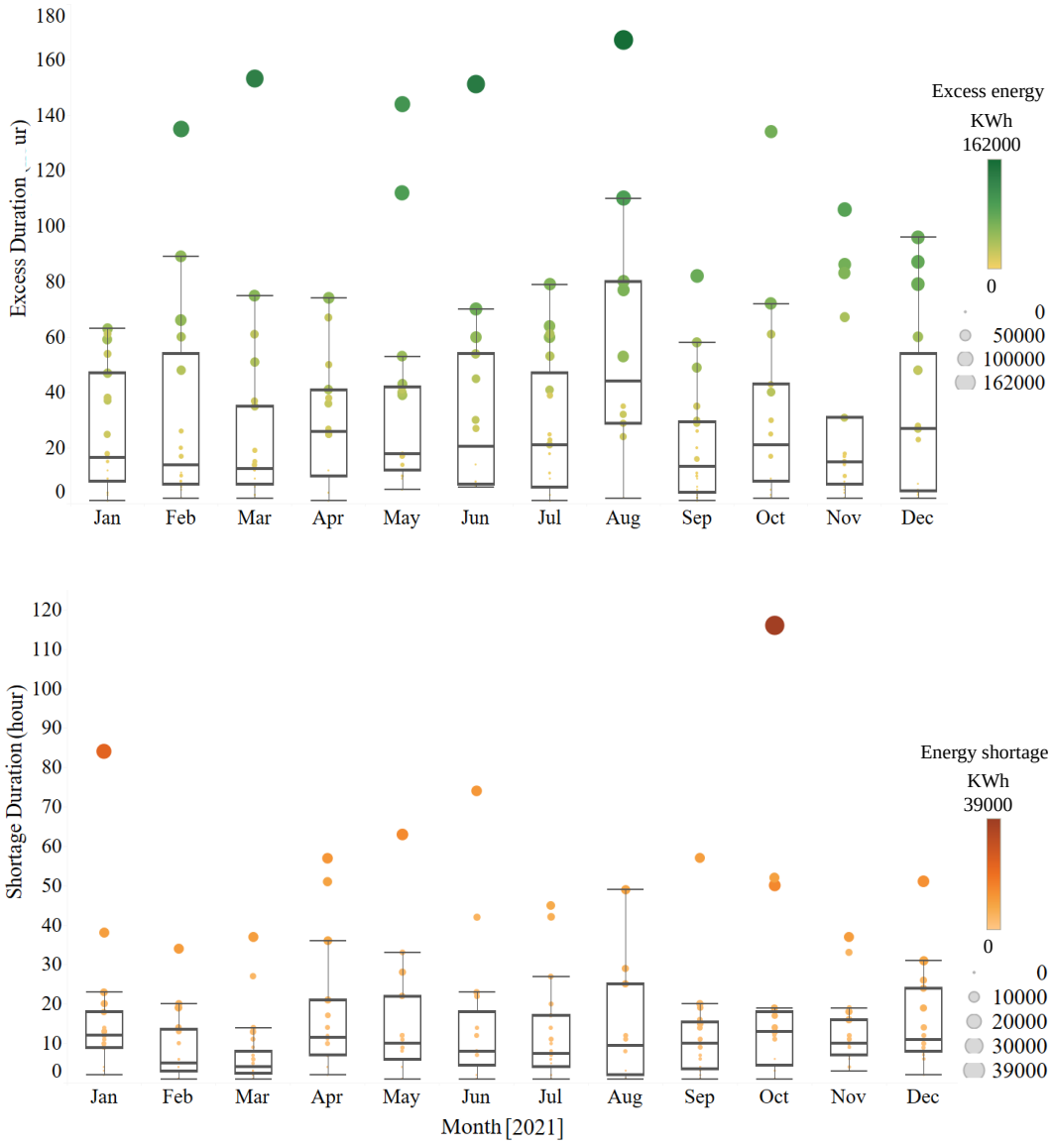

Figure E.2: Duration of excess (upper graph) and shortage (lower graph) events for each month, considering two wind turbines in the village of Kangirsuk in 2021; dashed grey lines depict how excess outliers can be utilized to cover shortage outliers.